Characterisation of Electrodes, Electrolytes and Interphases for Lithium Metal and Potassium-Ion Batteries



Ben Jagger
St. Edmund Hall
University of Oxford

A thesis submitted for the degree of
Doctor of Philosophy

Hilary Term 2025

Abstract

A range of complementary battery technologies will be required to meet the ever-growing demand for energy storage. Lithium metal batteries (LMBs) are promising owing to their high energy and power densities, enabling electrification to extend to new industries, while potassium-ion batteries (KIBs) are attractive due to their low cost and the abundance of potassium resources, minimising the risk of supply shocks. However, the commercialisation of both systems is hindered by their poor cycle life as a result of solid electrolyte interphase (SEI) formation. The composition and properties of the SEI are determined by the chemistries of both the electrode and the electrolyte, and electrolyte transport properties further determine cell rate capability, so accurate characterisation of electrodes, electrolytes and interphases will be vital to understand battery performance and degradation.

In this thesis, first the concentration-dependent salt diffusivities, cation transference numbers, ionic conductivities and thermodynamic factors are characterised in equivalent lithium- and potassium-ion electrolytes. It is revealed that the potassium-ion system displays superior salt diffusivities and cation transference numbers, but the salt dissociates to a lesser extent. This is attributed to the lower charge density of the cation reducing species-species interactions.

Second, systematic X-ray photoelectron spectroscopy depth profiling studies are performed to uncover the influence that temperature, electrolyte chemistry and formation time have on the composition of the SEI formed on lithium metal. At low temperature and concentration the SEI is primarily organic and porous, permitting electrolyte impregnation, while at high temperature and concentration it is more conductive and anion derived. These trends are related to the solvation structure of the electrolyte. Significant differences are observed in the SEI species formed on lithium and potassium metal, which are attributed to steric effects caused by the different ionic radii of the two cations.

Finally, two-phase In-In_4K and Bi-Bi_2K alloys are explored as reference electrodes for KIBs. Bi-Bi_2K is most promising as it displays a stable potential of 1.07 V vs. K^+/K and it results in significantly less electrolyte reduction than potassium metal. Three-electrode cells are used to cycle graphite with Bi-Bi_2K as the reference electrode, proving its successful implementation. This paves the way for future studies on the SEI that forms on graphite without the need for potassium metal, eliminating any influence from cross-talk.

Acknowledgements

First, I would like to thank my supervisor, Prof. Mauro Pasta, for his mentorship throughout my DPhil. I have appreciated the freedom that he has given me, allowing me to steer my research in the directions that interest me most, while his continual guidance has kept me on track and ensured that my research builds towards real-world goals. The insights he has provided into what it takes to pursue a successful research career have been valuable to me.

I am grateful to Dr Shobhan Dhir for the training and support he provided throughout my DPhil, as well as his ongoing friendship. Shobhan's attention to detail has left a lasting impact on my own approach to research, and I thoroughly enjoyed collaborating with him. I must also thank Dr Sudarshan Narayanan, Dr Maximilian Schart and Dr Yvonne Chart for their time and expertise in getting me set up in the lab, and Dr Esther Townsend for keeping the lab running smoothly.

The work presented in this thesis would not have been possible without the help of Alen Maguire, Dr Jack Aspinall, Souhardh Kotakadi, Dr John Cattermull, Dr Stephen Turrell and Yiming Xu, and additional discussions and collaborations with Junyi Zhao, Yi Liang, Dr Matthew Burton, Dr Lorenz Olbrich, Dr Johannes Ihli and Dr Nicolò Pianta have been vital to broaden my understanding of the battery field. The rest of the Pasta Group, both past and present, have all been incredibly kind, welcoming and hard-working, and they have made it a wonderful place to work.

I am grateful for the financial support of the Clarendon Fund Scholarships, in partnership with the St. Edmund Hall Frederick Brockhues Scholarship and the Department of Materials Studentship, that enabled me to undertake this DPhil.

To my family, thank you for always encouraging me to follow my own path and for your constant support. I could not have made it to this point without it and I will always be grateful for the opportunities you have provided me.

Finally, to my wife, Laura, thank you for everything. I could not have imagined completing this DPhil without you by my side.

List of Publications

The results presented in this thesis have directly contributed to the following publications:

1. Dhir, S.*, **Jagger, B.***, Maguire, A. & Pasta, M. Fundamental Investigations on the Ionic Transport and Thermodynamic Properties of Non-Aqueous Potassium-Ion Electrolytes. *Nat. Commun.* **14**, 3833 (2023). (* these authors contributed equally.)

2. **Jagger, B.** & Pasta, M. Solid Electrolyte Interphases in Lithium Metal Batteries. *Joule* **7**, 2228–2244 (2023).

3. **Jagger, B.**, Aspinall, J., Kotakadi, S., Cattermull, J., Dhir, S. & Pasta, M. Potassium Alloy Reference Electrodes for Potassium-Ion Batteries: The K-In and K-Bi Systems. *ACS Mater. Lett.* **6**, 4498–4506 (2024).

Additional contributions have been made to the following publications:

4. Zhao, J., **Jagger, B.**, Olbrich, L. F., Ihli, J., Dhir, S., Zyskin, M., Ma, X. & Pasta, M. Transport and Thermodynamic Properties of KFSI in TEP by *Operando* Raman Gradient Analysis. *ACS Energy Lett.* **9**, 1537–1544 (2024).

5. Aspinall, J., Sada, K., Guo, H., Kotakadi, S., Narayanan, S., Chart, Y., **Jagger, B.**, Milan, E., Brassart, L., Armstrong, D. & Pasta, M. The Impact of Magnesium Content on Lithium-Magnesium Alloy Electrode Performance with Argyrodite Solid Electrolyte. *Nat. Commun.* **15**, 4511 (2024).

6. Olbrich, L. F., **Jagger, B.**, Ihli, J. & Pasta, M. *Operando* Raman Gradient Analysis for Temperature-Dependent Electrolyte Characterization. *ACS Energy Lett.* **9**, 3636–3642 (2024).

7. Dhir, S., Cattermull, J., **Jagger, B.**, Schart, M., Olbrich, L. F., Chen, Y., Zhao, J., Sada, K., Goodwin, A. & Pasta, M. Characterisation and Modelling of Potassium-Ion Batteries. *Nat. Commun.* **15**, 7580 (2024).

8. Liang, Y., Burton, M., **Jagger, B.**, Guo, H., Ihli, J. & Pasta, M. *In Situ* XPS Investigation of the SEI Formed on LGPS and LAGP with Metallic Lithium. *Chem. Commun.* **60**, 12597 (2024).

9. Burton, M., Narayanan, S., **Jagger, B.**, Olbrich, L. F., Dhir, S., Shibata, M., Lain, M. J., Astbury, R., Butcher, N., Copley, M., Kotaka, T., Aihara, Y. & Pasta, M. Techno-Economic Assessment of Thin Lithium Metal Anodes for Solid-State Batteries. *Nat. Energy* **10**, 135–147 (2024).

10. Turrell, S. J., Liang, Y., Cai, T., **Jagger, B.** & Pasta, M. Origin of Stability in the Solid Electrolyte Interphase Formed Between Lithium and Lithium Phosphorus Oxynitride. *Chem. Mater.* **37**, 3504–3518 (2025).

11. Burton, M., **Jagger, B.**, Liang, Y., Gibson, J. S., Aspinall, J., Swallow, J. E. N., Weatherup, R. S. & Pasta, M. The Role of Phosphorous in the Solid Electrolyte Interphase of Argyrodite Solid Electrolytes. *Preprint on ChemRxiv*, 10.26434/chemrxiv-2024-1727n-v2 (2025).

Contents

Abstract i

Acknowledgements ii

List of Publications iii

1 Introduction 1

1.1 Lithium Metal Batteries . . . 3
1.2 Potassium-Ion Batteries . . . 5
1.3 Transport in Liquid Electrolytes . . . 7
1.4 Solid Electrolyte Interphases . . . 9
1.4.1 Solid Electrolyte Interphase Properties . . . 11
1.4.2 Factors Affecting the Solid Electrolyte Interphase . . . 20
1.4.3 Critical Research Fronts . . . 24
1.5 Thesis Objectives . . . 27

2 Method Background 29

2.1 X-ray Photoelectron Spectroscopy . . . 29
2.1.1 Probing Depth . . . 30
2.1.2 Peak Shapes . . . 31
2.1.3 Quantification . . . 32
2.2 Electrochemistry . . . 33
2.2.1 Electrode Potentials . . . 33
2.2.2 Reference Electrodes . . . 35
2.2.3 Overpotentials . . . 36
2.2.4 Electrochemical Impedance Spectroscopy . . . 37

3 Ionic Transport in Lithium- and Potassium-Ion Electrolytes 40

3.1 Introduction . . . 41
3.2 Potassium Metal Electrode Preparation . . . 42
3.3 Transport and Thermodynamic Property Characterisation . . . 48
3.3.1 Cation Transference Number . . . 49
3.3.2 Ionic Conductivity . . . 51
3.3.3 Thermodynamic Factor . . . 54

3.3.4 Salt Diffusivity . . . 59
3.3.5 Thermodynamic and Stefan-Maxwell Diffusivities . . . 63
3.4 Conclusion . . . 65
3.5 Experimental Methods . . . 67

4 Solid Electrolyte Interphases on Lithium and Potassium Metal 72
4.1 Introduction . . . 73
4.2 Sample Preparation . . . 74
4.2.1 Sensitivity Factors . . . 75
4.2.2 Sample Damage . . . 75
4.2.3 Solvent Rinsing . . . 76
4.2.4 Depth Profiling . . . 77
4.2.5 Calibrating Sputter Rate . . . 78
4.3 Lithium Metal Electrodes . . . 80
4.3.1 Model System . . . 80
4.3.2 Role of Temperature . . . 91
4.3.3 Role of Concentration . . . 97
4.3.4 Role of Time . . . 102
4.3.5 Role of Solvent . . . 104
4.4 Potassium Metal Electrodes . . . 106
4.5 Conclusion . . . 112
4.6 Experimental Methods . . . 114

5 Potassium Alloy Reference Electrodes for Potassium-Ion Batteries 117
5.1 Introduction . . . 118
5.2 The K-In System . . . 119
5.3 The K-Bi System . . . 122
5.3.1 Synthesis and Characterisation . . . 125
5.3.2 Potential Stability . . . 129
5.3.3 Electrochemical Stability . . . 132
5.4 Conclusion . . . 137
5.5 Experimental Methods . . . 138

6 Conclusion and Future Research 144

Appendices

A Solid Electrolyte Interphase Reporting Checklist 148

B Additional X-ray Photoelectron Spectroscopy Data 152

C Electrolyte Transport Property Parameterisation 167

D Electrochemical Impedance Spectroscopy Fitting **169**

References **173**

1 Introduction

Contents

1.1 Lithium Metal Batteries 3
1.2 Potassium-Ion Batteries 5
1.3 Transport in Liquid Electrolytes 7
1.4 Solid Electrolyte Interphases 9
1.4.1 Solid Electrolyte Interphase Properties 11
1.4.1.1 Nanostructure 11
1.4.1.2 Composition 14
1.4.1.3 Transport 15
1.4.1.4 Mechanical Properties 18
1.4.2 Factors Affecting the Solid Electrolyte Interphase 20
1.4.2.1 Formation Conditions 20
1.4.2.2 Cross-Talk 23
1.4.3 Critical Research Fronts 24
1.5 Thesis Objectives 27

First commercialised in the 1990s, lithium-ion batteries (LIBs) have been instrumental in enabling the electrification necessary for a clean energy transition. Driven predominantly by the widespread adoption of electric vehicles (EVs), global battery demand is projected to increase rapidly in the coming years, growing from 1 TWh yr^{-1} in 2023 to 13 TWh yr^{-1} by 2050 to meet net zero targets.[1]

Conventional LIBs, shown schematically in Figure 1.1, utilise graphite as a negative electrode material (often referred to as the 'anode' in battery literature), while a range of positive electrode ('cathode') materials have been used commercially. Early LIBs employed lithium cobalt oxide (LCO) cathodes, but lithium nickel manganese cobalt

oxide (NMC) chemistries are now far more prevalent owing to their higher capacities.[2] Cheaper, lower-energy-density lithium iron phosphate (LFP) chemistries are also expected to take up an increasing proportion of the market share in the future.[1,2] The active anode and cathode materials are often mixed with binders and conductive additives and then cast onto current collectors, forming porous electrodes.[3] Aluminium is the preferred positive electrode current collector owing to its high conductivity, low cost, low density and stability at high potentials, but copper is required for the negative electrode due to the ability of lithium to alloy with aluminium at low potentials. A porous separator prevents the two electrodes from coming into electrical contact and an electrolyte (typically consisting of $LiPF_6$ in carbonate-based solvents[4]) fills the pores in both electrodes and the separator. The electrolyte is ionically conductive and allows cations to be transported between the two electrodes but it is electronically insulating.

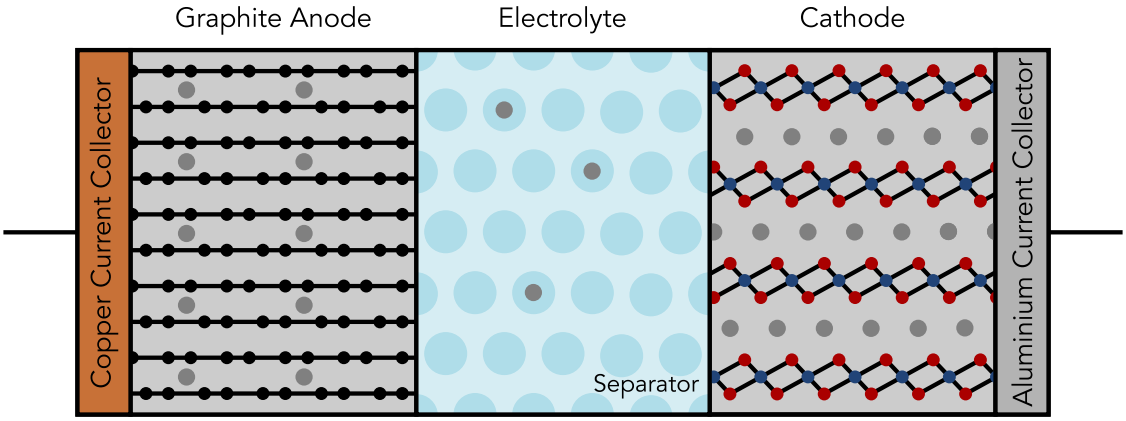


Figure 1.1: Schematic representation of a lithium-ion battery.

During charge the cathode is oxidised, releasing Li^+ into the electrolyte and e^- into the current collector. The Li^+ are transported through the electrolyte while the e^- pass through an external circuit to the anode where they recombine, leading to reduction. These processes are reversed during discharge. The common LIB anode and cathode materials store Li^+ through intercalation, where the Li^+ become incorporated within the host structure, so these reactions result in Li^+ being shuttled back and forth between the electrodes during cycling. Hence this is often known as a "rocking-chair" mechanism.

LIBs, however, are a mature technology and their performance is already approaching the theoretical limits of the battery chemistry, so battery capacity and rate performance

will only improve marginally through further optimisation. This translates to limited improvement in EV driving ranges and charging rates, requiring the development of new battery chemistries to enable a step-change in battery performance. Additionally, the large projected battery demand will put significant strain on the supply chains for critical minerals necessary for LIBs, including copper, lithium, nickel and cobalt, so battery technologies without reliance on these critical elements will also become increasingly important.

1.1 Lithium Metal Batteries

Lithium metal batteries (LMBs), with lithium metal as the anode, have recently received enormous interest as a higher energy density alternative to conventional LIBs. LMBs, shown schematically in Figure 1.2, function in much the same was as LIBs, except there is no host material to store Li^+ in the anode and it instead plates as lithium metal. This reduces the inactive mass in the anode, and lithium metal has the highest theoretical specific capacity (3860 mAh g^{-1}) and lowest electrode potential (−3.04 V vs. standard hydrogen electrode) of any candidate material. It is therefore anticipated that LMBs will find applications in high-end EVs[5] and they could enable novel applications including electric flight,[6] although the latter would also require significant enhancements in positive electrode specific capacities.[7]

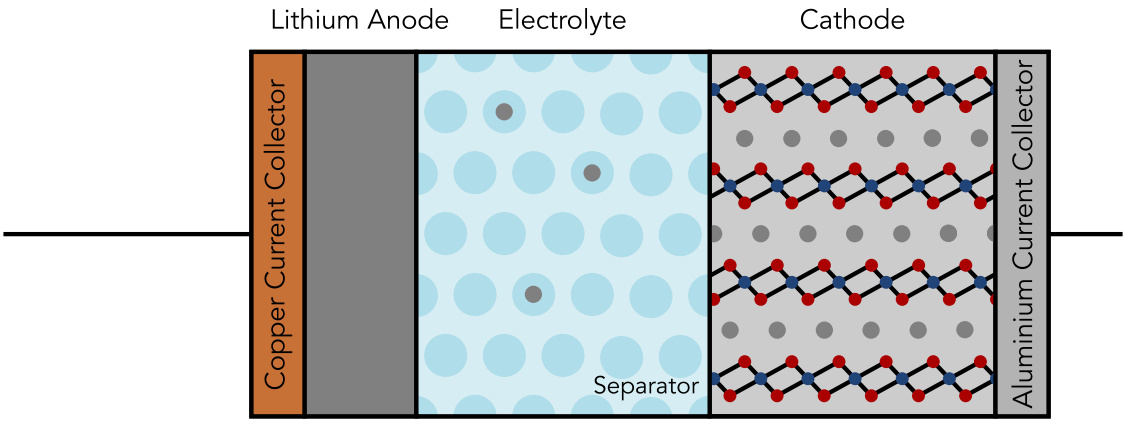


Figure 1.2: Schematic representation of a lithium metal battery.

It is important to note that this theoretical specific capacity of 3860 mAh g^{-1} is not directly comparable to the typically reported graphite specific capacity of 372 mAh g^{-1}.

This is because for lithium metal this specific capacity defines the total charge able to be extracted per gram of active material, while for graphite it defines the total charge able to be stored per gram of inactive host material. Lithium metal, with no inactive host, would therefore result in an infinite specific capacity if it was calculated in the same way as for graphite. It would be more appropriate to consider the charge that can be extracted per gram of fully lithiated graphite, LiC_6, resulting in a theoretical specific capacity of 339 mAh g^{-1}.[8] Lithium metal therefore has a significantly higher specific capacity than graphite.

Successful LMB commercialisation will demand batteries with high specific energies (above 500 Wh kg^{-1}) at low cost (below US\$100 kWh^{-1}).[9] Batteries must also retain 80–90% of their capacity over 1000 cycles, requiring a coulombic efficiency (CE) of over 99.99% in zero-excess-lithium cells.[10,11]

Achieving these targets additionally requires the development of novel electrolytes compatible with both electrodes. Liquid electrolytes are particularly promising as cost-effective manufacturing routes have already been established for LIBs,[5] and prior knowledge and equipment will facilitate large-scale LMB production, expediting their commercialisation. Additionally, liquid electrolytes enable lithium metal cycling at high current densities with large per-cycle areal capacities compared to solid inorganic and polymer electrolytes,[12] although they often use a large excess of lithium and the total cycle life is currently poor. Liquid electrolytes can also flow to fill pores, ensuring good contact with the electrodes.

However, lithium metal anodes operate outside of the electrochemical stability window of any electrolyte, and spontaneous reduction of electrolyte species occurs when the anode potential is reduced below the potential of electrolyte reduction.[13] Kinetic stability is afforded by the formation of a surface layer composed of the insoluble reaction products,[14] which was first named the solid electrolyte interphase (SEI) by Peled in 1979.[15]

LMB cycle life is currently limited by inhomogeneous lithium plating/stripping which exposes additional lithium to the electrolyte and results in active-lithium loss due to the formation of SEI and electrochemically isolated 'dead' lithium.[16] This lowers the CE so excess lithium in the form of lithium foil is currently needed to extend cycle life to practical values,[17] reducing the specific energy. The CE of the lithium metal anode (determined from

Cu||Li half cells, for example[10]) is therefore a useful metric for assessing cell stability. The origin of this non-uniform lithium plating and stripping behaviour will be discussed below.

1.2 Potassium-Ion Batteries

The prices of critical minerals necessary for LIB and LMB production have experienced exceptional volatility in recent years, especially following the COVID-19 pandemic.[18,19] While, at the time of writing, these prices have returned to pre-pandemic levels, battery demand is rapidly increasing and LIBs are projected to make up over 90% of the market share.[1] This will pose significant strain on the supply chains for critical minerals necessary for both LIBs and LMBs, including copper, lithium, nickel and cobalt. The demands for nickel and cobalt can be reduced by switching to LFP-based cathode chemistries, as is projected,[1] but expected copper and lithium supply is still set to fall far short of demand.[1]

To minimise the risks associated with an overdependence on lithium-based batteries it is therefore important to consider alternative chemistries based on abundant minerals which can replace LIBs in certain applications, such as sodium-ion batteries (NIBs) or potassium-ion batteries (KIBs).[20]

NIBs and KIBs are both attractive owing to the low cost and high abundance of sodium and potassium resources, and their inability to alloy with aluminium further enables the use of aluminium current collectors at the negative electrode, rather than the copper required in LIBs.[21,22] KIBs, however, display several key advantages over NIBS, as K^+ reversibly intercalates into graphite,[23] while Na^+ cannot, so one of the primary anode materials for KIBs is already produced at commercial scale. The larger size of the K^+ cation compared to Li^+ and Na^+ also results in a reduced charge density, and this has been proposed to lead to improved electrolyte transport properties,[22,24] which will be investigated in Chapter 3. Combining this with the higher graphite intercalation potential in KIBs compared to LIBs (300 mV vs. K^+/K and 100 mV vs. Li^+/Li, respectively[22]) could contribute to enhanced rate performance in KIBs.

Various cathode materials have been proposed for KIBs, including Prussian blue analogues (PBAs), layered transition metal oxides, and polyanionic compounds.[20,24–27] Of these the potassium manganese hexacyanoferrate $K_2Mn[Fe(CN)_6]$ (KMF) PBAs are

typically reported to be one of the most promising owing to a combination of a high specific capacity, high average voltage, good cycling stability and low cost.[22,28] Importantly, they do not rely on any critical minerals.

A schematic representation of a KIB is shown in Figure 1.3, and it functions through the same rocking-chair mechanism as LIBs.

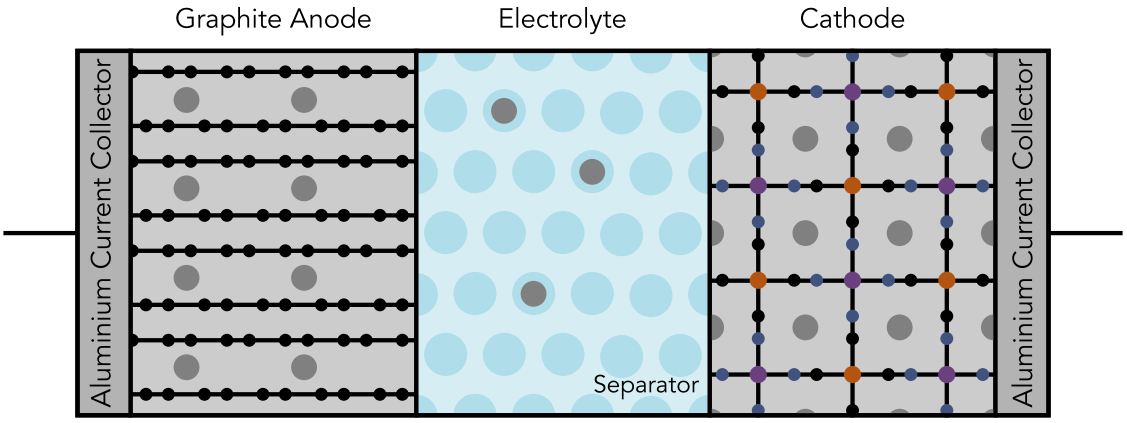


Figure 1.3: Schematic representation of a potassium-ion battery.

KIBs, however, are not without their limitations. The fully charged graphite intercalation compound in KIBs is KC_8, compared to LiC_6 in LIBs,[29] so the theoretical specific capacity of the graphite anode in KIBs is reduced to 279 mAh g^{-1}. This reduces further to 199 mAh g^{-1} if the mass of the additional potassium atom is considered. Combining this with the relatively low specific capacity of KMF cathodes (155 mAh g^{-1}), KIBs cannot compete with NMC-based LIBs in terms of specific energy or energy density.[22] On the other hand, the specific energies of KMF-based KIBs and LFP-based LIBs are comparable[22] and recent evidence suggests that they could have similar rate performance.[30] LFP-based LIBs are projected to take up over 30% of the market share by 2040,[1] so KIBs could be a promising complementary technology.

Like LMBs, in KIBs the graphite anode operates outside of the electrochemical stability window of the electrolyte, so SEI formation similarly leads to capacity losses and reduces cycling efficiencies.[31] Additionally, there is currently no electrolyte with sufficient stability against both low voltage negative electrode and high voltage positive electrode materials, so, as for LMBs, rational electrolyte design will be the key to commercialising KIBs.[32]

1.3 Transport in Liquid Electrolytes

Binary liquid electrolytes, consisting of a single salt dissolved in a single solvent, can be accurately described by Newman's concentrated-solution theory by determining three transport properties and three thermodynamic properties, which are summarised in Table 1.1, along with their standard measurement methods.[33] Electrolyte behaviour can be accurately predicted if these properties are known.[34]

Table 1.1: Summary of the transport and thermodynamic properties required to describe a binary electrolyte with concentrated-solution theory[33]

Property	Symbol	Description	Measurement Method
Transport Properties			
Ionic conductivity	κ	Quantifies the mobility of ions under and electric field	Electrochemical impedance spectroscopy
Salt diffusivity	D	Determines the ionic flux due to salt concentration gradients	Restricted diffusion
Cation transference number	t_+^0	The fraction of current carried by the cation, relative to the solvent velocity	Hittorf method
Thermodynamic Properties			
Thermodynamic factor	χ_M	Accounts for deviations from ideal Nernstian behaviour	Concentration cells
Partial molar volume of salt	$\overline{V}_e$	Describes the contribution that salt makes to the total volume	Densitometry
Partial molar volume of solvent	$\overline{V}_0$	Describes the contribution that solvent makes to the total volume	Densitometry

Measuring each property traditionally requires a separate experiment, making full electrolyte characterisation time-consuming and expensive. The air sensitivity of lithium- and potassium-ion electrolytes also complicates experiment design, meaning there are few reports of full electrolyte characterisations.[35–37] The recent development of *operando* Raman gradient analysis (ORGA), however, could enable rapid transport property measurement in a single experimental setup.[38,39]

These transport properties govern the development of salt concentration gradients and overpotentials during cell operation. The cation transference number, t_+^0, defines the fraction of the total current carried by the cation, and it is typically reported to be below 0.5 in battery electrolytes.[33] This means the anion carries a significant proportion of the current. In lithium- and potassium-based batteries the electrodes are typically anion blocking, so during cell operation anions migrate towards the electrode that is being oxidised and build up at the interface. Similarly, the electrolyte close to the electrode

being reduced becomes depleted in anions, and, due to electroneutrality, a corresponding gradient of cation concentration develops. This formation of a salt concentration gradient drives diffusion in the opposite direction to anion migration to reduce the gradients and the rate of this is determined by the salt diffusivity, D. Salt concentration gradients are therefore more pronounced in electrolyte systems with low t_+^0 and D.

The ionic conductivity, κ, determines the Ohmic drop over the electrolyte, and the thermodynamic factor χ_M is required to calculate the concentration overpotential from the differences in electrolyte concentration between the two electrodes. These overpotentials reduce the energy efficiency of the cell and can lead to cell cut-off voltages being reached early at high charging rates.[30] Electrolyte transport is therefore important for determining cell rate performance.

In extreme cases, the electrolyte can become completely depleted of salt at the anode interface during charge. In LMBs this results in dendrite formation, which are fractal, tip-growing deposits caused by diffusion-limited aggregation.[40] Dendrites can grow across a cell and short it, potentially igniting the flammable electrolyte.

According to classical theories developed for copper, this salt depletion and dendritic growth can only occur once the current density reaches a limiting current density, J_{lim}, given by Equation 1.1:[41]

$$J_{\text{lim}} = \frac{2c_0FD}{(1-t_+^0)L} \tag{1.1}$$

where c_0 is the bulk salt concentration in the electrolyte, F is the Faraday constant, D is the salt diffusivity, t_+^0 is the cation transference number, and L is the distance between electrodes. The time it takes for the interfacial salt concentration to reduce to zero at a current density greater than J_{lim} was first derived by Sand,[41] and has become known as Sand's time, t_{Sand}, given by Equation 1.2:

$$t_{\text{Sand}} = \frac{\pi D}{4}\left[\frac{c_0F}{J(1-t_+^0)}\right]^2, \qquad J \geq J_{\text{lim}} \tag{1.2}$$

where J is the applied current density, and all other variables are as above.

Determination of the salt diffusivity and cation transference number enables t_{Sand} to be calculated. Studies of dendrite growth during lithium electrodeposition have confirmed

that the dendrite onset time shows a current density dependence in agreement with t_{Sand},[40] although the onset time decreases if the lithium electrode is allowed to soak in the electrolyte prior to current application,[42] so bulk electrolyte transport cannot be the only process determining dendrite initiation.

Additionally, Bai et al. observed that lithium always deposits inhomogeneously as root-growing needle-like filaments that interweave into a 'mossy' morphology, even at currents well below J_{lim}.[40] Mossy lithium also preferentially nucleates at surface inhomogeneities due to local enhancement of the current density,[43] so the lithium surface structure influences deposition. These filamentary deposits are distinct from the dendritic growths described above, although they are often erroneously treated the same in the literature.

These discrepancies between copper and lithium electrodeposition are caused by the high reactivity of lithium relative to copper, as an SEI spontaneously forms on lithium. Lithium preferentially deposits at weak points in the SEI, and more SEI forms rapidly on the fresh lithium, preventing separate filaments from coalescing into a uniform film.[40,44] No such film forms on copper, so electrodeposition is uniform until t_{Sand} and ultimately it is the SEI that controls cycling performance in LMBs.

1.4 Solid Electrolyte Interphases

Much of the discussion in this chapter will focus on the SEI that forms in LMBs as it is a more mature research field, but understanding the SEI and its relationship with electrolyte chemistry and cycling conditions will also be critical to enable the successful development of KIBs.

The discussion in this chapter has contributed to the following publication:

Jagger, B. & Pasta, M. Solid Electrolyte Interphases in Lithium Metal Batteries. *Joule* **7**, 2228–2244 (2023).

The SEI controls LMB stability by regulating lithium morphology and dead lithium formation.[45] This is represented schematically in Figure 1.4, which shows how the SEI can lead to early dendrite initiation, and how it can promote filamentary growth and the subsequent formation of dead lithium.

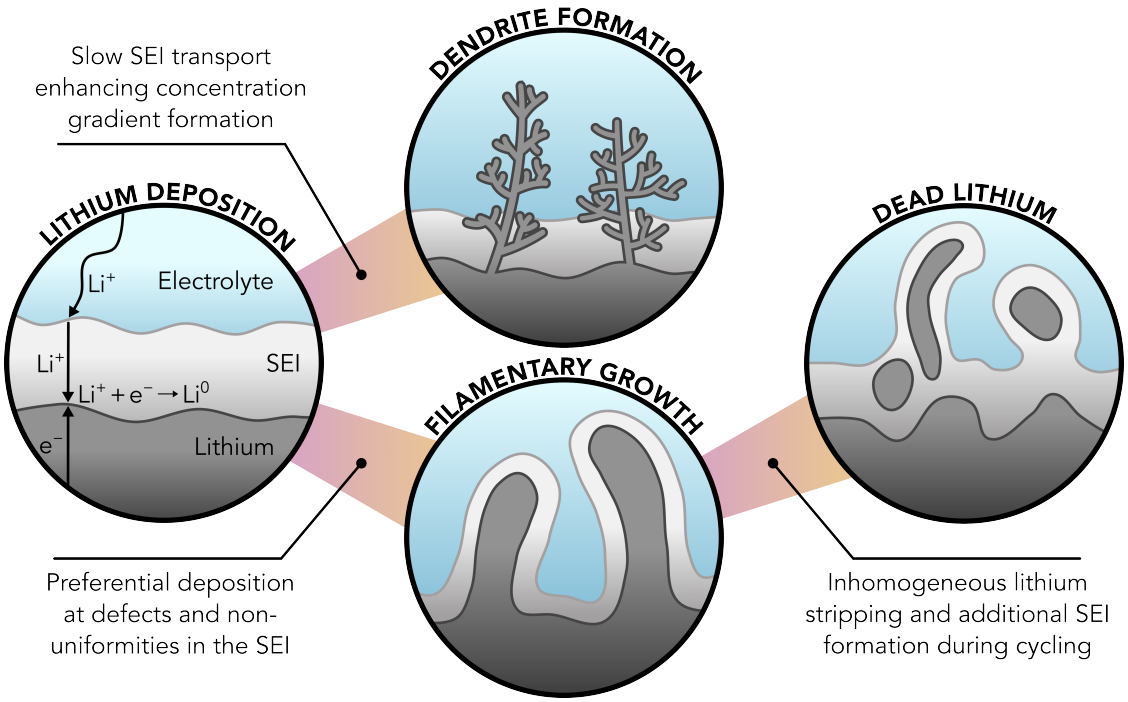


Figure 1.4: Influence of the solid electrolyte interphase (SEI) on lithium deposition morphology. Schematics of the formation of dendrites, lithium filaments, and dead lithium. The SEI can enhance Li^+ concentration gradients, causing dendrite formation before the bulk electrolyte diffusion limitation and causing cell failure.[42] Preferential lithium deposition can also occur at weak points or defects in the SEI, resulting in non-uniform filamentary growth. Lithium filaments can grow and interweave into a high-surface-area mossy morphology.[40] Inhomogeneous stripping and additional SEI formation during cycling can leave electrochemically isolated dead lithium.[16]

The SEI needs to be electrically insulating, ionically conductive, and mechanically robust to effectively passivate the lithium anode,[44] and it has been widely thought that the SEI should be rich in inorganic components,[46] with a positive correlation observed between LiF-content and cycling performance.[47] This has led to the development of numerous strategies to produce SEIs with desired compositions through design of advanced electrolytes with controlled chemistries and solvation structures.[5,48–56] Artificial SEIs have also been implemented to promote stable LMB cycling,[57,58] although these are unable to self-repair. However, these strategies have not been sufficient to achieve the high cycling stabilities required for LMB commercialisation. Fang et al. and Hobold and Gallant have demonstrated that electrolyte systems with CEs above 95% result in limited dead lithium formation during cycling,[16,59] so additional losses due to continuous SEI formation must be reduced for further improvement. This will require better understanding of the properties of the SEI and their influence on cycling performance, enabling the rational

design of SEIs to guide future electrolyte development.

1.4.1 Solid Electrolyte Interphase Properties

1.4.1.1 Nanostructure

A complete understanding of the SEI first requires an accurate characterisation of its structure and composition. One of the most popular structural models of SEI is the mosaic model (Figure 1.5a), first proposed by Peled et al. in 1997.[60] It is assumed that multiple SEI components form simultaneously, producing a heterogeneous "mosaic of microphases". The driving force for reduction is greatest at the anode surface, producing an inner SEI layer composed of inorganic, fully reduced salt decomposition products. This shields the remaining electrolyte, so the outer layer is composed of more organic, partially reduced phases from solvent decomposition. Recent evidence additionally suggests that this outer organic layer is porous and permits electrolyte impregnation,[61,62] potentially facilitating desolvation.[63] A summary of typical liquid electrolyte solvents, salts and additives used in LMB research, and their main reduction products is provided in Table 1.2.

The recent utilisation of cryogenic transmission electron microscopy (cryo-TEM) techniques has enabled direct imaging of the SEI with reduced beam damage.[65] In some electrolyte systems the observed SEI structures are in agreement with the mosaic model, and generally consist of small crystalline domains of Li_2O and Li_2CO_3 in an amorphous organic matrix, with a total thickness on the order of tens of nanometres (Figure 1.5b).[64,65] However, this is not always the case and the SEI has been reported to be completely amorphous (Figure 1.5c),[66,67] or to form with a multilayered structure (Figure 1.5d).[65,68] The structure can significantly impact cycling performance, with a heterogeneous mosaic SEI observed to lead to non-uniform stripping, which is prevented by a multilayered SEI.[45] Cryo-TEM alone can only identify crystalline SEI components, requiring additional spectroscopic tools like energy dispersive X-ray spectroscopy (EDX),[66] X-ray photoelectron spectroscopy (XPS)[67] or electron energy loss spectroscopy (EELS)[68] to determine the nature of amorphous components, revealing that they can be either organic or inorganic. Han et al. have also reported an amorphous lithium transition layer between the SEI and bulk lithium, believed to be generated by the doping of

Table 1.2: Typical liquid electrolyte solvents, salts and additives, and their main reduction products

Electrolyte Component	Reduction Products	References
Carbonate Solvents		
Ethylene carbonate EC	$LiO_2COCH_2CH_2OH$ $LiO_2COCH_2CH_2Li$ Li_2CO_3 C_2H_4 Polycarbonate Other lithium alkyl carbonates	70–72
Propylene carbonate PC	$LiO_2COCH_2CH(OCO_2Li)CH_3$ Li_2CO_3 Polycarbonate Other lithium alkyl carbonates	71,72
Diethyl carbonate DEC	$LiOCH_2CH_3$ LiO_2COCH_3	71,72
Dimethyl carbonate DMC	LiO_2COCH_3 $LiOCH_3$ Other lithium alkyl carbonates	70–72
Ether Solvents		
1,2-Dimethoxyethane DME	$LiCH_3$ $LiOCH_3$ Ethereal oligomers	71,72
1,3-Dioxolane DOL	$LiOCH_2CH_2OCH_3$ $LiOCH_2OCH_2CH_3$ Ethereal oligomers	71,73
Salts		
Lithium hexafluorophosphate $LiPF_6$	LiF $Li_xPF_yO_z$ P_xF_y Li_2O	71,72
Lithium bis(fluorosulfonyl)imide LiFSI	LiF $LiSO_2F$ LiNSO Li_2O Li_3N Li_2S Polymeric moieties	71,72,74
Lithium bis(trifluoromethanesulfonyl)imide LiTFSI	LiF $LiCF_3$ Li_3N $Li_2NSO_2CF_3$ $Li_2S_xO_y$ Li_2S Polymeric moieties	54,71–73
Additives		
Fluoroethylene carbonate FEC	LiF Li_2O Li_2CO_3 Polycarbonate Other lithium alkyl carbonates	71,72
Lithium nitrate $LiNO_3$	Li_3N Li_2O Li_xNO_y	54,71,72

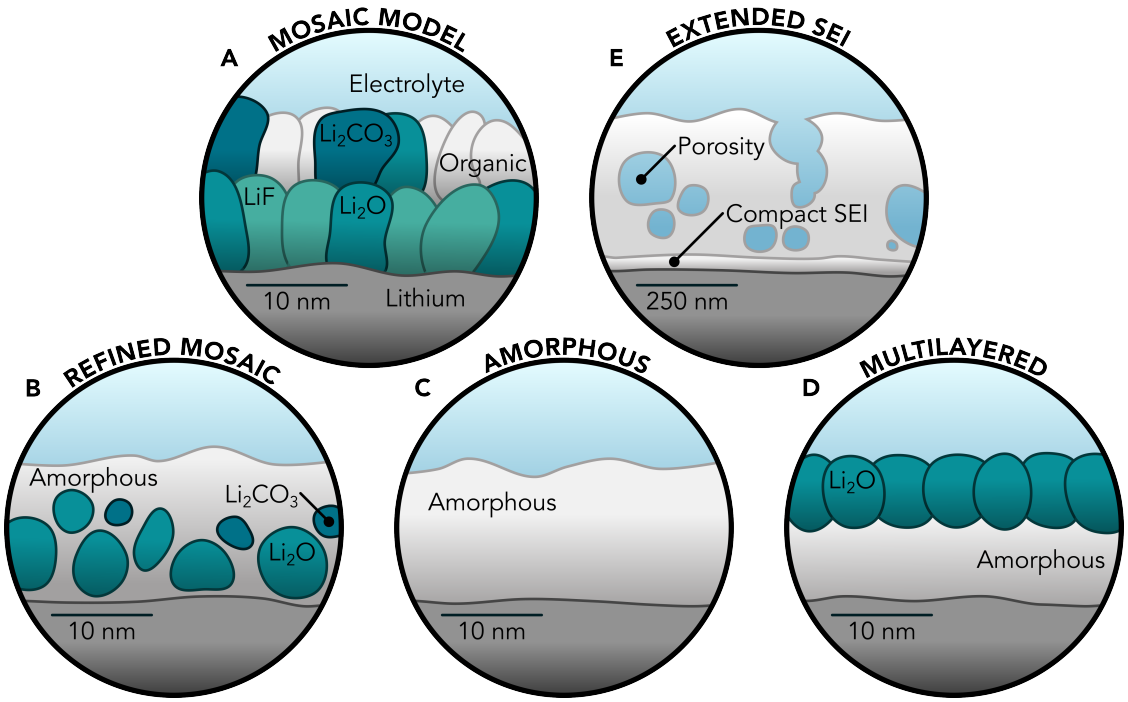


Figure 1.5: Solid electrolyte interphase (SEI) nanostructure. (a) The traditional mosaic model of the SEI.[60] The SEI is predominantly inorganic close to the lithium anode and becomes more organic towards the electrolyte. (b) Schematic representation of typical heterogeneous mosaic SEI structures.[64,65] (c) Schematic representation of typical amorphous SEI structures.[66,67] (d) Schematic representation of typical multilayered SEI structures.[65,68] (e) Schematic representation of an extended SEI. A porous extended SEI layer can form on the lithium surface and can be removed during sample preparation steps, leaving only the compact SEI.[69]

lithium with elements from electrolyte decomposition during electrodeposition.[68,75] This complicates the measurement of SEI thickness.

Additionally, the observed SEI thickness depends on how the sample is prepared. Zhang et al. adapted a thin film vitrification method to preserve the solid-liquid interface and found that the SEI swells in contact with electrolyte, resulting in thicknesses as much as twice as large as in the dry state. For example, 1 M lithium bis(fluorosulfonyl)imide (LiFSI) in 1,2-dimethoxyethane (DME) resulted in SEI thicknesses of approximately 17.5 and 10 nm in the vitrified and dry states, respectively.[76] This is indicative of a porous SEI, and a negative correlation was observed between swelling ratio and CE, suggesting excessive porosity may be detrimental to cell performance.[76] Zachman et al. also examined the structures formed at the solid-liquid interfaces in LMBs and observed lithium metal filaments surrounded by a porous, organic extended SEI of around 500 nm thickness, which is likely to be removed during typical sample washing steps, leaving

behind just the compact SEI described previously (Figure 1.5e).[69] Such an extended SEI has also been observed by *in-situ* liquid cell TEM,[47] and its presence suggests that more active lithium is lost during SEI formation than previously believed. It is therefore important to ensure that any sample preparation steps do not significantly alter the sample, and that SEI imaging and analysis is performed under operating conditions when possible. The majority of reported SEI characterisation is performed *ex situ* and may not be representative of the true state of the SEI.

1.4.1.2 Composition

The chemical composition of the SEI is typically determined using XPS.[77] In fact, XPS results led to the original mosaic model[60] and have prompted the exploration of highly-fluorinated electrolytes due to the belief that LiF is a crucial component in the SEI.[78] However, XPS measurements must be performed with care, as results have been demonstrated to vary with sample preparation method, and the surface chemistry can change over time even under the ultrahigh vacuum (UHV) in the analysis chamber.[77] Yu et al. also recently showed that several common salts decompose to form LiF during the Ar^+ sputtering often used for depth profiling.[79] Combining this with the low lateral resolution of XPS and the difficulties in accurately determining a composition from relative peak intensities,[80] any SEI structures determined solely with XPS should be treated as rough estimates and additional techniques are required for verification. The development of novel *in-situ* and *operando* techniques would also be incredibly valuable to probe the processes occurring at the solid-liquid interface under realistic operating conditions.[81,82]

Despite the belief that LiF is a major SEI component, it has rarely been observed in the compact SEI using cryo-TEM or high-resolution spectroscopy. Huang et al. instead found that the fluorine from electrolyte decomposition exists as LiF particles with a diameter of up to 400 nm, randomly distributed over the anode surface.[83] LiF particles were also observed in other studies,[84,85] further suggesting LiF in the SEI cannot solely be responsible for improved cycling performance observed in highly-fluorinated electrolytes.[10] The benefits of highly-fluorinated electrolytes could therefore be two-fold: (1) Fluorine is highly electronegative, and its presence raises the potential of electrolyte reduction

of fluorinated species relative to their non-fluorinated counterparts. This increases the driving force for electrolyte reduction,[53,78] enhancing the kinetics of SEI formation and potentially allowing fast SEI repair.[86] Oxidative stability is also increased, enabling improved performance with high-voltage cathodes. (2) Fluorinated solvents are typically weakly solvating, leading to significant ion-ion interactions that increase the activity of Li^+ in the electrolyte, increasing the electrode potential.[87,88] This weakens the reducing ability of the electrode, increases the rate of charge transfer, and increases the lithium surface energy, promoting low-surface-area deposition and an anion-derived SEI.[87–89]

Additional techniques to accurately determine SEI chemistry have also recently been developed, although this is often at the expense of structural information. Fang et al. developed a titration gas chromatography method capable of distinguishing lithium loss due to SEI or dead lithium formation.[16] This was extended by Hobold and Gallant to identify numerous solvent-derived components within the SEI, including lithium alkyl carbonates, organolithium compounds, and Li_2C_2. Li_2C_2 is believed to form through lithium alkyl carbonate reduction, and they found a negative correlation between Li_2C_2-content and CE, attributed to its relatively high electronic conductivity.[59] Recent work has additionally identified a strong positive correlation between Li_2O-content and CE.[90] Although it was not identified by the previous studies, other researchers have additionally observed LiH in the SEI.[91,92] LiH can form through solvent decomposition or the reaction of lithium with LiOH, and it can make up a significant proportion of the SEI.[69,93] However, despite these advances in SEI characterisation a significant proportion of the SEI in high CE electrolytes is still unidentified,[59,90] requiring the further development of techniques capable of quantifying SEI composition with high accuracy.

1.4.1.3 Transport

Knowledge of SEI nanostructure alone is currently insufficient to predict cell performance as it is not understood how SEI properties are affected by its structure and composition. The discovery of structure-property relationships would facilitate rational SEI design and guide future electrolyte development and is therefore one of the most pressing avenues for SEI research.

It is important to understand the transport properties of the SEI, as the transport of Li^+ through the SEI determines the rate capability of a cell and controls the morphology of electrodeposited lithium (Figure 1.6). Maraschky and Akolkar investigated dendrite initiation during lithium electrodeposition and found that dendrites initiate under conditions well below bulk diffusion limitation, with an onset time that decreases with increasing SEI thickness.[42] Analogously to Sand's time,[41] they assumed that a concentration gradient can form within the SEI and that dendrite initiation occurs when the Li^+ concentration at the lithium-SEI interface reaches zero.[42] Dendrites could therefore be prevented by increasing the diffusivity of Li^+ within the SEI, as demonstrated by an increase in onset time with temperature.[94] However, concentration gradients can only form within the SEI if the cation transference number is below unity, so this may only be applicable if the SEI is porous and filled with electrolyte, where both cations and anions are mobile. SEI transport additionally impacts electrodeposition morphology before dendrite initiation. Boyle et al. recently demonstrated that lithium can uniformly plate below the SEI at low current densities (≤ 1 mA cm^{-2}), and transport through the SEI is the rate-limiting step. However, SEI breakdown can occur at higher current densities, leading to simultaneous lithium plating and SEI formation that results in high-surface-area filamentary deposition, reducing the CE.[95] Improved cycling performance could therefore be achieved by increasing the diffusivity of Li^+ to enable lithium plating beneath the SEI at higher rates, and by designing an SEI with greater resistance to mechanical failure. Furthermore, the diffusivity should not only be high, but must be uniform across the SEI to prevent preferential localised lithium deposition which can contribute to SEI failure.[96]

There are currently few experimental techniques capable of quantifying transport through the SEI, and it is frequently estimated using electrochemical impedance spectroscopy (EIS). EIS is particular attractive as it can provide information about the resistance due to charge transfer, the SEI, and diffusion in the electrolyte under real *operando* conditions,[97] although these processes typically overlap and there is not yet a consensus on how to accurately deconvolve them. Impedance spectra are typically fitted to equivalent circuit models to assign features in the data to physical processes, however these circuits are not unique.[97] There have therefore been numerous different

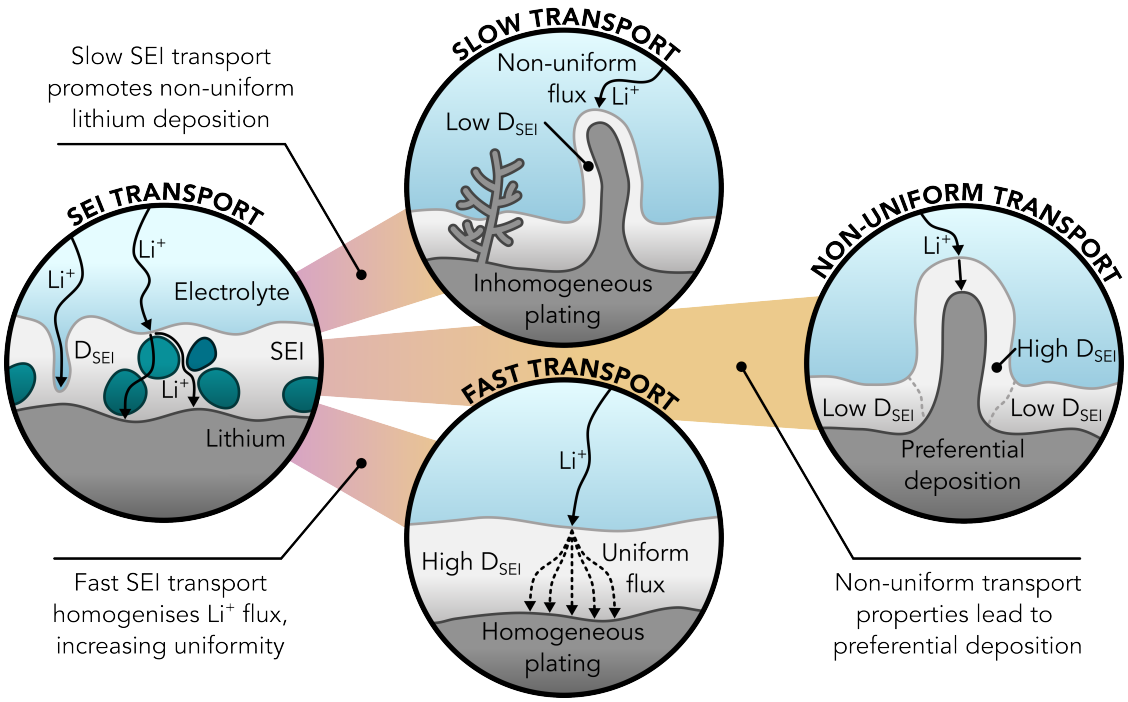


Figure 1.6: Solid electrolyte interphase (SEI) transport. Schematics of potential SEI transport mechanisms and the influence of SEI transport on lithium deposition morphology. Slow transport can enhance dendrite formation[42] and lead to the formation of mossy lithium.[95] Fast transport enables the homogenisation of lithium flux through the SEI, resulting in more uniform deposition.[95] However, preferential lithium deposition will occur below regions with fast transport properties if the SEI is non-uniform, resulting in filamentary deposition.[96]

models proposed to fit impedance data,[60,98–100] many of which only consider the high-frequency data believed to relate to a compact inner SEI layer.[100] It is also often assumed that SEI resistance dominates the impedance, however, Boyle et al. demonstrated that electron charge-transfer resistance can make up as much as 26% of the total interfacial resistance.[101] Despite the prevalence of EIS in the literature, there has not yet been a comprehensive study to verify the suitability of equivalent circuit models and ensure apparent physical properties display the expected trends.

The SEI resistance additionally varies with time. Nojabaee et al. observed that the interfacial impedance increases with resting time, which they attributed to growth of the SEI by assuming resistance is directly proportional to SEI thickness.[102] Tracking impedance evolution may therefore give insight into SEI growth kinetics. On the other hand, Lim et al. instead observed that SEI resistance increases during ageing as a result of densification, reducing the number of interconnected pores within the SEI that may act as fast-conduction pathways.[61] It is generally believed that the SEI resistance

should be minimised, and Hobold et al. demonstrated a negative correlation between SEI resistance and CE over a wide range of electrolyte systems.[103] Some of the best performing electrolytes additionally displayed a significant reduction in impedance during cycling, although it has not yet been established whether this is due to a change in SEI chemistry or an increase in the area of active lithium due to non-uniform deposition. Contrasting results were observed by Boyle et al., who reported no correlation between SEI resistance and CE, however it should be noted that the EIS and CE measurements were performed under very different SEI formation conditions.[89]

Owing to the difficulty in experimentally measuring the diffusion coefficient of Li^+ in the SEI, there has been much interest in predictive modelling. Shi et al. combined density functional theory (DFT) with a multiscale diffusion model and developed a "two-layer/two-mechanism" model which considers the transport of Li^+ through both a porous outer SEI layer and a compact inner layer.[104] They demonstrated that both anions and cations can rapidly move through the porous outer layer, while only cations can diffuse through the inner layer, which is the rate-limiting step. Subsequent studies have therefore focussed on ion transport through the typical inorganic components of the inner layer (Li_2CO_3, Li_2O, LiF and LiOH). Diffusion coefficients have been calculated for transport through bulk phases,[105,106] along grain boundaries and interfaces between components,[107,108] and for surface diffusion.[109] However, the predicted diffusion coefficients vary from 10^{-16}–10^{-9} $m^2\ s^{-1}$ at room temperature, and it is difficult to determine which mechanism is likely to be prevalent without experimental measurements for comparison. Furthermore, real SEIs can differ significantly from simple modelled systems, and SEI components can have very different properties to their bulk counterparts,[100] so more accurate characterisations of SEI structure and composition will be required to guide future modelling efforts.

1.4.1.4 Mechanical Properties

The SEI must be able to resist large volume changes during cycling and it should be robust enough to support itself without breaking.[110] The SEI also needs to have strong adhesion to both the current collector and lithium metal,[111] with near-perfect wetting required to allow the SEI to be refilled during plating.[75] It is therefore necessary to

consider the mechanical properties of the SEI and their influence on cycling performance; although this poses a great experimental challenge.

One popular technique to probe the mechanical properties of the SEI is atomic force microscopy (AFM).[112] It can be used for *in-situ* observations of the lithium surface during operation, demonstrating that preferential lithium deposition occurs in regions where the SEI is thinner.[113] A uniform SEI is therefore beneficial to prevent non-uniform filamentary growth, as confirmed by simulations performed by Shen et al.,[114] which also concluded that an SEI elastic modulus above 3 GPa results in optimal stability. Consistent with this, Yuan et al. measured SEI elastic moduli with AFM in a range of electrolytes and observed high CEs when the elastic modulus is above 4 GPa.[115] However, it is challenging to accurately determine the elastic modulus of thin films, and the measured value has been shown to strongly depend on the underlying substrate.[116] To combat this, Yoon et al. prepared model SEI layers on freestanding poly(dimethylsiloxane) (PDMS) substrates. The SEI generated from an ionic liquid electrolyte formed with residual compressive stress, resulting in film buckling with a characteristic wavelength related to the SEI elastic modulus (≈ 1 GPa).[117] In contrast, the SEIs formed in carbonate electrolytes were not under compression, and Yoon et al. used a membrane-bulge configuration to determine the stress-strain behaviour, measuring elastic moduli around 200–350 MPa.[118] Reported elastic moduli are therefore prone to uncertainties and can vary by several orders of magnitude. Furthermore, the modulus can change significantly under different sample preparation conditions,[76] requiring the development of techniques capable of accurate mechanical characterisation under realistic operating conditions.

The elastic modulus has been the primary focus of many SEI studies, but it is not the only property that impacts cycling performance. Gao et al. used AFM-based nanoindentation to determine the SEI elastic modulus, plus its thickness and elastic strain limit.[119] They observed that CE did not directly correlate with either the elastic modulus or the elastic strain limit, but instead with the maximum elastic deformation energy, which is dependent on both properties. The performance of an SEI therefore not only depends on its rigidity, but also on its ability to withstand permanent deformation (Figure 1.7). Analysis of AFM nanoindentation force curves can also give information about

the structure of the SEI, as SEI layers with different properties produce characteristic features.[120] This has been utilised to demonstrate that multilayered SEIs with both organic and inorganic layers result in improved cycling stability,[121,122] likely due to the balance between the rigidity and ductility afforded by the structure.[123] Future work should focus on uncovering the optimal balance of SEI mechanical properties necessary for stable LMB operation, and how these are related to the nanostructure. This would enable rational SEI design with a consideration of the mechanical and transport properties, providing guidelines for the development of next-generation electrolytes.

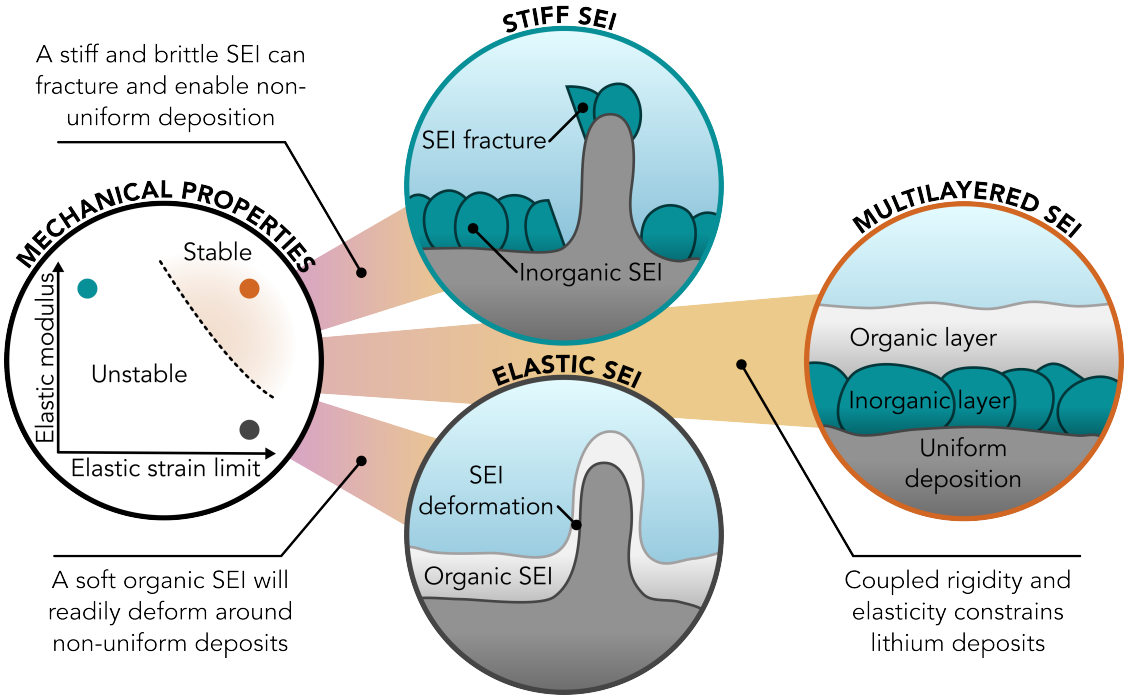


Figure 1.7: Solid electrolyte interphase (SEI) mechanical properties. Schematic representing the balance of SEI mechanical properties required for stable cycling. A stiff inorganic SEI can be brittle and can fracture at low strain, while a soft organic SEI will readily deform, allowing non-uniform deposition.[120] A combination of inorganic and organic SEI layers affords both rigidity and elasticity, constraining lithium deposits and promoting uniform deposition.[122,123]

1.4.2 Factors Affecting the Solid Electrolyte Interphase

1.4.2.1 Formation Conditions

Determination of accurate SEI nanostructures and properties is further complicated by the fact that the SEI is not uniquely determined by the electrolyte, and instead is highly dependent on its formation conditions. Temperature, for example, can have a large impact, and higher temperatures increase the reactivity of lithium metal, generally producing

a thicker SEI that degrades cycling performance.[124] However, Wang et al. observed a change in SEI structure at high temperature, forming a Li_2O-rich outer layer that promoted stable cycling.[125] Similarly, a less resistive SEI can form at low temperature,[126] so LMBs for high- and low-temperature applications could be realised through rational design of electrolyte systems that produce favorable SEIs.

The initial surface of lithium metal is also always covered with a native passivation layer (NPL) composed of Li_2O, Li_2CO_3 and LiOH, although the exact thickness and composition depends on the storage conditions and duration.[127] The NPL influences the resulting SEI that forms on top,[128] making it far more difficult to determine the role of the SEI. To negate the influence of the NPL, Kühn et al. adapted a technique to cut lithium metal electrodes in electrolyte, allowing only SEI to form at the freshly exposed surfaces. The exclusion of the NPL generally reduced impedances and overpotentials, although cycling performance was only improved in one of the systems investigated.[129] Nevertheless, it is important to consider the SEI without the NPL to determine the true impact of electrolyte chemistry on cycling performance, and to appreciate that the SEI will be highly influenced by any electrode preparation steps prior to cell assembly. Any differences in lithium preparation methods used by different researchers could therefore impact results.

The NPL can also be excluded by electrodepositing lithium directly onto the current collector;[128] a process that is crucial to the development of zero-excess-lithium cells.[9] However, this introduces additional complexities into SEI analysis, as while lithium metal is able to chemically react with electrolyte species and immediately reduce them, alternative current collectors like copper are unable to reduce the electrolyte in the absence of an applied potential.[130] SEI formation on these higher-electrode-potential substrates instead occurs through electrochemical reduction once the potential of the substrate is reduced below the reduction potential of the electrolyte components.[63,131] As such, SEI nanostructure depends on how the potential is varied during its formation, and it may be very different to that formed on lithium. For example, Wang et al. compared the SEIs formed on copper by linear sweep voltammetry and by using a potential step, with a potential step producing a thinner, more inorganic SEI as a result of the lower potential during the entire formation process.[132] Additionally, the SEI that formed on

lithium metal was even thinner and more inorganic, and repeated lithium stripping and plating was only observed within SEI shells that formed directly on lithium metal,[132] suggesting this type of SEI is most beneficial. This is further supported by a recent *in-situ* plasmon-enhanced Raman spectroscopy study which revealed the initial SEI that forms on copper is restructured after lithium deposition, and performance is enhanced if lithium deposition precedes SEI formation.[133]

This electrochemical formation route also offers opportunities to control the structure and chemistry of the SEI, as different electrolyte components undergo reduction at different potentials.[134,135] This could enable the development of formation protocols to produce SEIs with a designed nanostructure by understanding and balancing the thermodynamics and kinetics of the separate reduction reactions.[136] In this way, Gu et al. developed an electrochemical polishing process to control SEI formation while simultaneously generating a near-atomically flat lithium surface,[121] which is beneficial as the SEI is known to mirror the non-uniformities of the underlying substrate,[130,137] producing weak points that can fracture and lead to filament growth.[138] This electrochemical polishing process significantly improved the cycling stability, with a multilayered SEI giving the best performance,[121] possibly due to the formation of a resilient cross-linked organic layer.[73] SEI performance is further influenced by current density during formation and cycling. Oyakhire et al. demonstrated that preforming an SEI with constant current cycling at 0.5 mA cm^{-2} (the lowest current density tested) resulted in the highest CE during subsequent cycling.[136] In contrast, Ding et al. reported a reduction in capacity loss due to continuous SEI formation during cycling and an increase in CE when the current density during stripping was increased.[139] The impact of current density on SEI performance therefore requires additional study.

Finally, the SEI can also change dynamically during cycling,[140] with carbonate species observed to form during plating and become partially lost during stripping,[141] likely caused by the non-negligible solubility of most SEI components in typical solvents.[142] Recent evidence further revealed that as much as 60% of the mass of the SEI can be lost due to dissolution, and CE was observed to decrease with increasing SEI dissolution.[143] The nanostructure of the SEI is therefore influenced by numerous factors, as summarised

in Figure 1.8, all of which need to be kept as consistent as possible between experiments to ensure that accurate conclusions can be drawn. The implementation of standard SEI formation protocols would also greatly facilitate the comparison of results obtained by different researchers, accelerating systematic study of the SEI to uncover its role in LMBs.

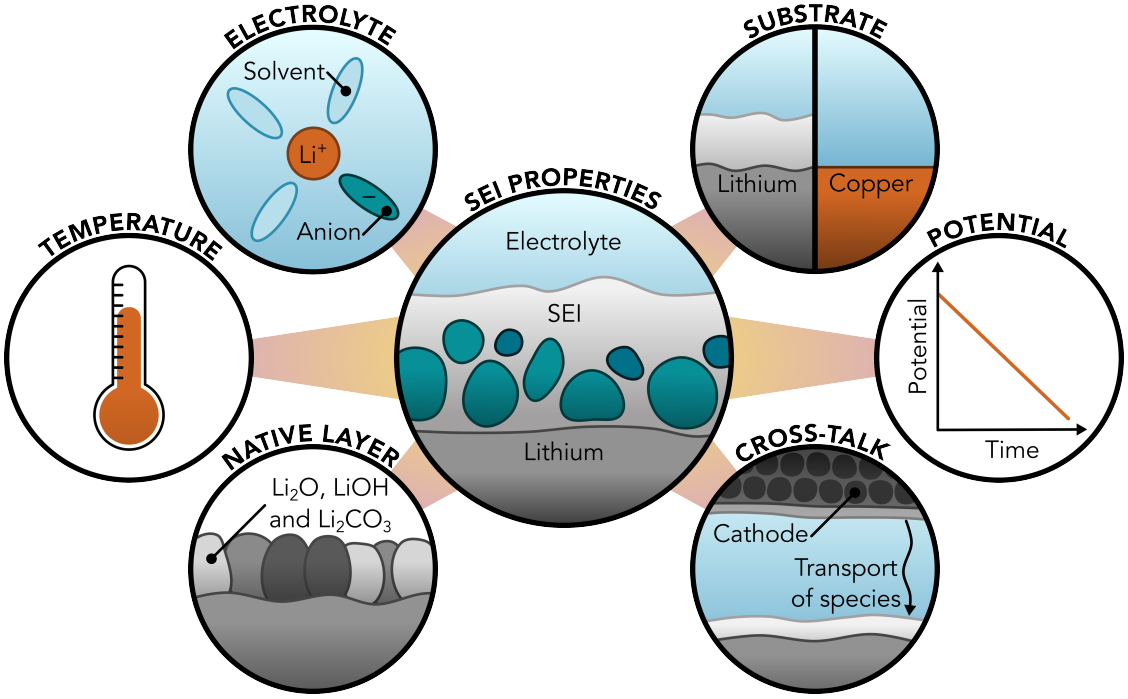


Figure 1.8: Factors affecting solid electrolyte interphase (SEI) properties. The structure and composition of the SEI are affected by numerous factors, including the electrolyte chemistry and concentration, the temperature during formation, the composition of the native passivation layer on lithium, the choice of substrate material, and the potential of the working electrode during formation. The influence of cross-talk must also be considered when examining full cells.

1.4.2.2 Cross-Talk

The above discussion applies to the SEI formed in symmetric (Li||Li) or half-cell (Cu||Li) configurations. However, an additional phenomenon must be considered in the case of full cells: cross-talk. Cross-talk describes any process in which (electro)chemical reactions at one electrode produce products that travel to the other electrode and react.[144] One of the more infamous cases of cross-talk occurs when using transition metal oxide cathodes, which suffer from transition metal dissolution. The dissolved metal ions are able to migrate to the anode where they are reduced to form metallic deposits within the SEI, leading to capacity loss.[144,145] The role of dissolved Mn^{2+} ions on SEI formation was further investigated by Zhang et al., revealing that the presence of Mn^{2+} in the electrolyte

alters the electrolyte decomposition reactions and forms a non-uniform manganese-rich SEI, leading to inhomogeneous lithium deposition and significantly reducing the CE.[146] Electrolyte species may also be oxidised at the cathode, generating soluble products that degrade anode performance.[147] On the other hand, cross-talk is not always detrimental.[148] For example, CO_2 gas generated by electrolyte oxidation at the cathode can be consumed at the anode to form Li_2CO_3, extending cell lifetime.[144] It has also been proposed that high-voltage cathodes can catalyse anion decomposition, forming reactive products that contribute to a favourable SEI on lithium.[93] Understanding the SEI that forms on the anode in full cells therefore requires knowledge of the decomposition reactions occurring at both electrodes, and it presents a significant challenge.

Cross-talk is also particularly problematic for SEI studies in KIBs, as Madec et al. and Allgayer et al. have demonstrated that the presence of potassium metal in a cell can generate reduction products that deposit on the other electrode, altering its surface chemistry.[149,150] Potassium metal is often used as both a counter and reference electrode in KIB research, so an alternative, stable reference electrode should be developed for accurate SEI characterisation. This will be the focus of Chapter 5.

1.4.3 Critical Research Fronts

In this chapter the importance of the SEI in controlling lithium deposition morphology and cycling stability in LMBs has been highlighted and major breakthroughs in understanding the SEI have been discussed, with a focus on how performance is related to SEI nanostructure, transport, and mechanical properties. However, there still remain unanswered questions that would be instrumental in the rational design of an SEI for safe and stable LMBs. Several critical research fronts (Figure 1.9) that should be addressed have therefore been identified:

Correlating structure with transport and mechanics

Rational SEI design will first require a determination of the SEI properties needed for stable LMB operation, including Li^+ diffusivity, elastic modulus, and elastic strain limit. However, methods capable of directly probing Li^+ transport independently from other processes are currently lacking, so their development remains an important challenge.

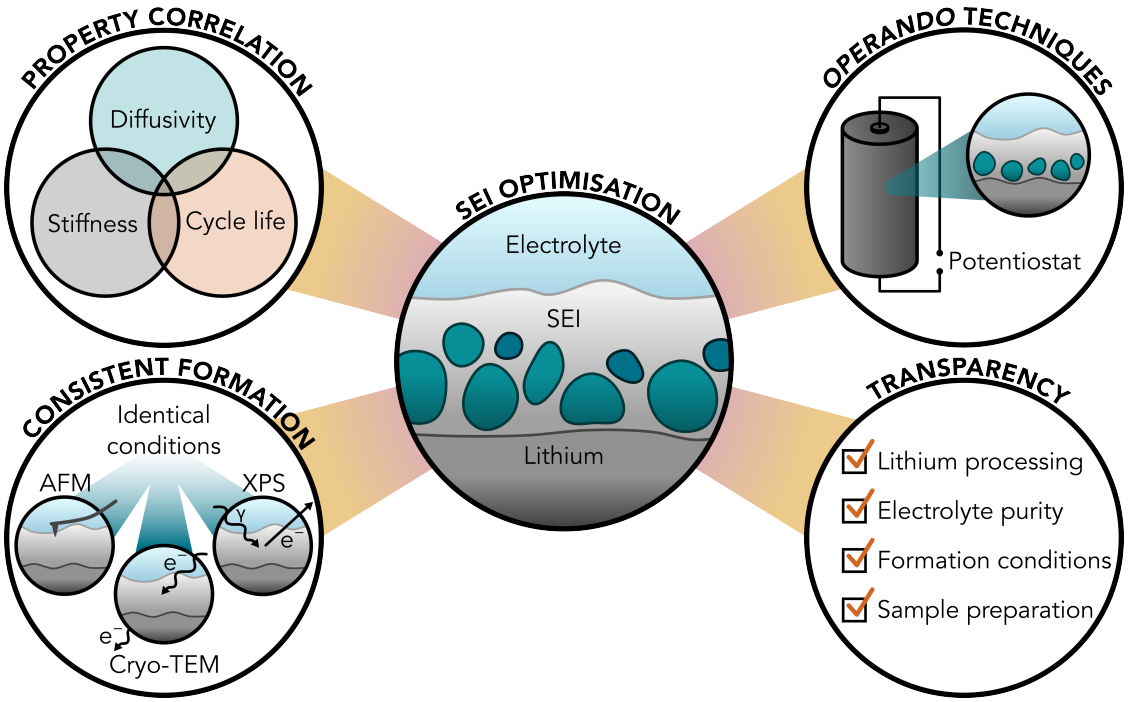


Figure 1.9: Critical research fronts for solid electrolyte interphase (SEI) characterisation.

Careful, systematic studies will additionally be necessary to correlate the structure and chemistry of an SEI to its properties, providing guidelines to tailor the performance of an SEI through control of its nanostructure. This would then enable the design of an optimal SEI, further directing the rational development of novel electrolyte formulations and SEI formation protocols capable of achieving this structure, facilitating the commercialisation of safe and stable, high-energy-density LMBs.

Operando characterisation techniques

The nanostructure of the SEI can change dynamically during cell operation, and it is strongly influenced by the sample preparation steps used during current post-mortem analysis. This could potentially enable misleading structure-property relationships to direct future research efforts, as may have been the case with the recent interest in a LiF-rich SEI.[83] It is therefore necessary to implement *operando* techniques capable of investigating the SEI under realistic operating conditions, allowing its true nanostructure to be determined. To this end, electrochemical techniques, such as EIS, are particularly promising and widely available. Recent developments like dynamic impedance spectroscopy could also offer improved temporal resolution,[151] enabling transient states to be resolved

and providing invaluable insight into the mechanisms taking place during SEI formation and cell operation. However, EIS alone cannot give a complete picture of the SEI, requiring the further development of *operando* spectroscopic and tomographic techniques able to probe the SEI with the necessary resolution, such as structured illumination Raman microscopy[152] and ptychographic X-ray laminography.[153]

Consistent SEI formation

Most current SEI characterisation techniques, including cryo-TEM, AFM and XPS, can only be performed *in situ* or *ex situ*. While these techniques are unable to probe the SEI during operation, they can still provide useful information about the SEI, particularly when used together, provided the SEI under investigation has been produced consistently. As discussed throughout this chapter, the nanostructure of the SEI is influenced by a wide range of factors, including the lithium surface, temperature, time, potential during formation, and any sample processing steps. All these factors should be kept the same when producing SEI samples for characterisation with different techniques to ensure that results from separate experiments can be accurately combined. One potential method of excluding the influence of initial lithium metal topography and surface chemistry is to implement a zero-excess-lithium configuration and form SEI directly on alternative substrates like copper. While this will be a useful approach for fundamental SEI studies, it is important to note that the SEI formed on copper is likely to differ significantly from that formed on lithium and, as such, they should not be assumed to be equal. Alternatively, the use of different formation protocols on the same electrolyte system could produce several different SEI nanostructures, facilitating the elucidation of the impact of SEI structure on cycling stability without the need to change electrolyte chemistry.

Transparency in reporting

The wide range of possible SEI formation conditions complicates the comparison of results gathered by different researchers. It is therefore essential that detailed SEI formation conditions are accurately reported, including any lithium processing, the potential during SEI formation, formation time, and sample preparation steps, as summarised in Figure 1.8. It is further recommended that, where possible, the lithium metal and electrolyte are also

characterised. For example, the composition of the native passivation layer on the lithium surface can be examined with XPS, the surface topography can be measured with AFM, and nuclear magnetic resonance (NMR) can be used to verify the purity of electrolyte components. Accurate study of the SEI is a complex problem as all these factors influence its formation and evolution, however it will be greatly facilitated by thorough reporting that allows all results to be considered in the correct context. SEI reporting checklists have therefore been proposed for both excess-lithium and zero-excess-lithium cells, which are provided in Appendix A. Furthermore, the adoption of standard SEI formation protocols would aid the sharing of results between researchers.

1.5 Thesis Objectives

In summary, LMBs and KIBs are promising alternatives to conventional LIBs. LMBs have the potential for high performance that will enable the electrification of novel industries, while KIBs only rely on abundant raw materials, minimising the risk of future supply shocks. However, the electrolyte is a crucial missing piece to enabling the commercialisation of both of these systems.

The electrolyte needs to simultaneously enable sufficiently fast ionic transport to allow cells to cycle with high energy efficiency at high rates, and to result in the formation of a passivating SEI that provides kinetic stability to the electrodes without reducing the coulombic efficiency below practical levels. Accurate characterisation of electrolyte transport and thermodynamic properties, as well as the chemistry and properties of the SEI, will therefore be vital to provide the understanding required to develop guidelines for future rational electrolyte design.

The objectives of this thesis are to:

1. Characterise electrolyte ionic transport and thermodynamic properties in equivalent lithium- and potassium-ion electrolytes and uncover the role that cation size has on these properties. This is the focus of Chapter 3.

2. Uncover the impact that temperature, salt concentration, time and solvent have on solid electrolyte interphase chemistry, and compare lithium and potassium systems. This is conducted in Chapter 4.

3. Develop a stable reference electrode for potassium-ion battery research to enable future studies of solid electrolyte interphase formation and electrochemical performance without influence from reactive potassium metal. This is presented in Chapter 5.

2
Method Background

Contents

2.1 X-ray Photoelectron Spectroscopy 29
2.1.1 Probing Depth 30
2.1.2 Peak Shapes 31
2.1.3 Quantification 32
2.2 Electrochemistry 33
2.2.1 Electrode Potentials 33
2.2.2 Reference Electrodes 35
2.2.3 Overpotentials 36
2.2.4 Electrochemical Impedance Spectroscopy 37

2.1 X-ray Photoelectron Spectroscopy

X-ray photoelectron spectroscopy (XPS) is a surface-sensitive technique used to characterise sample surface chemistry. XPS is based upon the photoelectric effect and during an XPS measurement the sample is irradiated with monochromatic X-rays, ejecting electrons from its surface. Measuring the kinetic energy, E_k, of these ejected electrons allows the binding energy, E_b, of the atomic orbital from which the electron is emitted to be calculated using Equation 2.1:[154]

$$E_b = h\nu - E_k - \Phi_s \tag{2.1}$$

where $h\nu$ is the incident X-ray photon energy and Φ_s is the work function of the spectrometer. In this work an $Al_{K\alpha}$ source is used, as is typical, generating X-rays with $h\nu = 1486.6$ eV. Φ_s is typically just a few eV. XPS is performed under ultrahigh vacuum (UHV) conditions to prevent the emitted electrons from being scattered by gas molecules before they can reach the detector.

The binding energy of an electron is related to the energy difference between the initial and final states after a photoelectron has been emitted, and it depends on the element and core level the electron has been emitted from, enabling the chemical composition of surfaces to be determined.[154] The binding energy is further influenced by the chemical environment of an atom, including its oxidation state and nearest neighbours, so XPS can additionally probe the species present in a sample.[155]

Electron photoemission can result in samples becoming positively charged, shifting the measured binding energies. XPS systems are therefore often equipped with charge compensation mechanisms such as electron flood guns and peaks are charge corrected by shifting a known peak to its defined binding energy. Often this is performed by shifting the C 1s peak associated with adventitious carbon to 284.8 eV.[154]

2.1.1 Probing Depth

XPS is surface sensitive owing to the limited inelastic mean free path (IMFP) of electrons. Therefore, although photoelectrons will be generated within a few micrometres of the surface, only those that originate within a few nanometres of the surface can leave the surface without energy loss, resulting in useful peaks in the spectra.[154]

Electron IMFPs in elemental solids have been calculated by Tanuma, Powell and Penn,[156] and the IMFP for metallic lithium is plotted as a function of electron kinetic energy in Figure 2.1.

The kinetic energies of typical transitions analysed in this work are also plotted in Figure 2.1. The Li 1s transition has the lowest E_b, so it has the highest E_k and the largest IMFP of approximately 5 nm. In XPS approximately 95% of the electrons will originate from a depth of less than 10 nm,[155] hence its surface sensitivity.

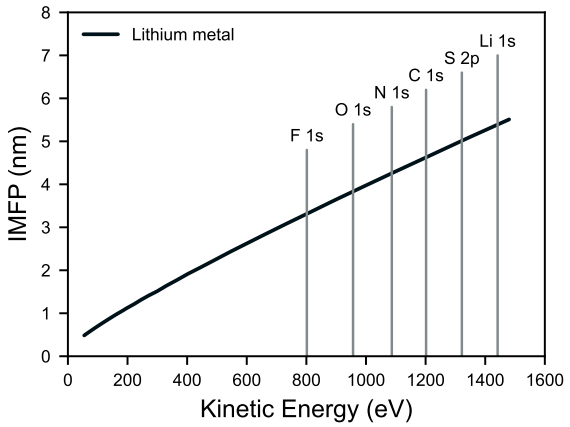


Figure 2.1: Electron inelastic mean free path (IMFP) in lithium metal reported by Tanuma, Powell and Penn.[156] The kinetic energies of electrons from transitions often detected in this work are also plotted for $h\nu = 1486.6$ eV.

The electron IMFPs can further be estimated for different materials and kinetic energies using the TPP-2M formula given by Tanuma, Powell and Penn.[156]

Depth profiling is achieved by alternating between analysing the sample and etching away its surface, often using an argon-ion gun. However, care should be taken when interpreting data from etched samples as the argon-ion beam can alter the surface chemistry.[77,79,155]

2.1.2 Peak Shapes

Electron s orbitals have an angular momentum quantum number, l, of 0, so they result in singlet peaks. However, p, d and f orbitals have an l of 1, 2 and 3, respectively. For these orbitals spin-orbit coupling results in the total angular momentum quantum number, j, taking values of $j = l \pm \frac{1}{2}$. The $j - \frac{1}{2}$ peak appears at a higher binding energy than the $j + \frac{1}{2}$ peak, producing a doublet peak with an energy separation that is characteristic of the element and transition the electrons are emitted from. These two energy levels have degeneracies given by $2j + 1$, so the $j - \frac{1}{2}$ and $j + \frac{1}{2}$ peaks have intensity ratios of 1:2, 2:3 and 3:4 for p, d and f orbitals, respectively.[155]

The core hole generated by photoemission has a finite lifetime, resulting in broadening of XPS peaks with a Lorentzian shape. Additional peak broadening occurs in the spectrometer during detection, adding Gaussian character to the peak. Observed peak shapes therefore often have a shape described by a Voigt function, which is a convolution of

the Lorentzian and Gaussian profiles. In practice, Gaussian-Lorentzian product functions that approximate the Voigt function are often used during peak fitting.[157]

The full width at half maximum (FWHM) of a peak is determined by the natural linewidth of the core energy level, the linewidth of the incident photons, and broadening that takes place within the hemispherical analyser used to detect electrons.[157] Electrons are retarded to a pass energy, E_{pass}, before they enter the hemispherical analyser. A lower E_{pass} increases the energy resolution of the detector, but reduces the measured signal intensity.[154,157] Therefore in this work $E_{\text{pass}} = 224$ eV for survey scans, while $E_{\text{pass}} = 55$ eV for high-resolution core-level spectra.

The peak shapes encountered in this work are often symmetric, but differences can be observed for metallic peaks. In metals a portion of the incident energy can be lost in the promotion of electrons to a series of unfilled electron levels in the conduction band, resulting in an asymmetric peak with a tail to higher binding energy.[157,158] Energy losses can also occur due to the formation of plasmons, which are group oscillations of conduction electrons. Energy is transferred in well-defined quanta, resulting in plasmon loss peaks at discrete binding energy separations from the main peak.[154]

In addition to photoelectrons, Auger electrons can also be generated and detected during XPS. Auger electrons are emitted when an outer electron fills the core electron hole generated by photoemission, ejecting an additional electron. For example, a KLL Auger electron occurs when an electron from an L shell fills a hole in the K shell, ejecting an additional electron from an L shell.[154] Photoelectrons always appear at the same binding energy, independent of incident photon energy, while Auger electrons have the same kinetic energy.

2.1.3 Quantification

The peak area of a particular transition detected during an XPS measurement is proportional to the concentration of that element within the analysis area, the photoemission cross-section for that transition, the IMFP of the photoelectrons, and additional efficiency factors relating to the detection system and its geometry.[154]

A relative sensitivity factor, S_i, can be defined for each transition, i, that encompasses these factors such that the relative concentrations, c_i, of species can be related to their peak areas, A_i, using Equation 2.2:[154,159]

$$\frac{c_1}{c_2} = \frac{A_1/S_1}{A_2/S_2} \tag{2.2}$$

These relative sensitivity factors have been tabulated based on both empirical observations and theoretical calculations, and for accurate quantification it is important to ensure the selected sensitivity factors are valid for the XPS system being used.[160] Alternatively, they can be calculated from measurements on reference samples of known composition.

2.2 Electrochemistry

2.2.1 Electrode Potentials

Consider the situation in which two metallic electrodes are separated by an electrolyte of uniform concentration containing a salt of the metal. The first electrode is phase α, the second electrode is phase β, and the electrolyte is phase δ.

Let the metallic electrodes undergo the reaction given by Equation 2.3:

$$\mathrm{M} \rightleftharpoons \mathrm{M}^{n+} + n\mathrm{e}^- \tag{2.3}$$

where n is the number of electrons released when M is oxidised. In each phase, A, each species, i, will have an electrochemical potential, $\overline{\mu}_i^A$, given by Equation 2.4:

$$\overline{\mu}_i^A = \mu_i^A + z_i F \phi^A \tag{2.4}$$

where μ_i^A is the chemical potential of species i in phase A, z_i is the charge of species i, F is the Faraday constant and ϕ^A is the electric potential in phase A. For neutral species $z_i = 0$, so the electrochemical and chemical potentials are equal, but for charged species electric fields can influence the electrochemical potential.[161]

Phase equilibrium is established among the phases such that $\overline{\mu}^{\alpha}_{\mathrm{M}^{n+}} = \overline{\mu}^{\delta}_{\mathrm{M}^{n+}}$ and $\overline{\mu}^{\delta}_{\mathrm{M}^{n+}} = \overline{\mu}^{\beta}_{\mathrm{M}^{n+}}$, and at equilibrium the reaction in Equation 2.3 results in a relationship between the electrochemical potentials of the three species in electrode α, given by Equation 2.5:[162]

$$\overline{\mu}^{\alpha}_{\mathrm{M}} = \overline{\mu}^{\alpha}_{\mathrm{M}^{n+}} + n\overline{\mu}^{\alpha}_{\mathrm{e}^-} = \overline{\mu}^{\delta}_{\mathrm{M}^{n+}} + n\overline{\mu}^{\alpha}_{\mathrm{e}^-} \tag{2.5}$$

An equivalent relation can be derived for electrode β.

The measured cell potential, E, between the two electrodes is related to the difference between the electrochemical potentials of electrons in the two electrodes and is given by Equation 2.6:[162]

$$E = \frac{\overline{\mu}^{\alpha}_{\mathrm{e}^-} - \overline{\mu}^{\beta}_{\mathrm{e}^-}}{F} = \frac{\left(\frac{1}{n}\overline{\mu}^{\alpha}_{\mathrm{M}} - \frac{1}{n}\overline{\mu}^{\delta}_{\mathrm{M}^{n+}}\right) - \left(\frac{1}{n}\overline{\mu}^{\beta}_{\mathrm{M}} - \frac{1}{n}\overline{\mu}^{\delta}_{\mathrm{M}^{n+}}\right)}{F} = \frac{\overline{\mu}^{\alpha}_{\mathrm{M}} - \overline{\mu}^{\beta}_{\mathrm{M}}}{nF} \tag{2.6}$$

Equation 2.6 gives the voltage of electrode β measured relative to α and shows that the cell potential (in the absence of electrolyte concentration gradients) is determined by the electrochemical potentials of the neutral atoms in the electrodes, which are identical to their chemical potentials. The chemical potential of a species, i, in a phase, A, can be related to the chemical potential in a standard state, μ^0_i, and the activity of the species, a^A_i, according to Equation 2.7:[161]

$$\mu^A_i = \mu^0_i + RT \ln a^A_i \tag{2.7}$$

where R is the gas constant and T is the absolute temperature. Combining Equations 2.6 and 2.7 results in Equation 2.8, which is a special case of the Nernst equation.

$$E = -\frac{RT}{nF} \ln \frac{a^{\beta}_{\mathrm{M}}}{a^{\alpha}_{\mathrm{M}}} \tag{2.8}$$

The difference in cell potential is therefore determined by the relative activities of the metal M in the two electrodes. If both electrodes are pure then $a^{\alpha}_{\mathrm{M}} = a^{\beta}_{\mathrm{M}} = 1$ and there will be no potential difference between them, but if the activity of M in electrode β is reduced (by introducing an additional alloying element, for example) then a positive cell potential will develop. This cell potential is related to the free energy change for the reaction, ΔG, according to Equation 2.9:

$$\Delta G = -nFE \tag{2.9}$$

If E is positive then ΔG is negative, so if the electrodes are connected electrons would spontaneously flow from α to β, oxidising the electrode at α and reducing the electrode at β. If E is negative then the reverse reactions would occur.

2.2.2 Reference Electrodes

It is not possible to measure the absolute potential of an individual electrode in isolation. Only the relative potentials between pairs of electrodes can be measured. It is therefore helpful to introduce reference electrodes against which the potential of a working electrode can be measured. An ideal reference electrode should have a stable, well-defined potential and should not alter the system under study.

For non-aqueous lithium-based battery research metallic lithium is frequently used as a reference electrode, and cell voltages are reported relative to Li^+/Li. Similarly, potassium metal is used in potassium-ion battery (KIB) research, giving cell voltages relative to K^+/K. Elemental electrodes have a constant potential, independent of the state of charge of a cell. This can be rationalised with consideration to the Gibbs Phase Rule (Equation 2.10) which relates the number of degrees of freedom, f, to the number of components, C, and the number of phases, P, in a system in thermodynamic equilibrium:[163]

$$f = C - P + 2 \tag{2.10}$$

In a pure metallic electrode $C = 1$ and $P = 1$, so $f = 2$. Therefore, fixing the temperature and pressure reduces f to zero, and the chemical potential, and therefore potential of the electrode, is constant.[163]

However, lithium and potassium metal are highly reactive, spontaneously forming a native passivation layer before cell assembly and a solid electrolyte interphase (SEI) immediately upon electrolyte addition. While this generally has limited impact on the reference electrode potential,[163] excessive electrolyte consumption by the reference electrode should be avoided, especially in KIBs where the presence of a potassium metal can alter the surface chemistry of the other electrodes.[150]

A range of binary lithium alloys have therefore been explored as reference electrodes.[164] According to Equation 2.8, this reduces the lithium activity and therefore increases the

electrode potential relative to pure lithium, reducing their reactivity. These alloys introduce an additional component, and therefore degree of freedom, so single-phase binary alloys do not have a fixed potential. On the other hand, in two-phase alloys $C = 2$ and $P = 2$, so the electrode potential is stable at constant temperature and pressure (Equation 2.10). When these alloys are cycled within the two-phase region the relative proportions of the phases change but the lithium chemical potential and the electrode potential remain constant.

Reference electrodes can be used in both two- and three-electrode cells. In two-electrode cells the reference additionally acts as the counter electrode, and any overpotentials associated with cycling the counter/reference electrode will contribute to the observed potential response of the working electrode. In contrast, in three-electrode cells a separate counter electrode is introduced. Three-electrode cells are beneficial as no current passes through the reference and the potentials of both the working and counter electrodes can be recorded separately, but they are generally more challenging to assemble with a realistic cell geometry.

2.2.3 Overpotentials

The electrode potentials considered above were derived assuming equilibrium and give the cell open-circuit voltages (OCVs). This is the voltage that would be measured when there is zero current flowing between the two electrodes and the rates of the forward and reverse electrode reactions are equal.

In order to extract current from a cell a driving force is required to force an electrochemical reaction to occur. This driving force is known as the surface overpotential, η_s.[162] In the same way, if a cell is cycled galvanostatically, where a constant current is applied, then a corresponding η_s must be generated. In lithium- and potassium-based battery systems this η_s encompasses a range of interfacial phenomena, including charge-transfer kinetics and cation migration through the SEI.[34,101,165] The Butler-Volmer equation can be used to provide an approximate conversion between the applied current and η_s, and a larger surface overpotential is required to sustain a larger current.[162]

Two additional overpotentials develop when current is applied to a cell: the Ohmic drop, η_{Ohmic}, and the concentration overpotential, η_c.

η_{Ohmic} is typically dominated by the ionic resistance of the electrolyte, which is inversely proportional to the ionic conductivity, κ, and it is directly proportional to the applied current.[162] η_{Ohmic} appears immediately when current is applied .

η_c is caused by the development of concentration gradients within the cell. As discussed in Chapter 1, the salt diffusivity, D, and cation transference number, t_+^0, control the extent to which concentration gradients form during cell cycling,[33] and the thermodynamic factor, χ_M, is required to convert the electrolyte concentration differences at the two electrodes into η_c.[162] η_c is proportional to the applied current and it grows over time.[34,35]

When charging a cell η_s, η_{Ohmic}, and η_c all act to increase the cell voltage above the OCV, requiring more energy to be input into the system. During discharge they act to reduce the cell voltage, reducing the energy that can be extracted, leading to hysteresis in cell voltage profiles.[162] These overpotentials are therefore important in controlling cell energy efficiency.

When the current is stopped η_s and η_{Ohmic} disappear rapidly, but η_c decays slowly over time as the concentration gradients in the electrolyte dissipate through diffusion.

2.2.4 Electrochemical Impedance Spectroscopy

In electrochemical impedance spectroscopy (EIS), a small-amplitude potential (or current) perturbation is applied to a system and the resulting current (or potential) response is recorded as a function of angular frequency.[166]

Consider applying a sinusoidally oscillating potential, $V(t)$, with amplitude V_0 and angular frequency ω. If the amplitude of the perturbation is small enough to maintain linearity then the resulting current response, $I(t)$, will have the same angular frequency but may experience a phase shift, φ (Equation 2.11). The current amplitude, I_0, and φ will be a function of ω.

$$V(t) = V_0 \cos(\omega t), \qquad I(t) = I_0(\omega) \cos(\omega t - \varphi(\omega)) \tag{2.11}$$

Equation 2.11 can alternatively be expressed in phasor notation, where $\tilde{V}(\omega)$ and $\tilde{I}(\omega)$ are complex, time-invariant numbers accounting for the amplitude and phase of the voltage and current, respectively,[166] as presented in Equation 2.12:

$$V(t) = \tilde{V}(\omega)e^{i\omega t}, \quad \tilde{V}(\omega) = V_0, \qquad I(t) = \tilde{I}(\omega)e^{i\omega t}, \quad \tilde{I}(\omega) = I_0(\omega)e^{-i\varphi(\omega)} \tag{2.12}$$

where $i = \sqrt{-1}$.

The angular frequency-dependent impedance, $Z(\omega)$, of the system can be calculated from these phasors according to Equation 2.13:[166]

$$Z(\omega) = \frac{\tilde{V}(\omega)}{\tilde{I}(\omega)} = \frac{V_0}{I_0(\omega)}e^{i\varphi(\omega)} = |Z(\omega)|\left(\cos\varphi(\omega) + i\sin\varphi(\omega)\right) = Z' + iZ'' \tag{2.13}$$

where Z' and Z'' are the real and imaginary components of Z, respectively. Impedance spectra are typically presented in Nyquist plots where Z' is plotted against $-Z''$.

For accurate analysis impedance spectra must satisfy the conditions of linearity, stability and causality. Linearity ensures the response is a linear function of the single-frequency input signal and it is achieved by using a small input perturbation. Stability requires that the response to a perturbation does not grow with time and the system does not change during a measurement. Causality demands that the response of the system is entirely determined by the applied perturbation.[166,167] Unfortunately, battery systems do not always meet these conditions as they are known to vary with time, which places a lower limit on the frequency that can be probed using EIS.

EIS spectra can contain a wealth of information about a sample and it has been used to probe electrolyte ionic conductivity,[35,38] charge-transfer,[30,101] SEI evolution[102] and diffusion in both electrolyte and electrodes,[166] to name a few, all under *operando* conditions. This information is often extracted from the impedance spectra by fitting equivalent circuit models that are believed to represent the physics of the system, but battery systems are complicated and many different models can result in a good fit to the same data.[97,166] Additionally, many of the processes occur at overlapping frequencies, further complicating the unambiguous assignment of impedance features to physical phenomena.

In two-electrode cells the measured impedance response contains contributions from both electrodes, and this can be dominated by the large impedance of alkali metal counter/reference electrodes. In three-electrode cells, however, the working electrode can be investigated in isolation.[166]

3

Ionic Transport in Lithium- and Potassium-Ion Electrolytes

Abstract

Electrolyte ionic transport and thermodynamic properties influence battery degradation and rate capability, so their accurate characterisation is vital to understand cell performance and guide electrolyte development. In this chapter a protocol is developed to produce potassium metal electrodes with enhanced potential stability, enabling the concentration-dependent salt diffusivities, cation transference numbers, ionic conductivities and thermodynamic factors to be measured for the non-aqueous potassium-ion electrolyte, potassium bis(fluorosulfonyl)imide (KFSI) in 1,2-dimethoxyethane (DME). Comparison with the equivalent lithium-ion system (LiFSI in DME) reveals that the lower charge density of K^+ compared to Li^+ enhances salt diffusivities and cation transference numbers, but reduces salt dissociation.

The results presented in this chapter have contributed to the following publication:
Dhir, S.*, **Jagger, B.***, Maguire, A. & Pasta, M. Fundamental Investigations on the Ionic Transport and Thermodynamic Properties of Non-Aqueous Potassium-Ion Electrolytes. *Nat. Commun.* **14**, 3833 (2023). (* these authors contributed equally.)

Contents

3.1 Introduction 41
3.2 Potassium Metal Electrode Preparation 42
3.3 Transport and Thermodynamic Property Characterisation . 48
3.3.1 Cation Transference Number 49
3.3.2 Ionic Conductivity 51
3.3.3 Thermodynamic Factor 54
3.3.4 Salt Diffusivity 59
3.3.5 Thermodynamic and Stefan-Maxwell Diffusivities 63
3.4 Conclusion 65
3.5 Experimental Methods 67

3.1 Introduction

Fast charging rates (up to 4 C)[168] are becoming increasingly important for batteries, particularly in electric vehicles (EVs), but conventional lithium-ion batteries (LIBs) are inherently limited in their rate capability.[169] Potassium-ion batteries (KIBs), however, may have an advantage over LIBs in terms of rate and power. The larger size of K^+ compared to Li^+ results in a lower charge density, and thus weaker interactions with solvent molecules and a smaller Stokes radius,[170] which is expected to facilitate faster ionic transport in the electrolyte.[22] This is supported by the results from Landesfeind et al. who reported improved transport properties of in a non-aqueous Na-ion electrolyte compared to its Li-ion equivalent.[171] It also appears from various data sources collated by Landesfeind et al. that aqueous K-ion electrolytes may show faster transport properties compared to Li- and Na-ion,[171] and K^+ has been found to have the lowest desolvation activation energy of the three cations.[172,173]

Though many reports suggest this improved rate performance, a comprehensive understanding of mass transport in K-ion electrolytes can only be obtained through full and accurate characterisation of the fundamental ionic transport and thermodynamic properties: the salt diffusion coefficient, D, the cation transference number, t_+^0, the ionic conductivity, κ, and the thermodynamic factor, χ_M.[33]

There are a growing number of studies which have fully characterised these properties for Li-ion electrolytes using a variety of electrochemical techniques.[36,174–179] Spectroscopic

techniques, capable of determining these properties through direct visualisation of concentration gradients, have also recently been developed. These include X-ray spectroscopy,[180] Raman spectroscopy,[35] or magnetic resonance imaging (MRI).[34,181] However, when this project was undertaken there was no study which had fully characterised the ionic transport and thermodynamic properties (D, t_+^0, κ and χ_M) for a K-ion electrolyte. These properties are traditionally challenging and time-consuming to obtain for Li-ion electrolytes, and the need to use potassium metal electrodes for non-aqueous K-ion electrolyte characterisation introduces additional challenges.

In this chapter the critical transport and thermodynamic properties of non-aqueous K-ion electrolytes are characterised as a function of electrolyte concentration, and these are compared with the corresponding Li-ion system. The K-ion electrolyte system investigated was potassium bis(fluorosulfonyl)imide (KFSI) in 1,2-dimethoxyethane (DME), while lithium bis(fluorosulfonyl)imide (LiFSI) in DME was the Li-ion electrolyte. FSI^- in DME was used as the model electrolyte system because of the proven ability of FSI^- to effectively passivate both lithium and potassium metal[74,182,183] and due to the stability of ether solvents at low potentials.[5,183]

The objectives of this chapter are to:

1. Develop a methodology to produce potassium metal electrodes with enhanced potential stability and reproducibility.

2. Fully characterise the ionic transport and thermodynamic properties of equivalent lithium- and potassium-ion electrolytes.

3. Investigate the impact that cation size has on electrolyte transport.

3.2 Potassium Metal Electrode Preparation

Several of the electrochemical techniques used to determine electrolyte transport properties rely on the measurement of concentration overpotentials in symmetric cells with metallic electrodes. These concentration overpotentials are often just a few mV, requiring the metallic electrodes to have a stable potential during the measurement. In the absence of electrolyte concentration gradients the open-circuit voltage (OCV) measured in a

symmetric cell should be 0 V as both electrodes are identical. Supporting this, Hosaka et al. reported that in both symmetric Li||Li and Na||Na cells the measured OCV is below 5 mV,[182] and in this work Li||Li cells typically exhibited stable OCVs below 1 mV. In contrast, in symmetric K||K cells the measured OCV can be upwards of 500 mV and it has been reported to vary significantly over time and between cells.[182] Using a standard potassium electrode preparation methodology reported in the literature,[184] where as-received potassium metal chunks are rolled into foils and punched into electrodes, resulted in a similar high and irreproducible OCV, as seen in Figure 3.1. This inconsistent OCV would prevent accurate electrolyte transport property characterisation, so an alternative electrode preparation method must be employed.

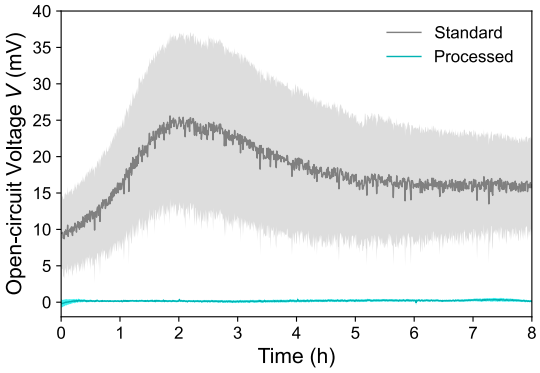


Figure 3.1: OCV in symmetric K||K cells comparing electrodes prepared using the standard methodology with those produced from the processed potassium. Measurements were performed in 1 m KFSI DME at 20°C. Light shaded areas depict standard error in the mean, calculated from at least 5 cells.

The non-zero OCV measured when using as-received potassium metal suggests that the two electrodes have different activities, which could be caused by inhomogeneous distributions of impurity species. The potassium metal was therefore processed prior to use and a preparation methodology was developed to minimise the concentration of impurities on the electrode surface during cell assembly. The first step involved melting the potassium metal chunks in an Ar-filled glovebox, skimming off any solid impurities from the surface of the melt and then quenching the potassium into clean mineral oil. The potassium was then transferred to hexane that had been dried over molecular sieves for storage. Potassium metal electrodes were then produced by rolling the potassium into an approximately 0.6 µm thick foil and punching it into discs that were then stuck

onto the current collector. Immediately before electrolyte addition the surface of the potassium was polished using a microtoming technique adapted from a methodology developed for metallic lithium,[185] producing a mirror-like finish. As evident in Figure 3.1, this results in a stable OCV below 1 mV with much greater reproducibility. Additionally, the polishing process results in electrodes with reduced roughness, and atomic force microscopy (AFM) height mapping (Figure 3.2) gives root mean square roughnesses of 33 and 253 nm for the processed and standard samples, respectively.

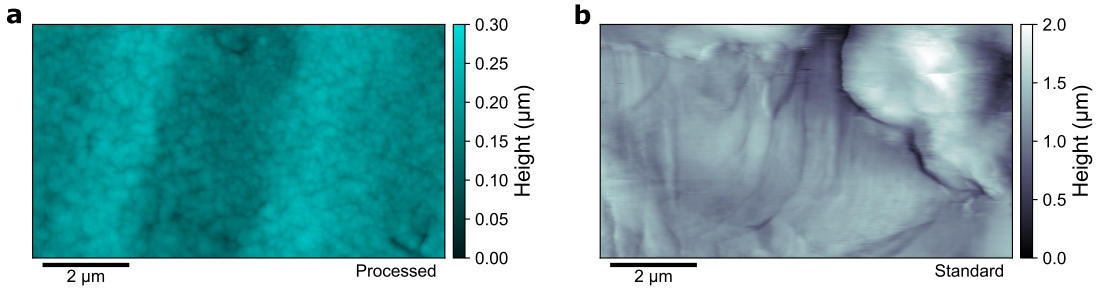


Figure 3.2: Comparison AFM height maps of the surface of pristine potassium metal samples prepared using (a) the processed potassium, (b) the standard procedure.

X-ray photoelectron spectroscopy (XPS) with Ar^+ depth profiling was utilised to examine the surfaces of the potassium electrodes prepared using both the standard literature method and the processed potassium to determine the chemistry of the native passivation layer (NPL) and understand the observed differences in stability. These results are presented in Figure 3.3 and full spectra are provided in Appendix B.1.

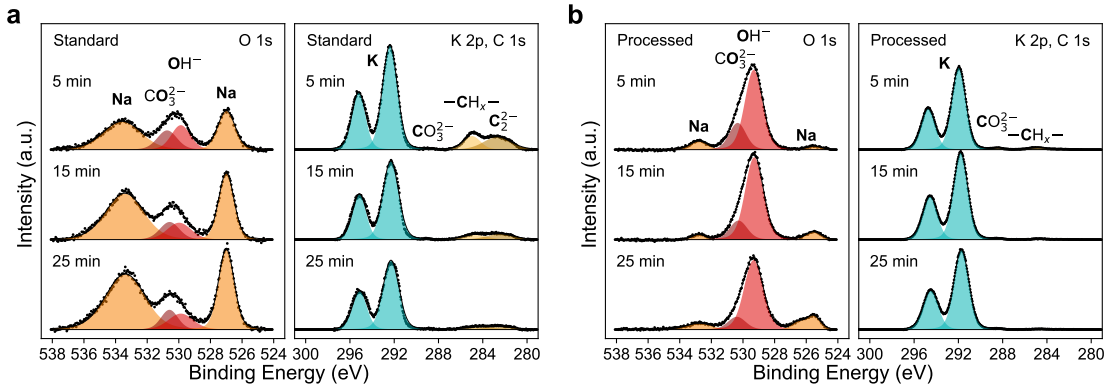


Figure 3.3: XPS depth profiles on potassium metal after 5, 15 and 25 min of Ar^+ sputtering. (a) O 1s, K 2p and C 1s spectra from a standard potassium electrode. (b) O 1s, K 2p and C 1s spectra from the processed potassium.

The O 1s spectra from the standard preparation in Figure 3.3a exhibit peaks at

533.6 and 527.0 eV as a result of Na KLL Auger electron emission[186] and sodium is the main element identified throughout the majority of the examined depth (Figure 3.4a). Such a high concentration of sodium is surprising, and it likely remains as an impurity from the potassium metal manufacturing process, which involves passing sodium vapour through a distillation column containing molten potassium salts, where potassium is reduced and it condenses.[187] Sodium and potassium will readily alloy and the liquid phase is stable over much of the composition range at room temperature,[188] so it is likely that a significant quantity of sodium could become incorporated into the potassium. Nevertheless, beyond 10 min of sputtering the detected concentration of sodium is higher that that of even potassium, so surface segregation may be enriching the surface in sodium. Similar sodium impurities were also observed in higher purity potassium metal that was analysed immediately after it was opened. Inhomogeneous distributions of impurity elements like sodium could alter the activity of the potassium metal electrodes, leading to the non-zero OCV evident in Figure 3.1.[189]

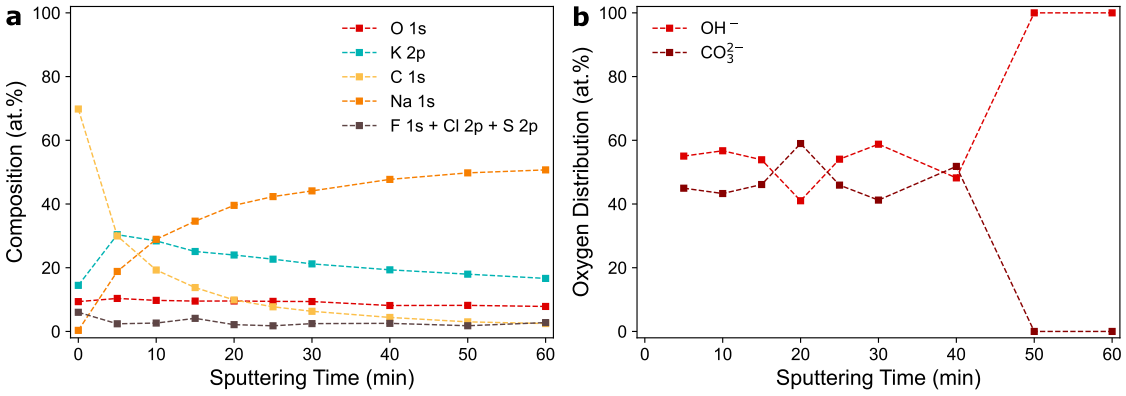


Figure 3.4: Quantification of the composition during XPS depth profiling on a potassium metal electrode produced using the standard preparation. (a) Overall composition. (b) Breakdown of oxygen-containing species.

The two O 1s peaks at binding energies of 529.9 and 530.7 eV in Figure 3.3a are attributed to hydroxide and carbonate environments, respectively, and they have similar areas (Figure 3.4b). The binding energy of the hydroxide peak is consistent with NaOH, while the carbonate peak appears at a binding energy between those of the K_2CO_3 and Na_2CO_3 compounds, suggesting both may be present but cannot be resolved.[186] The C 1s XPS spectra in Figure 3.3a demonstrate a corresponding minor carbonate peak around

289 eV and an adventitious carbon peak at 285 eV. There is an additional broad C 1s peak at 282.7 eV, which is characteristic of a carbide species and an additional XPS experiment was performed to uncover its origin. Figure 3.5 presents the XPS spectra obtained during Ar^+ depth profiling for a total of 5 minutes. It is evident from the C 1s spectra in Figure 3.5b that this peak once again emerges, appearing as a shoulder on the adventitious carbon peak after 1 min of Ar^+ sputtering, and then increasing in intensity with increasing sputtering time. The only other peak that appears in the survey spectra during this period (Figure 3.5a) is the small peak at a binding energy of approximately 240 eV. Core-level spectra around this energy (Figure 3.5c) reveal the emergence of a doublet peak that is consistent with Ar 2p,[190] indicating that argon implantation is taking place at the surface.

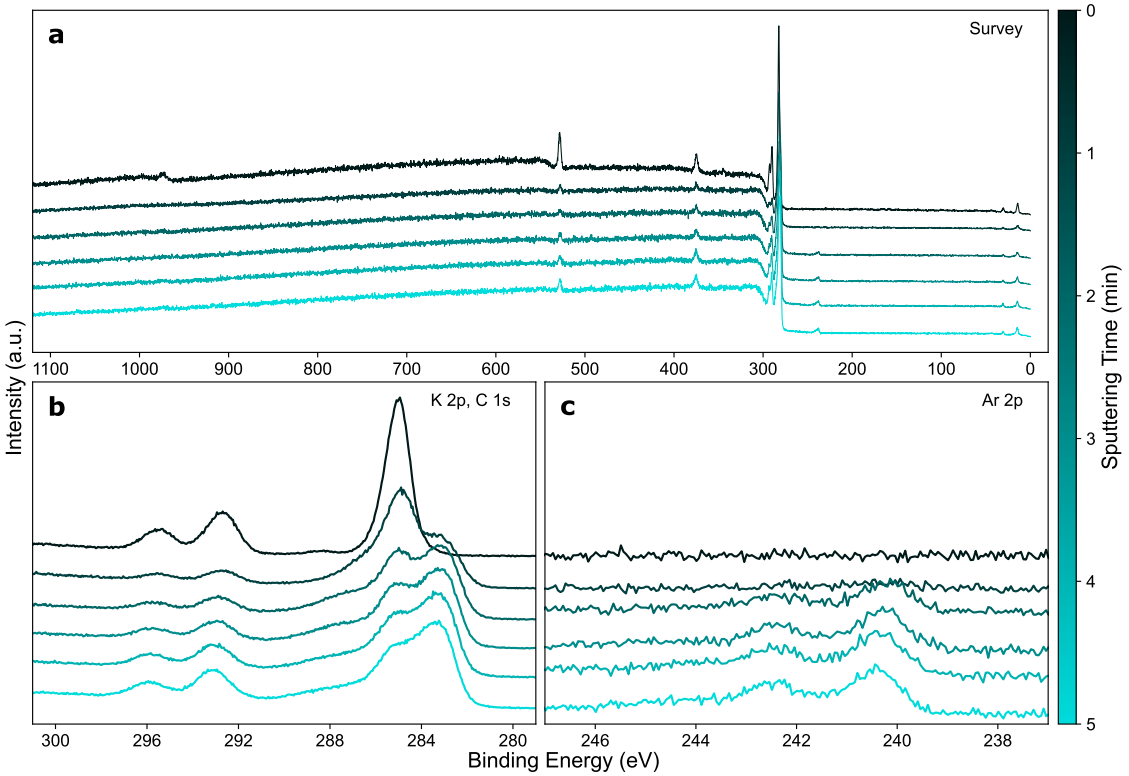


Figure 3.5: XPS depth profiles to determine the origin of the carbide species at the surface of a potassium metal electrode produced using the standard preparation. (a) Survey spectra. (b) K 2p and C 1s regions. (c) Ar 2p region.

No peaks were detected corresponding to transition metals, so a transition metal carbide cannot be the responsible species. It is therefore likely that the C 1s peak is instead due to either a potassium or sodium carbide species. Although there are few reports on these materials, the presence of Li_2C_2 has been confirmed in battery grade

lithium metal[191] and it generates a C 1s peak at a binding energy similar to that observed here.[192] It has been speculated that Li_2C_2 is present as a bulk impurity from lithium production,[191] or that it forms due to a reaction between metallic lithium and organic matter.[193] It is probable that similar processes could occur for sodium or potassium, producing a carbide species that is responsible for the observed peak. Alternatively, a Na_2C_2 or K_2C_2 species could form during the high-energy Ar^+ sputtering process. Ar-ion bombardment-induced mixing has been reported to induce carbide formation during the sputtering of silicon[194] and titanium.[195] In this case, surface carbon-containing species could be mixed with sodium or potassium compounds during argon sputtering, promoting the formation of a sodium or potassium carbide species.

In contrast, in the sample prepared from the processed potassium in Figure 3.3b the O 1s spectra present only minor Na KLL Auger peaks, consistent with the much lower proportion of sodium evident at the surface in Figure 3.6a. The O 1s carbonate and hydroxide peaks appear at 530.4 and 529.3 eV, respectively, consistent with K_2CO_3 and KOH,[150,186] and KOH makes up a much larger proportion of the oxygen-containing species (Figure 3.6b). Due to the high reactivity of potassium metal this KOH likely forms within the XPS as fresh potassium is exposed, suggesting the surface is rich in metallic potassium. The hydroxide peak in the standard sample was attributed to NaOH and had a lower intensity, suggesting there was limited metallic potassium available at the surface.

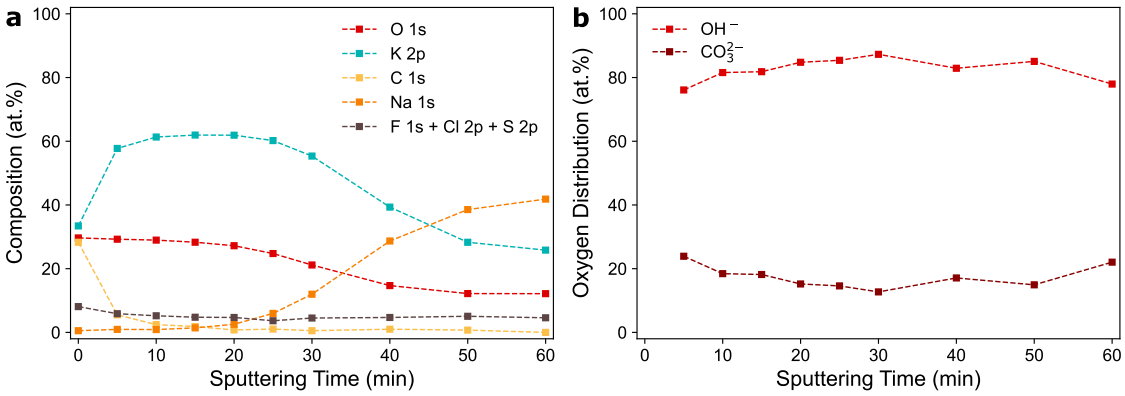


Figure 3.6: Quantification of the composition during XPS depth profiling on a processed potassium metal electrode. (a) Overall composition. (b) Breakdown of oxygen-containing species.

This is further supported by comparing the K 2p spectra in Figure 3.3. The K 2p XPS spectra from the standard electrode in Figure 3.3a show a decreasing K 2p doublet peak

area with sputtering depth, while the K 2p doublet from the processed potassium remains intense during sputtering in Figure 3.3b. The C 1s spectra in Figure 3.3b also show a minor carbonate peak at 288.4 eV and the adventitious carbon peak at 285 eV, with no evidence of a carbide species. These results therefore demonstrate that the processed potassium results in potassium-rich electrode surfaces with greater uniformity and reduced levels of impurity elements, allowing potassium metal electrodes to be prepared with greater reproducibility. This enables electrolyte transport properties to be characterised.

3.3 Transport and Thermodynamic Property Characterisation

Having successfully developed a potassium metal electrode production protocol to provide sufficient potential stability, it is possible to characterise the full suite of electrolyte transport and thermodynamic properties in both Li- and K-ion systems. These include the cation transference number, t_+^0, ionic conductivity, κ, thermodynamic factor, χ_M and salt diffusivity, D, as well as the partial molar volumes of salt, $\overline{V}_e$, and solvent, $\overline{V}_0$. This characterisation was performed with the assistance of Dr S. Dhir and A. Maguire.

In this work electrolytes were prepared gravimetrically as molal concentrations are temperature independent and can be prepared with greater accuracy. Densitometry is therefore required to convert between molal and molar concentrations. The electrolyte density as a function of molar concentration for the LiFSI DME and KFSI DME electrolytes is presented in Figure 3.7a, where it can be seen that the density increases approximately linearly with salt concentration.

The partial molar volumes of the salt, $\overline{V}_e$, and solvent, $\overline{V}_0$, can also be calculated from these density correlations using Equations 3.1 and 3.2, respectively:

$$\overline{V}_e = \frac{M_e - \frac{d\rho}{dc}}{\rho - c\frac{d\rho}{dc}} \tag{3.1}$$

$$\overline{V}_0 = \frac{M_0}{\rho - c\frac{d\rho}{dc}} \tag{3.2}$$

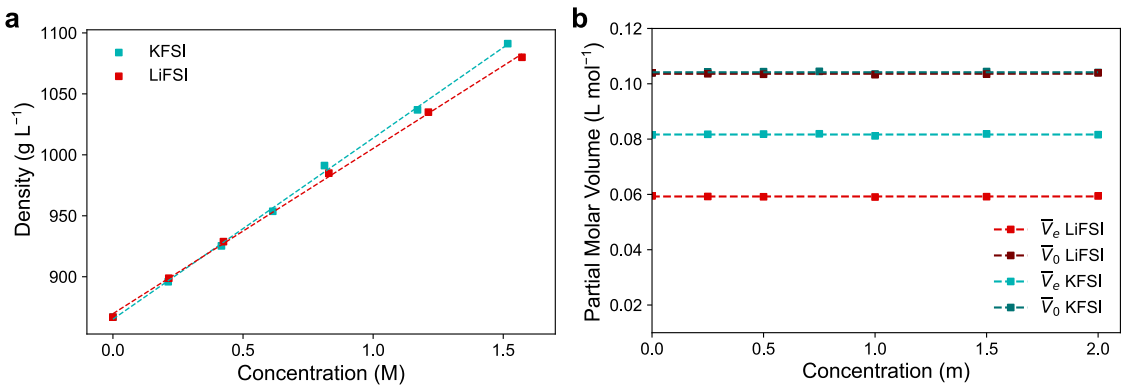


Figure 3.7: Densitometry. (a) Density correlations for KFSI and LiFSI in DME at 20°C. (b) Partial molar volumes of salt, $\overline{V}_e$, and solvent, $\overline{V}_0$, for LiFSI and KFSI in DME at 20°C.

where M_e is the molar mass of KFSI/LiFSI, M_0 is the molar mass of DME, ρ is the density, c is the molar concentration and $\frac{d\rho}{dc}$ is the slope of the density correlation. These are plotted in Figure 3.7b.

3.3.1 Cation Transference Number

The cation transference number, t_+^0, is the fraction of current carried by the cation. It has been shown that increasing the transference number by 0.2 can significantly improve accessible capacity during LIB charge and discharge.[196] t_+^0 is traditionally difficult to measure accurately, and is often mischaracterised as the transport number using steady-state techniques such as the Bruce-Vincent method,[197] relying on assumptions of electrolyte ideality and neglecting interactions between ionic species.[33,34] Here the densitometric Hittorf method was used to characterise the transference number relative to the solvent velocity.[34,36,37,198] This method involves applying a constant-current polarisation to a large symmetric cell, then closing two stopcocks to form three isolated chambers after a given pulse duration. The anodic chamber is in contact with the stripped electrode, the neutral chamber is in the centre of the cell, and the cathodic chamber is in contact with the plated electrode. Importantly, the pulse duration cannot be so high that concentration gradients progress into the neutral chamber, and the cell must be oriented vertically with the anodic chamber at the bottom to minimise the influence of natural convection.[162]

After the pulse the electrolyte is extracted from the three chambers and their densities are measured to determine the average concentration in each chamber using the correlation

in Figure 3.7a. The cation transference number is then calculated using Equation 3.3:[36]

$$t_+^0 = 1 - \frac{FV_{\text{chamber}}|c_f - c|}{I_{\text{pulse}}t_{\text{pulse}}(1 - \overline{V}_e c)} \tag{3.3}$$

where V_{chamber} is the volume of the cathodic or anodic chamber, c_f is the concentration of the electrolyte in that chamber after the experiment, c is the concentration of the neutral chamber, I_{pulse} is the current applied, t_{pulse} is the pulse duration and $\overline{V}_e$ is the partial molar volume of salt (Figure 3.7b).

Figure 3.8 shows the cation transference numbers from the Hittorf measurements for KFSI and LiFSI in DME determined from the anodic chamber. The results show that $t^0_{K^+}$ is higher than $t^0_{Li^+}$ at lower concentrations of 0.25 m (0.49 and 0.34, respectively), though $t^0_{K^+}$ decreases with increasing concentration so that it is only slightly higher than $t^0_{Li^+}$ from 1.5–2 m. Interestingly, $t^0_{K^+}$ and $t^0_{Li^+}$ appear to be trending towards similar values suggesting that the lower charge density of K^+ may delay some of the effects of ion-ion and ion-solvent interactions that occur with increasing concentration. $t^0_{K^+}$ decreases from around 0.49 to 0.38 over the concentration range indicating increasing ion-ion and ion-solvent interactions are acting to bind up K^+ more strongly than FSI^-. Whereas for Li^+ these interactions appear to have become significant at concentrations below those measured as $t^0_{Li^+}$ remains constant in this concentration range.

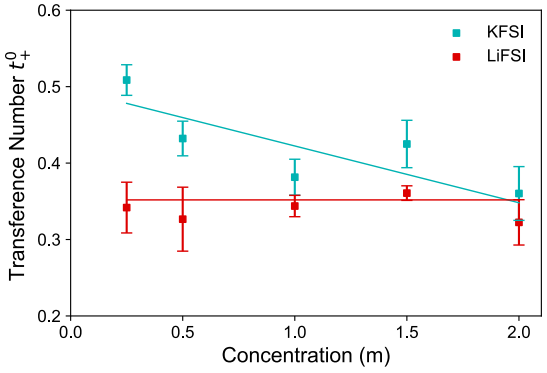


Figure 3.8: Cation transference numbers, t^0_+, of KFSI and LiFSI in DME at 20°C determined from the anodic chamber. Error bars depict error in the mean.

Characterisation of cation transference numbers in sodium-ion electrolytes remains rare and $t^0_{Na^+}$ has not been reported in NaFSI DME, preventing direct comparison to the results obtained here. Nevertheless, using electrophoretic nuclear magnetic resonance

(eNMR), Mönich et al. determined $t^0_{Na^+}$ to be on the order of 0.4 in high-concentration electrolytes consisting of NaTFSI in triethylene glycol dimethyl ether (G3),[199] which is similar to the $t^0_{K^+}$ values measured here. Additionally, the $t^0_{Na^+}$ results reported for $NaPF_6$ EC:DEC by Landesfeind et al. display a similar concentration dependence to that determined for $t^0_{K^+}$ in this work,[171] though it is important to note that their study treats the dual solvents as a single entity, assuming identical velocity of the two solvents, which Wang et al. have reported to have an impact on transference number measurements.[198]

In theory both the anodic and cathodic chambers can be used to calculate the cation transference number, but Figure 3.9 shows that the cathodic chamber typically gives a lower t^0_+, particularly for KFSI. This difference is likely caused by non-uniform metal deposition on the cathodic side, as evident by the discolouration evident in the cathodic solutions in Figure 3.10. In the K-ion electrolytes the cathodic solution often appeared blue (Figure 3.10a), while the Li-ion electrolytes appeared grey (Figure 3.10b), the same colours as the respective electrodes. Neither the anodic nor the neutral chamber displayed the same discolouration, so it is unique to the plating electrode and is most likely due to mossy deposits becoming disconnected from the electrode, forming a suspension of alkali metal filaments. This is further supported by evidence of non-uniform potassium deposition evident in Figure 3.10c. These deposits can reduce the measured cathodic transference number in two ways. First, both lithium and potassium metal are less dense than the electrolyte so they will reduce the overall solution density, and hence artificially reduce the measured concentration, reducing t^0_+ according to Equation 3.3. Second, mossy deposits have a high surface area and can lead to significant electrolyte consumption and solid electrolyte interphase (SEI) formation, reducing the salt concentration. The greater discrepancy in the KFSI electrolyte could therefore be caused by the high reactivity of potassium metal. For these reasons the cathodic data was discounted, as was found necessary by Hou and Monroe.[36]

3.3.2 Ionic Conductivity

The ionic conductivity, κ, quantifies the mobility of ions under an electric field and it can be simply measured using a commercial conductivity cell. Figure 3.11 shows the

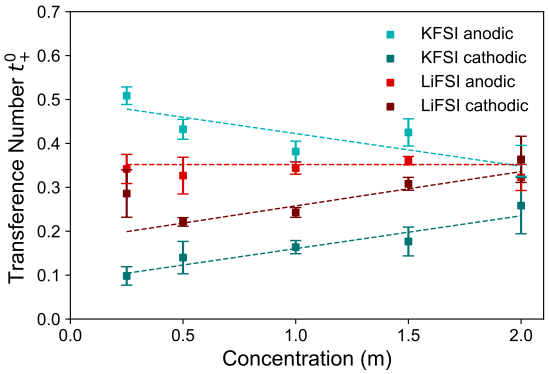


Figure 3.9: Cation transference numbers of KFSI and LiFSI in DME at 20°C determined from both the anodic and cathodic chambers. Error bars depict error in the mean.

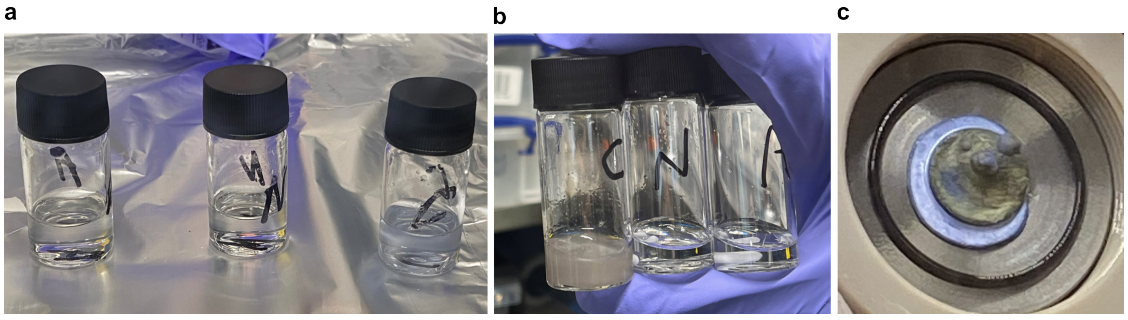


Figure 3.10: Cathodic chamber discolouration after Hittorf experiments in DME at 20°C. The cathodic, neutral and anodic solutions are labelled as C, N and A, respectively. (a) KFSI cathodic solution with neutral and anodic solutions for comparison. (b) LiFSI cathodic solution with neutral and anodic solutions for comparison. (c) Cathodic potassium electrode after plating in 1 m KFSI DME.

concentration-dependent ionic conductivities at 20°C, which were fitted with the function proposed by Casteel and Amis, given by Equation 3.4:[200]

$$\kappa(c) = \kappa_{\max} \left(\frac{c}{c_{\max}} \right)^{x_1} \exp\left(x_2 (c - c_{\max})^2 - \frac{x_1}{c_{\max}} (c - c_{\max}) \right) \tag{3.4}$$

where $\kappa_{\max}$ is the maximum ionic conductivity, $c_{\max}$ is the concentration at maximum ionic conductivity, and x_1 and x_2 are fitting constants.

LiFSI has a higher κ from low concentrations through until approximately 1.5 m as the concentration of charge carries increases. Beyond this κ decreases significantly, matching previous findings.[201] KFSI, however, continues increasing and appears to plateau at 2 m. It has been shown to decrease after this point.[202] This indicates there are likely more significant species-species interactions for the LiFSI electrolyte compared with the KFSI electrolyte above 1.5 m. The trend matches that found by Hosaka et al. for KPF_6

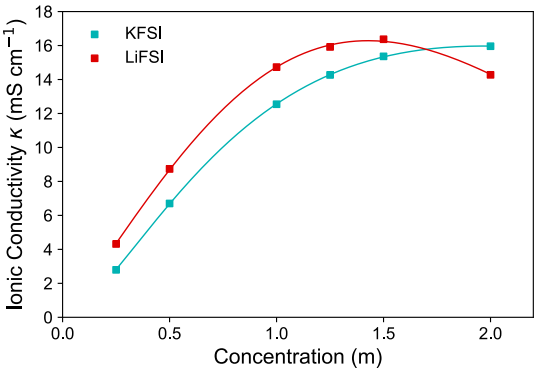


Figure 3.11: Ionic conductivities, κ, of KFSI and LiFSI in DME at 20°C.

and $LiPF_6$ in EC:DMC where the K-ion electrolyte conductivity was lower than the Li-ion electrolyte below 1.5 m. However, they also found KFSI PC had significantly higher conductivity than LiFSI PC at all concentrations tested.[24] In this electrolyte system the lower ionic conductivity for KFSI for the majority of the concentration range could be an indication of reduced KFSI salt dissociation compared to LiFSI,[24] reducing the number of available charge carriers.

At higher concentrations above 1.7 m, the drop in conductivity for LiFSI is likely due to the greater ion-solvent and ion-ion interaction for Li^+, where it is dragging more solvent than the K^+ due to its higher charge density and thus stronger solvation, while the stronger coulombic interaction of the Li^+ also results in greater ion-ion association, forming aggregates that increase the electrolyte viscosity.[201,203] Aggregates have been shown not to form in KFSI DME until concentrations above those tested here (> 3 M),[204] supporting the theory that species-species interactions are reduced in K-ion electrolytes.

Both electrolyte systems reach high maximum ionic conductivities of 16 mS cm^{-1} for KFSI DME at 2 m and 15 mS cm^{-1} for LiFSI DME at 1.5 m. These are higher than for carbonate-based equivalent electrolytes due to the lower viscosity of DME,[205] matching previous findings.[202,206]

κ was additionally measured at 15 and 25°C, enabling the activation energy, E_a, to be calculated as a function of concentration using Equation 3.5:[207]

$$\kappa = \kappa_0 e^{-\frac{E_a}{kT}} \tag{3.5}$$

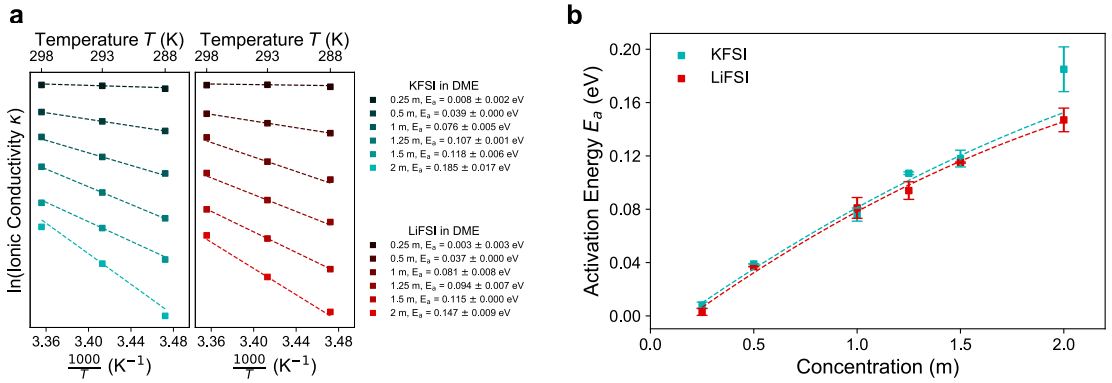


Figure 3.12: Activation energy for ionic conduction, E_a. (a) Arrhenius plots used to calculate E_a as a function of concentration. The different concentrations are shifted along the y-axis for clarity. (b) E_a for KFSI and LiFSI in DME. Error bars depict the standard error in each activation energy determined from the linear fits in (a).

where κ_0 is a constant, k is the Boltzmann constant and T is the temperature. The Arrhenius plots used to calculate E_a are shown in Figure 3.12a and the activation energies are plotted in Figure 3.12b where it can be seen that the activation energies of ionic conduction of KFSI and LiFSI in DME are similar and increase with concentration as a result of increasing ion-solvent interactions.[207]

3.3.3 Thermodynamic Factor

The thermodynamic factor, χ_M, measures the non-ideality of an electrolyte and accounts for deviations from Nernstian behaviour, reflecting how the mean molar activity coefficient, $f_\pm$, varies with molar concentration, c, according to Equation 3.6:[33]

$$\chi_M = 1 + \frac{d\ln(f_\pm)}{d\ln(c)} \tag{3.6}$$

Concentration cells were used in the measurement of χ_M, which place metallic electrodes into two electrolytes with the same constituents but different compositions in chemical contact, enabling measurement of the OCV that arises between them as a result of the difference in chemical potential from the different salt concentrations.[33] The concentration cell contains two chambers separated by a porous frit which enables electrochemical contact but reduces the rate of interdiffusion. One chamber is filled with a 'reference' solution of constant concentration, while the other chamber contains a 'test' solution with a concentration that varies between experiments. The OCV recorded

during a representative concentration cell measurement is presented in Figure 3.13a, and the results for both electrolyte systems are plotted in Figure 3.13b, where it can be seen that the OCV increases with concentration.

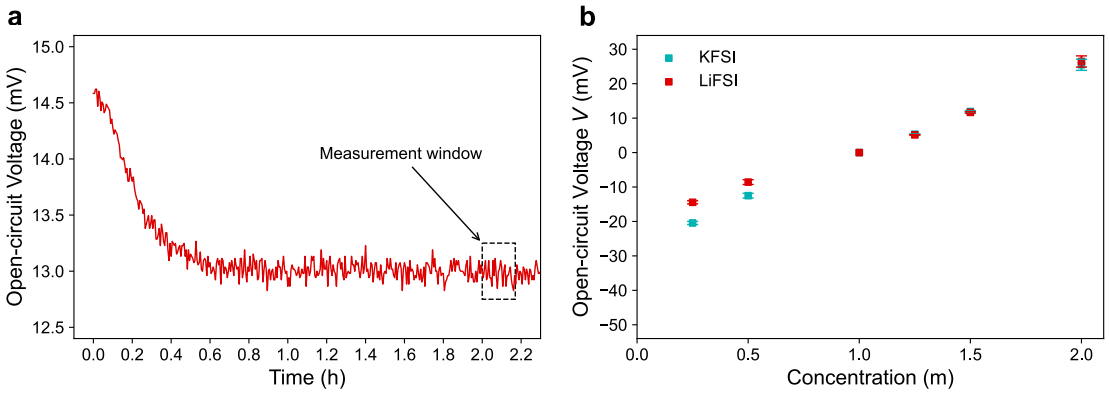


Figure 3.13: Concentration cell measurements. (a) OCV as a function of time for a representative concentration cell with a 1 m LiFSI DME reference concentration and a 1.5 m LiFSI DME test concentration at 20°C, demonstrating the stabilisation of the potential. The measurement window is visualised by the dashed box. (b) Concentration cell OCV, V, measured in LiFSI and KFSI in DME at 20°C using a reference concentration of 1 m. Error bars depict the standard error in the mean.

The thermodynamic factor, χ_M, is related to the change in the OCV measured across the concentration cells, V, with the molar concentration of the test electrolyte, c, by Equation 3.7:[33]

$$\chi_M = 1 + \frac{d\ln(f_\pm)}{d\ln(c)} = \frac{F}{2RT(1-t_+^0)}\frac{dV}{d\ln(c)} \tag{3.7}$$

where t_+^0 is the cation transference number, F is the Faraday constant, R is the gas constant and T is the absolute temperature. As evident from Equation 3.7, prior measurement of t_+^0 is required to calculate χ_M, so χ_M is also traditionally challenging to determine accurately.

The solvent concentration, $c_0 = \frac{1-\overline{V}_e}{\overline{V}_0}$, and the partial molar volume of the solvent, $\overline{V}_0$, can be used to map the thermodynamic factor to the molar basis from the molal basis in which it is defined.[208] It is also convenient to convert from molar concentration to molal concentration, c_m, resulting in Equation 3.8:

$$\chi_M = \frac{1}{c_0\overline{V}_0}\left(1 + \frac{d\ln(\gamma_\pm)}{d\ln(c_m)}\right) = \frac{F\frac{d\ln(c_m)}{d\ln(c)}}{2RT(1-t_+^0)}\frac{dV}{d\ln(c_m)} \tag{3.8}$$

where $\gamma_\pm$ is the mean molal activity coefficient. For a strong, binary electrolyte $\gamma_\pm$ is predicted to vary with c_m according to Equation 3.9:[208]

$$\frac{d\ln(\gamma_\pm)}{d\ln(c_m)} = \frac{z_+ z_- \alpha\sqrt{c_m}}{2(1+Ba\sqrt{c_m})^2} + A_2 c_m + \frac{3A_3}{2} {c_m}^{\frac{3}{2}} + \cdots \tag{3.9}$$

where the first term on the right-hand side comes from Debye-Hückel theory for the long-range electrical interactions between ions and the following terms account for additional concentrated-solution effects.[162] In Equation 3.9, z_i is the charge number of species i, α and B are constants given by Equation 3.10, a is the average ionic radius, and A_n are fitting constants.

$$\alpha = \frac{F^2 e\sqrt{2\rho_0}}{8\pi(\varepsilon_r\varepsilon_0 RT)^{3/2}}, \quad B = \frac{F\sqrt{2\rho_0}}{\sqrt{\varepsilon_r\varepsilon_0 RT}} \tag{3.10}$$

In Equation 3.10 e is electronic charge, ρ_0 is solvent density, ε_r is relative permittivity of the solvent, and ε_0 is vacuum permittivity. Taking the values for DME (ρ_0 = 866.9 g L^{-1}, ε_r = 7.2) gives α = 40.38 $kg^{\frac{1}{2}}$ $mol^{-\frac{1}{2}}$ and B = 10.20 $kg^{\frac{1}{2}}$ $mol^{-\frac{1}{2}}$ nm^{-1} at 20°C.

Combining Equations 3.8 and 3.9, and dropping terms beyond $A_2 {c_m}$[162] gives Equation 3.11:

$$\frac{dV}{d\ln(c_m)} = \frac{2RT(1-t_+^0)}{F\frac{d\ln(c_m)}{d\ln(c)}} \frac{1}{c_0\overline{V}_0}\left(1 + \frac{z_+ z_- \alpha\sqrt{c_m}}{2(1+Ba\sqrt{c_m})^2} + A_2 c_m\right) \tag{3.11}$$

In both electrolyte systems investigated $\frac{d\ln(c_m)}{d\ln(c)}$ was found to be constant and $\frac{1}{c_0\overline{V}_0}$ was well described by a function of the form $\frac{1}{c_0\overline{V}_0} = 1 + B_1 c_m$, where B_1 is a constant. Equation 3.11 was integrated with respect to $\ln(c_m)$, with the boundary condition that V = 0 V at c_m = 1 m, to find an expression for V as a function of c_m that was then fitted to the OCV data in Figure 3.13b.

This function is fitted to the LiFSI data in Figure 3.14, taking t_+^0 to be constant (Figure 3.8) and assuming a = 0.76 Å, the ionic radius of Li^+.[22] However, this resulted in a poor fit to the data.

Debye-Hückel theory assumes electrolytes are strong and fully dissociate,[37,162] which may not to be the case for the electrolytes studied here. This can be taken into account by introducing a second fitting constant, ξ,[37] to Equation 3.11, resulting in Equation 3.12:

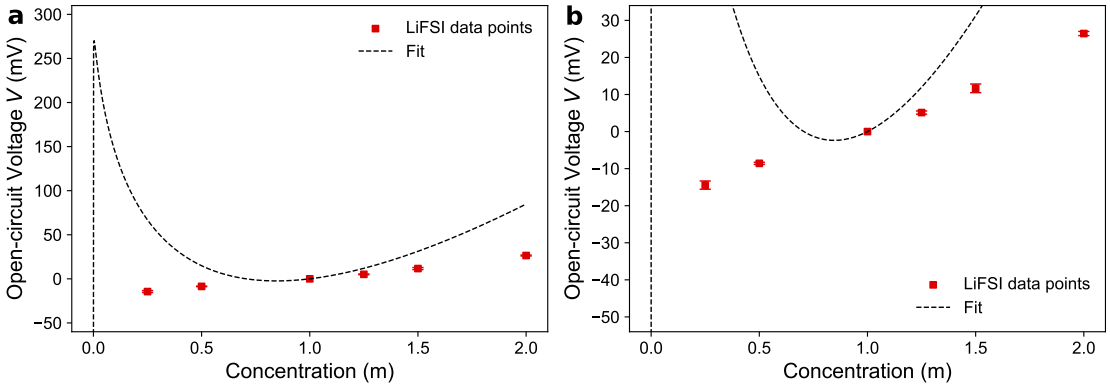


Figure 3.14: The fit to the LiFSI concentration cell OCV data measured at 20°C determined by Equation 3.11, plotted with a (a) full y-scale, (b) reduced y-scale.

$$\frac{dV}{d\ln(c_m)} = \frac{2RT(1-t_+^0)}{F\frac{d\ln(c_m)}{d\ln(c)}}\frac{1}{c_0\overline{V}_0}\left(1+\frac{z_+z_-\alpha\sqrt{\xi c_m}}{2(1+Ba\sqrt{\xi c_m})^2}+A_2c_m\right) \tag{3.12}$$

ξ can be thought of as a correction factor to the ionic strength, and its introduction leads to a much better fit to the data, as evident in Figure 3.15a.

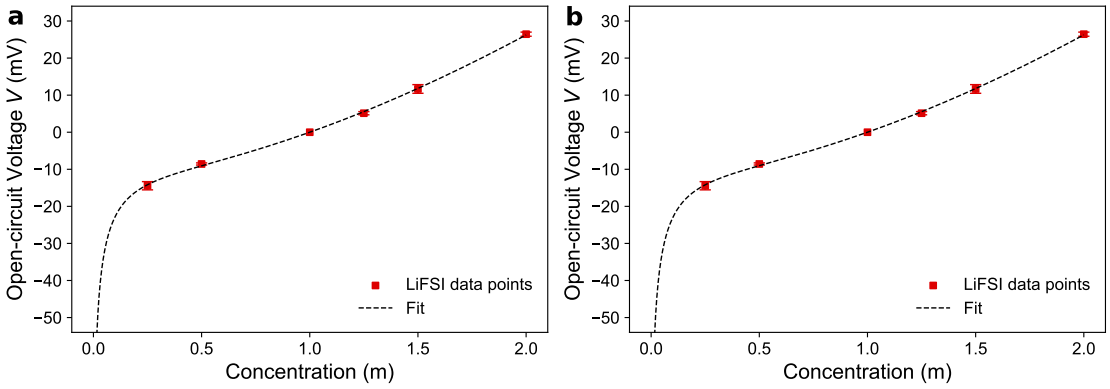


Figure 3.15: The fit to the LiFSI concentration cell OCV data measured at 20°C determined by (a) Equation 3.12, (b) Equation 3.13.

Additionally, the value of ξ determined by the fit is such that $1+Ba\sqrt{\xi c_m} \approx 1$, allowing Equation 3.12 to be simplified to Equation 3.13:

$$\frac{dV}{d\ln(c_m)} = \frac{2RT}{F\frac{d\ln(c_m)}{d\ln(c)}}(1-t_+^0)\frac{1}{c_0\overline{V}_0}\left(1+A_1{c_m}^{\frac{1}{2}}+A_2c_m\right) \tag{3.13}$$

where A_1 ($\approx \frac{z_+z_-\alpha\sqrt{\xi}}{2}$) is a fitting constant. Equation 3.13 results in just as good a fit to the data in Figure 3.15b, and allows the concentration dependence of $t^0_{K^+}$

to be taken into account. Once A_1 and A_2 are fitted to the OCV data, χ_M can be calculated using Equation 3.14:

$$\chi_M = \frac{1}{c_0 \overline{V}_0}(1 + A_1 c_m{}^{\frac{1}{2}} + A_2 c_m) \tag{3.14}$$

The fits to the OCV data for the two electrolyte systems are presented in Figure 3.16a.

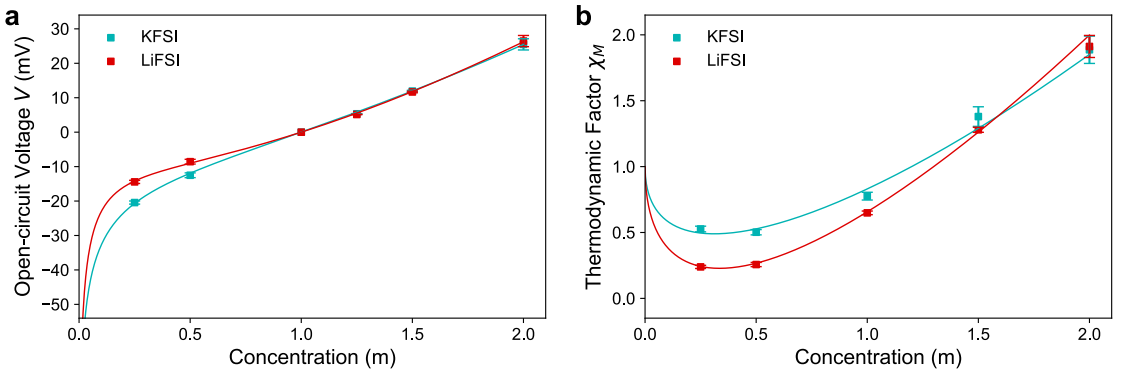


Figure 3.16: Thermodynamic factor determination. (a) Concentration cell OCV, V, measured in LiFSI and KFSI in DME at 20°C fitted with Equation 3.13. Error bars depict the standard error in the mean. (b) Thermodynamic factors, χ_M, as a function of concentration for the two electrolyte systems determined from (a).

Figure 3.16b shows how the thermodynamic factor changes with concentration. The trends match those found for other non-aqueous electrolytes.[33,35–37] By definition, $\chi_M = 1$ at infinite dilution and, with increasing concentration, first coulombic ion-ion interactions decrease the salt free energy relative to the DME, reducing the salt activity coefficient and hence causing a drop in χ_M. As the concentration increases further, ion-solvent interactions increase, resulting in DME becoming increasingly bound, decreasing solvent vapour pressure, and hence increasing the salt activity coefficient and χ_M.[37,209] The results demonstrate that the decrease in χ_M at lower concentrations is significantly less for KFSI than for LiFSI. This can be attributed to the following two factors. First the larger size and thus lower charge density of K^+ compared with Li^+, resulting in weaker K^+ coulombic ion-ion interactions, hence the smaller reduction in χ_M. Second, from Debye-Hückel theory the gradient of the χ_M decrease at lower concentrations for both LiFSI and KFSI in DME should be equal as it is determined by the dielectric constant, ε, of the solvent.[162] As Debye-Hückel theory assumes fully dissociated electrolytes, the lower KFSI gradient magnitude could further suggest poorer salt dissociation,[37] which

was also indicated by the lower ionic conductivity (Figure 3.11) at low concentrations. The low ε of DME also provides minimal electrostatic screening, thus having a limited effect on reducing ion-ion interactions.[210]

At higher concentrations, the increase in χ_M with increasing concentration is also higher for LiFSI than for KFSI. This may again be due to the reduced charge density of K^+ resulting in weaker interactions with solvent molecules and thus a smaller solvation shell of K^+ compared to Li^+. The weaker K^+ solvation results in more free DME compared to Li^+ at higher concentrations and, therefore, the salt activity coefficient and χ_M increase with increasing salt concentration at a reduced rate for KFSI. This is the same trend identified by Landesfeind et al. comparing $NaPF_6$ and $LiPF_6$ in EC:DMC.[171] Additionally, using Raman spectroscopy, Le Pham et al. observed a constant solvation number for KFSI DME across this concentration range, confirming that a larger proportion of the solvent molecules become bound up in the cation solvation shell as the salt concentration increases.[204] A similar study also found significant ion-pairing and solvent binding in the LiFSI DME system.[201] χ_M is below unity until approximately 1.4 m for both LiFSI and KFSI, indicating the point at which the effects of the ion-ion and ion-solvent interactions balance.

Further experiments could characterise χ_M over a wider concentration range with greater accuracy using the shifting-reference concentration cell technique developed by Wang et al.[37] Given the relatively narrow concentration range tested here, this was not deemed necessary for this study.

3.3.4 Salt Diffusivity

The salt diffusivity, D, determines the rate of ionic flux in response to salt concentration gradients. Here, steady-state polarisation and long-term relaxation restricted diffusion[36,211–214] was used to characterise D as it has been identified as being more accurate than pulse polarisation methods, being less susceptible to double layer relaxation effects.[214] In a restricted diffusion measurement a current pulse is applied to form a concentration gradient that is then allowed to relax under open-circuit conditions while the concentration overpotential is tracked. At long times decay of the concentration overpotential is well described by an exponential function and the salt diffusivity, D,

can be determined the linear time dependence of the logarithm of the OCV, V, using Equation 3.15:[174]

$$\frac{d\ln(V)}{dt} = -\frac{\pi^2 D}{L^2} = -\frac{1}{\tau_{\text{diff}}} \tag{3.15}$$

where L is the electrode separation, t is time and τ_{diff} is the characteristic decay time $= \frac{L^2}{\pi^2 D}$.

In this work, a custom restricted diffusion cell designed by Dr S. Dhir was used. The cell has a large electrode separation of approximately 10 mm, increasing τ_{diff} and enabling longer relaxation periods, increasing the robustness of the fit to the data. Contrary to many recent studies,[36,171,214] no separators were used in the restricted diffusion experiments to eliminate any errors introduced through separator tortuosity estimation and variability.[36,37] Like the Hittorf cell, the restricted diffusion cell was oriented vertically to suppress natural convection.[36,162] Representative voltage relaxation curves for 1 m KFSI and LiFSI in DME are presented in Figure 3.17a and 3.17b, respectively.

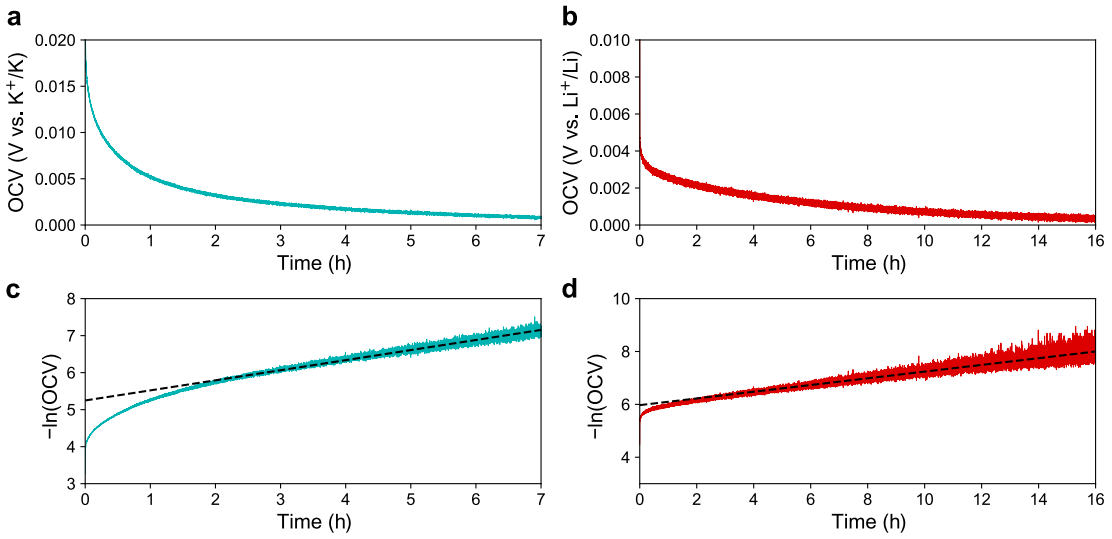


Figure 3.17: Representative restricted diffusion voltage relaxation data at 20°C for (a) 1 m KFSI DME, (b) 1 m LiFSI DME. Semi-log plots of potential with the linear fits used to calculate D using Equation 3.15 for (c) KFSI, (d) LiFSI.

Newman and Thompson demonstrated that the voltage relaxation can be approximated by a single exponential, independent of the initial concentration profile, for times greater than $0.05L^2/D$ ($\approx 0.5\ \tau_{\text{diff}}$).[215] An iterative fitting protocol was therefore developed to fit the voltage relaxation data for times greater than $0.5\ \tau_{\text{diff}}$. This protocol requires an

initial guess for D, calculates τ_{diff}, and then fits the data to calculate a new value of D, repeating this loop until a stable value is determined. Similar to Bergstrom et al.,[174] in many cases here it was found to be necessary to impose an upper time limit on the fitting range when the relaxation deviated from exponential behaviour, indicating that additional processes may be influencing the measured voltage. One major parasitic process that would alter the electrolyte concentration at the electrode interface is SEI formation. Electrochemical impedance spectroscopy (EIS) measurements during relaxation in a 0.5 m KFSI DME cell in Figure 3.18 reveal that the impedance grows continuously over time, which is often believed to indicate SEI growth[102] This suggests electrolyte reduction reactions continue to occur at the potassium metal-electrolyte interfaces, justifying the introduction of an upper fitting limit. Representative fitting results for 1 m KFSI and LiFSI in DME are shown in Figure 3.17c and 3.17b, respectively.

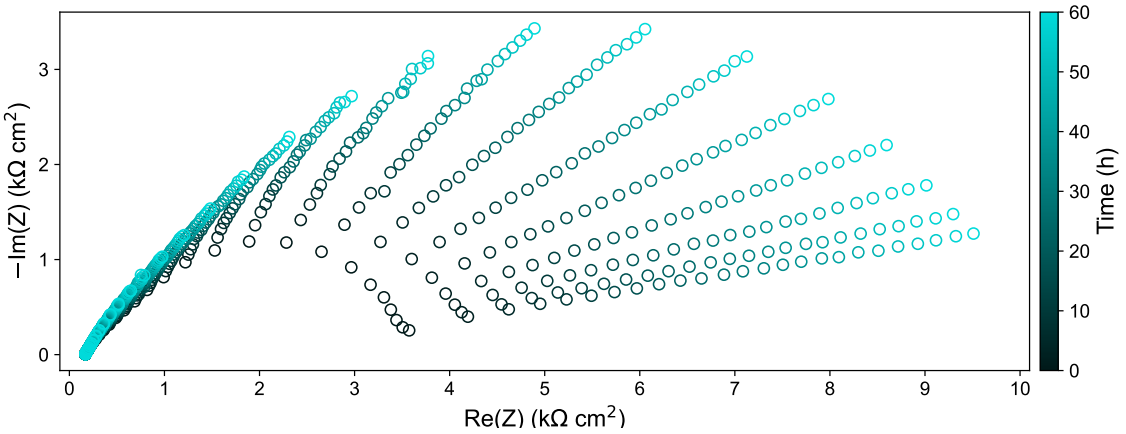


Figure 3.18: Time evolution of the EIS spectra in 0.5 m KFSI DME during concentration gradient relaxation after a 20 h current pulse at 20°C.

The concentration-dependent salt diffusivities measured for the two electrolyte systems are presented in Figure 3.19, where it can be seen that the salt diffusivity decreases with increasing concentration in both systems. This decrease is typical for non-aqueous electrolytes,[35–37,171] and is likely caused by an increase in viscosity with increasing concentration.

Figure 3.19 shows that D is higher for KFSI than for LiFSI at all concentrations. At 1 m D_{KFSI} is over 50% higher than D_{LiFSI} (7.6×10^{-10} m^2 s^{-1} and 5.0×10^{-10} m^2 s^{-1}, respectively). The difference is most significant at low concentrations where D_{KFSI} is

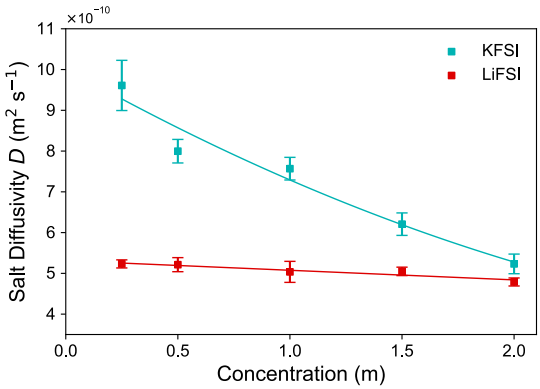


Figure 3.19: Salt diffusivities, D, of KFSI and LiFSI in DME at 20°C. Error bars depict the standard error in the mean.

almost double that for D_{LiFSI} (9.6×10^{-10} m^2 s^{-1} and 5.2×10^{-10} m^2 s^{-1}, respectively at 0.25 m). This higher diffusivity in KFSI is clearly evident in Figure 3.20 which compares the normalised voltage relaxation profiles of KFSI and LiFSI at 0.25 m.

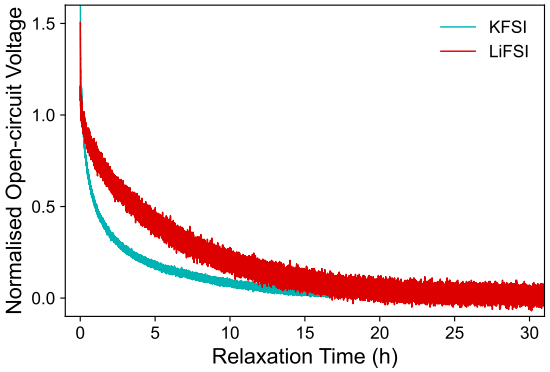


Figure 3.20: Voltage relaxation profiles of 0.25 m LiFSI and KFSI in DME at 20°C, normalised to the potential after 100 s to exclude double layer effects, demonstrating faster relaxation in the potassium-ion electrolyte.

With increasing concentration the difference between D_{KFSI} and D_{LiFSI} decreases, and they have values of 5.2×10^{-10} m^2 s^{-1} and 4.8×10^{-10} m^2 s^{-1}, respectively at 2 m. This appears again to be due to increasing ion-ion and ion-solvent interactions occurring for K^+ at higher concentrations having a greater relative impact compared to minimal interaction at lower concentrations, matching the same trend observed for t_+^0. Both D_{KFSI} and D_{LiFSI} appear to be trending to similar values with increasing concentration, again matching the trends for t_+^0 and supporting the theory that the lower charge density of K^+ delays some of the ion-ion and ion-solvent interaction effects of increasing concentration.

The higher D_{KFSI} also matches the trend observed by Landesfeind et al. with $NaPF_6$ showing higher D than $LiPF_6$.[171] However, the difference is much more significant for the K-ion electrolyte here. Additionally, D_{KFSI} is higher than those typically reported for Li- and Na-ion electrolytes, with 2.9×10^{-10} m^2 s^{-1} found for 1 M $NaPF_6$ EC:DEC at higher temperature of 25°C,[171] and with D for the majority of 1 M $LiPF_6$-based electrolytes reported to be around 2–3 $\times 10^{-10}$ m^2 s^{-1} at 25°C.[33,36,37,214] The values obtained for D_{LiFSI} here are also higher than most carbonate-based Li-ion electrolytes and this is attributed to the lower viscosity of DME compared to carbonate solvents.[210]

3.3.5 Thermodynamic and Stefan-Maxwell Diffusivities

Having now characterised t_+^0, κ, χ_M and D for the KFSI and LiFSI electrolyte systems (parameterisations of all properties are provided in Appendix C) it is possible to calculate the thermodynamic diffusivity, $\mathscr{D}$, which relates to ionic flux in response to salt chemical potential gradients, rather than concentration gradients. $\mathscr{D}$ is calculated from D, χ_M, the total molarity, c_T, and partial molar volume of solvent, $\overline{V}_0$, according to Equation 3.16:[33]

$$\mathscr{D} = \frac{D}{c_T \overline{V}_0 \chi_M} \tag{3.16}$$

The total molarity, $c_T = c_0 + c_- + c_+$, where c_0 is the solvent molarity ($c_0 = \frac{1-\overline{V}_e}{\overline{V}_0}$), and c_- and c_+ are the cation and anion molarities, respectively.

Figure 3.21 presents the thermodynamic diffusivities, $\mathscr{D}$, for the two electrolyte systems. The observed $\mathscr{D}$ decrease with increasing concentration matches those in literature.[35–37,176] At lower concentrations $\mathscr{D}_{\mathrm{LiFSI}}$ is higher than $\mathscr{D}_{\mathrm{KFSI}}$ as a result of greater coulombic ion-ion interactions reducing the mean activity coefficient, hence the lower χ_M in Figure 3.16b. This implies that at low concentration associated ions experience reduced resistance to motion than unpaired ions.[37] At higher concentration, however, D decreases and χ_M increases, so $\mathscr{D}$ decreases significantly, reflecting the increase in viscosity caused by additional species-species interactions. These interactions are more significant in LiFSI, so $\mathscr{D}_{\mathrm{LiFSI}}$ decreases more with concentration, falling below $\mathscr{D}_{\mathrm{KFSI}}$. It is interesting to note that $\mathscr{D}_{\mathrm{LiFSI}}$ and $\mathscr{D}_{\mathrm{KFSI}}$ display similar trends and they are closer in magnitude than

D_{LiFSI} and D_{KFSI}, indicating that more significant differences in diffusion rates will be observed in response to concentration gradients rather than chemical potential gradients.

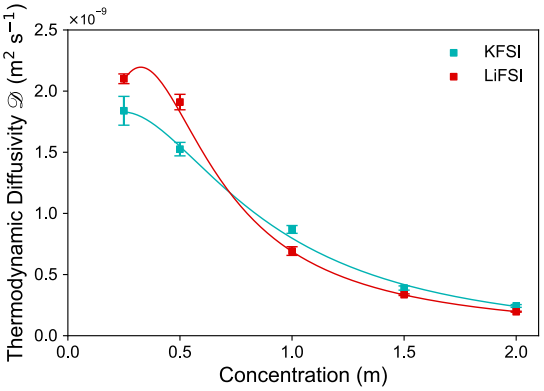


Figure 3.21: Thermodynamic diffusivities, $\mathscr{D}$, of KFSI and LiFSI in DME at 20°C. Error bars depict the propagated uncertainty.

Finally, the Stefan-Maxwell diffusivities can also be calculated from the measured transport properties. In the Stefan-Maxwell formalism the diffusivity, $\mathscr{D}_{ij}$, describes the interaction between species i and j and they can be considered as inverse friction coefficients.[162] In binary electrolytes there are three independent Stefan-Maxwell diffusivities. These are $\mathscr{D}_{0-}$, $\mathscr{D}_{0+}$ and $\mathscr{D}_{+-}$, describing solvent-anion, solvent-cation and cation-anion interactions, respectively, and they can be calculated using Equations 3.17–3.19:[162]

$$\mathscr{D}_{0-} = \frac{z_+}{z_+ - z_-}\frac{\mathscr{D}}{t_+^0} \tag{3.17}$$

$$\mathscr{D}_{0+} = \frac{-z_-}{z_+ - z_-}\frac{\mathscr{D}}{1 - t_+^0} \tag{3.18}$$

$$\frac{1}{\mathscr{D}_{+-}} = -\frac{z_+ z_- c_T F^2}{RT\kappa} - \frac{z_+ - z_-}{z_+ \nu_+}\frac{c_0 t_+^0 (1 - t_+^0)}{c\mathscr{D}} \tag{3.19}$$

where c_T is the total molarity, c_0 is the solvent molarity and z_i and ν_i are the charge number and the number of ions of species i into which the salt molecule dissociates, respectively.

The Stefan-Maxwell diffusivities for the KFSI and LiFSI electrolytes are presented in Figure 3.22a and 3.22b, respectively.

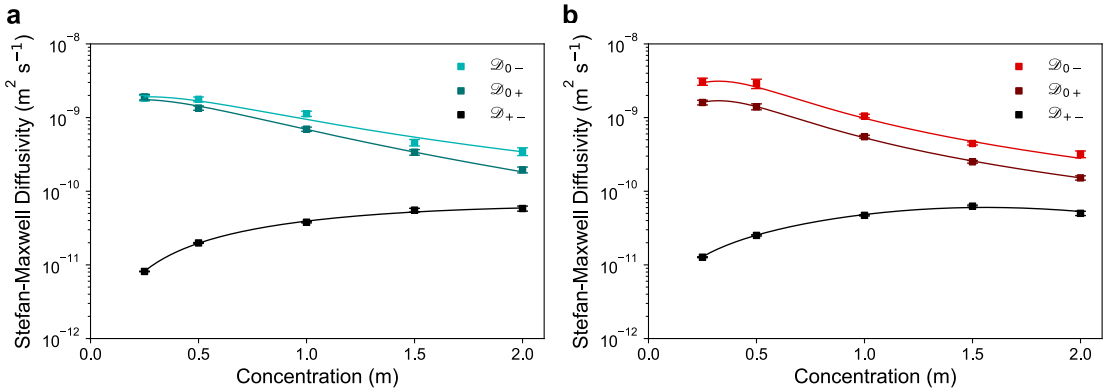


Figure 3.22: Stefan-Maxwell diffusivities, $\mathscr{D}_{ij}$, at 20°C of (a) KFSI DME, (b) LiFSI DME. Error bars depict the propagated uncertainty.

The diffusivities in Figure 3.22 are similar for both KFSI and LiFSI due to their similar thermodynamic diffusivities. Both of the solvent-ion coefficients, $\mathscr{D}_{0+}$ and $\mathscr{D}_{0-}$, for LiFSI and KFSI decrease by about an order of magnitude over the concentration range, demonstrating the drag from the DME solvent becomes stronger on both cation and anion with increasing salt concentration. $\mathscr{D}_{0-}$ is higher than $\mathscr{D}_{0+}$ across the concentration range for LiFSI, indicating weaker interaction of the FSI^- with the DME compared with the Li^+ interaction with DME. However, for KFSI, $\mathscr{D}_{0-}$ and $\mathscr{D}_{0+}$ are much closer and at low concentrations are almost the same. This is due to t_+^0 being close to 0.5 for K^+ at 0.25 m, indicating K^+ and FSI^- can carry similar fractions of the current. With increasing concentration, the difference between $\mathscr{D}_{0-}$ and $\mathscr{D}_{0+}$ increases, matching the decreasing $t^0_{K^+}$ as ion-solvent interactions increase. The ion-ion diffusivity $\mathscr{D}_{+-}$ is approximately two orders of magnitude lower than the solvent-ion diffusivities for both electrolyte systems. $\mathscr{D}_{+-}$ is particularly low at lower concentrations, indicating significant ion-ion interactions. Similar to that found for $LiPF_6$ PC,[36] for both KFSI and LiFSI the maximum in $\mathscr{D}_{+-}$ matches the concentration of the maximum κ.

3.4 Conclusion

In summary, in this chapter it is revealed that commercially available potassium metal is rich in sodium and other impurities, resulting in potassium electrodes with an unstable potential if they are prepared without further processing. A potassium metal preparation protocol was developed to reduce the concentration of impurities, producing electrodes with

greatly improved potential stability and reproducibility. This enabled the concentration-dependent ionic transport and thermodynamic properties to be measured in equivalent lithium- and potassium-ion electrolytes (LiFSI and KFSI in DME), allowing the impact of cation size to be uncovered. The larger size of the K^+ ion results in weaker species-species interactions, so the potassium-ion electrolyte displays a superior salt diffusivity and cation transference number at all concentrations tested. Despite its very high diffusivity at low concentration, the potassium-ion electrolyte has a lower ionic conductivity, indicative of poorer salt dissociation and this is further supported by its smaller reduction in the thermodynamic factor at low concentration. The thermodynamic factor also increases less rapidly at high concentration, suggesting that solvent molecules are bound up less strongly by K^+, so the ionic conductivity continues to increases with concentration across the concentration range tested, exceeding that of the lithium-ion electrolyte above 1.7 m. Overall, these results confirm the belief that increasing cation radius improves electrolyte transport and that electrolytes for potassium-ion batteries can enable faster charging rates.

3.5 Experimental Methods

Unless otherwise stated, all experiments were performed in argon-filled MBraun gloveboxes with O_2 and H_2O concentrations below 0.1 ppm and all equipment was cleaned and dried overnight under vacuum at 70°C before being brought into the glovebox.

Electrode Preparation

Standard potassium metal electrodes were prepared by rinsing as-received potassium metal (chunks, 98%, Sigma-Aldrich) with hexane (95% anhydrous, Sigma-Aldrich), rolling it by hand between two sheets of weighing paper (grade 2122, Whatman), using additional hexane to prevent sticking, to a thickness of approximately 500 µm, and then punching it into discs using a wad punch.

The processed potassium metal electrodes were prepared by first melting the potassium in a beaker on a hot plate, a spatula was used to remove the dross, and the molten potassium was quenched into clean mineral oil before being transferred into hexane (95% anhydrous, Sigma-Aldrich) that had been dried over 3 Å molecular sieves for storage.

The clean potassium chunks were rolled by hand as above and punched into discs. Immediately before cell assembly the surface of the potassium electrodes was polished with a microtome blade (polytetrafluoroethylene coated, Epredia, Shandon), producing a mirror-like finish.

Lithium metal electrodes were prepared for use by first brushing the lithium (99.9% trace metal basis, Sigma-Aldrich) surface with a plastic brush, then calendering to a thickness of 300 µm in a polypropylene bag, before finally punching into discs of required diameter using a wad punch.

Electrolyte Preparation

Prior to preparing electrolytes, potassium bis(fluorosulfonyl)imide (KFSI, 99.9%, Solvionic) was dried under vacuum at 100°C for at least 48 h, lithium bis(fluorosulfonyl)imide (LiFSI, battery grade, Fluorochem) was dried under vacuum at 70°C for at least 48 h, and 1,2-dimethoxyethane (DME, 99.5% anhydrous, Sigma-Aldrich) was dried over 3 Å molecular sieves.

Electrolytes were prepared gravimetrically by stirring together the desired masses of salt and solvent. The water content of the electrolytes was measured by Karl Fischer titration and recorded to be below 10 ppm.

Densitometry

Electrolyte densities were measured using an Anton Paar DMA 4100 density meter at 20°C.

Electrochemical Measurements

Unless otherwise stated, all electrochemical measurements were performed at 20°C (± 0.3°C) in either a Binder Oven or an ESPEC SH-262 temperature and humidity chamber using a Biologic VMP3 potentiostat.

Hittorf Measurements

A densitometric Hittorf cell, designed by Hou and Monroe,[36] was used to measure the cation transference number. Each Hittorf cell was assembled with two 10 mm diameter electrodes and approximately 12 mL of electrolyte. Before the measurement the two stopcocks were open and the cell was oriented vertically, with the stripping electrode at the bottom. After assembly the cell was allowed to rest for 4 h before a 20 h current pulse was applied. The current used for polarisation for all K-ion Hittorf experiments was 100 µA, except at 0.25 m where 50–100 µA was used. For the Li-ion Hittorf experiments the current was 200 µA, except at 0.25 m where 50 µA was used.

After the current pulse the two stopcocks were immediately closed, creating three isolated chambers. The electrolyte was extracted from each chamber, stirred for at least 1 h, and the density was measured using the Anton Paar DMA 4100 density meter at 20°C, allowing the concentration to be determined. The cation transference number can then be calculated using Equation 3.3. Three repeat measurements were performed at each concentration for KFSI and LiFSI concentrations above 0.5 m. Two measurements were performed for LiFSI at 0.25 m and 0.5 m.

Ionic Conductivity Measurements

The ionic conductivity was measured in a commercial conductivity cell of known cell constant (CLR, 401-S-138C). The cell was filled with approximately 0.5 mL electrolyte and tested with an impedance analyser (BioLogic MTZ-35 with ITS-e temperature chamber) at 15, 20 and 25°C. The ionic conductivity of the electrolyte was calculated by dividing the cell constant by the series resistance extracted from a Nyquist plot.

Concentration Cell Measurements

For the concentration cell experiments an H-cell was designed including a Grade 5 frit to mitigate the faster diffusion from the K-ion electrolyte. A Grade 4 frit was found to be insufficient to suppress interdiffusion in the K-ion electrolyte, but gave reliable results with the Li-ion electrolyte. Potassium and lithium metal were prepared and cut into approximately 5 mm × 20 mm strips. Each chamber of the H-cell was filled with 4 mL of electrolyte, with 1 m electrolyte used as the constant reference concentration for both electrolyte systems. The electrodes were then lowered into the electrolyte and the cell was sealed and immediately brought into the Binder Oven. The OCV was tracked for 2 h to allow the cell to stabilise and reach the correct temperature, and the OCV was then averaged over the next 10 min (Figure 3.13a). At least three repeat measurements were made for each concentration.

Restricted Diffusion Measurements

Restricted diffusion measurements were performed in a custom cell requiring two 8 mm diameter electrodes and approximately 1 mL of electrolyte. The electrode separation, L, for each cell was measured using digital calipers. The cell was oriented vertically, with the stripping electrode at the bottom, and was allowed to rest for 10 h. A 20 h current pulse was then applied. The current was 35 µA for all Li-ion cells and 30 µA for K-ion cells above 0.5 m. 25 µA was used for 0.25 and 0.5 m for K-ion. After the current pulse the open-circuit voltage was tracked for several days as the concentration gradient relaxed. At least five cells were analysed for each K-ion concentration and at least three for each Li-ion.

The impedance spectra in Figure 3.18 were measured every 30 min over the frequency range of 200 kHz–500 mHz (6 measurement points per decade) with an applied potentiostatic signal of amplitude 10 mV.

Atomic Force Microscopy

Atomic force microscopy (AFM) was performed with a Bruker Dimension Icon system. Surface height maps were gathered in the ScanAsyst imaging mode with ScanAsyst-Air probes (Bruker) at a scan rate of 0.25 Hz. Gwyddion software was used for data analysis.[216]

X-ray Photoelectron Spectroscopy

XPS was performed with an ULVAC PHI Versaprobe III XPS system generating monochromatic $Al_{K\alpha}$ X-rays (1486.6 eV, 15 kV anode voltage, 25 W beam power) under ultrahigh vacuum (UHV) conditions (10^{-7}–10^{-6} Pa). Potassium metal samples were prepared in an Ar-filled glovebox and transferred to the XPS intro chamber using a vacuum transfer vessel (ULVAC PHI) to prevent air exposure. A 500 µm × 500 µm area of each sample was analysed. Survey spectra were gathered at a pass energy of 224 eV, and 55 eV was used for core-level spectra. In-built electron and low-energy Ar^+ sources were utilised for neutralisation. Depth profiling was achieved with consecutive XPS analysis and Ar^+ sputtering (4 kV, 3 mm × 3 mm) for a total of 60 min. Acquired spectra were fitted with Gaussian-Lorentzian product lineshapes using CasaXPS software.[217] All spectra were charge referenced to the adventitious C 1s peak at 285 eV.[186] Atomic percentages were estimated using Scofield relative sensitivity factors.

Error Analysis

The error bars in Figures 3.1, 3.13b and 3.19 represent the standard error in the mean, $\sigma_{\overline{x}}$, estimated from the sample standard deviation, σ_x, and the number of data points, n, using Equation 3.20:

$$\sigma_{\overline{x}} = \frac{\sigma_x}{\sqrt{n}} \tag{3.20}$$

Due to the high sensitivity of the calculated cation transference numbers to changes in solution densities, the limited resolution of the densitometer results in transference

numbers with a non-negligible uncertainty. Each calculated transference number can take any value between $t^0_{+,\min}$ and $t^0_{+,\max}$, with equal probability, giving each measurement, i, an uncertainty variance, σ_i^2, of $\frac{1}{12}(t^0_{+,\max} - t^0_{+,\min})^2$. The error in the mean t^0_+, $\sigma_{\overline{x}}$, was then estimated by taking into account the sample standard deviation, σ_x, and the uncertainty variance, σ_i^2, for each of the n data points through Equation 3.21:

$$\sigma_{\overline{x}} = \sqrt{\frac{\sigma_x^2}{n} + \frac{1}{n^2}\sum_{i=1}^{n}\sigma_i^2} \tag{3.21}$$

Estimated errors in D and t^0_+ were then propagated through to χ_M, and the thermodynamic and Stefan-Maxwell diffusivities using the standard propagation rules summarised in Equation 3.22:

$$x = \frac{uv}{w}, \quad \sigma_x = x\sqrt{\left(\frac{\sigma_u}{u}\right)^2 + \left(\frac{\sigma_v}{v}\right)^2 + \left(\frac{\sigma_w}{w}\right)^2} \tag{3.22}$$

4

Solid Electrolyte Interphases on Lithium and Potassium Metal

Abstract

Understanding the solid electrolyte interphase (SEI) is vital to the development of post-lithium-ion battery chemistries. In this chapter chemical SEI formation on lithium metal is investigated in the model electrolyte system, lithium bis(fluorosulfonyl)imide (LiFSI) in tetraethylene glycol dimethyl ether (G4). First a standard SEI formation and measurement protocol is developed to enable the SEI chemistry to be probed reliably using X-ray photoelectron spectroscopy depth profiling. SEI samples are then prepared by systematically varying the temperature, salt concentration, time and solvent during formation, providing insights into the effects these factors have on the SEI chemistry and revealing that the electrolyte solvation structure is most important in determining the species that are reduced to form the SEI. Additionally, the SEI that forms on potassium metal is further probed to understand the differences between SEI chemistries in lithium- and potassium-based battery systems, revealing significant differences in the stable inorganic species observed.

The results presented in this chapter are currently being prepared for publication.

Contents

4.1 Introduction . . . 73
4.2 Sample Preparation . . . 74
4.2.1 Sensitivity Factors . . . 75
4.2.2 Sample Damage . . . 75
4.2.3 Solvent Rinsing . . . 76
4.2.4 Depth Profiling . . . 77
4.2.5 Calibrating Sputter Rate . . . 78
4.3 Lithium Metal Electrodes . . . 80
4.3.1 Model System . . . 80
4.3.1.1 F 1s Region . . . 84
4.3.1.2 O 1s Region . . . 84
4.3.1.3 N 1s Region . . . 87
4.3.1.4 C 1s Region . . . 87
4.3.1.5 S 2p Region . . . 88
4.3.1.6 Li 1s Region . . . 89
4.3.2 Role of Temperature . . . 91
4.3.3 Role of Concentration . . . 97
4.3.4 Role of Time . . . 102
4.3.5 Role of Solvent . . . 104
4.4 Potassium Metal Electrodes . . . 106
4.5 Conclusion . . . 112
4.6 Experimental Methods . . . 114

4.1 Introduction

Lithium metal is the most desirable negative electrode material for high-performance batteries as it has the highest specific capacity and lowest electrode potential of any candidate material. However, as discussed in Chapter 1, the use of lithium metal in batteries is currently impeded by the lack of understanding of the solid electrolyte interphase (SEI) that forms when lithium is in contact with the electrolyte.

The composition, and therefore properties, of the SEI are influenced by numerous factors (Figure 1.8), including the electrolyte chemistry, concentration and temperature, and the composition may change as a function of time. Despite this, systematic studies on the influence of these factors on SEI composition/properties have rarely been reported in the literature, making it challenging to understand the role these factors play in controlling SEI formation and growth.

In this chapter, chemical SEI formation in a model electrolyte system is investigated using X-ray photoelectron spectroscopy (XPS). The model electrolyte system studied here

was lithium bis(fluorosulfonyl)imide (LiFSI) in tetraethylene glycol dimethyl ether (G4). LiFSI has emerged as a popular salt in LMB electrolytes[10,218] and it is often included for its ability to form a "favourable" SEI, although there is currently no consensus on which attributes of an SEI are beneficial to battery performance. Glymes are often used in LMBs due to their stability in contact with lithium metal and G4 in particular exhibits low flammability and volatility.[219] LiFSI G4 has therefore served as a model system in the Pasta Group for several years, and its transport and thermodynamic properties have been comprehensively characterised as a function of both concentration[35] and temperature.[39] Additionally, a systematic electrochemical impedance spectroscopy (EIS) study has been performed by Dr L. F. Olbrich and Dr N. Pianta to understand the concentration- and temperature-dependent impedance evolution in this electrolyte system,[220] which will be used to guide the interpretation of the XPS results here.

By systematically varying temperature, salt concentration, formation time, and solvent, insight can be gained into the impact of these on the chemical composition of the SEI formed on lithium metal. Additionally, SEI formation on potassium metal will also be investigated, providing an understanding of the differences in SEI chemistry between lithium- and potassium-based battery systems.

The objectives of this chapter are to:

1. Develop an SEI sample preparation methodology for consistent and reliable XPS characterisation.

2. Explore the impact that temperature, electrolyte concentration, time and solvent have on SEI formation on lithium metal.

3. Uncover the differences in the chemistry of the SEI formed on lithium and potassium metal.

4.2 Sample Preparation

In order to reliably characterise the SEI using XPS it is first important to optimise the sample preparation steps and measurement protocol.

4.2.1 Sensitivity Factors

To enable a quantitative determination of chemical composition several reference standards were measured to determine sensitivity factors for the transitions corresponding to the expected elements. LiFSI, Li_2O and KF were therefore measured to determine the relative sensitivity factors for the Li 1s, N 1s, O 1s, F 1s, S 2p and K 2p transitions. C 1s and Na 1s sensitivity factors were further estimated from LiOH and sodium metal samples that contained intense peaks attributable to Li_2CO_3 and Na_2CO_3/NaOH, respectively. The sensitivity factors, relative to the Li 1s transition, used here are presented in Table 4.1.

Table 4.1: Relative sensitivity factors determined from reference samples.

Transition	Sensitivity Factor
Li 1s	1
C 1s	7.2
N 1s	17.3
O 1s	33.5
F 1s	30.5
Na 1s	61.9
S 2p	26.6
K 2p	59.9

4.2.2 Sample Damage

XPS depth profiling is achieved by alternating between analysis and sample sputtering using an argon-ion gun. Previous reports suggest that this sputtering step can lead to degradation of lithium salts and SEI species,[77,79] so this was tested by performing a simulated depth profiling measurement on pure LiFSI salt with an Ar^+ accelerating voltage of 4 kV, as presented in Figure 4.1a. Prior to depth profiling (denoted by "0 min" on the plot) the spectra are consistent with pure LiFSI, with minor LiF and adventitious carbon impurities present. However, after just 5 min of sputtering the LiF F 1s peak at 685.1 eV significantly increases in intensity, the O 1s peak broadens, and additional sulphur-containing species appear in the S 2p spectra, clearly showing significant degradation of the salt. With increasing sputtering the proportions of the peaks attributed to degradation products increase gradually in relative intensity.

To examine the influence that Ar^+ accelerating voltage has on this degradation process, depth profiling was additionally performed on pure LiFSI for 5 min at accelerating voltages

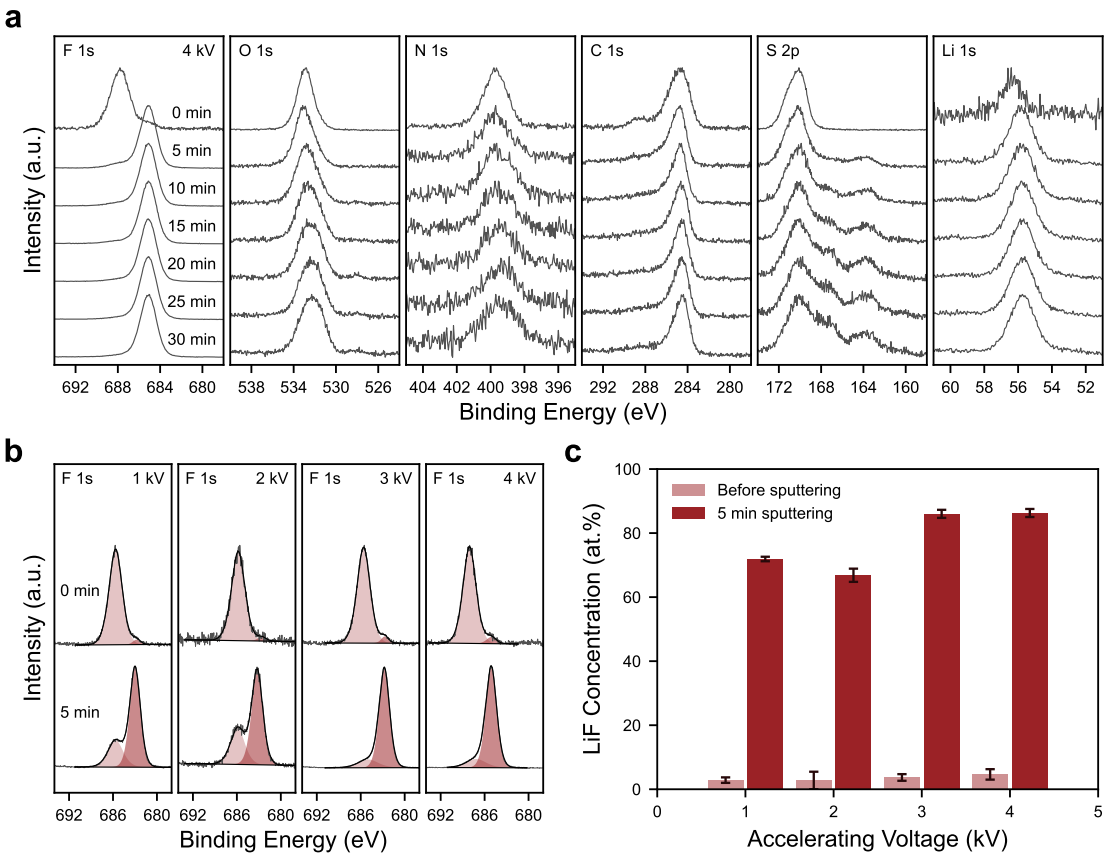


Figure 4.1: Quantifying depth profiling damage. (a) Changes to LiFSI F 1s, O 1s, N 1s, C 1s, S 2p and Li 1s spectra during depth profiling at 4 kV. (b) Changes to F 1s spectra after 5 min of sputtering at various accelerating voltages. (c) Proportion of LiF in the F 1s spectra before and after 5 min of sputtering as a function of ion gun accelerating voltage. Error bars take into account the peak fitting uncertainty.

of 1, 2 and 3 kV. The F 1s spectra are presented in Figure 4.1b, where it is clear that severe salt degradation occurs in all conditions tested and the LiF peak at 685.1 eV grows significantly after sputtering. Quantification of the relative area of this LiF peak in Figure 4.1c reveals that, prior to sputtering, LiF accounts for just 3–5 at.% of the total fluorine, but this increases to 70–85 at.% after sputtering. While it appears that higher accelerating voltages may result in more LiF formation, the LiF concentration is significantly increased no matter which accelerating voltage is used. Any residual salt remaining on an SEI sample is therefore likely to decompose to form LiF during depth profiling.

4.2.3 Solvent Rinsing

The results presented above suggest that residual salt could significantly alter the measured composition during XPS depth profiling, so an initial set of standard SEI samples were

formed by submerging lithium metal in 1 m LiFSI G4 overnight at room temperature to explore whether sample rinsing is necessary. One sample was not rinsed prior to depth profiling at 4 kV, while the other was rinsed with 1,2-dimethoxyethane (DME). The XPS spectra recorded from the surface of the sample without rinsing in Figure 4.2a appear similar to those measured from the LiFSI powder (Figure 4.1a), indicating a large quantity of residual salt remaining on the sample surface. As expected, this salt decomposes during depth profiling, resulting in a large LiF F 1s peak at 685.1 eV and generating several other salt degradation species.

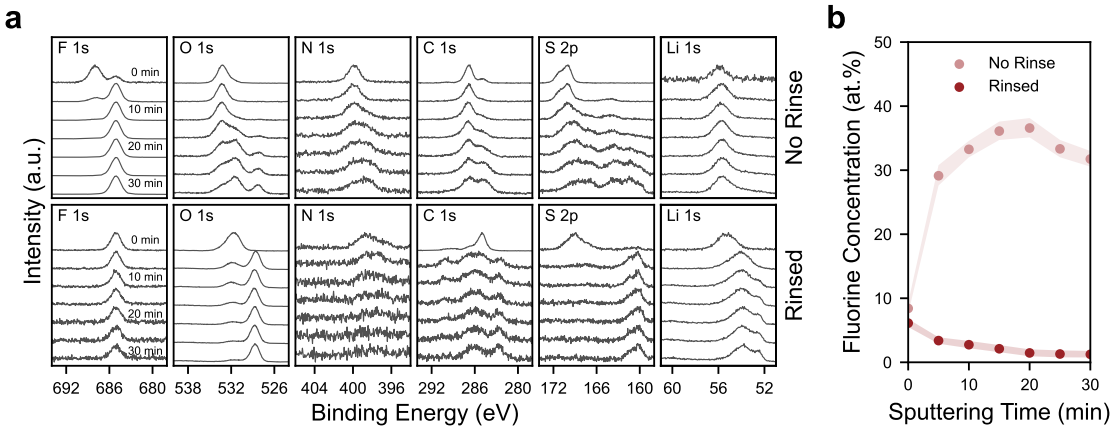


Figure 4.2: Effects of sample rinsing. (a) F 1s, O 1s, N 1s, C 1s, S 2p and Li 1s spectra during depth profiling at 4 kV for an SEI sample that has not been rinsed (top) compared to one that has been rinsed with DME (bottom). (b) Fluorine concentration in the SEI as a function of sputtering time for SEI samples in (a). Error bars take into account the peak fitting uncertainty.

In contrast, in the rinsed sample in Figure 4.2a there is no LiFSI peak at the surface and the peaks that emerge during depth profiling appear at different binding energies to those associated with salt decomposition products in Figure 4.1a. Quantification of the fluorine concentration as a function of depth in the two samples in Figure 4.2b reveals that the sample without rinsing is enriched in fluorine while fluorine only has a concentration of a few at.% in the rinsed sample. Sample rinsing therefore appears to be an important step to prevent residual salt from obscuring the chemistry of the SEI.

4.2.4 Depth Profiling

To decide on the most suitable accelerating voltage for depth profiling measurements three additional standard SEI samples were prepared as before and were rinsed with

DME to remove residual salt. Depth profiling was then performed for a total of 30 min with Ar^+ accelerating voltages of 1, 2 or 4 kV. The F 1s, O 1s and Li 1s spectra gathered from these sample are presented in Figure 4.3. With an accelerating voltage of 1 kV (Figure 4.3a) the F 1s peak gradually reduces in intensity, the Li 1s peak shifts to lower binding energy and an O 1s peak at 528.5 eV emerges and grows with increasing sputtering time, consistent with the emergence of Li_2O. However, there is no evidence of a metallic lithium peak. In contrast, when sputtering at 4 kV (Figure 4.3c), the F 1s peak rapidly reduces in intensity and an intense O 1s Li_2O peak is evident after the first sputter step. A shoulder also appears in the Li 1s spectra at low binding energy after just 15 min of sputtering, consistent with metallic lithium. The SEI therefore appears to be etched away too rapidly at 4 kV, but too slowly at 1 kV.

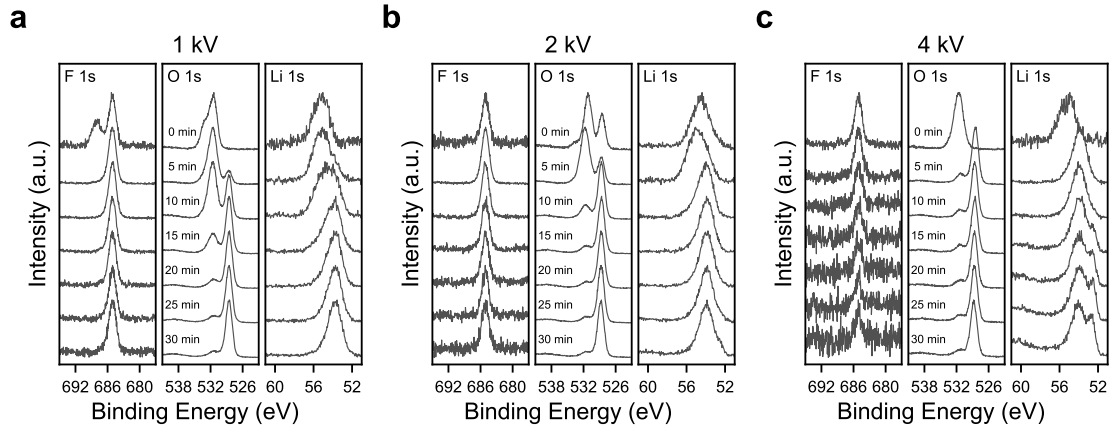


Figure 4.3: Comparing ion gun accelerating voltages. F 1s, O 1s and Li 1s spectra measured from an SEI sample during depth profiling with an ion gun accelerating voltage of (a) 1 kV, (b) 2 kV, (c) 4 kV.

An accelerating voltage of 2 kV (Figure 4.3b), however, provides a good balance. The F 1s, O 1s and Li 1s spectra display the gradual changes observed at 1 kV at low sputtering times, and the sputtering rate is high enough to enable a metallic lithium peak to be observed after 30 min of sputtering. 2 kV will therefore be used for depth profiling on all subsequent SEI samples.

4.2.5 Calibrating Sputter Rate

The XPS spectra presented in Figure 4.3 suggest that Li_2O is prevalent in the SEI, so it would be helpful to estimate the rate at which Li_2O is etched away during depth profiling.

A thin Li_2O film was therefore deposited onto a glass substrate using radio-frequency magnetron sputtering. This calibration standard was deposited by Dr S. Turrell. To determine the film thickness a step was created by scratching off a portion of the film and this was measured using atomic force microscopy (AFM). The height map across this step is presented in Figure 4.4a, and the mean film thickness is determined to be 140 nm with a root mean square roughness of 50 nm (Figure 4.4b, c).

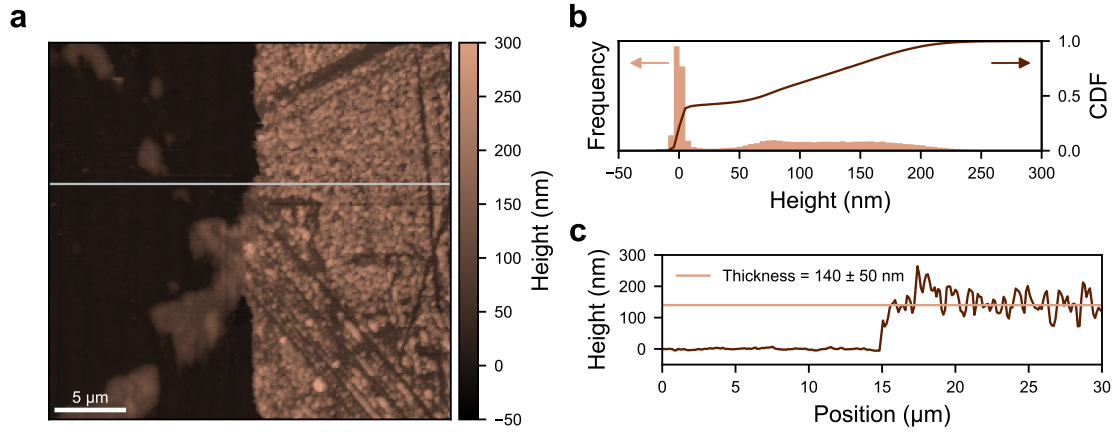


Figure 4.4: Li_2O film thickness measurement. (a) AFM height map across a step created through the Li_2O film. (b) Histogram of heights in (a) and corresponding cumulative distribution function (CDF), showing peaks corresponding to both the substrate and the film. (c) Height across the 1D section marked in (a) compared with the average film thickness.

Depth profiling was performed on this Li_2O film with Ar^+ accelerating voltages from 1 to 4 kV to calibrate the sputter rate. Example O 1s spectra measured using a 2 kV accelerating voltage are plotted in Figure 4.5a, where, aside from at the surface due to contamination, an intense Li_2O peak can be observed at 528.5 eV at low sputtering times. After approximately 70 min of sputtering the relative proportion of this peak decreases and two new peaks originating from the glass substrate emerge and their proportion increases with increasing sputtering, indicating that the Li_2O has been etched away.

The proportion of Li_2O in the O 1s region is plotted as a function of sputtering time for the different accelerating voltages in Figure 4.5b, where it is clear that Li_2O initially accounts for approximately 80 at.% of the total oxygen and after a certain sputtering time its concentration decreases rapidly as the glass substrate is exposed. This time reduces as the accelerating voltage increases. The Li_2O film is assumed to have been etched away once its concentration decreases to 50% of the maximum, or approximately 40 at.%, as

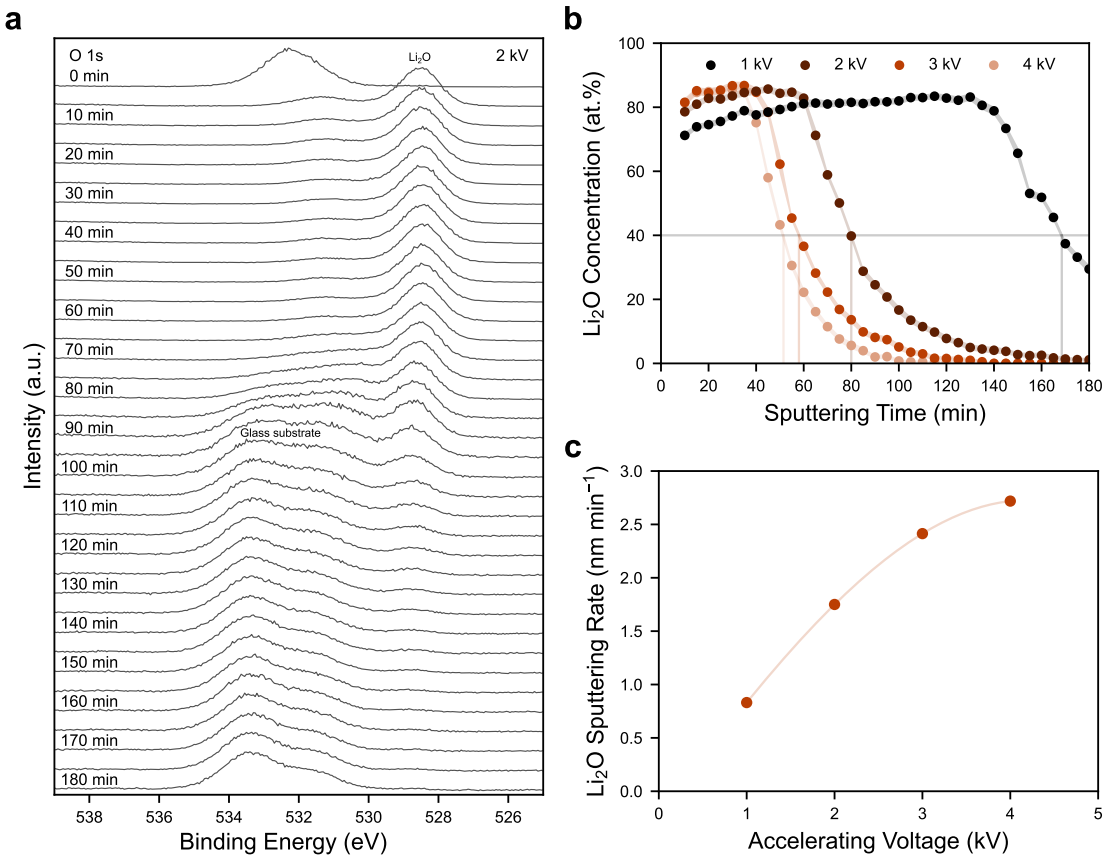


Figure 4.5: Measuring Li_2O sputtering rate. (a) O 1s spectra during depth profiling through the Li_2O film using a 2 kV accelerating voltage. (b) Li_2O concentration in the O 1s region as a function of sputtering time for various accelerating voltages. Error bars take into account the peak fitting uncertainty. (c) Li_2O sputtering rate as a function of ion gun accelerating voltage.

plotted on Figure 4.5b. Dividing the Li_2O thickness by this sputtering time results in the approximate Li_2O sputtering rates presented in Figure 4.5c.

4.3 Lithium Metal Electrodes

Having now decided on an SEI sample preparation and measurement protocol to provide reliable, comparable results between samples, the SEI formed on lithium metal can now be characterised and the impact that temperature, salt concentration, time and solvent have on SEI chemistry can be uncovered.

4.3.1 Model System

To ensure that results gathered under different conditions can be meaningfully compared it is important that samples are produced in a consistent manner, with only one variable

changing between each sample. It is therefore helpful to clearly state the steps taken during sample preparation and discuss their purpose here.

The lithium metal electrodes were always prepared from high-purity foils by first brushing them to remove the native passivation layer (NPL) that builds up during manufacture and storage, which can vary depending on storage conditions.[127] The immediate formation of a new NPL on the lithium surface is inevitable and its composition is likely to vary from that present initially, so the purpose of this step is to homogenise the NPL across samples. The brushed foil was then calendered to a thickness of 300 µm inside a dried polypropylene bag and punched into 8 mm diameter discs using a wad punch. XPS depth profiling (performed with a 4 kV Ar^+ accelerating voltage) results gathered from the pristine lithium metal foil to investigate the chemistry of the NPL are presented in Figure 4.6.

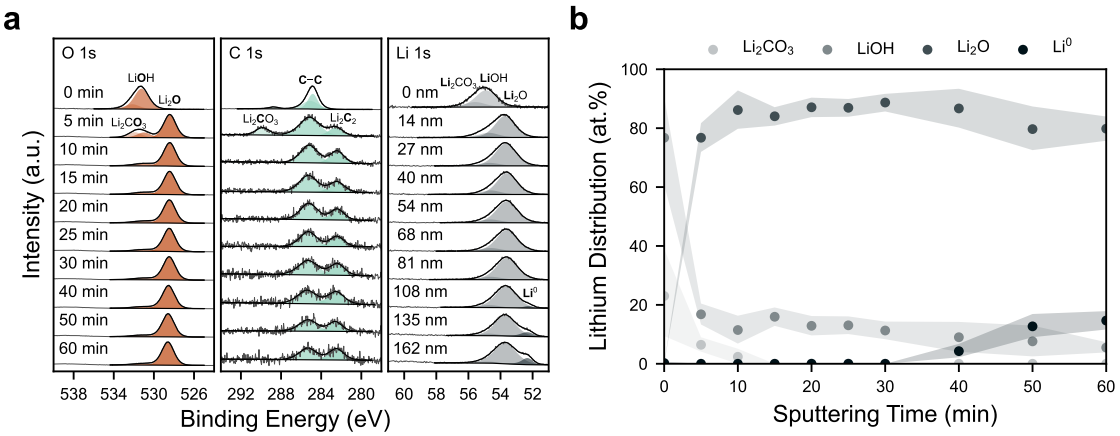


Figure 4.6: XPS depth profiles from a pristine lithium metal foil. (a) O 1s, C 1s and Li 1s spectra. (b) Breakdown of lithium-containing species. Error bars take into account the peak fitting uncertainty.

Prior to sputtering the O 1s spectrum in Figure 4.6a displays two separable peaks attributed to Li_2CO_3 at 532.1 eV and LiOH at 531.2 eV. Corresponding peaks are observed in the Li 1s spectrum, but the C 1s spectrum is masked by adventitious carbon. After 5 min of sputtering the O 1s Li_2CO_3 and LiOH peaks reduce in relative intensity and a major peak emerges at 528.4 eV, consistent with Li_2O. The Li 1s spectrum also becomes dominated by a corresponding Li_2O peak at 53.7 eV and the majority of the adventitious carbon is removed, revealing low-intensity Li_2CO_3, C−C and Li_2C_2 peaks in the C 1s spectrum. After 10 min of sputtering the O 1s Li_2CO_3 and LiOH peaks further reduce in

intensity and the C 1s Li_2CO_3 peak disappears, but further sputtering results in minimal changes to the XPS spectra until 40 min, where a peak emerges at 52.2 eV, consistent with metallic lithium. Quantification of components identified in the Li 1s spectra as a function of sputtering time in Figure 4.6b reveal that at the surface the NPL is rich in LiOH and Li_2CO_3, but Li_2O quickly becomes the dominant species during depth profiling. This NPL structure is consistent with that reported by Otto et al.[127]

Interestingly, the NPL is typically reported to be just a few nanometres in thickness,[127] but the metallic lithium peak does not emerge until after 40 min of sputtering, corresponding to 108 nm using the Li_2O sputter rate determined in Figure 4.5. However, metallic lithium is known to oxidise rapidly, even under ultrahigh vacuum (UHV) conditions,[127,221,222] so the absence of a metallic lithium peak does not necessarily mean that the NPL has not been etched away. Considering this, the depth at which the apparent composition reaches an approximate steady state could provide a better indication of NPL thickness. In Figure 4.6b this occurs after 10 min of sputtering, corresponding to approximately 27 nm.

Lithium has a low density (0.534 g cm^{-3}) and it would float in electrolytes, so it was pressed onto a stainless steel spacer and then submerged in 1 mL of electrolyte. Of course, lithium is far more active than stainless steel, so they form a galvanic couple when submerged in electrolyte and the lithium metal will be oxidised, releasing Li^+ into the electrolyte while the electrons lead to electrolyte reduction on the stainless steel surface. While this may be an important capacity loss mechanism in lithium metal batteries (LMBs) with limited excess lithium,[223] it is not expected to significantly alter the composition of the SEI formed on the lithium metal in this case. In fact, this configuration may better approximate the conditions experienced in a real cell, where the current collector and cell case will inevitably be exposed to electrolyte while in electrical contact with the lithium.

The lithium was submerged in electrolyte for a set amount of time inside a heated glovebox antechamber at a fixed temperature (or in a cooled oven for temperatures below room temperature). This results in spontaneous, chemical SEI formation, and will model the real-world situation in which a LMB is assembled with excess lithium and then allowed to rest at open-circuit. This situation would be encountered during the wetting process,

where time is allowed for the electrolyte to fully penetrate the porous cell components, and it can require several days as well as elevated temperatures for LIBs.[224]

The samples were then removed from the electrolyte and rinsed three times with 200 µL of pure solvent to remove residual salt, as this was found to be necessary in Chapter 4.2.3. Many studies choose to rinse with a highly volatile solvent, such as 1,2-dimethoxyethane (DME)[225] or dimethyl carbonate (DMC),[77] but here the same solvent as the electrolyte was used to prevent any chemical changes due to the introduction of an additional species. Excess solvent was then blotted away with tissue, ensuring contact was not made with the sample surface.

The samples were then mounted to the XPS stage using double-sided insulating tape to prevent electrical contact to the stage and double-sided carbon tape to ensure good adhesion. The samples were insulated from the stage to mitigate the issue of differential charging, where metallic and insulating regions of the sample may charge differently, leading to inconsistent peak shifts.[226] This also prevents the electron flood gun used for charge neutralisation from driving electrochemical reactions and causing lithium to plate through the SEI, which is the basis of the virtual electrode plating XPS (VEP-XPS) technique used for in-situ SEI studies in solid-state batteries.[222,227] The samples were then immediately transferred into the introduction chamber of the XPS using an airless transfer vessel and were pumped for several hours to allow any residual solvent to evaporate.

Samples were then transferred into the XPS analysis chamber and depth profiling was performed using a 2 kV accelerating voltage as this was determined to be most appropriate in Chapter 4.2.4. This results in an approximate sputter rate of 1.75 nm min^{-1} for Li_2O (Figure 4.5c), which is expected to be a major species. Alternating analysis and sputtering were performed for a total of 60 min of sputtering, and dual charge neutralisation was used during analysis. The pressure during analysis was always between 10^{-7} and 10^{-6} Pa.

First, a baseline SEI sample was formed in 1 m LiFSI G4 for 20 h at 30°C. The XPS spectra measured during depth profiling are presented in Figure 4.7a, where they have been normalised such that the recorded intensity scales between 0 and 1 and then offset for clarity. The sputtering times and approximate corresponding Li_2O depths are

marked on the plot for each set of spectra. Full spectra without normalisation, plus survey spectra, are provided in Appendix B.2.

Only peaks consistent with the presence of F, O, N, C, S and Li were detected, so the F 1s, O 1s, N 1s, C 1s, S 2p and Li 1s regions are included in Figure 4.7a and peak models were fit to the data. For each depth profiling step an equivalent homogeneous atomic fraction, X_i, was calculated using the total peak area, A_i, and sensitivity factor, S_i, for each transition, i, with Equation 4.1[159] and these are plotted in Figure 4.7b.

$$X_i = \frac{A_i/S_i}{\sum_j A_j/S_j} \times 100 \tag{4.1}$$

4.3.1.1 F 1s Region

In the F 1s spectra in Figure 4.7a there are two peaks present before depth profiling with a separation of 2.8 eV, consistent with LiFSI and LiF at higher and lower binding energy, respectively. The LiFSI peak is a minor species with a 7 times lower area than LiF, but its presence suggests the rinsing process does not remove all of the residual salt from the sample surface. After 5 min of sputtering only the LiF remains, suggesting the LiFSI is either localised to the sample surface and is fully removed or is converted entirely to LiF, as was observed to occur during sputtering in Chapter 4.2.2. Nevertheless, the relatively low concentration of LiFSI detected would not significantly enhance the amount of LiF present even if it decomposes. Upon further depth profiling only the LiF peak remains. LiF is therefore present in all F 1s spectra and it has a reasonable signal-to-noise ratio, making it a suitable reference for charge correction. Caracciolo et al. reported a LiF F 1s binding energy of 685.1 eV,[186] so this was used here. Despite the previous belief that LiF is an important, major SEI component fluorine only makes up 2.1 ± 0.3 at.% here after 5 min of sputtering, dropping to 0.9 ± 0.4 at.% after 15 min.

4.3.1.2 O 1s Region

The O 1s spectrum before sputtering contains two separable peaks at 533.3 and 532.1 eV. The peak at 533.3 eV is consistent with LiFSI, while the lower binding energy peak is likely contributed to by SO_x-containing species and a number of adventitious species

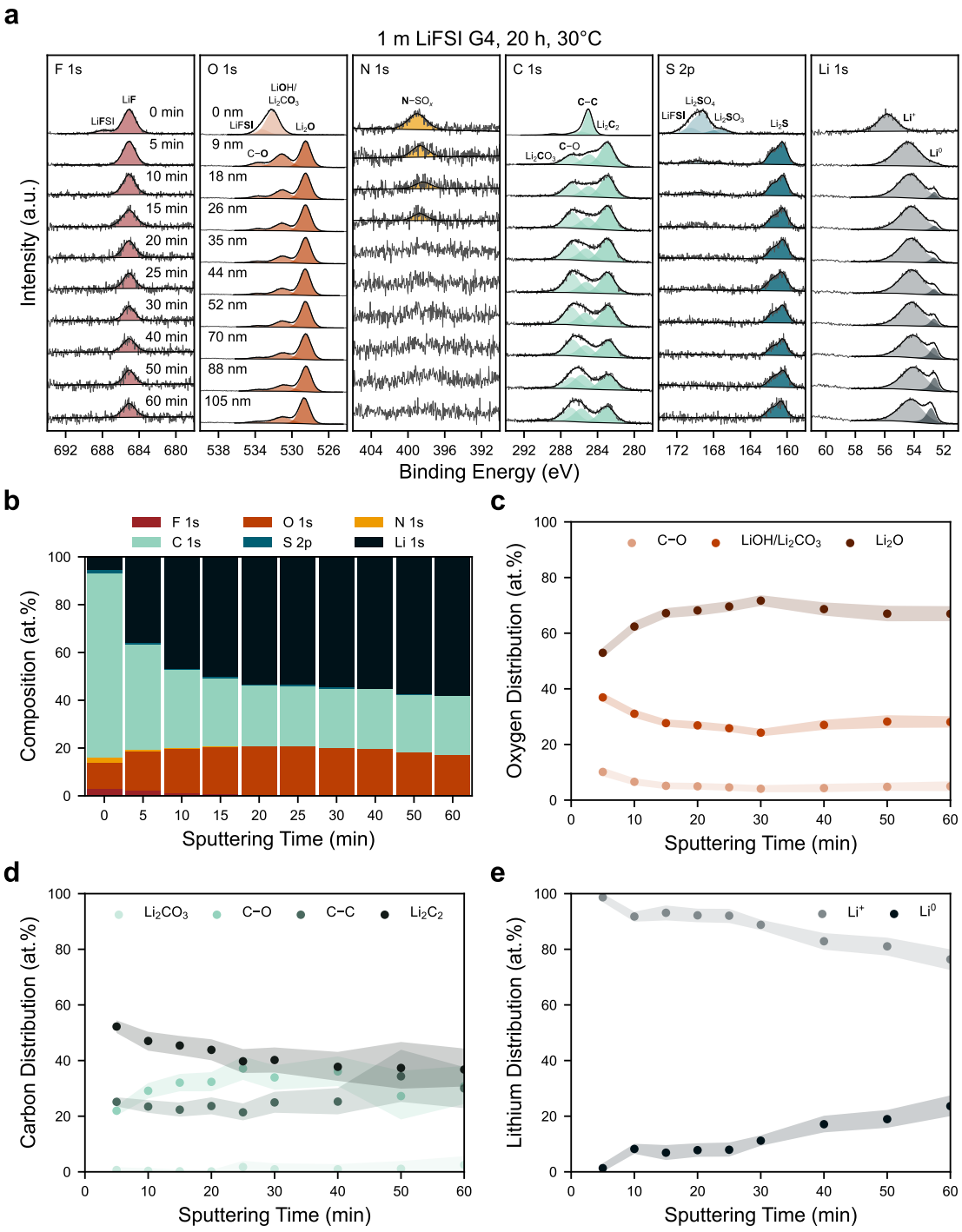


Figure 4.7: XPS depth profiles from an SEI sample formed in 1 m LiFSI G4 for 20 h at 30°C. (a) F 1s, O 1s, N 1s, C 1s, S 2p and Li 1s spectra. (b) Elemental composition. (c) Breakdown of oxygen-containing species. (d) Breakdown of carbon-containing species. (e) Breakdown of lithium-containing species. Error bars take into account the peak fitting uncertainty.

including C−O, C=O and O−C=O bonds.[228] After 5 min of sputtering there are three separable peaks at 528.5, 531.1 and 533.7 eV, attributable to Li_2O, $LiOH/Li_2CO_3$ and

an organic species containing C−O bonds, respectively.[127,186] The breakdown of these identified oxygen-containing species is plotted in Figure 4.7c as a function of sputtering time, where the shaded regions represent the difference between the maximum, $X_{i,\max}$, and minimum, $X_{i,\min}$, atomic fractions estimated from the fitted peak area, A_i, and its standard deviation, σ_i, for each species i using Equations 4.2 and 4.3.

$$X_{i,\max} = \frac{A_i + \sigma_i}{A_i + \sigma_i + \sum_{j \neq i}(A_j - \sigma_j)} \times 100 \tag{4.2}$$

$$X_{i,\min} = \frac{A_i - \sigma_i}{A_i - \sigma_i + \sum_{j \neq i}(A_j + \sigma_j)} \times 100 \tag{4.3}$$

From Figure 4.7c it is clear that Li_2O is already the majority species after 5 min of sputtering, and its proportion increases from 53 ± 2 to 72 ± 2 at.% as the sputtering time increases from 5 to 30 min. At the same time the proportions of $LiOH/Li_2CO_3$ and C−O decrease, suggesting the surface of the SEI is more enriched in these species. Within measurement uncertainty, the proportions of the species do not change significantly beyond 30 min of sputtering and Li_2O remains the major oxygen-containing species at all depths. Since oxygen makes up a large proportion of all elements (20 ± 1 at.% after 30 min of sputtering, Figure 4.7b), Li_2O is therefore one of the most prevalent species detected within the SEI. However, Li_2O can form through several routes. First, Li_2O is expected to form during complete LiFSI reduction by cleavage of the S=O bonds in the sulfonyl group.[225] Second, lithium metal spontaneously reacts with residual oxygen within both gloveboxes and ultrahigh vacuum (UHV) systems to form Li_2O,[127,222] and the rate of reaction within the XPS depends on the chamber pressure.[221] Finally, other oxygen-containing species are reported to decompose to form Li_2O during depth profiling.[229] Despite these uncertainties associated with XPS measurements, Li_2O has also recently been identified as a major SEI component in a range of electrolyte systems using quantitative titration,[90] where a strong, positive correlation was observed between Li_2O-content and coulombic efficiency (CE). Li_2O is also frequently observed when the SEI is examined using cryogenic transmission electron microscopy (cryo-TEM).[65,68,75,90] Li_2O formation mechanisms and the role it plays in promoting the CE therefore require further study.

4.3.1.3 N 1s Region

In Figure 4.7a there is one low intensity N 1s peak evident before sputtering, and its intensity decreases with increasing sputtering time, falling below the detection limit after approximately 20 min of sputtering. The low intensity makes accurate assignment challenging, but its position at approximately 399 eV is between those expected for LiFSI and Li_3N, and it has previously been attributed to a species where nitrogen is bonded to a single sulphur atom, such as $N{-}SO_x$.[225] Nevertheless, this is only a minor SEI species (Figure 4.7b), making up 2.3 ± 0.6 at.% at the surface and only 0.7 ± 0.5 at.% after 5 min of sputtering.

4.3.1.4 C 1s Region

The surface C 1s spectrum in Figure 4.7a displays the typical shape expected from adventitious carbon contamination,[228] so carbon is the main element detected at the surface in Figure 4.7b. After 5 min of sputtering the majority of this adventitious carbon is removed, revealing four separable peaks consistent with Li_2CO_3 at 289.8 eV,[186] organic C−O bonds at 286.9 eV,[228] organic C−C bonds at 284.9 eV, and a carbide species at 282.9 eV.[192] Carbon-containing species make up a large proportion of the SEI (Figure 4.7b), with carbon accounting for 44 ± 2 at.% after 5 min of sputtering, reducing to 25 ± 2 at.% after 60 min.

The presence of C−O and C−C bonds indicate that the SEI contains organic species, which would likely be composed of ethereal oligomers that are expected to form when ether solvents are reduced (Table 1.2). Contrary to the previously proposed two-layer SEI structure, believed to be composed of an inorganic inner layer and an organic outer layer,[62,104] here the organic components make up approximately 50–60 at.% of the total carbon at all depths (Figure 4.7d) and they are therefore prevalent throughout the sample. Figure 4.7d further reveals that Li_2CO_3 is only a minor component, so the O 1s peak at 531.1 eV will be dominated by LiOH.

Interestingly, the dominant carbon-containing species detected near the surface is Li_2C_2, accounting for 52 ± 2 at.% of the total carbon after 5 min of sputtering and only dropping to 37 ± 7 at.% after 60 min. Li_2C_2 is often detected in the SEI[59,90,230]

as well as in bulk metallic lithium,[192,221] but its origin is not well understood. Some authors propose that Li_2C_2 is formed through the reduction of Li_2CO_3 (also generating Li_2O) or lithium alkyl carbonates,[59,68,231] while others believe it to form through a sputtering-induced reaction involving organic species.[221] It has also been suggested to be a common impurity present in metallic lithium that is formed during the manufacturing process.[191] Here, the higher concentration of Li_2C_2 at low sputtering times makes it unlikely to originate from the lithium metal, and Li_2CO_3 and lithium alkyl carbonates are not expected to form during reduction in this electrolyte system. However, Li_2CO_3 is known to be present on the surface of the NPL (Figure 4.6), but is not detected in any significant concentration here, suggesting it may have been reduced and would therefore contribute to both Li_2C_2 and Li_2O. Unfortunately, here the possibility that Li_2C_2 is simply an artefact of the depth profiling process cannot be eliminated, requiring further study into its formation mechanism.

4.3.1.5 S 2p Region

There are several sulphur-containing species identified in the S 2p region in Figure 4.7a. At the surface the peak with its $2p_{3/2}$ component at 170.4 eV is consistent with residual LiFSI, while there is disagreement in the literature about the assignment of the other two peaks. Some authors attribute the peak at 169.1 eV to $-SO_2F$ species,[225] but this is unlikely given the absence of a corresponding peak in the F 1s spectra here. They therefore likely result from SO_x-containing species, with the 169.1 and 167.0 eV peaks consistent with SO_4^{2-} and SO_3^{2-} species, respectively.[232,233] In Figure 4.7a these peaks have therefore been attributed to Li_2SO_4 and Li_2SO_3, respectively. After 5 min of sputtering another peak appears at 160.5 eV, consistent with fully-reduced Li_2S,[232] and accounts for 84 ± 10 at.% of the total sulphur, increasing to 100 at.% after 15 min of sputtering. Similar to the other species from LiFSI reduction, however, sulphur only makes up a minor proportion of the detected elements (Figure 4.7b), decreasing from 1.4 ± 0.2 at.% at the surface to 0.6 ± 0.2 at.% after 15 min of sputtering.

4.3.1.6 Li 1s Region

At the surface the Li 1s region in Figure 4.7a displays a single separable peak at 55.8 eV, consistent with overlapping peaks from LiFSI, LiF and Li_2SO_4, which are the main lithium-containing species identified from the other regions. After 5 min of sputtering this peak shifts to a lower binding energy of 54.5 eV, and its binding energy and width both decrease with increasing sputtering time, consistent with Li_2O making up an increasing proportion of the sample with increasing depth.[229] At the same time, a metallic lithium peak at 52.6 eV emerges after 5 min of sputtering and grows with increasing depth. This Li^0 peak is accompanied by the emergence of a plasmon loss feature just above 60 eV in Figure 4.7a, further confirming the presence of metallic lithium.[127] From Figure 4.7b, lithium initially makes up just 5 ± 2 at.% of the total atoms, increasing to 50 ± 2 and 58 ± 2 at.% after 15 and 60 min of sputtering, respectively.

Interestingly, the Li^0 peak only accounts for 24 ± 4 at.% of the total lithium after 60 min of sputtering, but, as discussed above, since Li_2O forms dynamically during depth profiling on lithium metal the intensity of the Li^0 peak is not necessarily a reliable indicator to estimate SEI thickness. It is therefore helpful to introduce a metric to assess when the SEI has been etched through. In Figure 4.7b the composition changes significantly between sputtering steps at low time, but then the composition approaches an approximate steady state. This was previously observed to indicate the removal of the NPL when performing depth profiling on pristine lithium foil, so the depth at which this steady-state composition is reached could enable a qualitative comparison of SEI thickness between samples. This depth can be estimated by considering the total change in measured equivalent homogeneous composition, ΔX, between each sputtering step, n, calculated from the atomic fraction, X_i, of each element i using Equation 4.4.

$$\Delta X_n = \sum_i |X_{i,n} - X_{i,n-1}| < 5 \text{ at.\%} \tag{4.4}$$

Here the SEI thickness is estimated as the depth at which ΔX falls below 5 at.%, corresponding to 25 min of sputtering for this model system. After 25 min of sputtering fluorine, nitrogen and sulphur each make up less than 1 at.% of detected elements and the oxygen and carbon distributions in Figures 4.7c and 4.7d, respectively, have also

reached a steady state within experimental uncertainty. This suggests that, despite its arbitrary nature, ΔX falling below 5 at.% gives a sensible estimate. 25 min of sputtering corresponds to an SEI thickness of approximately 44 nm, although this assumes the SEI sputters at a similar rate to Li_2O, which may not be the case and it is possible that different SEI components will sputter at different rates. Nevertheless, cryo-TEM imaging of the SEI formed on lithium metal typically reveals SEI thicknesses between approximately 10–50 nm,[65,68,75,76,90] which is in agreement with the thickness estimated here.

It is also interesting to note that a clear Li^0 peak appears in Figure 4.7a at much lower sputtering time than for the pristine lithium metal sample in Figure 4.6, suggesting the SEI does not simply form on top of the NPL and the NPL likely becomes incorporated within the SEI. This is not surprising considering their similar chemistries, and it is supported by impedance results gathered by Olbrich et al. that do not contain any features attributable to the presence of an NPL of constant composition.[220] This result is in disagreement with the proposal by Srout et al. that the NPL is responsible for the low-frequency semi-circle often observed when performing EIS in symmetric Li||Li cells,[234] but recent evidence suggests this feature is actually an artefact introduced when the electrolyte wets both the lithium electrode and the metallic cell casing, as often happens in coin cells.[235] Uncovering the impact that NPL chemistry has on the resulting SEI therefore requires further study.

In summary, the XPS depth profiling results gathered here indicate that the SEI formed in 1 m LiFSI G4 for 20 h at 30°C is compositionally inhomogeneous through its thickness. Close to the SEI-electrolyte interface the SEI is rich in carbon-containing species, especially Li_2C_2, and contains a small proportion of species that can be generated by salt decomposition alone, including LiF, $N{-}SO_x$, Li_2SO_4, Li_2SO_3 and Li_2S. With increasing depth the inorganic species become more fully reduced and fluorine, nitrogen and sulphur concentrations decrease significantly. At the same time the carbon concentration decreases gradually, so Li_2C_2 and ethereal organic species remain prevalent throughout the SEI. In contrast, the oxygen concentration increases gradually with depth, up to a maximum after 25 min of sputtering, with Li_2O becoming the majority SEI species after 10 min of sputtering. Beyond 25 min of sputtering, corresponding to approximately 44 nm, the equivalent homogeneous composition changes little with depth, suggesting the SEI has

been etched through. These results therefore indicate that the SEI is likely composed of an amorphous organic matrix (formed by solvent reduction) containing inorganic components that become more fully reduced, more Li_2O rich, and occupy a larger volume fraction towards the Li-SEI interface. This proposed structure is in good agreement with the SEI structures observed by Han et al. using cryo-TEM to image the SEI formed in ether-based electrolytes.[75]

4.3.2 Role of Temperature

To explore the impact that temperature has on chemical SEI formation, SEI samples were additionally formed for 20 h at 20, 40 and 50°C, using the same 1 m LiFSI G4 electrolyte.

The XPS results gathered from the 20°C sample are presented in Figure 4.8, where it is clear that they are broadly similar to those gathered from the 30°C sample. The surface spectra in Figure 4.8a are again dominated by adventitious carbon and, aside from lithium, carbon makes up the majority of all detected elements at all depths in Figure 4.8b, accounting for 45 ± 2 at.% after 5 min of sputtering. As evident in Figure 4.8d, the carbon distribution is also similar, with Li_2C_2 being more prevalent nearer the SEI-electrolyte interface and organic components remaining throughout the examined depth. Fluorine, nitrogen and sulphur make up an even smaller proportion of the SEI than at 30°C, accounting for 1.6 ± 0.4, 0.9 ± 0.8 and 0.6 ± 0.2 at.% at the surface, respectively. Their proportions again decrease with increasing depth.

The same three O 1s peaks are observed in Figure 4.8a, corresponding to organic oxygen-containing species, LiOH and Li_2O (the C 1s Li_2CO_3 peak has a low intensity). Excluding the surface, Li_2O is again the majority oxygen-containing species at all depths, accounting for 65 ± 2 at.% after 5 min of sputtering, but, unlike the 30°C sample, the oxygen distribution remains constant within the experimental error as the depth increases, as seen in Figure 4.8c. Oxygen also makes up a reducing proportion of the SEI with increasing depth in this case, decreasing from 15.1 ± 0.7 to 13.7 ± 0.7 at.% between 5 and 25 min of sputtering. Li_2O therefore is not the dominant SEI species at any depth, indicating that the SEI formed at lower temperature is more organic-rich and suggesting that solvent decomposition may be more favourable. Interestingly, applying the same

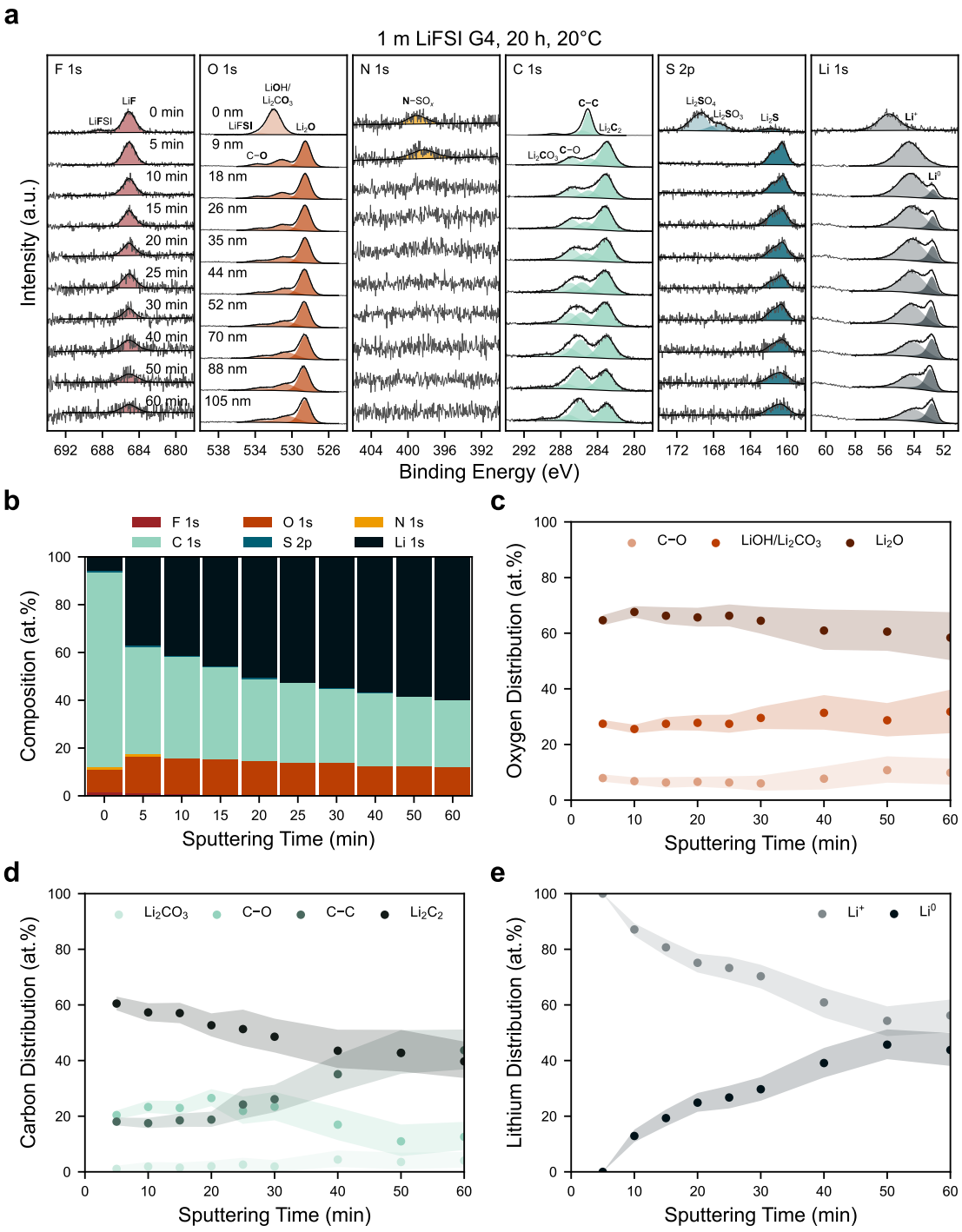


Figure 4.8: XPS depth profiles from an SEI sample formed in 1 m LiFSI G4 for 20 h at 20°C. (a) F 1s, O 1s, N 1s, C 1s, S 2p and Li 1s spectra. (b) Elemental composition. (c) Breakdown of oxygen-containing species. (d) Breakdown of carbon-containing species. (e) Breakdown of lithium-containing species. Error bars take into account the peak fitting uncertainty.

criterion that the SEI has been etched away when ΔX falls below 5 at.% again estimates the SEI thickness to be approximately 44 nm.

Results gathered from the 40°C sample in Figure 4.9 are also broadly similar to the two lower temperature samples (Figure 4.9a), with carbon-containing species making up a significant proportion of all elements at all depths (Figure 4.9b). The concentrations of fluorine, nitrogen and sulphur are also higher than in the 20°C sample, accounting for 2.0 ± 0.4, 2.0 ± 0.8 and 1.1 ± 0.2 at.% at the surface, respectively. Within error, these are identical to the surface concentrations of these species measured in the 30°C sample. Much like the 30°C sample, the proportion of Li_2O in the O 1s spectra increases with increasing depth, while the proportion of LiOH decreases, as evident in Figure 4.9c. Li_2O also becomes the majority SEI species after 25 min of sputtering, and the SEI thickness is estimated to be approximately 35 nm, suggesting that changing the temperature between 30 and 40°C has minimal impact on the SEI.

Further increasing the temperature to 50°C does, however, have a significant impact on the SEI. In Figure 4.10a the normalised surface spectra appear similar to those observed in the lower temperature samples, but the concentrations of fluorine-, nitrogen- and sulphur-containing species are significantly enhanced, as evident in Figure 4.10b. Fluorine, nitrogen and sulphur contribute to 9.0 ± 0.5, 3.1 ± 0.7 and 3.3 ± 0.3 at.% at the surface, respectively, with the fluorine and sulphur concentrations increasing to 11.1 ± 0.6 and 4.9 ± 0.4 at.%, respectively, after 5 min of sputtering. The additional Li 1s peak at 55.7 eV is therefore attributed to LiF. The proportion of fluorine then decreases with increasing sputtering time (Figure 4.10b,e), while the proportion of sulphur remains approximately constant with depth. The composition of the sulphur-containing species, however, does vary with depth. At the surface the majority species in the S 2p region is Li_2SO_4, but the proportion of Li_2SO_4 decreases and the proportion of fully-reduced Li_2S increases with increasing depth, with Li_2S becoming the major sulphur-containing species after 20 min of sputtering. In contrast to the samples formed at lower temperature, the peaks attributed to Li_2SO_4 and Li_2SO_3 remain fairly intense, and Li_2SO_4 still accounts for 33 ± 3 at.% of the total sulphur after 60 min of sputtering. The S 2p spectra in Figure 4.10a also contain an additional peak at 161.8 eV, consistent with lithium polysulphide species, Li_2S_n.[232]

Due to this increased concentration of Li_2SO_4 near the SEI-electrolyte interface, SO_x-containing species account for the majority of the oxygen at low sputtering times (Figure

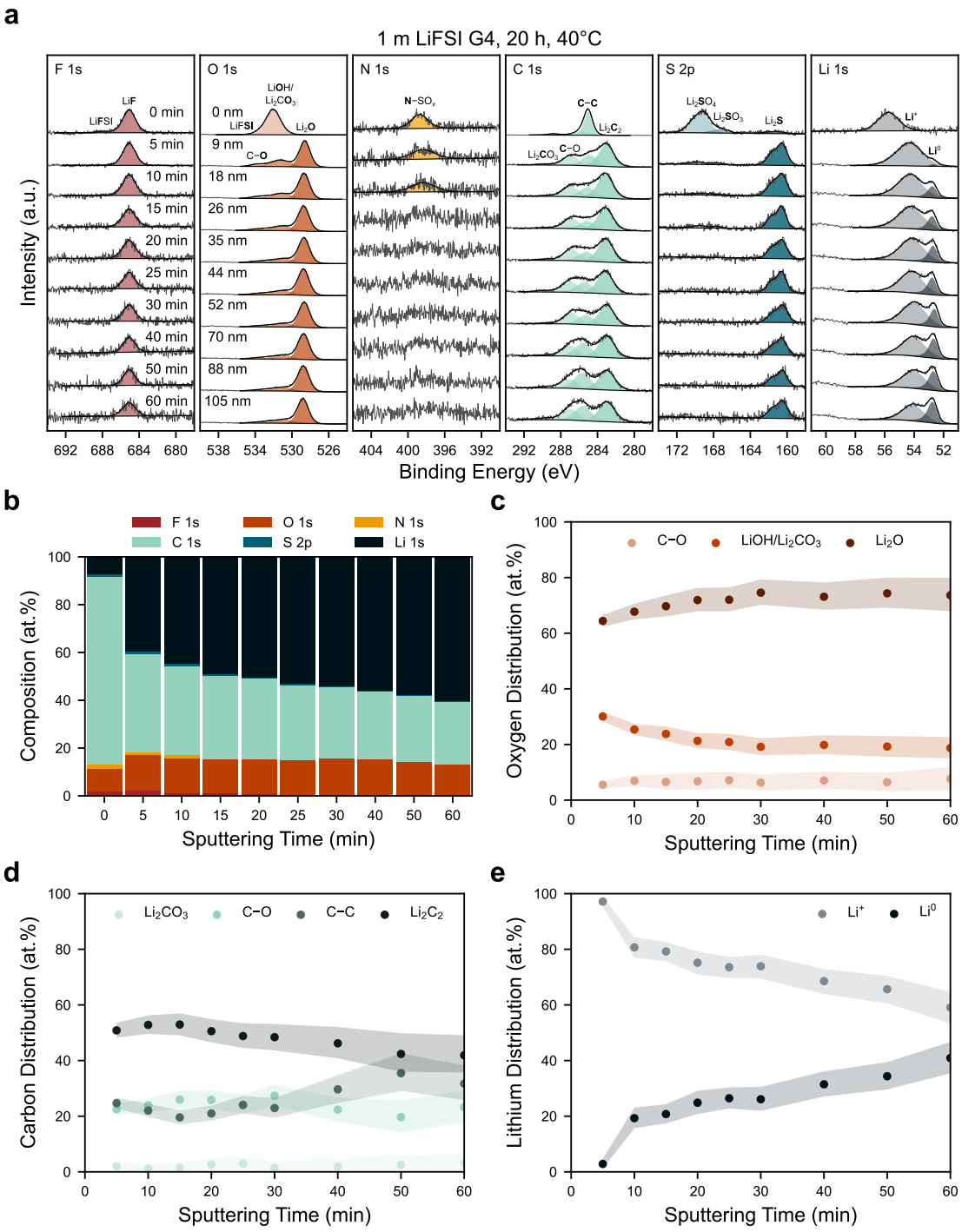


Figure 4.9: XPS depth profiles from an SEI sample formed in 1 m LiFSI G4 for 20 h at 40°C. (a) F 1s, O 1s, N 1s, C 1s, S 2p and Li 1s spectra. (b) Elemental composition. (c) Breakdown of oxygen-containing species. (d) Breakdown of carbon-containing species. (e) Breakdown of lithium-containing species. Error bars take into account the peak fitting uncertainty.

4.10c). The proportion of Li_2O does, however, increase with depth, so Li_2O again becomes the major SEI species after 15–20 min of sputtering. Aside from lithium, oxygen also

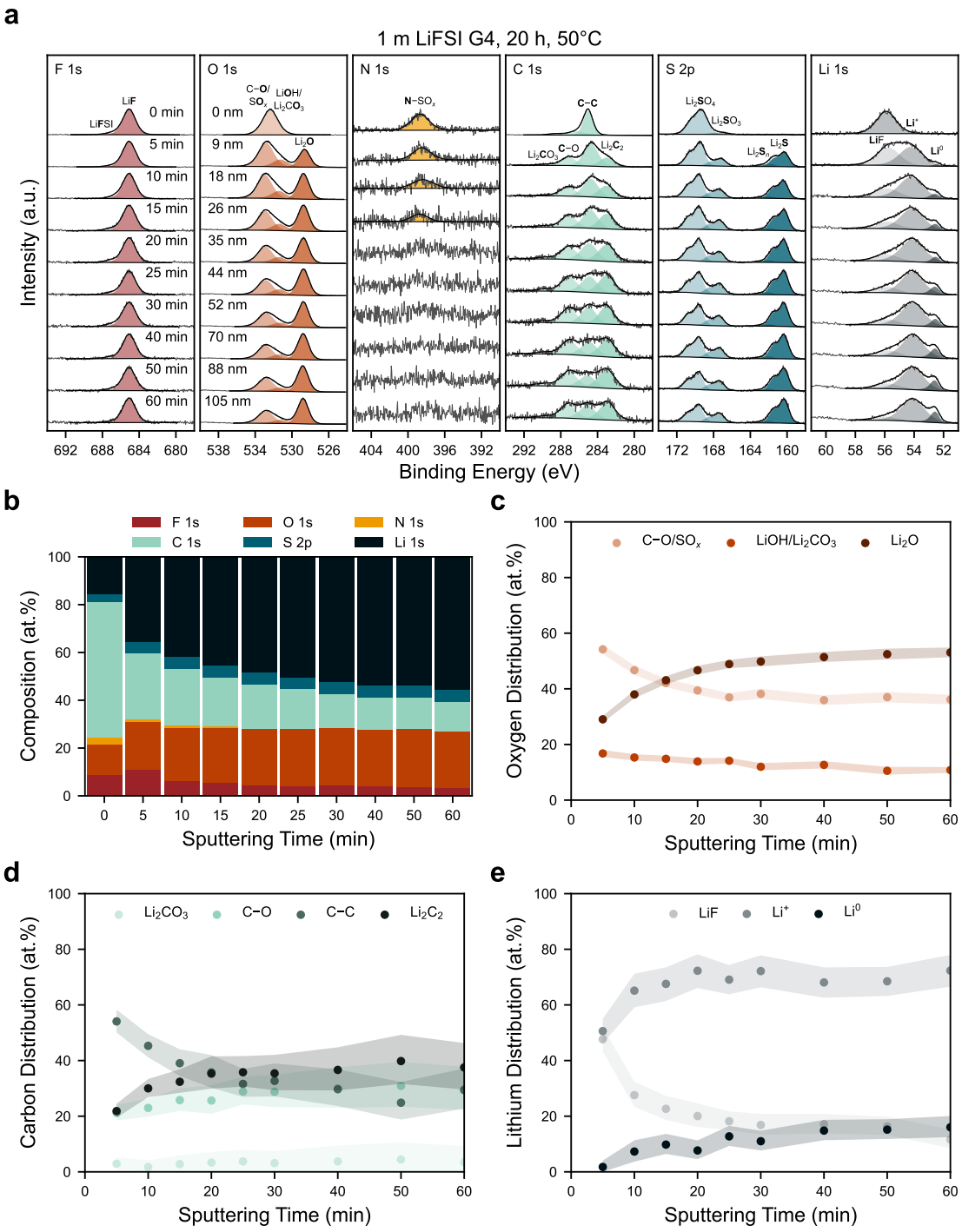


Figure 4.10: XPS depth profiles from an SEI sample formed in 1 m LiFSI G4 for 20 h at 50°C. (a) F 1s, O 1s, N 1s, C 1s, S 2p and Li 1s spectra. (b) Elemental composition. (c) Breakdown of oxygen-containing species. (d) Breakdown of carbon-containing species. (e) Breakdown of lithium-containing species. Error bars take into account the peak fitting uncertainty.

becomes the element with the highest concentration after 15 min of sputtering. Carbon makes up a significantly lower proportion of the SEI at 50°C, with its concentration

decreasing from 27 ± 2 to 12 ± 2 at.% as the sputtering time increases from 5 to 60 min, suggesting the SEI is less rich in organic components. Interestingly, Li_2C_2 is not the major carbon-containing species at low sputtering times (Figure 4.10d), in contrast to the samples prepared at lower temperature.

Applying the same criterion to estimate SEI thickness yields approximately 52 nm, so the SEI formed at higher temperature may be slightly thicker. However, it should be noted that the SEI thicknesses estimated here are rough approximations and only vary from each other by ±1 sputter step. Caution should therefore be exercised when considering any apparent trends between temperature and SEI thickness.

In conclusion, varying the temperature between 20–40°C has minimal impact on the SEI formed in 1 m LiFSI G4. However, when the temperature is raised further to 50°C the composition of the SEI changes dramatically. The SEI becomes enriched in salt decomposition species, including LiF, Li_2SO_4, Li_2SO_3 and Li_2S, and organic species are less prevalent. LiF is most concentrated close to the SEI-electrolyte interface, while Li_2S and Li_2O increase in concentration with increasing depth. This temperature dependence is also supported by EIS measurements performed by Olbrich et al.[220] In 1 m LiFSI G4 the total resistance, believed to be dominated by transport processes through the SEI,[101,102] increases over time in a similar way for temperatures between 20–40°C and the resistances follow an Arrhenius relationship, suggesting the composition, and hence mechanism of conduction, is likely to be similar. In contrast, at 50°C the total resistance initially increases with time, reaching a maximum after 2 h and then decreasing approximately linearly with time. The resistance is also lower than would be expected by extrapolation from the Arrhenius relationship established at lower temperature.[220] These observations can be explained by the change in SEI composition seen between 40 and 50°C using XPS here, and they suggest that the inorganic-rich SEI formed at higher temperature has a higher ionic conductivity.

To understand why the SEI composition displays this temperature dependence it is necessary to consider the species available for reduction at the lithium surface. SEI formation is generally believed to originate predominantly from reduction of the species present in the inner Helmholtz plane (IHP) of the double layer[63] as these will be closest

to the electrode surface. Since the lithium electrode potential is lower than the potential of zero charge,[89,236] the lithium surface will have a negative surface charge density, meaning the (IHP) will be composed of positively-charged Li-ions and the species in their primary solvation shell. Olbrich et al. explored the temperature-dependent transport and thermodynamic properties in 1 m LiFSI G4, as well as solvation.[39] At 20°C approximately 50% of the FSI^- is "free" while the rest is "bound", denoting FSI^- that is not associated with the Li^+ and FSI^- that is in the primary solvation shell of the Li^+, respectively. This leads to a solvation number (average number of ions/molecules surrounding the central ion) of approximately 0.5, while the solvation number of G4 is 1.3.[35] The IHP will therefore likely be primarily composed of G4 which will contribute to the organic-rich SEI observed at lower temperature. The proportion of bound FSI^- increases with increasing temperature, reaching 59% at 50°C,[39] so there will be more FSI^- available for reduction in the IHP. Combining this with the higher reactivity at higher temperature appears to result in the anion-rich SEI observed at 50°C here. This observation has severe implications for practical LMBs as the wetting process is usually performed at elevated temperatures to reduce wetting times in LIBs,[224] which could result in significant changes to the structure and properties of the SEI and the amount of salt consumed during SEI formation. These changes may not always be detrimental, however, as the SEI formed at higher temperature here may have an increased ionic conductivity, so understanding the impact that temperature has on SEI formation could enable the development of rational formation protocols to produce an SEI with favourable properties.

4.3.3 Role of Concentration

To investigate the impact that salt concentration has on SEI chemistry additional SEI samples were formed in 0.25 m and 2 m LiFSI G4 for 20 h at 30°C.

The results from the 0.25 m LiFSI G4 sample are presented in Figure 4.11, where it is clear that the spectra in Figure 4.11a are broadly similar to those measured from the 1 m sample at the same temperature. Carbon is again the majority element detected at low sputtering times (Figure 4.11b) and its proportion reduces gradually with increasing depth, still making up 20 ± 2 at.% after 60 min of sputtering. The distribution of carbon species

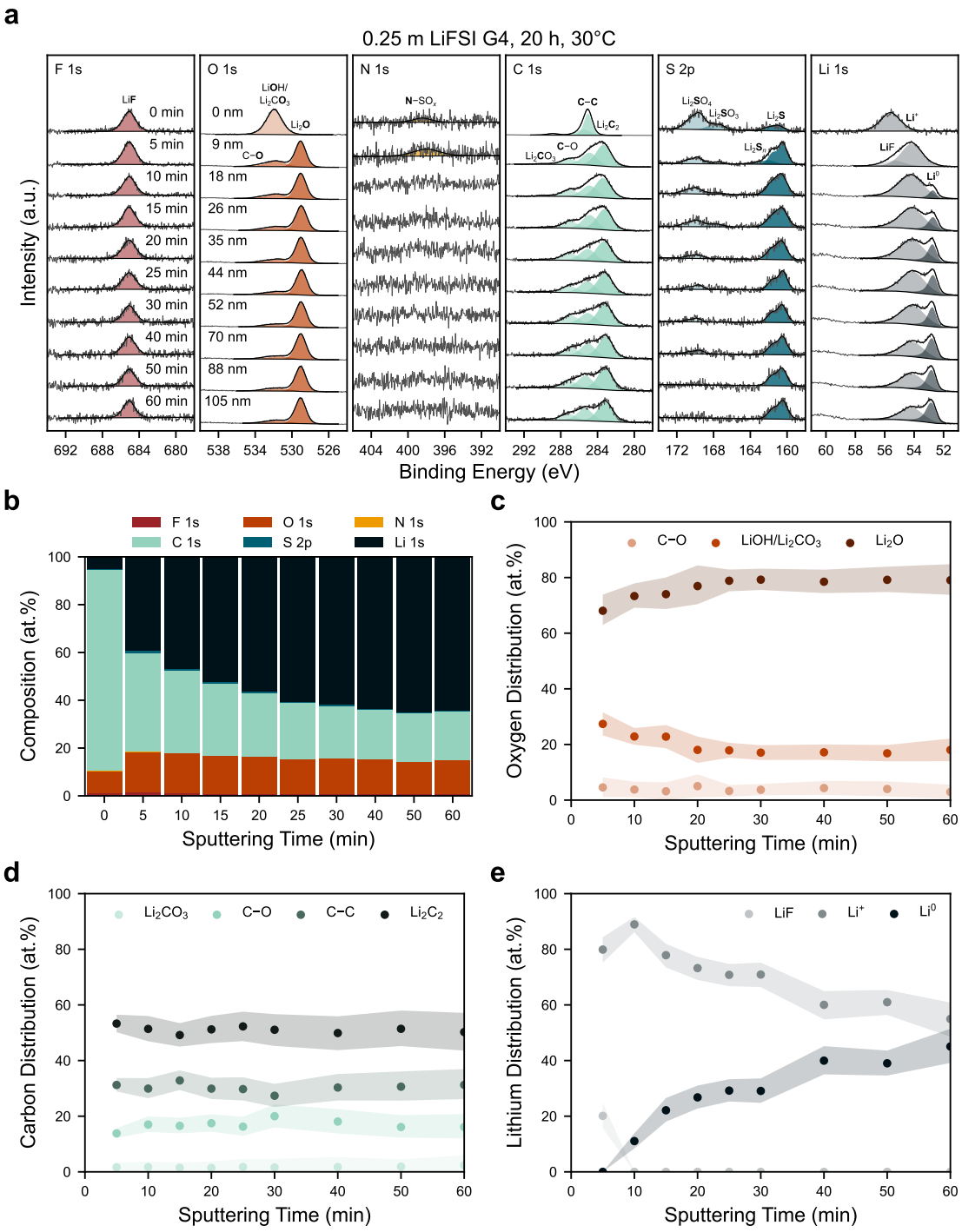


Figure 4.11: XPS depth profiles from an SEI sample formed in 0.25 m LiFSI G4 for 20 h at 30°C. (a) F 1s, O 1s, N 1s, C 1s, S 2p and Li 1s spectra. (b) Elemental composition. (c) Breakdown of oxygen-containing species. (d) Breakdown of carbon-containing species. (e) Breakdown of lithium-containing species. Error bars take into account the peak fitting uncertainty.

in Figure 4.11d also remains approximately constant with depth, with Li_2C_2 accounting for approximately 50 at.% of the total carbon at all depths. Aside from carbon and lithium,

oxygen is the next most prevalent element with concentrations of 16.7 ± 0.7 and 14.3 ± 0.9 at.% after 5 and 60 min of sputtering, respectively. Li_2O is the major oxygen-containing species, accounting for 68 ± 6 at.% after 5 min of sputtering and increasing to 79 ± 4 at.% after 25 min. Li_2O therefore becomes the main SEI species after 10 min of sputtering.

Unsurprisingly, given the lower concentration of salt in the electrolyte, salt decomposition species make up a small proportion of the SEI, with fluorine, nitrogen and sulphur contributing to 1.5 ± 0.3, 0.5 ± 0.5 and 1.0 ± 0.2 at.% after 5 min of sputtering, respectively. Their proportions then decrease with increasing depth. The approximate thickness, estimated using the same criterion as before, is 52 nm which is similar to the 1 m LiFSI G4 sample.

In contrast, fluorine, nitrogen and sulphur have much larger concentrations in the SEI formed in 2 m LiFSI G4, as summarised in Figure 4.12. After 5 min of sputtering, fluorine, nitrogen and sulphur account for 11.6 ± 0.6, 1.1 ± 0.4 and 3.2 ± 0.3 at.%, respectively, and their proportions decrease with increasing depth (Figure 4.12b). Interestingly, these concentrations are similar to those found in the 1 m LiFSI G4 sample formed at 50°C, so salt concentration is not the only variable that can be changed to tune the composition of an SEI. The higher nitrogen concentration enables several species to be identified in the N 1s region in Figure 4.12a, rather than just the single peak identified previously. At the surface the two peaks at 399.9 and 398.6 eV are attributed to LiFSI and $N{-}SO_x$, respectively. After sputtering LiFSI is removed and an additional peak emerges at 396.5 eV, consistent with fully-reduced Li_3N.[225] The proportion of Li_3N then increases with increasing depth. Similarly, the sulphur-containing species also become more reduced as the sputtering time increases. Close to the surface the main species is Li_2S, but Li_2SO_4 and Li_2SO_3 also make up a significant proportion. Additionally, there are also minor peaks consistent with Li_2S_n at 162.0 eV, and another species at 163.9 eV, which could be attributed to elemental sulphur.[232] With increasing depth Li_2S makes up an increasing proportion of the sulphur-containing species.

Similar to the 50°C sample formed in 1 m LiFSI G4, the increased concentration of Li_2SO_x close to the SEI-electrolyte interface results in a large corresponding peak in the O 1s spectra in Figure 4.12a, so Li_2O is not the major oxygen-containing species

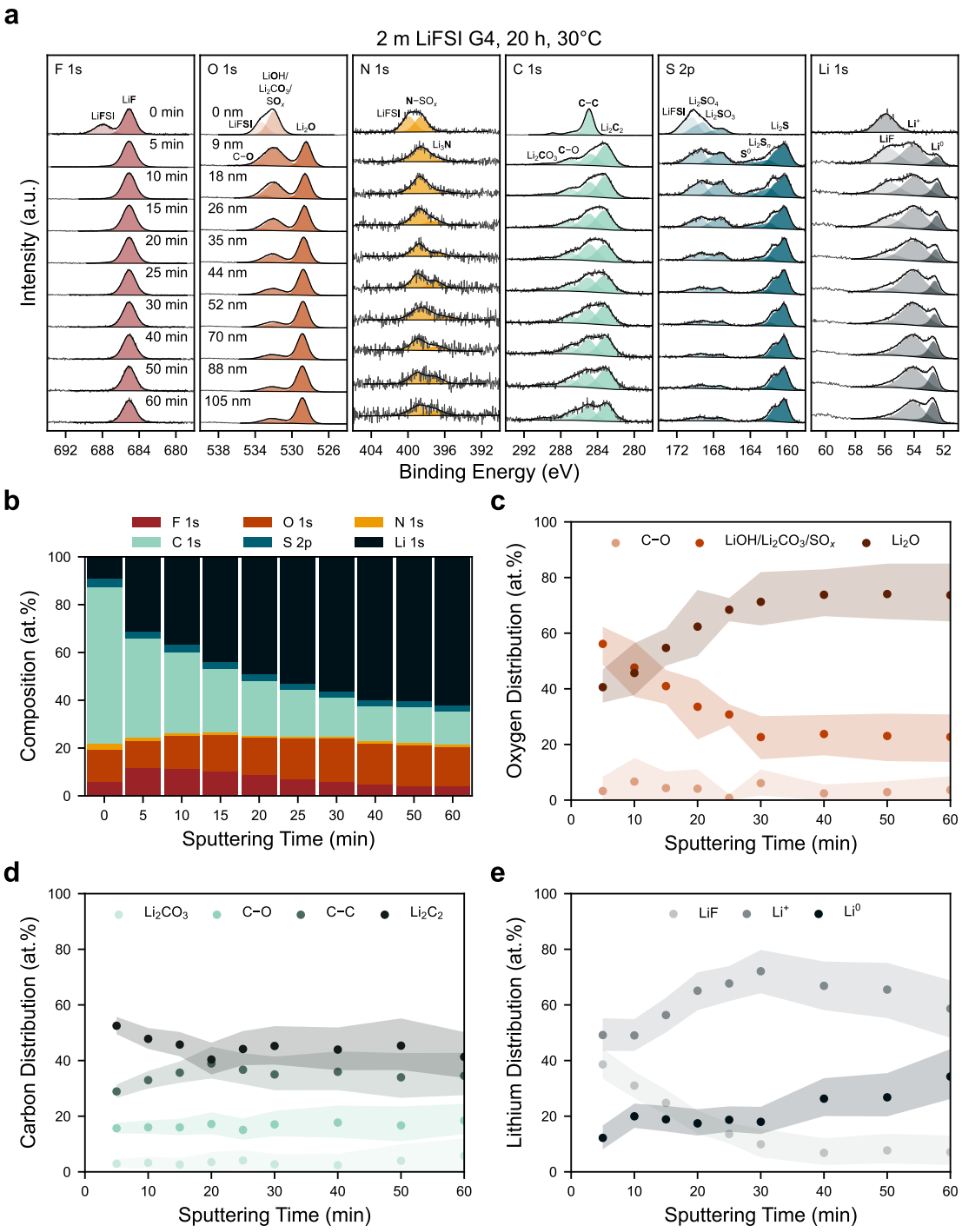


Figure 4.12: XPS depth profiles from an SEI sample formed in 2 m LiFSI G4 for 20 h at 30°C. (a) F 1s, O 1s, N 1s, C 1s, S 2p and Li 1s spectra. (b) Elemental composition. (c) Breakdown of oxygen-containing species. (d) Breakdown of carbon-containing species. (e) Breakdown of lithium-containing species. Error bars take into account the peak fitting uncertainty.

close to the surface (Figure 4.12c). The concentration of oxygen within the SEI, however, increases with depth, increasing from 11.6 ± 0.6 to 18 ± 1 at.% between 5 and 30 min of

sputtering, and Li_2O accounts for an increasing proportion of this oxygen with increasing depth, making up 72 ± 10 at.% of the total oxygen after 30 min of sputtering. The SEI is also rich in carbon close to the surface, with the carbon concentration decreasing from 41 ± 2 to 16 ± 2 at.% between 5 and 30 min of sputtering. As before, Li_2C_2 accounts for approximately 50 at.% of this total carbon, while the rest is found in organic species. Li_2O therefore becomes the majority SEI species after 15 min of sputtering, and the SEI composition does not reach a steady state until after 50 min of sputtering, corresponding to an approximate thickness of 88 nm, suggesting the SEI formed in 2 m LiFSI G4 may be thicker than that formed at lower concentration.

This observed increase in the concentration of inorganic, salt-derived SEI products at high concentration is expected given that the proportions of FSI^- forming contact-ion pairs (CIPs) and aggregates (AGGs) increase significantly as the salt concentration is increased.[35] There will therefore be more FSI^- in the primary solvation shell of the Li^+ which will be brought into the IHP of the electrode and will be able to participate in SEI formation reactions. It might be more surprising, however, that despite the four-fold reduction in salt concentration between 1 m and 0.25 m, the SEI appears to have a similar composition. This can again be rationalised by considering the solvation structures present at these two concentrations. As discussed above, at a concentration of 1 m the primary solvation shell will primarily contain G4, and the solvation number of G4 has been reported to remain approximately constant at 1.3 for concentrations below 1 m and the majority of the solvent molecules are not required to directly solvate each cation.[35] The SEI will therefore primarily be composed of solvent reduction products at both 0.25 and 1 m, as observed here.

Interestingly, although this analysis suggests the SEI to have a similar composition and thickness at both 0.25 and 1 m, they display different resistances, with the SEI formed in 0.25 m LiFSI G4 displaying a total resistance that is approximately twice as high as that measured in 1 m electrolyte.[220] A similar trend can be observed in the ionic conductivity, where 0.25 m LiFSI G4 displays an approximately 2.5 times lower ionic conductivity than at 1 m.[35] It has been reported that the SEI can swell in contact with electrolyte, particularly when the SEI contains a lower concentration of inorganic components,[76]

which suggests that the electrolyte can penetrate the organic components of the SEI. If the primary transport mechanism is then conduction through the liquid electrolyte phase within the SEI then this could result in the resistance trend observed by Olbrich et al.[220] Evidence for this mechanism has been reported by Ma et al. who observed salt fragments within the organic components of the SEI using time-of-flight secondary ion mass spectrometry (ToF-SIMS),[62] and it would support the theory that salt concentration gradients can form within the SEI[42] as this requires a sub-unity cation transference number. As the concentration increases from 1 to 2 m both the ionic conductivity[35] and the total SEI resistance decrease,[220] so the resistance at higher concentration is lower than would be expected if the transport mechanism is still conduction through the liquid phase, suggesting the conduction mechanism is different. The results presented here suggest that the SEI formed in 2 m LiFSI G4 is thicker than that formed at low concentration, implying that it must have a higher ionic conductivity. Similar to the SEI formed at 50°C in 1 m electrolyte, the SEI formed in 2 m electrolyte is rich in inorganic salt decomposition products, again suggesting that these are beneficial and increase SEI ionic conductivity.

4.3.4 Role of Time

To investigate how the chemistry of the SEI changes over time, one additional sample was formed in 1 m LiFSI G4 at 30°C for just 1 h, and the results are presented in Figure 4.13.

As evident by the large LiFSI peaks in Figure 4.13a, this sample contains the highest proportion of residual salt at the surface than any of the previous samples. The rinsing process was identical for all samples, so this could suggest the SEI is porous at low time and therefore traps the electrolyte.

Counter-intuitively, the SEI is more rich in salt decomposition products than the sample formed for 20 h, with fluorine, nitrogen and sulphur concentrations of 3.3 ± 0.4, 1.4 ± 0.5 and 1.5 ± 0.2 at.% after 5 min of sputtering, respectively (Figure 4.13b). However, these may be contributed to by decomposition of the residual LiFSI. The oxygen concentration is also lower than any of the other samples, making up approximately 12 at.% at all depths, and approximately 60 at.% of this can be assigned to Li_2O (Figure 4.13b).

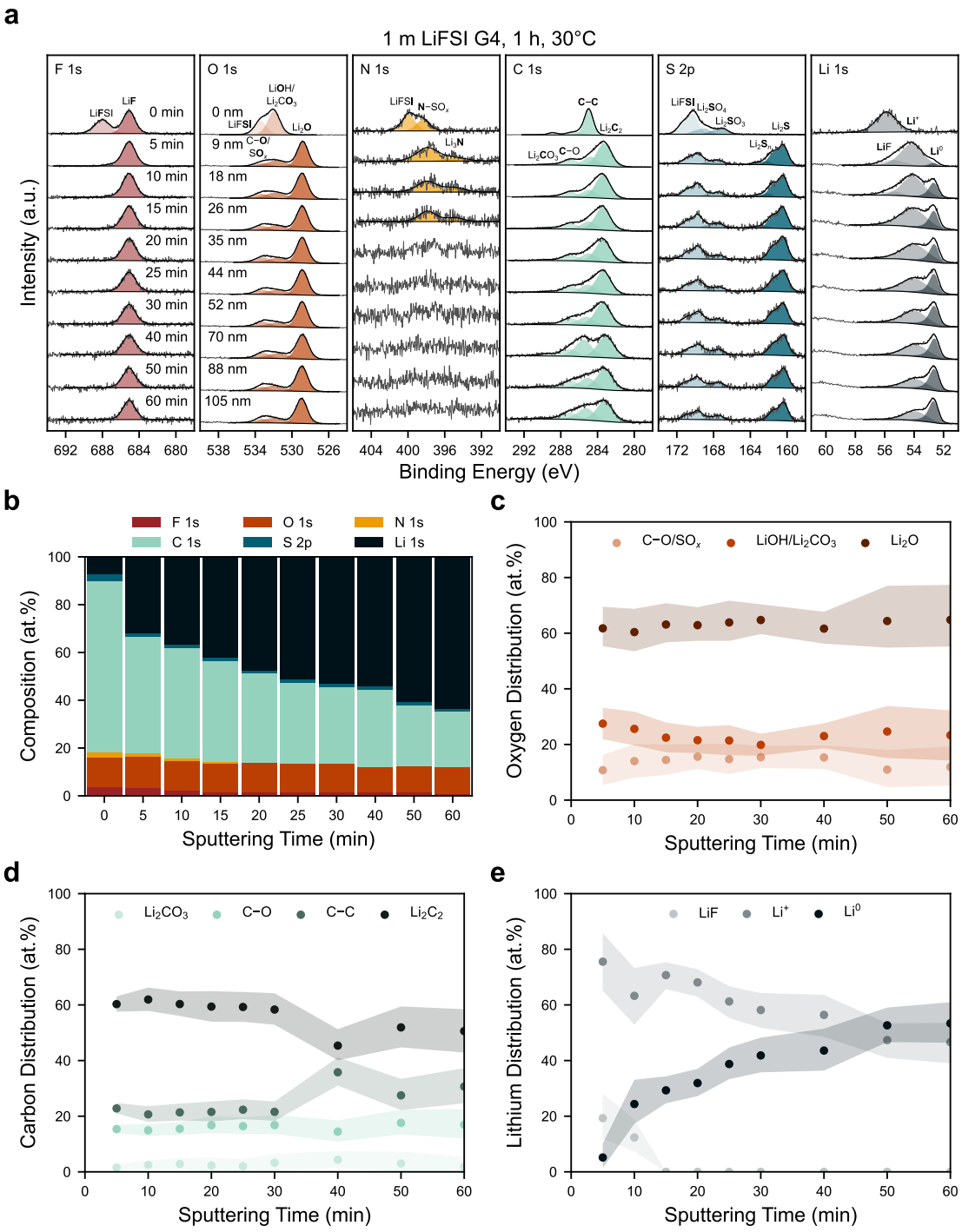


Figure 4.13: XPS depth profiles from an SEI sample formed in 1 m LiFSI G4 for 1 h at 30°C. (a) F 1s, O 1s, N 1s, C 1s, S 2p and Li 1s spectra. (b) Elemental composition. (c) Breakdown of oxygen-containing species. (d) Breakdown of carbon-containing species. (e) Breakdown of lithium-containing species. Error bars take into account the peak fitting uncertainty.

Carbon-containing compounds make up a significant percentage of the SEI, with carbon accounting for 49 ± 2 at.% after 5 min of sputtering, reducing to 32 ± 2 after 30

min. Li_2C_2 is the major detected carbon-containing compound in Figure 4.13d, and the main SEI species detected throughout the whole depth. Here the detected composition reaches a steady state after 30 min of sputtering, corresponding to an approximate thickness of 52 nm, which is similar to the sample formed for 20 h.

Previously it has been assumed that the SEI increases in thickness over time, leading to an increase in SEI resistance.[102] A similar increase in resistance over time has been observed by Olbrich et al.,[220] but the results presented here suggest that the SEI resistance may increase due to a change in SEI composition rather than thickness. At low time the SEI is carbon-rich (and potentially porous), while the proportion of inorganic oxygen-containing species increases as the time increases from 1 to 20 h. These observations are consistent with the SEI densification mechanism proposed by Lim et al. where at low time the SEI is believed to be porous, allowing electrolyte impregnation that provides a fast conduction pathway. Over time the SEI densifies, filling in the porosity with inorganic components (primarily Li_2O in this case) that reduce the overall SEI ionic conductivity,[61] leading to a higher measured resistance.

4.3.5 Role of Solvent

Finally, to explore the effect that the solvent has on chemical SEI formation on lithium an SEI sample was additionally formed in 1 m LiFSI 1,2-dimethoxyethane (DME) for 20 h at 30°C, which is the lithium-ion electrolyte system characterised in Chapter 3. This sample was rinsed with DME, rather than G4. The XPS results are presented in Figure 4.14.

The peaks, and therefore species, evident in Figure 4.14a are broadly similar to those observed with the G4 solvent and there is no evidence of any additional species in the SEI here. The composition of the SEI, however, is significantly different (Figure 4.14b). At the surface carbon has a concentration of just 24 ± 2 at.%, and its concentration does not exceed 10 at.% after sputtering. This low carbon concentration makes it more challenging to reliably separate the peaks so the carbon distribution in Figure 4.14d has a large uncertainty, but the same carbon-containing species are identified with roughly the same proportions as in the G4 electrolyte.

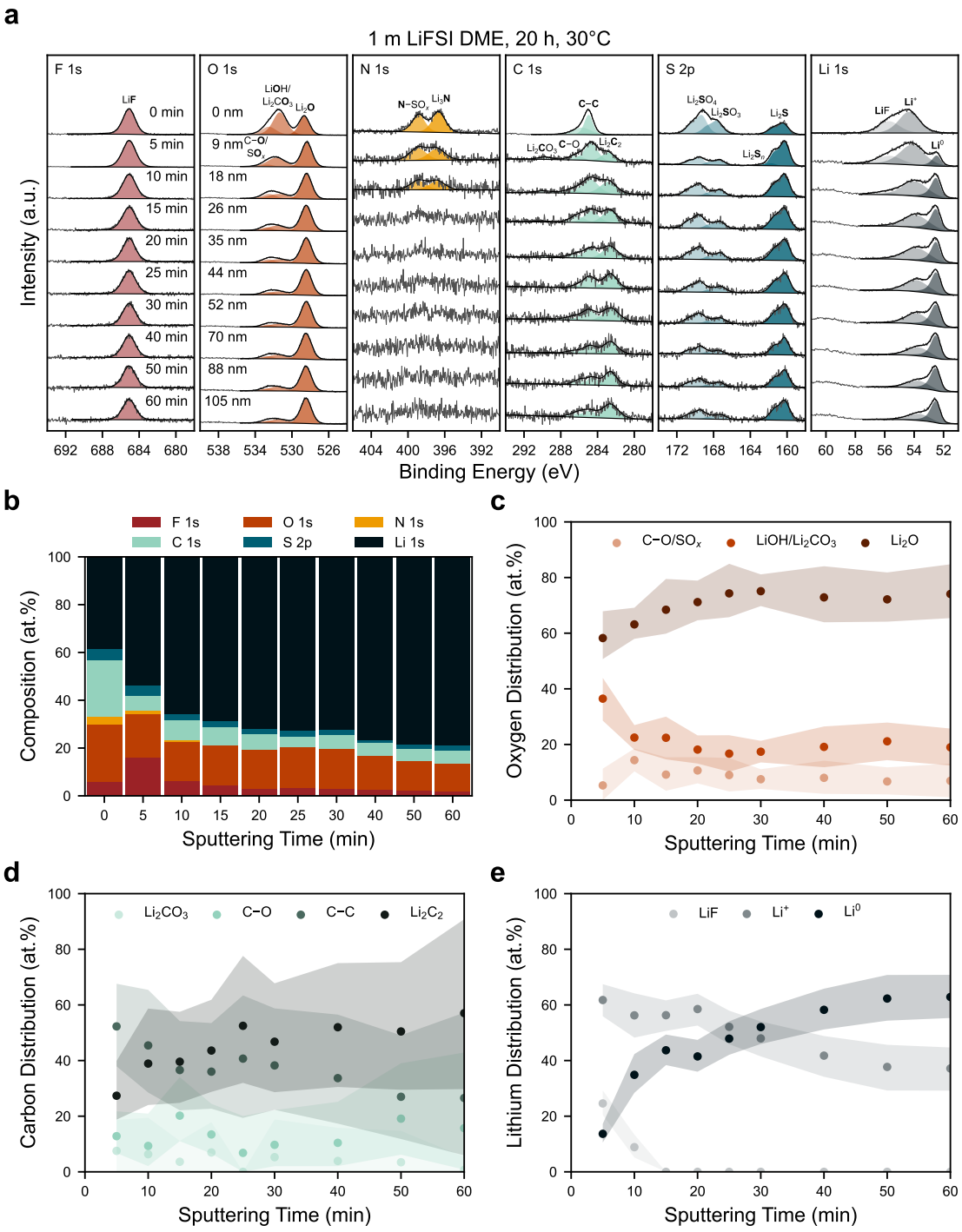


Figure 4.14: XPS depth profiles from an SEI sample formed in 1 m LiFSI DME for 20 h at 30°C. (a) F 1s, O 1s, N 1s, C 1s, S 2p and Li 1s spectra. (b) Elemental composition. (c) Breakdown of oxygen-containing species. (d) Breakdown of carbon-containing species. (e) Breakdown of lithium-containing species. Error bars take into account the peak fitting uncertainty.

The SEI formed in DME is richer in inorganic, salt-derived products, with fluorine, nitrogen and sulphur having concentrations of 15.9 ± 0.9, 1.3 ± 0.4 and 4.2 ± 0.4 at.%

after 5 min of sputtering. With increasing depth their concentrations decrease and the sulphur-containing species become more reduced, so Li_2S dominates over Li_2SO_4 and Li_2SO_3. Aside from lithium, oxygen is the most prevalent element at all depths with a concentration of 18.5 ± 0.9 at.% after 5 min of sputtering, reducing to approximately 16 at.% after 10 min of sputtering and remaining stable until after 40 min. As evident in Figure 4.14c, Li_2O is again the major oxygen-containing species and is the main SEI species at all depths. The composition reaches a steady state after 25 min of sputtering, giving the same thickness estimate of 44 nm as for the G4 sample.

These observations can again be rationalised by considering the differences in solvation between DME and G4. Simulations reveal that DME has an average solvation number of approximately 2.75 at 1 m,[237] which, given the much shorter chain of DME, results in fewer carbon atoms entering the primary solvation shell of the cation compared to G4. This could also suggest that DME reduction products are more soluble than those formed from G4. Additionally, Raman measurements by Zhao et al. suggest that a greater proportion of the FSI^- forms CIPs and AGGs in DME compared to G4,[238] so more FSI^- will be available in the IHP for reduction.

4.4 Potassium Metal Electrodes

Potassium-ion batteries (KIBs) are likely to utilise graphite as the negative electrode material,[22] and, although there is research interest into potassium metal batteries,[189] the high reactivity and low melting point of potassium metal make it far less attractive for commercial applications. Nevertheless, potassium metal can serve as model system to enable an understanding of the differences in SEI formation between lithium and potassium systems.

Potassium metal has the advantage that, like lithium metal, it will lead to spontaneous, chemical SEI formation immediately upon electrolyte addition. In contrast, graphite electrodes would first need to be potassiated to bring the potential of the electrode below the potential of electrolyte reduction, requiring a potassium source. This potassiation is frequently performed electrochemically using potassium metal as a counter/reference electrode, but as Madec et al. and Allgayer et al. have reported the presence of

potassium metal in a cell can alter the surface chemistry of the working electrode through cross-talk.[149,150] Reliable SEI studies on graphite KIB electrodes can therefore only be performed once suitable counter and reference electrodes have been developed, which will be discussed further in Chapter 5.

An SEI sample was prepared in the same way as for the lithium samples in Chapter 4.3, and the potassium metal was prepared using the process described in Chapter 3. The electrolyte used was 1 m KFSI DME, the same potassium-ion electrolyte system characterised in Chapter 3, and it was formed for 20 h at 30°C before rinsing with DME. The XPS results from this sample are presented in Figure 4.15.

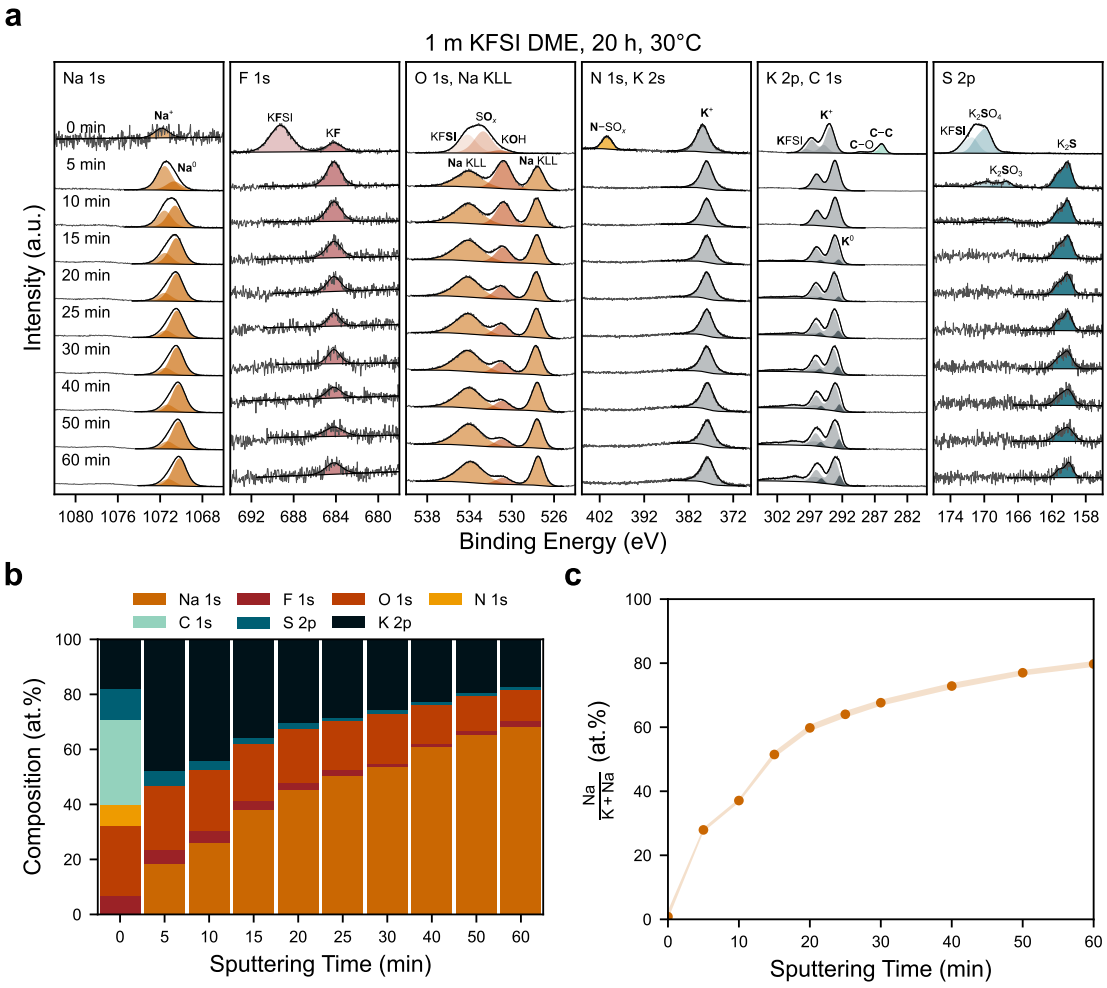


Figure 4.15: XPS depth profiles from an SEI sample formed in 1 m KFSI DME for 20 h at 30°C. (a) Na 1s, F 1s, O 1s, N 1s and K 2s, K 2p and C 1s, and S 2p spectra. (b) Elemental composition. (c) Percentage of sodium out of the total alkali metal atoms. Error bars take into account the peak fitting uncertainty.

At the surface the F 1s spectrum in Figure 4.15a displays two peaks consistent

with KFSI and KF at higher and lower binding energy, respectively. Like the lithium samples, KF was used for charge referencing and its binding energy was set to 684.2 eV.[186] Corresponding KFSI peaks are identified in the O 1s, K 2p and S 2p regions, and K_2SO_4, N$-SO_x$, and organic species are also observed.

Interestingly, a minor peak consistent with the presence of Na^+ is also identified at the surface in Figure 4.15a, but Na has a negligible concentration at the surface (Figure 4.15b). However, the composition changes drastically after sputtering, with the N 1s and C 1s peaks disappearing completely after just 5 min of sputtering. In the F 1s spectra only KF remains, and fluorine has a concentration of 5 ± 2 at.% after 5 min of sputtering, reducing to 3 ± 2 at.% after 15 min. The sulphur-containing species become more reduced after sputtering, with K_2S becoming the main identified species. Similar to the fluorine, sulphur accounts for 6 ± 1 at.% after 5 min of sputtering, reducing to 2 ± 0.6 at.% after 15 min.

The concentration of sodium increases significantly during sputtering, increasing from 18 ± 1 at.% after 5 min of sputtering to 38 ± 3 at.% after 15 min. As was seen in Chapter 3, sodium rapidly becomes the main element detected in this sample and its proportion increases with increasing depth, even becoming more concentrated than potassium after 15 min of sputtering (Figure 4.15c). The Na 1s spectra in Figure 4.15a contain two separable peaks at 1071.6 and 1070.7 eV, and the relative intensity of the 1070.7 eV peak increases with increasing sputtering time. No other peaks display a corresponding increase, so this peak is attributed to metallic sodium and the 1071.6 eV peak is attributed to Na^+. Similarly, the K 2p spectra display two sets of doublet peaks at 293.2 and 292.4 eV. The relative proportion of the 292.4 eV peak increases with increasing depth and its emergence coincides with the appearance of plasmon loss features, suggesting it can be attributed to potassium metal.[239]

Unfortunately, the high sodium concentration results in intense Na KLL Auger electron peaks that overlap with the O 1s region in Figure 4.15a, making accurate assignment of the O 1s peaks challenging. Nevertheless, the peak identified at 530.8 eV may correspond to NaOH/KOH, as observed in the NPL on potassium metal in Chapter 3. However, Na_2O_2 and K_2O_2 would also likely appear at a similar binding energy to this,[240,241] so it is not possible to confirm the origin of this peak using XPS alone.

Overall, the results presented in Figure 4.15 demonstrate that the concentration of electrolyte decomposition species is low except for at the surface, suggesting the SEI is thin. This is a surprising result considering the high reactivity or potassium metal, but is consistent with previous reports on the SEI that forms in KIBs using ether-based electrolytes.[31] Like the 1 m LiFSI DME electrolyte, in 1 m KFSI DME the solvation number of DME is 2.7 and the majority of the FSI^- is not contained within CIPs or AGGs,[204] so an organic, solvent-derived SEI might be expected. The lack of detectable carbon-containing species here after sputtering could therefore support theories that potassium-based organic SEI compounds are more soluble that their lithium-based counterparts.[242]

Alternatively, the NPL formed in this case could have been sufficiently passivating to prevent the electrolyte from direct exposure to metallic potassium, reducing the rate at which reduction could occur. One final SEI sample was therefore produced by plating potassium metal, which will expose fresh potassium metal to the electrolyte. However, it should be noted that a portion of the applied current could be consumed by parasitic electrolyte decomposition reactions, so SEI formation is likely to be a combination of chemical and electrochemical.

This sample was prepared by Y. Xu using the Hittorf cell described in Chapter 3. Potassium was plated at 600 µA cm^{-2} to a capacity of approximately 5 mAh cm^{-2} in 1 m KFSI DME at 20°C and the plating electrode was then removed from the cell and rinsed with DME for analysis. The suspension of potassium filaments produced at the same time (Figure 3.10) was also extracted for future complementary characterisation. The XPS results gathered from this sample are presented in Figure 4.16.

In the surface spectra in Figure 4.16a the Na 1s, O 1s, N 1s, K 2p and S 2p regions are similar to the previous sample, however, the major fluorine-containing species appears at a binding energy of 685.5 eV, which is not consistent with KF. During depth profiling the proportion of this peak decreases while proportion of the KF peak at 684.2 eV increases. Fluorine makes up a large proportion of all detected elements near the surface, with a concentration of 38±1 at.% after 5 min of sputtering, decreasing to 33±1 at.% after 20 min (Figure 4.16b). This fluorine-containing species at 685.5 eV accounts for approximately 60 at.% of the total fluorine over this same range (Figure 4.16c), so it is a major SEI species.

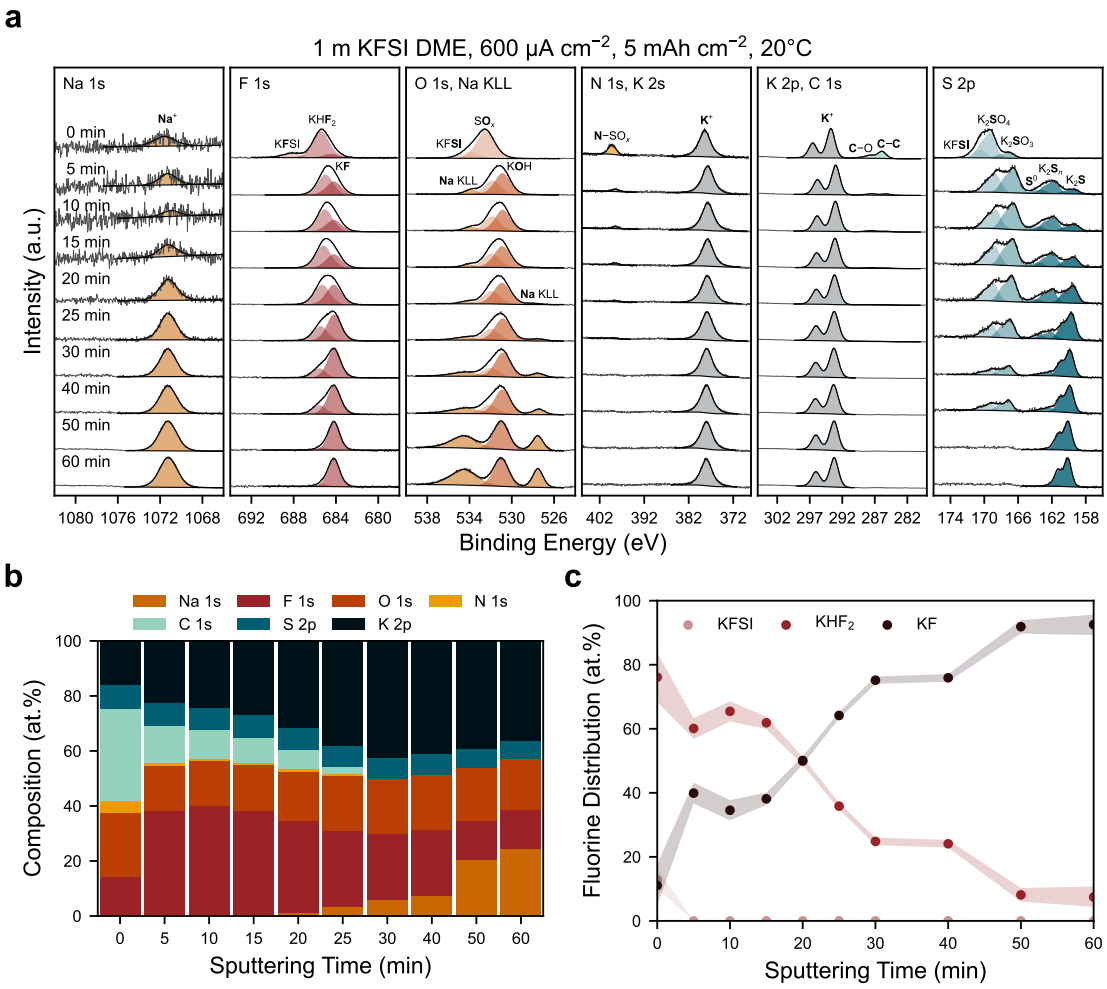


Figure 4.16: XPS depth profiles from an SEI sample formed in 1 m KFSI DME by plating at 600 µA cm^{-2} to a capacity of 5 mAh cm^{-2} at 20°C. (a) Na 1s, F 1s, O 1s, N 1s and K 2s, K 2p and C 1s, and S 2p spectra. (b) Elemental composition. (c) Breakdown of fluorine-containing species. Error bars take into account the peak fitting uncertainty.

A similar XPS peak has been identified in several SEI studies in potassium-based battery systems, and it has been attributed to KFSI,[243] $-SO_xF$ species,[24] or simply to KF.[244] However, here the detected potassium and sulphur concentrations are too low to match any of these assignments. Ells et al. additionally observed this species in a KFSI-based electrolyte and found a corresponding ^{19}F solid-state nuclear magnetic resonance (SS-NMR) peak at -144 ppm, which they suggested could be related to a partially potassiated fluoride, K_xF.[245] Interestingly, the bifluoride anion, HF_2^-, appears at a similar chemical shift of -142 ppm,[246] so KHF_2 could be a likely candidate. A K:F ratio of 1:2 would also be consistent with the compositions presented in Figure 4.16b.

To confirm whether KHF_2 would appear at this binding energy, reference F 1s spectra

were gathered from commercially available KHF_2, as well as KFSI and KF. These are presented in Figure 4.17 where it is clear that KHF_2 in Figure 4.17b does result in a F 1s peak with binding energy consistent with that observed in Figure 4.16a, so the peak at 685.5 eV is attributed to KHF_2 here. The origin of this species, however, requires further study. KHF_2 is traditionally prepared by treating KOH or K_2CO_3 with HF, but the water content of the prepared electrolytes is always measured to be below 5 ppm, so the electrolyte should contain negligible HF.

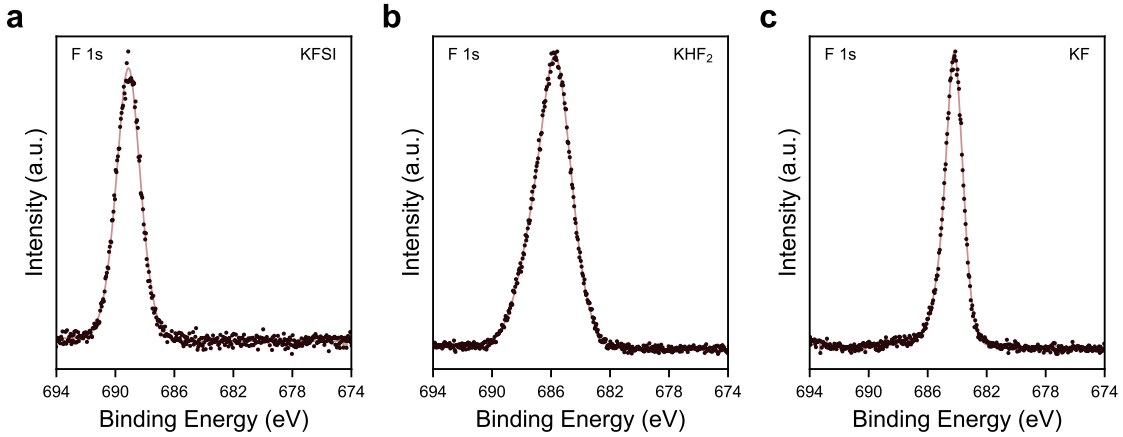


Figure 4.17: XPS on reference samples. (a) F 1s spectrum of KFSI. (b) F 1s spectrum of KHF_2. (c) F 1s spectrum of KF.

In addition to fluorine, the SEI is also rich in oxygen and sulphur, which have concentrations of 16.1 ± 0.8 and 8.3 ± 0.6 at.% after 5 min of sputtering, respectively. Close to the SEI-electrolyte interface the main sulphur-containing species are K_2SO_4 and K_2SO_3, and, similar to the lithium systems, S^0, K_2S_n and K_2S are detected after 5 min of sputtering. With increasing depth the proportion of K_2S increases and it becomes the major sulphur-containing species after 25 min of sputtering. In the O 1s spectra there is a corresponding peak consistent with SO_x-containing species and a peak at 530.9 eV, attributed again to KOH. With increasing depth the proportion of KOH increases and Na KLL Auger peaks again appear. These coincide with the increase in the sodium concentration after 20 min of sputtering (Figure 4.16b). The KFSI salt does not contain measurable sodium impurities so only potassium metal should be electrodeposited, hence the lower concentration of sodium observed here compared to

the previous sample. In this case the SEI also appears to be thicker, and no metallic sodium or potassium peaks are observed.

Aside from the KHF_2, another major difference between the lithium and potassium systems is the oxide species detected. In all lithium samples Li_2O makes up a large proportion of the SEI, while no equivalent species is identified in the potassium systems. In fact, a thorough search revealed few convincing reports on the presence K_2O in the SEI in literature. This can be explained by considering the relative size of the alkali metal cations. Li^+ has a small ionic radius and can form a stable structure with the larger O^{2-} anions with a large, negative lattice energy. In contrast, the larger K^+ cations experience steric repulsion in K_2O. This steric effect is reduced in K_2O_2 and KO_2 due to the larger size of the peroxide, O_2^{2-}, and superoxide, O_2^-, anions. The lattice energy also becomes less negative with increasing cation size, so Li_2O is most stable for lithium, Na_2O_2 becomes most stable for sodium, while the superoxides are most stable for potassium, rubidium and caesium.[247,248]

Similar steric hindrance effects are responsible for the instability of K_3N, so this species is not identified in Figure 4.16a. The ability of K^+ to stabilise larger anions than Li^+ may therefore be the reason for the higher stability of KHF_2[249] and could explain why $LiHF_2$ is not observed in the lithium samples. Additionally, this effect could explain the larger proportion of potassium polysulphide species observed close to the SEI-liquid interface.

4.5 Conclusion

In summary, in this chapter X-ray photoelectron spectroscopy depth profiling was used to examine the impact that temperature, salt concentration, time and solvent have on chemical SEI formation on lithium metal in a model electrolyte system (LiFSI in G4). It was revealed that at 1 m varying the temperature between 20–40°C has minimal impact on the SEI and it is rich in Li_2C_2 and organic species, with an increasing proportion of Li_2O towards the SEI-lithium interface and an approximate thickness on the order of 40 nm. Further increasing the temperature results in a more anion-derived SEI, which is rationalised by considering the solvation structure of the electrolyte, and comparison with impedance measurements suggest this type of SEI has a higher ionic conductivity.

Reducing the concentration to 0.25 m at 30°C results in the same organic-rich SEI as at 1 m, and impedance trends suggest that lithium ions are transported within an electrolyte phase in the SEI, implying it is porous. Increasing the concentration to 2 m promotes salt reduction, leading to an ionically conductive, anion-derived SEI, and similar behaviour is observed when a DME solvent is used at 1 m. Additionally, analysing the changes in SEI chemistry over time suggest the impedance of an SEI may grow over time as a result of densification reducing its ionic conductivity rather than simply an increase in thickness.

Finally, comparing the SEI formed on lithium and potassium metal revealed that organic potassium-containing compounds may be more soluble than their lithium-containing counterparts, and while Li_2O is a major SEI species in all examined lithium systems, no corresponding K_2O species is detected. Instead a previously unidentified fluorine-containing species is found to be a major SEI species on a plated potassium sample, which could be assigned to KHF_2. The differences between the observed inorganic SEI species in lithium- and potassium-based battery systems are attributed to steric effects caused by the differences in cation size, providing insights into the factors determining SEI stability.

4.6 Experimental Methods

Unless otherwise stated, all sample preparation was performed in argon-filled MBraun gloveboxes with O_2 and H_2O concentrations below 0.1 ppm and all equipment was cleaned and dried overnight under vacuum at 70°C before being brought into the glovebox.

Electrolyte Preparation

Prior to preparing electrolytes, lithium bis(fluorosulfonyl)imide (LiFSI, battery grade, Fluorochem) was dried under vacuum at 70°C for at least 48 h, potassium bis(fluorosulfonyl)imide (KFSI, 99.9%, Solvionic) was dried under vacuum at 100°C for at least 48 h, and tetraethylene glycol dimethyl ether (G4, 99%+, Sigma-Aldrich) and 1,2-dimethoxyethane (DME, 99.5% anhydrous, Sigma-Aldrich) were dried over 3 Å molecular sieves.

Electrolytes were prepared gravimetrically by stirring together the desired masses of salt and solvent. The water content of the electrolytes was measured by Karl Fischer titration and recorded to be below 5 ppm.

Electrode Preparation

Lithium metal electrodes were prepared for use by first brushing the lithium (99.9% trace metal basis, Sigma-Aldrich) surface with a plastic brush, then calendering to a thickness of 300 µm in a polypropylene bag, before finally punching into discs 8 mm diameter discs using a wad punch. The electrodes were pressed onto a stainless steel spacer (304SS, MTI).

Before use, potassium metal (chunks, 98%, Sigma-Aldrich) was processed according to the method developed in Chapter 3. The potassium was melted in a beaker on a hot plate, a spatula was used to remove the dross, and the molten potassium was quenched into clean mineral oil before being transferred into hexane (95% anhydrous, Sigma-Aldrich) that had been dried over 3 Å molecular sieves for storage.

The clean potassium chunks were rolled by hand between two sheets of weighing paper (grade 2122, Whatman), using additional hexane to prevent sticking, to a thickness of approximately 500 µm. The potassium foil was then punched into 8 mm diameter electrodes using a wad punch and pressed onto a stainless steel spacer (304SS, MTI).

Immediately before electrolyte addition the surface of the potassium electrodes was polished with a plastic blade, producing a mirror-like finish.

Li_2O Film Deposition

The Li_2O film was deposited onto glass substrates by radio-frequency (RF) magnetron sputtering in an MBraun MB-Evap physical vapor deposition system. A target composed of Li_2O powder (99.5%, Thermo Fisher) was used with a sputtering power of 50 W. The sputtering chamber was pumped down to a pressure of 10^{-6} mbar prior to sputtering. Argon gas was used as the sputtering gas and was injected at a flow rate of 20 SCCM, resulting in a working pressure of 3×10^{-3} mbar. Prior to deposition the target was cleaned of impurities by pre-sputtering, with the substrate shutter closed, for 30 min at the same power. During deposition the substrate was rotated at a rate of 33 rpm.

Atomic force microscopy (AFM) was performed with a Bruker Dimension Icon system. To determine the thickness of the Li_2O film it was scratched with the tip of stainless steel tweezers to produce a sharp step. This was then imaged in contact mode using an SNL-B probe (Bruker) at a scan rate of 0.5 Hz (256 px × 256 px). Gwyddion software was used for data analysis.[216]

X-ray Photoelectron Spectroscopy

Unless otherwise stated, SEI samples for X-ray photoelectron spectroscopy (XPS) were prepared by submerging either lithium or potassium metal electrode in 1 mL of electrolyte. These were then kept in a glovebox antechamber heated to the stated temperature (30–50°C), except the sample formed at 20°C was placed in a Binder Oven. The samples were kept in electrolyte for the stated time (1–20 h) before they were removed from the electrolyte and rinsed three times each with 200 µL of pure solvent to remove residual salt. The excess solvent was then removed with tissue, taking care not to touch the electrode surface. Samples were then immediately transferred to the XPS intro chamber using a vacuum transfer vessel (ULVAC PHI) to prevent air exposure.

XPS was performed with an ULVAC PHI Versaprobe III XPS system generating monochromatic $Al_{K\alpha}$ X-rays (1486.6 eV, 15 kV anode voltage, 25 W beam power) under ultrahigh vacuum (UHV) conditions (10^{-7}–10^{-6} Pa). A 500 µm × 500 µm area of each

sample was analysed. Survey spectra were gathered at a pass energy of 224 eV, and 55 eV was used for core-level spectra. In-built electron and low-energy Ar^+ sources were utilised for neutralisation. Depth profiling was achieved with consecutive XPS analysis and Ar^+ sputtering (1–4 kV, 3 mm × 3 mm). Acquired spectra were fitted with Gaussian-Lorentzian product lineshapes (with an asymmetric lineshape necessary to fit the Li^0 Li 1s peak) using CasaXPS software.[217] Spectra were either charge referenced to the adventitious carbon peak at 284.8 eV, the LiF peak at 685.1 eV, or the KF F 1s peak at 684.2 eV,[186] as appropriate. Atomic percentages were estimated using relative sensitivity factors determined from LiFSI (battery grade, Fluorochem), KF (≥99.9%, Sigma-Aldrich), Li_2O (99.5%, Thermo Fisher), LiOH (98%, Sigma-Aldrich) and sodium metal (99.9%, Sigma-Aldrich).

Reference F 1s XPS spectra were gathered from KFSI (99.9%, Solvionic), KHF_2 (99%, Sigma-Aldrich) and KF (≥99.9%, Sigma-Aldrich). No Ar^+ sputtering was performed prior to analysis of these reference compounds.

5

Potassium Alloy Reference Electrodes for Potassium-Ion Batteries

Abstract

Potassium-ion batteries (KIBs) are a promising alternative to conventional lithium-ion batteries, but accurate three-electrode characterisation is hindered by the lack of a suitable reference electrode. Potassium metal is frequently used as a reference electrode out of necessity, but its high reactivity and unstable potential limit its reliability. In this chapter the K-In and K-Bi alloy systems are investigated, two-phase In-In_4K and Bi-Bi_2K alloys are synthesised, and Bi-Bi_2K is identified as a promising material owing to its stable potential of 1.07 V vs. K^+/K. The use of Bi-Bi_2K as a reference electrode is demonstrated by cycling graphite in three-electrode cells and it is shown that it results in significantly less electrolyte reduction than potassium metal, facilitating the accurate electrochemical characterisation necessary to accelerate KIB development.

The results presented in this chapter have contributed to the following publication:
Jagger, B., Aspinall, J., Kotakadi, S., Cattermull, J., Dhir, S. & Pasta, M. Potassium Alloy Reference Electrodes for Potassium-Ion Batteries: The K-In and K-Bi Systems. *ACS Mater. Lett.* **6**, 4498–4506 (2024).

Contents

5.1 Introduction 118
5.2 The K-In System 119
5.3 The K-Bi System 122
5.3.1 Synthesis and Characterisation 125
5.3.2 Potential Stability 129
5.3.3 Electrochemical Stability 132
5.4 Conclusion 137
5.5 Experimental Methods 138

5.1 Introduction

Potassium-ion batteries (KIBs) are still in the early stages of development, requiring further electrolyte and electrode optimisation before they can be commercialised.[30,243] Accurate electrochemical characterisation will be vital to guide such optimisation, necessitating the use of three-electrode cells to accurately assign electrochemical behaviour to each electrode. A key requirement for this is a suitable reference electrode, which should have a stable, well-defined potential, should be chemically inert, and should operate within the electrochemical stability window of KIB electrolytes.

There are few available reports on the production of reference electrodes for KIBs,[22,250,251] so many studies use potassium metal, which does not satisfy the requirements of a reference electrode. The potential of potassium metal suffers from irreproducibility and it can drift over time,[182] which may be caused by the presence of high concentrations of sodium and other impurities identified in the previous chapters. Potassium metal pre-treatment has therefore been necessary to achieve satisfactory reliability of rest potential,[182] as explored in Chapter 3. Potassium metal is also highly reactive, decomposing all known electrolytes on contact and forming resistive solid electrolyte interphases (SEIs). Electrolyte decomposition products formed at potassium metal electrodes have further been observed to travel across cells and deposit on the other electrode as a result of cross-talk,[149,150] which could alter electrochemical behaviour and lead to inaccuracies in SEI characterisation. For this reason the SEI formed on

graphite electrodes in KIBs was not explored in Chapter 4. The development of a stable reference electrode for KIBs is therefore of critical importance.

A suite of alloy reference electrodes have been investigated for use in lithium- and sodium-based batteries, including the Li-Al, Li-Sn, Na-Sn, Li-Bi and Li-Au systems.[164,252] The Li-In system has also recently received much attention as a counter/reference electrode in solid-state lithium metal battery research due to its high potential of 0.62 V vs. Li^+/Li in the In-InLi two-phase region and the high diffusivity of the InLi intermetallic phase.[253,254] Despite this, there have been no reports investigating potassium alloys to fulfil this role in KIBs.

In this chapter, the K-In and K-Bi alloy systems are investigated as reference electrode materials for KIBs.

The objectives of this chapter are to:

1. Identify and synthesise two-phase potassium alloys to serve as reference electrode materials for KIBs.

2. Evaluate the potential and electrochemical stability of promising alloy materials.

3. Demonstrate the use of potassium alloys as reference electrodes by cycling three-electrode cells.

5.2 The K-In System

Owing to the success of In-InLi reference electrodes, the K-In system was investigated. The K-In phase diagram in Figure 5.1 demonstrates that potassium and indium have limited solid solubility and form several intermetallic phases,[255] of which only the existence of In_4K has been verified experimentally[256] and other reports suggest $In_{41}K_{17}$[257] and $In_{11}K_8$[258] are also stable. Nevertheless, In_4K is expected to have the lowest potassium activity, and hence highest potential, so an In-10at.%K alloy was synthesised to form a two-phase alloy, ensuring a constant potential independent of random composition fluctuations. Dr J. Aspinall assisted with all alloy synthesis. The high volume fraction of In allows the alloy to be calendered into a foil.

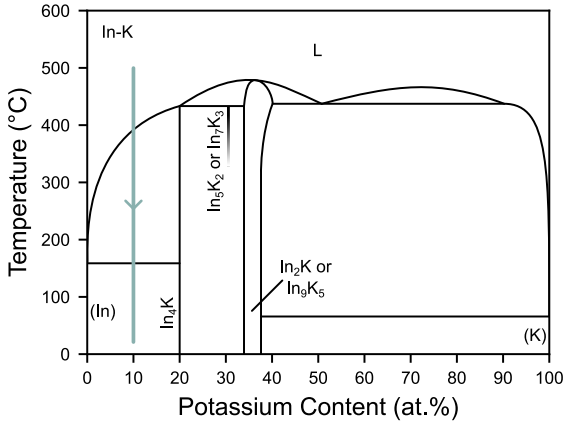


Figure 5.1: K-In phase diagram, adapted from Okamoto.[255] The heat treatment to synthesise the target composition of In-10at.%K is marked in blue.

The X-ray diffraction (XRD) pattern from this material in Figure 5.2 confirms the presence of both In and In_4K, with no evidence of impurity phases. Pawley refinements performed by Dr J. Cattermull reveal the In phase has the expected tetragonal crystal structure ($I4/mmm$, a = 3.25869(7) Å, c = 4.95224(15) Å), and In_4K has the $BaAl_4$-type tetragonal crystal structure ($I4/mmm$, a = 4.84447(15) Å, c = 12.6840(4) Å), consistent with previous reports.[256]

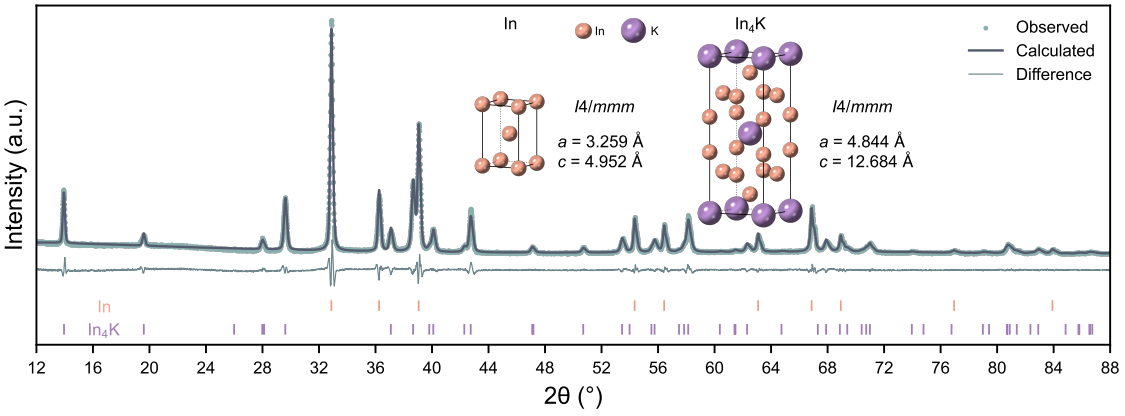


Figure 5.2: XRD of In-10at.%K (λ = 1.5406 Å) and Pawley refinement. The crystal structures of the identified In and In_4K phases are shown in the inset.

To test the suitability of this alloy as a reference electrode it was assembled into coin cells against potassium metal and the open-circuit voltage (OCV) was tracked over 100 h at 30°C. 2.5 M potassium bis(fluorosulfonyl)imide (KFSI) in triethyl phosphate (TEP) was used as the electrolyte. Importantly, the potassium metal electrodes were produced following the remelting, quenching, rolling, and polishing methodology developed in

Chapter 3, providing a sufficiently stable potential to evaluate new reference materials. The OCV of the In-In_4K is plotted in Figure 5.3, where it can be observed that the initial OCV is 980 ± 10 mV vs. K^+/K, and it relaxes to 632 ± 4 mV vs. K^+/K after 100 h, suggesting this is the true potential of K^+/In_4K. Several different methods of polishing the electrode surface prior to cell assembly were attempted but all cells displayed the same behaviour. While the potential of 632 ± 4 mV vs. K^+/K will reduce the driving force for electrolyte reduction, it is unlikely to fall within the electrolyte electrochemical stability window, so spontaneous In_4K oxidation is expected upon electrolyte addition. It is therefore suspected that the initial OCV of 980 ± 10 mV vs. K^+/K results from complete depletion of potassium at the surface, and the gradual decay in potential is limited by the diffusion of potassium to replenish the lost atoms. The OCV takes several days to stabilise, indicating sluggish diffusion kinetics, so the average potential over the last 90 h in Figure 5.3 (allowing for a 10 h stabilisation period) is 645 ± 15 mV vs. K^+/K, with a high average potential drift of -0.7 ± 0.9 mV h^{-1}.

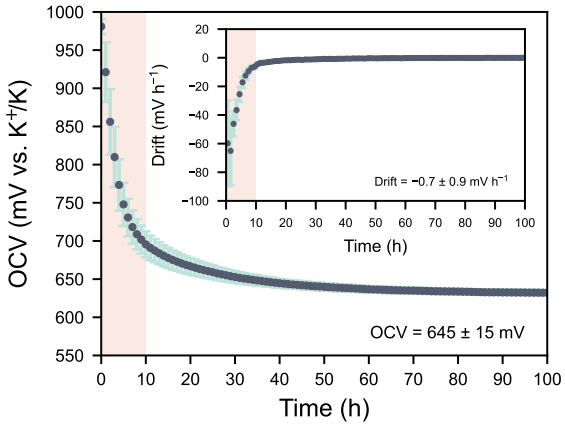


Figure 5.3: OCV of In-10at.%K vs. potassium metal in 2.5 M KFSI TEP at 30°C. The voltage drift is plotted in the inset. An initial 10 h stabilisation period is marked in orange and is excluded from the averages. Error bars represent the standard error in the mean determined from 7 repeat cells.

This long stabilisation period would hinder the implementation of In-In_4K as a reference electrode, and the sluggish kinetics of the K-In system explains the lack of available reports on its use for KIB applications and why, despite several attempts, indium metal was unable to be reversibly cycled against potassium. It is therefore necessary to investigate other alloy systems.

5.3 The K-Bi System

A range of potassium alloy systems have been explored as alternative KIB anode materials, including K-Sn, K-Pb, K-Sb and K-Bi.[24,259] Of these, the K-Bi system appears most promising for reference electrode applications as it undergoes several two-phase reactions during cycling.[259] Its successful use as an anode material also suggests it will not experience the same kinetic limitations as the K-In system.

To investigate the K-Bi system a thin bismuth electrode was produced by radio-frequency magnetron sputtering with the assistance of S. Kotakadi. The atomic force microscopy (AFM) height map of this electrode in Figure 5.4 reveals that it is highly faceted and dense, with a thickness of 0.90 ± 0.14 µm (Figure 5.5).

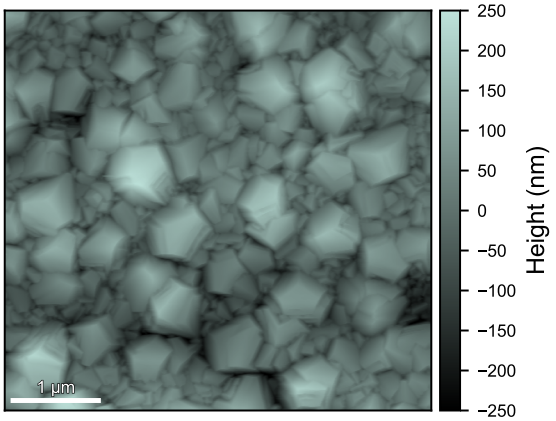


Figure 5.4: AFM height map of the sputtered bismuth electrode.

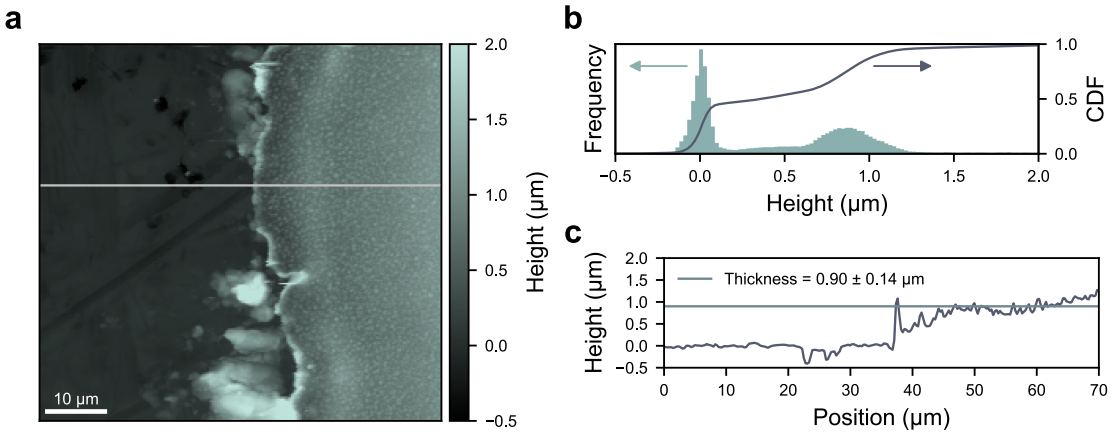


Figure 5.5: Bismuth film thickness measurement. (a) AFM height map across a step created through the bismuth film. (b) Histogram of heights in (a) and corresponding cumulative distribution function (CDF), showing peaks corresponding to both the substrate and the film. (c) Height across the 1D section marked in (a) compared with the average film thickness.

This bismuth electrode was cycled against potassium metal in Figure 5.6a, revealing one broad plateau during the first potassiation, and three distinct plateaus during all subsequent half-cycles, consistent with previous reports.[260,261] A 2 m KFSI TEP electrolyte was used due to its proven performance in KIB applications and compatibility with both graphite and cathode materials,[38,262,263] and all measurements were performed at 30°C, but similar behaviour is observed when using a 1 m KFSI in 1,2-dimethoxyethane (DME) electrolyte (Figure 5.6b).

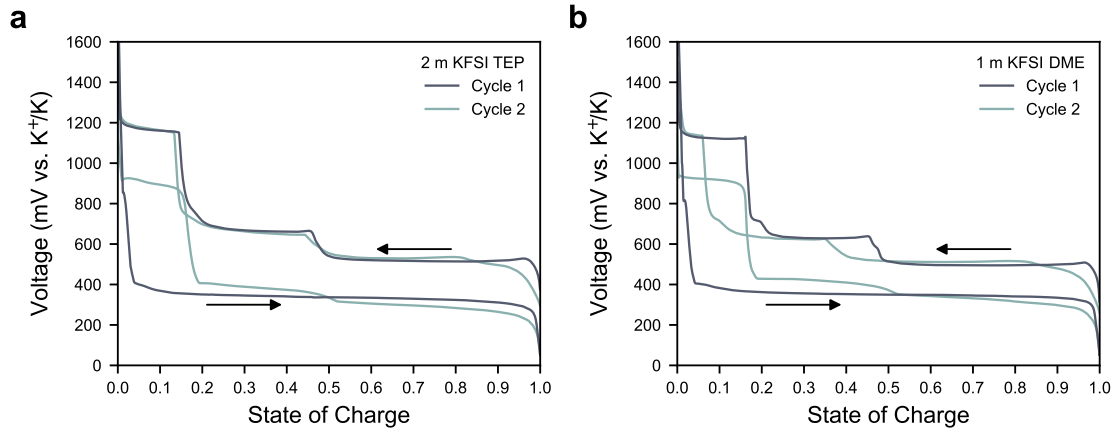


Figure 5.6: Potassiation-depotassiation curves of the bismuth electrode at C/20 at 30°C in (a) 2 m KFSI TEP, (b) 1 m KFSI DME.

The mechanisms taking place during cycling were investigated by Yao et al., revealing the first potassiation initiates at the bismuth surface and takes place through conversion to BiK_3 (via a Bi_2K intermediate). This results in over 400% volume expansion, causing the electrode to fracture into small fragments which both greatly increases the area available for reaction and reduces the mechanical constraint.[264] This enables additional reactions to take place on the following cycles, in accordance with the phase diagram in Figure 5.7.[265]

To better evaluate the potentials of the three plateaus a galvanostatic intermittent titration technique (GITT) measurement was performed during the first depotassiation to minimise the contribution of overpotentials to the observed voltages (Figure 5.8). GITT measurements are often performed to measure solid-state diffusivities within electrode materials, but the traditional analysis is generally only appropriate for single-phase materials,[266] so only the OCV was determined from the GITT measurements here.

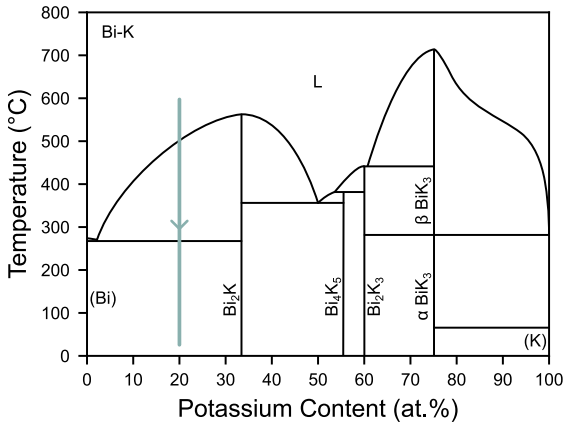


Figure 5.7: K-Bi phase diagram, adapted from Petric and Pelton.[265] The heat treatment to synthesise the target composition of Bi-20at.%K is marked in blue.

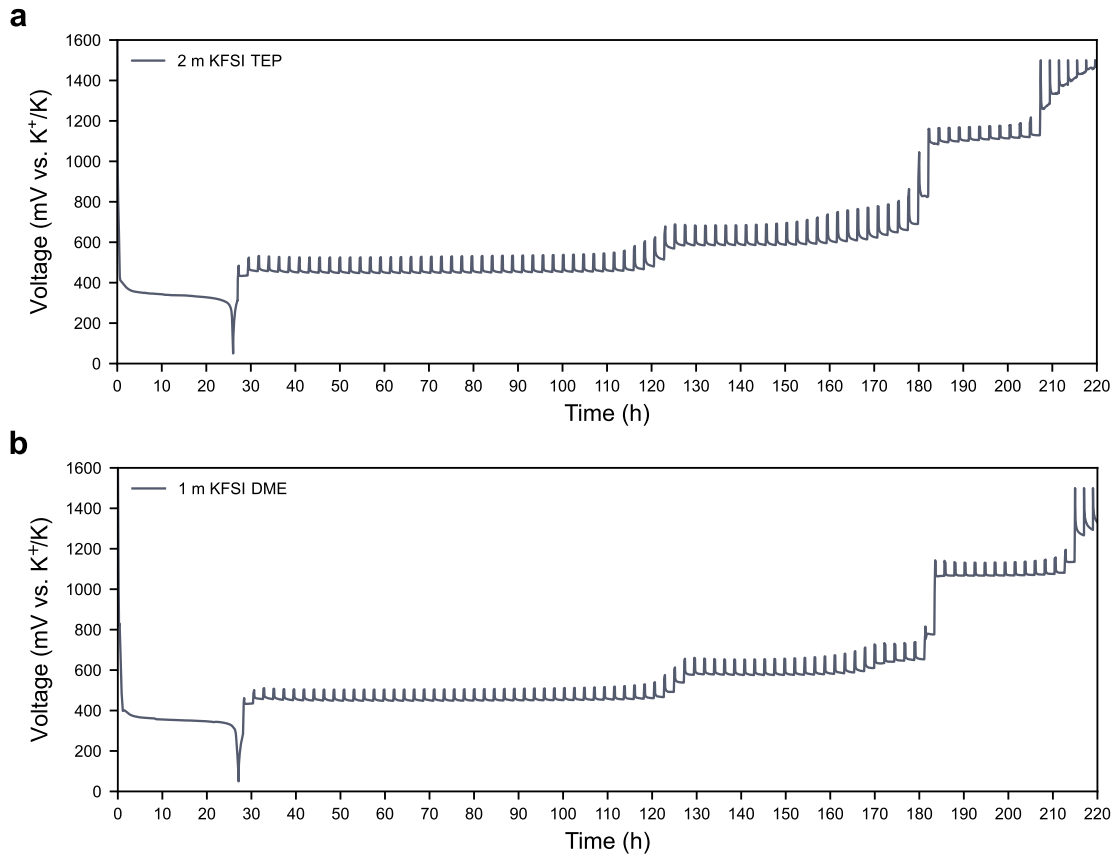


Figure 5.8: Raw GITT data gathered during the first depotassiation at 30°C in (a) 2 m KFSI TEP, (b) 1 m LiFSI DME.

The results of the GITT measurements are plotted in Figure 5.9 as a function of potassium content for both electrolyte systems, enabling direct comparison to the phase diagram. In accordance with both the phase diagram in Figure 5.7 and in-situ XRD measurements performed by Lei et al.,[260] the plateaus at approximately 1100 mV, 600

mV and 450 mV vs. K^+/K correspond to $2Bi + K^+ + e^- \rightleftharpoons Bi_2K$, $Bi_2K + 2K^+ + 2e^- \rightleftharpoons Bi_2K_3$ and $Bi_2K_3 + 3K^+ + 3e^- \rightleftharpoons 2BiK_3$, respectively.

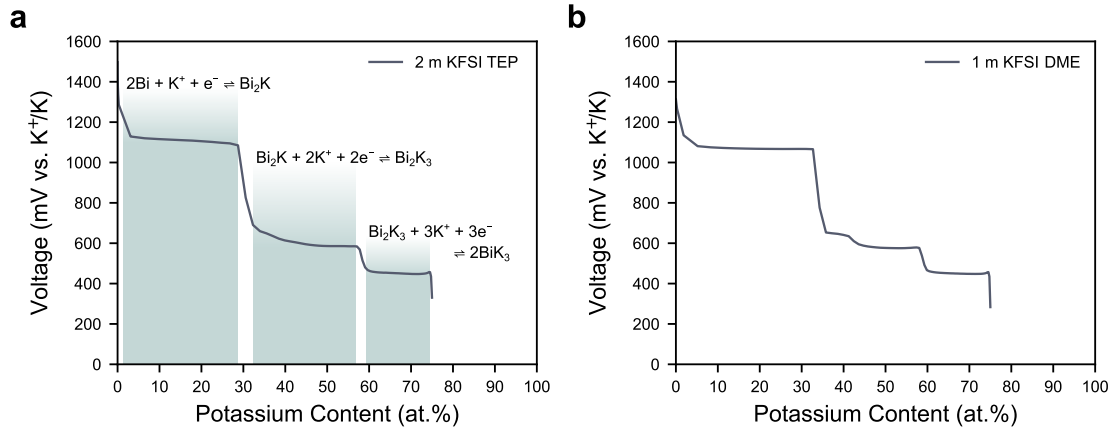


Figure 5.9: OCV as a function of potassium content determined by GITT during the first depotassiation at 30°C in (a) 2 m KFSI TEP, (b) 1 m KFSI DME. The reactions taking place during each plateau are marked on the plot in (a).

Interestingly, there is evidence of an additional plateau from approximately 33–40 at.%K in Figure 5.9a, suggesting the conversion from Bi_2K_3 to Bi_2K may take place through an additional phase. This plateau is even more evident when using 1 m KFSI DME (Figure 5.9b). Similarly, an additional oxidative peak has been observed in cyclic voltammetry (CV) studies,[267,268] but its origin has not been identified. The partial conversion of Bi_2K_3 to either Bi_4K_5 or metastable BiK[269] could explain these observations.

5.3.1 Synthesis and Characterisation

Of the plateaus identified in Figure 5.9a, the Bi-Bi_2K is most promising due to its high potential, greatly reducing the driving force for electrolyte reduction. A Bi-20at.%K alloy was therefore synthesised. Unlike the In-10at.%K, Bi-20at.%K is hard and brittle and cannot be calendered into a foil, but it can be easily ground into a powder and polished. To confirm the phases present in the alloy it was ground into a powder and loaded into capillaries for synchrotron XRD. Scanning electron microscopy (SEM) was performed on this powder (Figure 5.10), revealing approximate particle sizes between 10–100 µm. All SEM imaging was performed by S. Kotakadi.

As shown in Figure 5.11, synchrotron XRD reveals the presence of both Bi and Bi_2K, with no impurity phases. Bi has the expected rhombohedral crystal structure ($R\bar{3}m$,

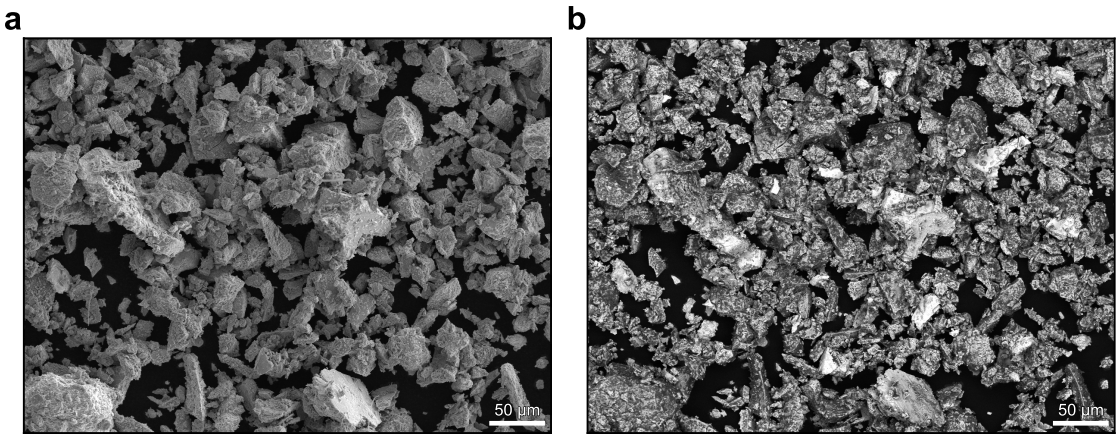


Figure 5.10: Bi-Bi_2K powder SEM. (a) Secondary electron (SE) image. (b) Backscattered electron (BSE) image, revealing contrast between the two phases.

a = 4.54628(12) Å, c = 11.8620(6) Å) and Bi_2K has a cubic Laves crystal structure ($Fd\bar{3}m$, a = 9.52539(3) Å), consistent with previous reports.[260,269]

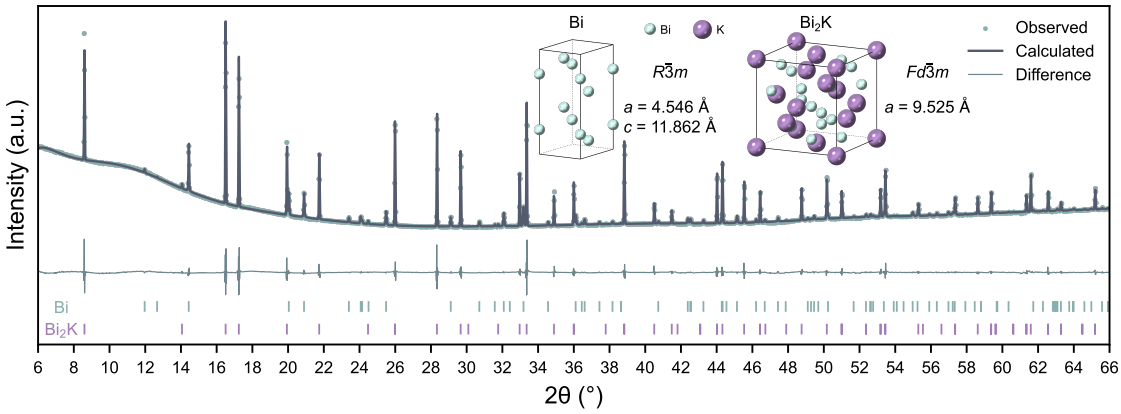


Figure 5.11: Synchrotron XRD of Bi-20at.%K (λ = 0.824316(2) Å) and Pawley refinement. The crystal structures of the identified Bi and Bi_2K phases are shown in the inset.

The Bi-Bi_2K was additionally polished for SEM characterisation to explore its microstructure. The secondary electron (SE) image in Figure 5.12a reveals that the microstructure consists of coarse dendrites of a primary phase with primary and secondary dendrite arm spacings of approximately 500 µm and 100 µm, respectively. These dendrites are embedded in a matrix of a secondary phase that is preferentially removed during polishing, suggesting it is softer. The backscattered electron (BSE) image in Figure 5.12a provides excellent contrast between the two phases, revealing that the matrix phase has a higher average atomic number. Energy-dispersive X-ray spectroscopy (EDX) was further employed to analyse the region highlighted by the grey box in Figure 5.12a. As

shown in Figure 5.12b, EDX mapping reveals the primary dendrites are rich in both potassium and bismuth, while the matrix only contains bismuth. These observations confirm that the primary dendritic phase is Bi_2K and the matrix is Bi, in agreement with the phase diagram (Figure 5.7).

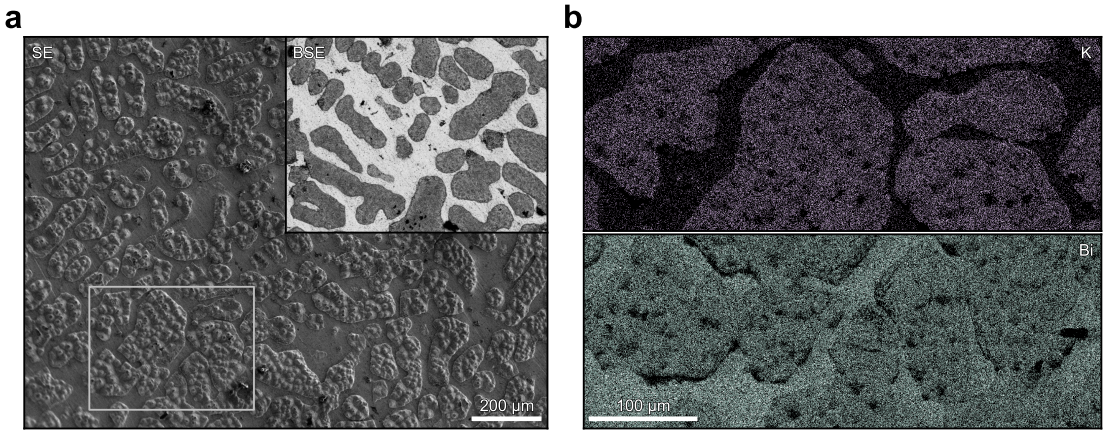


Figure 5.12: Scanning electron microscopy of polished Bi-20at.%K. (a) SEM SE and BSE images. (b) EDX mapping of the potassium (top) and bismuth (bottom) distributions in the region marked by the grey box in (a).

Analysis of the BSE image in Figure 5.12a reveals an alloy composition of Bi-22.2at.%K (Figure 5.13), which is close to the target composition of Bi-20at.%K. Interestingly, the phase diagram in Figure 5.7 suggests the existence of a eutectic reaction ($L \rightarrow Bi + Bi_2K$) at 271°C and 2.5 at.%K, but there is no evidence of a eutectic structure in Figure 5.12a or 5.12b.

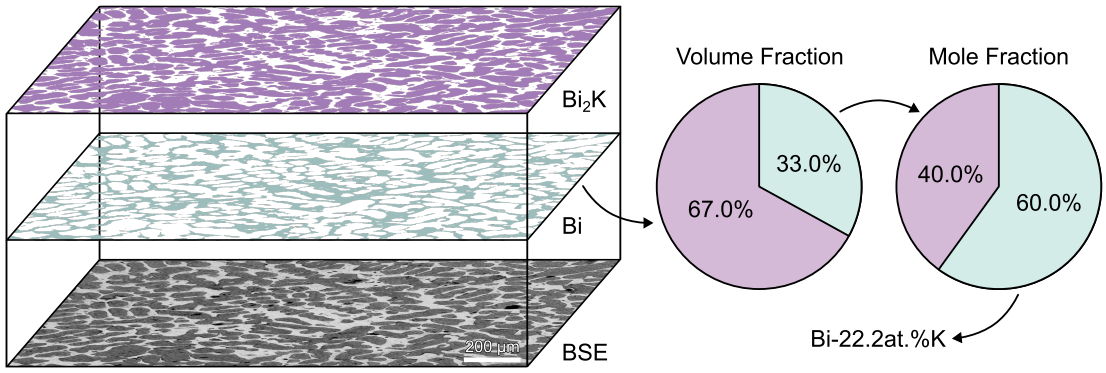


Figure 5.13: Bi-Bi_2K phase quantification. Backscattered electron (BSE) image and extracted Bi and Bi_2K phase distributions used to calculate phase volume and mole fractions, as well as alloy composition. The BSE image was analysed using ImageJ.[270]

In addition to the two-phase Bi-Bi_2K alloy, single-phase Bi_2K was synthesised to investigate the properties of the Bi_2K intermetallic in isolation. Synchrotron XRD (Figure 5.14a) confirms the Bi_2K is phase pure and the crystal structure ($Fd\bar{3}m$, $a = 9.52752(5)$ Å) is in excellent agreement with Figure 5.11. The SEM image in Figure 5.14b further reveals a single-phase microstructure consisting of equiaxed grains with an average diameter of approximately 500 µm and nanoindentation gives a Young's modulus of 38.2 ± 0.3 GPa and a hardness of 1.46 ± 0.01 GPa (Figure 5.14c). Nanoindentation was performed by Dr J. Aspinall. The Young's modulus of Bi_2K is similar to that of Bi (33–35 GPa[271]), while its hardness is significantly higher than that of Bi (50–100 MPa[271]), as would be expected due to the highly ordered structures and directional bonding in intermetallic materials. The discrepancy in hardness between the two phases explains why bismuth is preferentially polished away in Figure 5.12a.

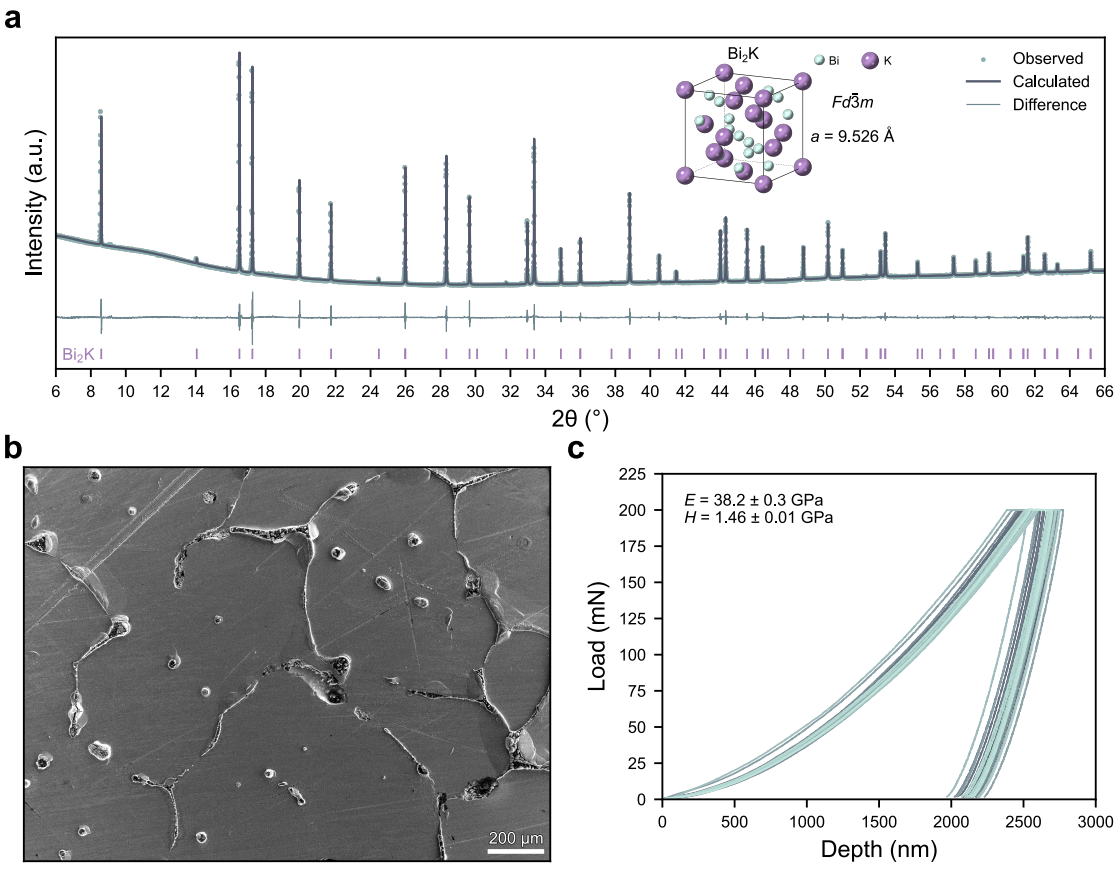


Figure 5.14: Bi_2K characterisation. (a) Synchrotron XRD ($\lambda = 0.824316(2)$ Å) and Pawley refinement. The crystal structure is shown in the inset. (b) SEM secondary electron (SE) image of polished Bi_2K. (c) Nanoindentation curves used to measure the Young's modulus, E, and hardness, H. 29 nanoindentations were performed.

5.3.2 Potential Stability

Having successfully produced a pure, two-phase Bi-Bi_2K alloy, it is now necessary to evaluate its suitability as a reference electrode. To serve as a reference electrode the alloy must have a stable potential, so it was assembled into coin cells against potassium metal. As the Bi-Bi_2K cannot be calendered into a foil on it own, Bi-Bi_2K powder was embedded into calendered bismuth granules to form an electrode, as shown in the SEM images in Figure 5.15.

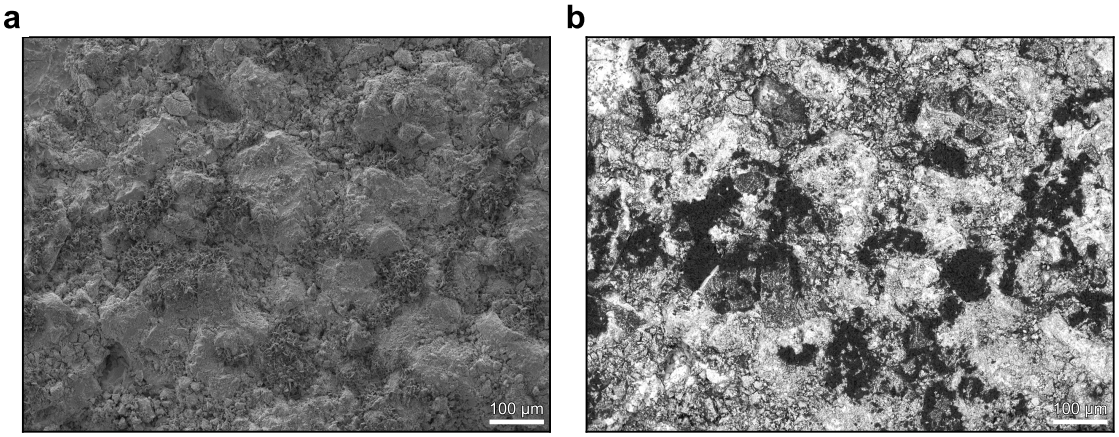


Figure 5.15: Bi-Bi_2K electrode SEM. (a) Secondary electron (SE) image. (b) Backscattered electron (BSE) image, revealing contrast between the two phases.

The OCV of these cells (at 30°C in 2 m KFSI TEP) was tracked over 100 h in Figure 5.16, revealing that it rapidly stabilises and, after an initial 10 h rest period, has an average potential of 1070 ± 3 mV vs. K^+/K over 90 h, consistent with Figure 5.9. The potential drift is also very low, with an average of -0.1 ± 0.1 mV h^{-1} over the same period. Combining this rapid stabilisation with its high potential of 1070 ± 3 mV vs. K^+/K, this makes the Bi-Bi_2K system an attractive system for further exploration.

To further test the use of Bi-Bi_2K as a reference electrode, it is necessary to assemble three-electrode cells to evaluate its performance in a realistic use case. Three-electrode ECC-Ref cells (EL-Cell) were therefore assembled with a graphite working electrode and a potassium metal counter electrode, using a small needle of the as-cast Bi-Bi_2K alloy as the reference electrode. The graphite electrode casting was prepared by Dr S. Dhir. A 2 m KFSI TEP electrolyte was again used and measurements were performed at 30°C.

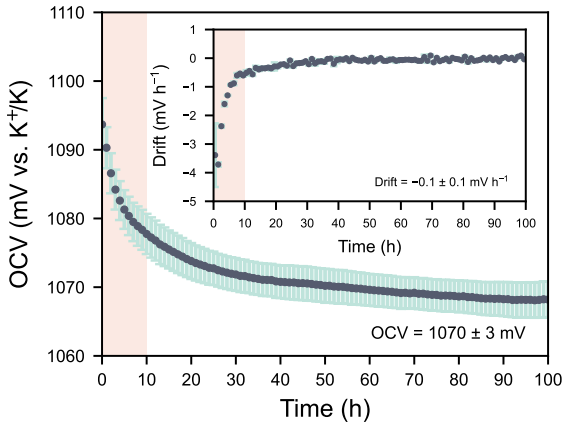


Figure 5.16: OCV of Bi-Bi_2K vs. potassium metal. The voltage drift is plotted in the inset. An initial 10 h stabilisation period is marked in orange and is excluded from the averages. Error bars represent the standard error in the mean determined from 3 repeat cells. Measurements were performed in 2 m KFSI TEP at 30°C.

Figure 5.17 shows the electrochemical impedance spectroscopy (EIS) spectra gathered from the three-electrode cell after a 24 h rest period at OCV, demonstrating that the impedance contributions from the graphite and the potassium metal can be separated successfully.

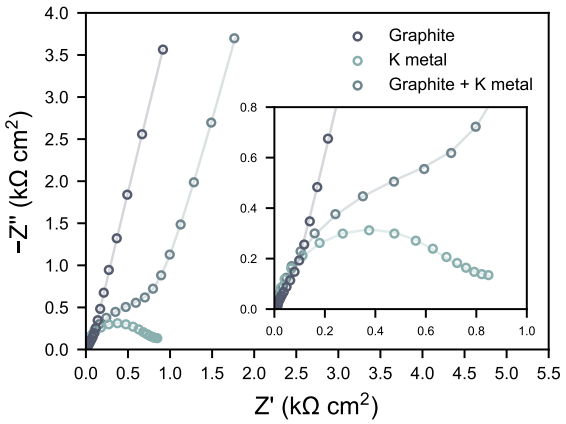


Figure 5.17: Impedance spectra from the graphite and potassium metal electrodes, plus their sum, after 24 h at OCV. Measurements were performed in 2 m KFSI TEP at 30°C.

Fitting of the impedance spectra (Appendix D.1) reveals a high total interfacial resistance of $1050 \pm 70\ \Omega\ \text{cm}^2$ for the potassium metal electrode, demonstrating that the potassium metal counter electrode would significantly impact the impedance response in two-electrode cells, as evident when the individual impedance spectra are summed together in Figure 5.17. This highlights the importance of three-electrode cells for accurate impedance characterisation. Without a suitable reference electrode, such

characterisation would require the *ex-situ* preparation of symmetric cells,[252] preventing *operando* measurements.

Following this rest period the graphite was cycled between −1.02 V and 0.93 V vs. K^+/Bi_2K (0.05–2 V vs. K^+/K) at C/10, as shown in Figure 5.18a. The first cycle potassiation capacity of 810 mAh g^{-1} is much higher than the theoretical capacity of 279 mAh g^{-1}, while the capacity extracted during the first depotassiation is close to theoretical. This high excess capacity on the first cycle is consistent with previous reports,[262] and is attributed to irreversible electrolyte reduction and SEI formation, which may be exacerbated by the large area of exposed metallic cell components and the low loading (0.5 mg cm^{-2}) used here. Therefore, although it decreases with increasing number of cycles, the potassiation capacity is consistently above 279 mAh g^{-1} in Figure 5.18a, while the depotassiation capacity remains close to theoretical. Nevertheless, this serves as a successful proof-of-concept for the use of Bi-Bi_2K, proving that potassium alloy materials can serve as reliable reference electrodes for KIBs.

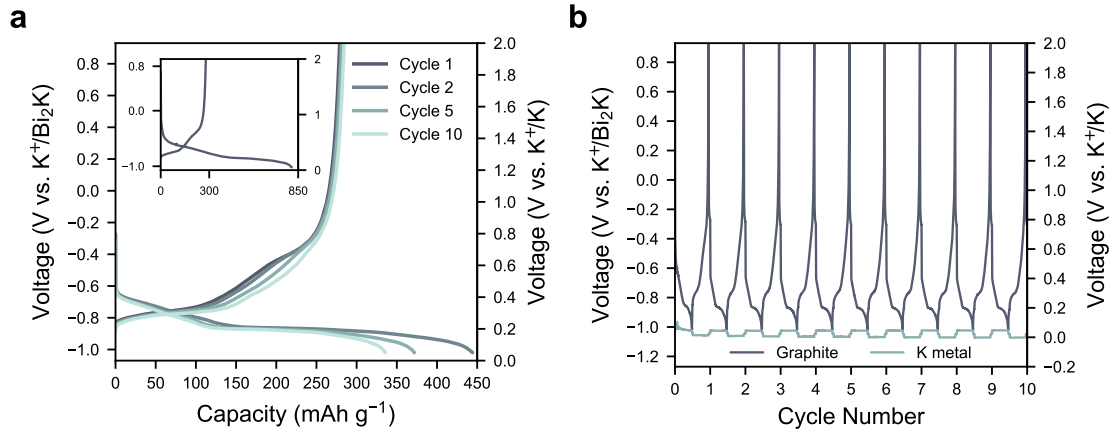


Figure 5.18: Use of Bi-Bi_2K as a reference electrode. (a) Graphite cycling at C/10. The full first cycle is shown in the inset. (b) Voltage profiles of both the graphite and potassium metal electrodes during the first 10 cycles. Measurements were performed in 2 m KFSI TEP at 30°C.

Figure 5.18b further shows the voltage profiles of both the graphite and potassium metal during cycling, demonstrating that the potentials of working and counter electrodes can be accurately separated and there is negligible reference drift. Stable cycling was maintained for several weeks with no evidence of reference degradation (Figure 5.19). This advancement will enable full-cell KIB characterisation in three-electrode cells without the need for potassium metal, eliminating any influence it may have on electrochemical

performance. Additionally, the stable potential of Bi-Bi_2K would allow the use of alternative counter electrodes that do not have a constant potential, further eliminating the need to utilise highly-reactive potassium metal in half-cell studies.

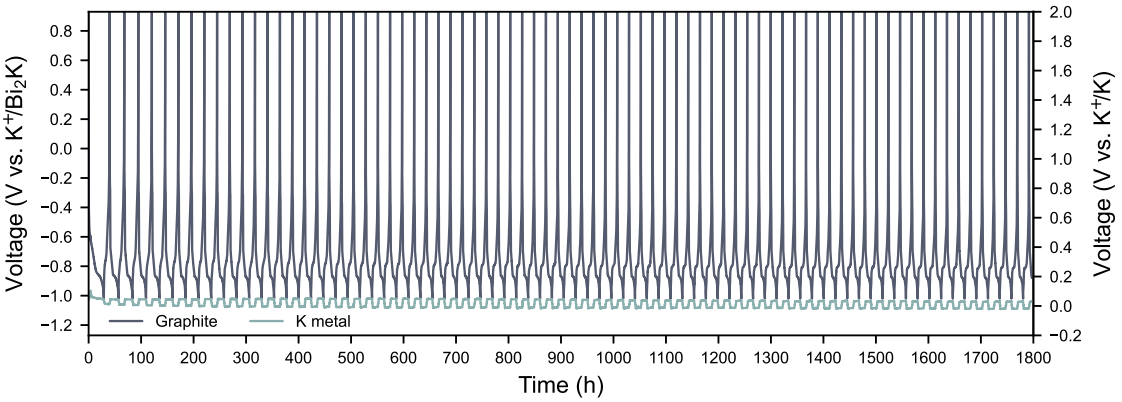


Figure 5.19: Extended three-electrode cycling. Voltage profiles of both the graphite and potassium metal electrodes over time during extended cycling in 2 m KFSI TEP at 30°C.

5.3.3 Electrochemical Stability

So far it has been demonstrated that Bi-Bi_2K has a stable, well-defined potential, satisfying one of the key reference electrode criteria. However, another key requirement is electrochemical stability to ensure that the reference will not have significant impact on the system under study.

To explore the potential at which electrolyte reduction reactions occur, cyclic voltammetry (CV) was performed to sweep an aluminium working electrode between 1800 and 50 mV vs. K^+/K at a scan rate of 100 µV s^{-1} (Figure 5.20). During the first cathodic sweep in the 2 m KFSI TEP electrolyte (Figure 5.20a) there are several broad reductive waves indicative of electrolyte reduction, with apparent peaks at approximately 850 and 600 mV vs. K^+/K followed by further reduction as the potential decreases. No corresponding oxidative peaks appear in the following anodic sweep and all subsequent cycles display pseudocapacitive behaviour with reduced current densities during the cathodic sweeps. This implies that the electrolyte reduction during the first cycle is irreversible and it forms a reasonably passivating SEI, preventing further decomposition.[272] Similar behaviour is observed when using the 1 m KFSI DME electrolyte (Figure 5.20b), suggesting FSI^- is the main species undergoing reduction, rather than the solvent. This is

consistent with the SEI characterisation on the plated potassium electrode in Chapter 4.4. Importantly, the potential of Bi-Bi_2K (1070 ± 3 mV vs. K^+/K) is higher than the potential of electrolyte reduction peaks, implying it will have good stability in the electrolyte systems considered here.

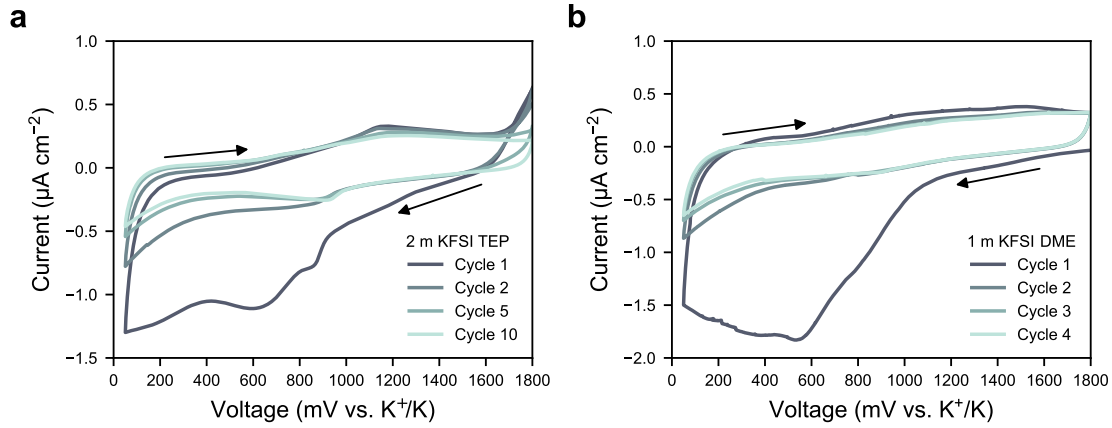


Figure 5.20: CV curves of an aluminium electrode at 100 µV s^{-1} at 30°C in (a) 2 m KFSI TEP, (b) 1 m KFSI DME.

While other electrolyte systems and electrolyte additives may undergo reduction at higher potentials,[273,274] Bi-Bi_2K will still be far less reactive than potassium metal. This reduced reactivity is evident when storing and disposing of the Bi-Bi_2K alloy. Potassium metal readily reacts with atmospheric gases, even in a well-controlled glovebox atmosphere, and it reacts violently with water, making its storage and disposal challenging. In contrast, Bi-Bi_2K maintained its shiny appearance and purity even after several months of glovebox storage. It also does not react violently with water, offering enhanced safety compared to potassium metal.

To further compare the electrochemical stability of Bi-Bi_2K to potassium metal, symmetric coin cells were assembled and EIS was performed over 100 h at OCV. The interfacial resistance of the potassium cells increases continuously during rest, increasing by a factor of approximately 7 over the 100 h (Figure 5.21). Similarly, the corresponding interfacial resistance of the Bi-Bi_2K cells increases by a factor of approximately 5 over the same period.

Exemplar impedance spectra and the equivalent circuit fitting results are presented Appendix D.2 and D.3 for the K||K and Bi-Bi_2K||Bi-Bi_2K cells, respectively.

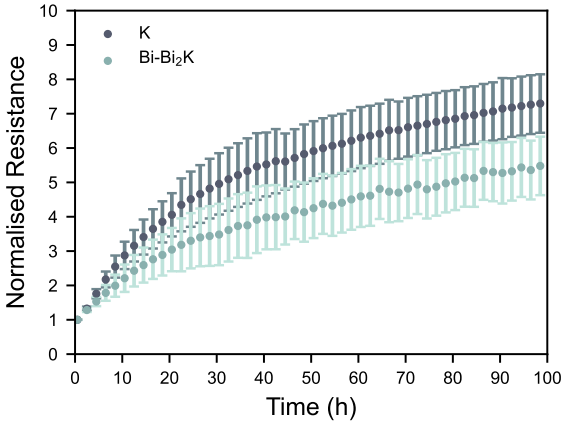


Figure 5.21: Interfacial resistance evolution from K||K and Bi-Bi_2K||Bi-Bi_2K cells at OCV, normalised by the resistance after 30 min, in 2 m KFSI TEP at 30°C. Error bars represent the standard error in the mean from at least 2 repeat cells.

The interfacial resistance in symmetric alkali metal cells is often assumed to be dominated by the resistance of cation migration through the SEI,[101] and an increasing resistance is attributed to SEI growth,[102] suggesting the SEI continuously increases in thickness at OCV in both systems. However, other theories suggest the SEI densifies over time and the increasing resistance is a result of a decreasing ionic conductivity,[61] which matches with the observations in Chapter 4.3.4. Due to the very different potentials of potassium and Bi-Bi_2K they are likely to form SEIs with different properties, requiring further SEI characterisation to interpret these trends in resistance.

X-ray photoelectron spectroscopy (XPS) depth profiling was therefore performed on potassium metal and Bi-Bi_2K samples that were submerged in 2 m KFSI TEP electrolyte for 20 h at 30°C, followed by rinsing with TEP to remove residual salt. This is the same XPS analysis methodology developed in Chapter 4 and full XPS spectra are presented in Appendix B.5. Examination of the XPS spectra from the potassium sample reveals that it is enriched in elements from salt decomposition and fluorine is especially prevalent. Two distinct fluorine environments are evident in the F 1s spectra in Figure 5.22a. The peak at 684.2 eV is attributed to KF[186] and was utilised for charge referencing, while the peak at 685.5 eV may be consistent with KHF_2, as discussed in Chapter 4.4. KF is already the majority F-containing species after 5 min of sputtering, and its proportion increases with sputtering time.

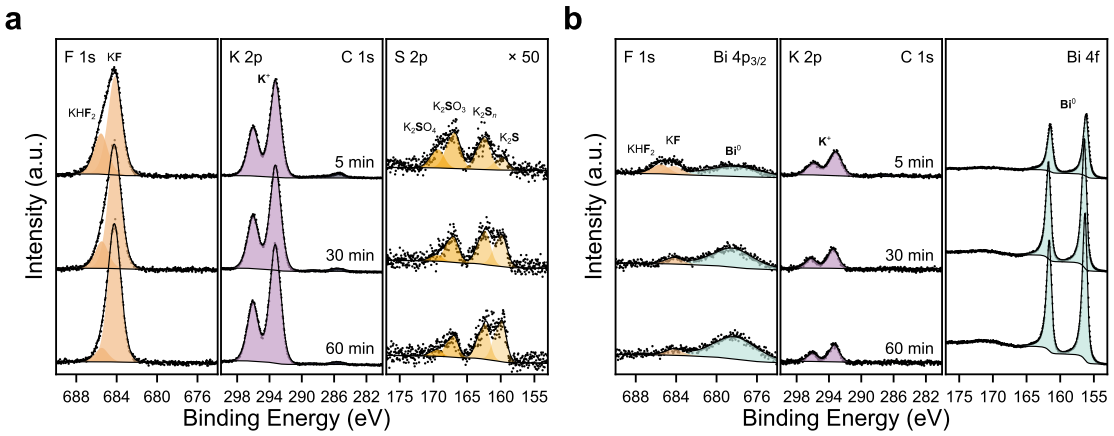


Figure 5.22: SEI characterisation. (a) F 1s, K 2p, C 1s and S 2p XPS spectra from depth profiles on the SEI formed on potassium metal. (b) F 1s, Bi $4p_{3/2}$, K 2p, C 1s and Bi 4f XPS spectra from depth profiles on the SEI formed on Bi-Bi_2K. Both SEI samples were formed by submersion in 2 m KFSI TEP for 20 h at 30°C. Spectra measured after 5, 30 and 60 min of sputtering are presented and consistent y-scales are used in (a) and (b), except the S 2p spectra in (a) are scaled by a factor of 50 relative to the Bi 4f spectra in (b).

The K 2p region displays an intense doublet peak that can not be deconvolved, preventing meaningful identification of species based on this region alone, while the C 1s peaks have low intensity, confirming that the SEI is primarily inorganic and the solvent does not significantly contribute to the SEI in this electrolyte system, as suspected from the CV results in Figure 5.20a. Four unique environments can be identified from the S 2p spectra, which could be attributed to K_2SO_4, K_2SO_3, K_2S_n and K_2S at approximately 169.0, 166.6, 162.1 and 159.7 eV, respectively.[262,275,276] Similar to the fluorine-containing species, the sulphur-containing species become more reduced as the sputtering time increases. This could result from the fact that the driving force for reduction is greatest closest to the potassium surface, so the SEI is composed of more reduced species there.[60] Alternatively, it has been reported that the argon sputtering used for XPS depth profiling can cause sample damage, which may contribute to the changes observed with sputtering time.[77] Nevertheless, the SEI formed on potassium metal here is rich in salt decomposition species throughout the entire examined depth (Figure 5.23), suggesting it is relatively thick.

In contrast, the SEI formed on the Bi-Bi_2K appears to be thinner and less fluorine rich (Figure 5.24). Like the potassium metal SEI, KHF_2 and KF are identified in the F 1s spectra in Figure 5.22b, but their intensities are lower and they decrease with increasing sputtering time. The K 2p and C 1s peaks also have lower intensity. After 5 min of

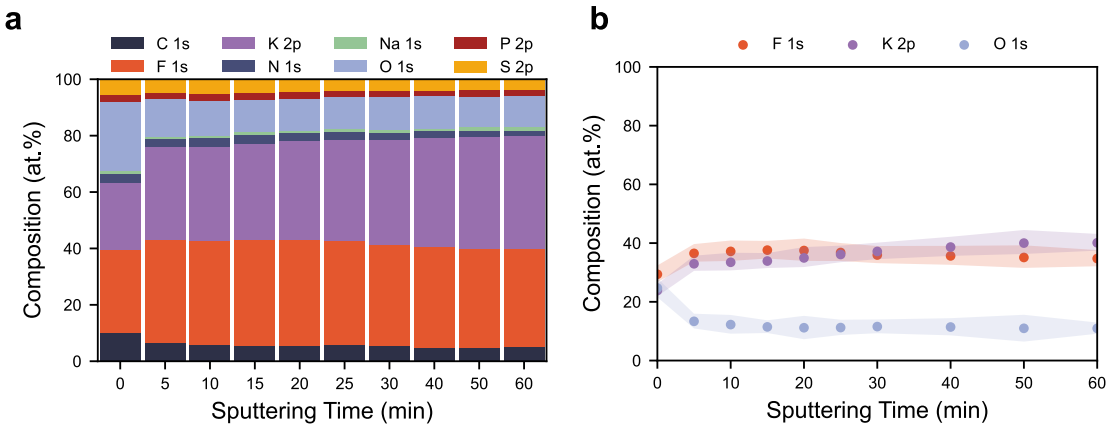


Figure 5.23: Potassium metal SEI quantification. (a) Composition as a function of sputtering time. (b) Concentrations of fluorine, potassium and oxygen as a function of sputtering time, with error bars taking into account the peak fitting uncertainty determined by CasaXPS.[217]

sputtering there is no evidence of S 2p peaks, and instead a doublet peak corresponding to metallic bismuth is present at 156.4 eV. The intensity of this peak initially grows with sputtering time and then reaches a plateau after approximately 20 min of sputtering, suggesting the SEI has been etched away. Beyond this point bismuth and potassium make up over 70% of all elements, as shown in Figure 5.24. Therefore, this suggests that, despite the normalised interfacial resistances increasing by similar factors in Figure 5.21, the Bi-Bi_2K results in significantly less electrolyte decomposition than potassium metal overall, confirming that Bi-Bi_2K satisfies another key reference electrode requirement.

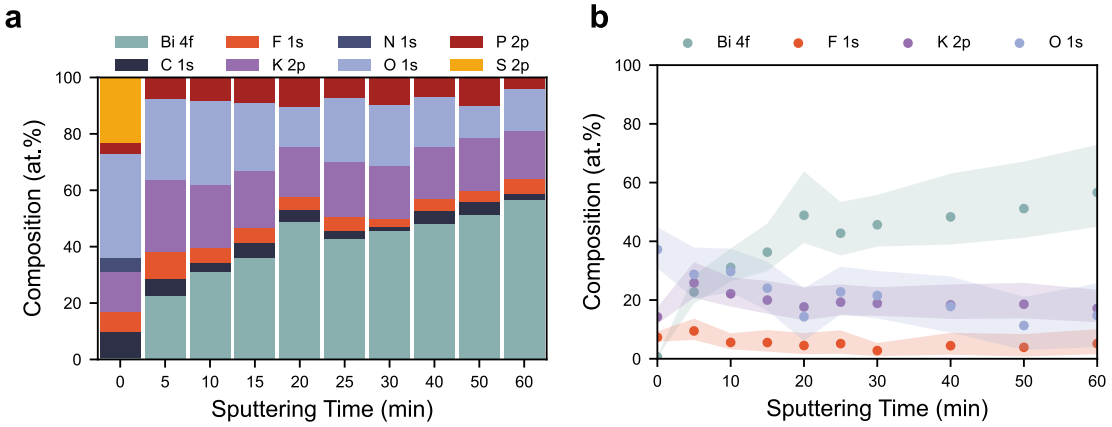


Figure 5.24: Bi-Bi_2K SEI quantification. (a) Composition as a function of sputtering time. (b) Concentrations of bismuth, fluorine, potassium and oxygen as a function of sputtering time, with error bars taking into account the peak fitting uncertainty determined by CasaXPS.[217]

5.4 Conclusion

In conclusion, in this chapter the K-In and K-Bi alloy systems have been investigated for use as reference electrode materials for potassium-ion batteries (KIBs). Pure two-phase In-In_4K and Bi-Bi_2K alloys have successfully been synthesised and these display potentials of 0.63 and 1.07 V vs. K^+/K, respectively. While it is revealed that the use of In-In_4K is hindered by a kinetic limitation, it is demonstrated than Bi-Bi_2K stabilises rapidly, enabling its implementation as a KIB reference electrode. By cycling graphite against potassium metal in three-electrode cells it has been shown that Bi-Bi_2K provides a stable potential with negligible drift, even after several weeks. It is further demonstrated that its high potential results in enhanced safety and significantly less electrolyte decomposition compared to potassium metal. This study paves the way for future full- and half-cell KIB studies without the need for potassium metal, eliminating any influence it has on electrochemical performance and solid electrolyte interphase formation.

5.5 Experimental Methods

Unless otherwise stated, all experiments were performed in argon-filled MBraun gloveboxes with O_2 and H_2O concentrations below 0.1 ppm and all equipment was cleaned and dried overnight under vacuum at 70°C before being brought into the glovebox.

Potassium Metal Processing

Before use, potassium metal (chunks, 98%, Sigma-Aldrich) was processed according to the method developed in Chapter 3. The potassium was melted in a beaker on a hot plate, a spatula was used to remove the dross, and the molten potassium was quenched into clean mineral oil before being transferred into hexane (95% anhydrous, Sigma-Aldrich) that had been dried over 3 Å molecular sieves for storage.

Alloy Synthesis

All potassium alloys were synthesised by weighing out processed potassium metal and either indium (pieces, 99.99%, Alfa Aesar) or bismuth (granules, >99.99%, Sigma-Aldrich) in the desired atomic ratio and adding them to a custom-designed stainless steel crucible[185] lined with molybdenum foil (Goodfellow). The mixtures were then heated in a box furnace (MTI KSL-1200X-J-UL or MTI KSL-1100X).

The In-In_4K (In-10at.%K) alloy was heated to 500°C over 100 min and then held for 2 h. The crucible was removed from the furnace and the melt was stirred with a stainless steel spatula, before being returned to the furnace for 1 h. The molybdenum foil and the melt were then removed from the crucible and quenched in mineral oil.

The Bi-Bi_2K (Bi-20at.%K) alloy and the single-phase Bi_2K (Bi-33.3at.%K) were heated to 600°C over 90 min and then held for 1 h, stirring with a stainless steel spatula once molten. They were then slow-cooled in the furnace.

X-ray Diffraction

For X-ray diffraction (XRD) the In-In_4K was rolled by hand to produce a flat foil. This was measured using a Rigaku Miniflex XRD contained within a nitrogen-filled glovebox at room temperature. A $Cu_{K\alpha}$ source ($\lambda = 1.5406$ Å) was used, with a nickel filter used to remove $Cu_{K\beta}$ radiation.

The Bi-Bi_2K and Bi_2K were ground by hand in an agate mortar and sealed into glass capillaries for XRD. Synchrotron XRD measurements were performed on the I11 beamline of the Diamond Light Source, UK, operating with an X-ray wavelength of 0.824316(2) Å. A position sensitive detector (PSD) was used to collect diffraction patterns in capillary transmission geometry. Room temperature X-ray diffraction patterns were collected using the Mythen-2 PSD. Two data collections of 20 s each were taken at angles 0.25° apart, then summed to account for gaps in the detector coverage.

Pawley refinements were carried out using TOPAS-Academic software[277] to determine the crystal structures and lattice parameters of the phases present. Pawley refinements were made using models from literature,[256,260] and a Thompson-Cox-Hasting pseudo-Voigt (TCHZ) peak shape function with peak intensities allowed to freely refine. The data from the In-In_4K presented in Figure 5.2 was shifted down by $2\theta = 0.368°$ to correct for zero error.

Electrode Preparation

The processed potassium chunks were rolled by hand between two sheets of weighing paper (grade 2122, Whatman), using additional hexane to prevent sticking, to a thickness of approximately 500 µm. The potassium foil was then punched into 10 mm diameter electrodes using a wad punch. Immediately before cell assembly the surface of the potassium electrodes was polished with a plastic blade, producing a mirror-like finish.

The In-In_4K electrodes were prepared by calendering the as-cast alloy down to a thickness of 300 µm and then punching 8 mm diameter electrodes with a wad punch.

The 10 mm diameter bismuth film electrodes were deposited onto masked stainless steel spacers (304SS, MTI) by radio-frequency (RF) magnetron sputtering in an MBraun MB-Evap physical vapor deposition system. A 50 mm diameter bismuth sputtering target (BI00-ST-000100, Goodfellow) was used with a sputtering power of 28 W. The sputtering chamber was pumped down to a pressure of 5×10^{-5} mbar prior to sputtering. Argon gas was used as the sputtering gas and was injected at a flow rate of 10 SCCM. Prior to deposition the bismuth target was cleaned of impurities by pre-sputtering, with the

substrate shutter closed, for 2 min at the same power. During deposition the substrate was rotated at a rate of 33 rpm. The sputtering duration was 2 h.

Bi-Bi_2K electrodes for two-electrode studies were prepared by calendering bismuth granules (>99.99%, Sigma-Aldrich) down to a thickness of 350 µm, adding Bi-Bi_2K powder (ground by hand in an agate mortar, Figure 5.10) on top, and then calendering to a thickness of 300 µm (Figure 5.15). Due to the brittle nature of bismuth, it was not possible to produce a large, uniform film, so these electrodes had approximate dimensions of 4 mm × 4 mm.

Bi-Bi_2K electrodes for three-electrode studies were prepared by breaking off small needles of the as-cast alloy, with approximate dimensions of 500 µm × 500 µm × 2 mm.

Graphite electrodes were prepared by mixing 92 wt.% graphite flakes (SGP5, SEC Carbon) with 8 wt.% sodium carboxymethyl cellulose (CMC) binder (Sigma-Aldrich), using ultrapure deionised water as the solvent. This slurry was cast onto a carbon-coated aluminium current collector (18 µm thick, MTI) and dried in air at room temperature for 24 h, and then under vacuum at 100°C for 24 h. The casting was then punched into 10 mm diameter electrodes, with a loading of approximately 0.5 mg cm^{-2}.

Aluminium electrodes for cyclic voltammetry studies were prepared by cleaning and drying aluminium foil before punching it into 10 mm diameter discs.

Electrolyte Preparation

Prior to preparing electrolytes, potassium bis(fluorosulfonyl)imide (KFSI, 99.9%, Solvionic) was dried under vacuum at 100°C for at least 48 h, triethyl phosphate (TEP, 99.8%+, Sigma-Aldrich) was dried over potassium metal strips for at least 1 week, and 1,2-dimethoxyethane (DME, 99.5% anhydrous, Sigma-Aldrich) was dried over 3 Å molecular sieves.

Electrolytes were prepared gravimetrically by stirring together the desired masses of salt and solvent. The water content of the electrolytes was measured by Karl Fischer titration and recorded to be below 5 ppm.

Electrochemical Measurements

All electrochemical measurements were performed at 30°C (± 0.3°C) in either a Binder Oven or an ESPEC SH-262 temperature and humidity chamber. Symmetric coin cells and three-electrode cells were measured using a Biologic VMP3 potentiostat, and a Biologic BCS battery cycler was used in all other cases.

Two-electrode CR2032 coin cells (304SS, MTI) were assembled with the electrodes described above using a wave spring (304SS, MTI), a single spacer (500 µm thick, 304SS, MTI) and a single glass microfiber separator (grade GF/F, Whatman). 200 µL of electrolyte was used. Unless otherwise stated, all cells were allowed to stabilise for at least 10 h at OCV before testing.

K||In-In_4K cells utilised 2.5 M KFSI TEP and were measured at OCV for 100 h.

K||Bi cells were cycled at approximately C/20 (18.78 µA cm^{-2}) between 0.05–1.5 V vs. K^+/K, with a 1 h rest at OCV between half cycles. For GITT characterisation, the cells were first potassiated at C/20 (18.78 µA cm^{-2}), followed by repeated 15 min C/20 current pulses and 2 h OCV periods until the upper cutoff voltage was reached during depotassiation (Figure 5.8). These measurements were performed with both 2 m KFSI TEP and 1 m KFSI DME.

K||Bi-Bi_2K cells utilised 2 m KFSI TEP and were measured at OCV for 100 h.

Cyclic voltammetry (CV) was performed on K||Al cells by cycling between 1.8 V and 0.05 V vs. K^+/K with a scan rate of 100 µV s^{-1}. Both 2 m KFSI TEP and 1 m KFSI DME were used.

Electrochemical impedance spectroscopy (EIS) was performed on symmetric K||K and Bi-Bi_2K||Bi-Bi_2K cells every 30 min for 100 h at OCV. A frequency range of 200 kHz–500 mHz (6 points per decade) was used with a voltage amplitude of 10 mV. 2 m KFSI TEP was used. Impedance spectra were fitted using the impedance.py Python package,[278] as described in Figures D.2 and D.3. The interfacial resistances in Figure 5.21 were normalised by the resistance after 30 min at rest to ensure temperature equilibration.

EL-Cell ECC-Ref three-electrode cells were constructed using a potassium metal counter electrode, graphite working electrode and Bi-Bi_2K reference electrode. A single glass microfiber separator (grade GF/F, Whatman) was used, with 600 µL of 2 m KFSI

TEP electrolyte. The cells were allowed to rest for 24 h at OCV, and EIS was performed every 30 min (200 kHz–500 mHz, 6 points per decade, 10 mV voltage amplitude). The impedance spectra after 24 h were fit using the impedance.py Python package,[278] as described in Figure D.1 and Tables D.1 and D.2. The graphite electrodes were then cycled at C/10 (13.82 µA cm^{-2} for the cell presented in Figures 5.18 and 5.19) between −1.02 V and 0.93 V vs. K^+/Bi_2K, corresponding to 0.05–2 V vs. K^+/K. The cell was allowed to rest at OCV for 1 h between half cycles.

Atomic Force Microscopy

Atomic force microscopy (AFM) was performed with a Bruker Dimension Icon system. The height map in Figure 5.4 was gathered in the ScanAsyst imaging mode with a ScanAsyst-Air probe (Bruker) at a scan rate of 1 Hz (512 px × 512 px). To determine the thickness of the bismuth film it was scratched with the tip of stainless steel tweezers to produce a sharp step (Figure 5.5). This was then imaged in contact mode using an SNL-B probe (Bruker) at a scan rate of 0.5 Hz (256 px × 256 px). Gwyddion software was used for data analysis.[216]

Electron Microscopy

Samples for scanning electron microscopy (SEM) were polished using silicon carbide grinding papers with grits from 800–4000, followed by final polishing with 1 µm and 0.5 µm diamond polishing pads (Kemet).

SEM and energy-dispersive X-ray spectroscopy (EDX) were performed within a TESCAN MIRA-3 FEG-SEM equipped with an Oxford Instruments EDX detector. SEM imaging and EDX mapping were both performed with a beam voltage of 10 kV. The SEM opens into an MBraun glovebox, preventing air exposure. ImageJ software was used to quantify phase fractions from backscattered electron (BSE) data (Figure 5.13).[270]

Nanoindentation

The Bi_2K sample for nanoindentation was mounted on an aluminium SEM stub with two-part Araldite epoxy and was polished in the same way as the SEM samples.

Nanoindentation was performed using a Bruker PI 89 nanoindenter contained within the TESCAN MIRA-3 FEG-SEM. A diamond Berkovich indentation tip (Hysitron) was

used. 29 indents were performed, where the load was linearly increased over 5 s to a maximum load of 200 mN, held for 2 s, then linearly unloaded over 5 s (Figure 5.14c). Young's modulus and hardness were calculated from indentation moduli using diamond values of $E = 1220$ GPa, $\nu = 0.07$.[279]

X-ray Photoelectron Spectroscopy

Samples for X-ray photoelectron spectroscopy (XPS) were prepared by submerging potassium metal and Bi-Bi_2K electrodes in 1 mL of 2 m KFSI TEP each. These were then kept in a glovebox antechamber heated to 30°C for 20 h before they were removed from the electrolyte and rinsed three times each with 200 µL of pure TEP to remove residual salt. The excess TEP was then removed with tissue, taking care not to touch the electrode surface. Samples were then immediately transferred to the XPS intro chamber using a vacuum transfer vessel (ULVAC PHI) to prevent air exposure.

XPS was performed with an ULVAC PHI Versaprobe III XPS system generating monochromatic $Al_{K\alpha}$ X-rays (1486.6 eV, 15 kV anode voltage, 25 W beam power) under ultrahigh vacuum (UHV) conditions (10^{-7}–10^{-6} Pa). A 500 µm × 500 µm area of each sample was analysed. Survey spectra were gathered at a pass energy of 224 eV, and 55 eV was used for core-level spectra. In-built electron and low-energy Ar^+ sources were utilised for neutralisation. Depth profiling was achieved with consecutive XPS analysis and Ar^+ sputtering (2 kV, 3 mm × 3 mm) for a total of 60 min. Acquired spectra were fitted with Gaussian-Lorentzian product lineshapes (with an asymmetric lineshape necessary to fit the Bi^0 Bi 4f doublet peak) using CasaXPS software.[217] Due to the lack of an intense adventitious carbon peak, all spectra were charge referenced to the KF F 1s peak at 684.2 eV.[186] Atomic percentages were estimated using Scofield relative sensitivity factors.

6

Conclusion and Future Research

In conclusion, this thesis has highlighted the important role that liquid-state lithium metal batteries (LMBs) and potassium-ion batteries (KIBs) could play in accelerating a clean energy transition. LMBs, with both a high energy and power density, have the potential to outperform current lithium-ion battery (LIB) chemistries and find applications in novel technologies with strict performance requirements. KIBs, on the other hand, are a promising complementary technology to lower-energy-density lithium iron phosphate-based LIBs and their advantages stem from their compatibility with current manufacturing processes, the ability of K^+ to reversibly intercalate into graphite, and the abundance of raw materials required to produce them. However, neither LMBs nor KIBs currently display the performance and cycle life necessary for widespread commercial use, requiring further electrolyte optimisation.

The electrolyte plays a crucial role in determining both cell performance and cycling stability. Ionic transport and thermodynamic properties control the evolution of salt concentration gradients and overpotentials during cycling, impacting energy efficiency and maximum cycling rates. LMB and KIB anodes additionally operate outside of the electrochemical stability window of the electrolyte, leading to electrolyte reduction and the formation of a solid electrolyte interphase (SEI). Ideally this SEI is stable and passivating, but it is often observed to form continuously during cycling, leading to significant capacity decay. Rational electrolyte design is currently hindered by a lack of understanding of the

interrelations between electrolyte chemistry, transport, and SEI properties. The work presented in this thesis begins to bridge these knowledge gaps.

In Chapter 3 the concentration-dependent ionic transport and thermodynamic properties are characterised and compared in equivalent lithium- and potassium-ion electrolyte systems. It is revealed that the larger size of the K^+ cation reduces species-species interactions, resulting in higher salt diffusivities and cation transference numbers. However, poorer salt dissociation was also observed, so the ionic conductivity is lower than the lithium-ion electrolyte at low concentration. Nevertheless, the properties of the potassium-ion electrolyte make it superior for high-rate applications.

Moving forward, *operando* Raman gradient analysis should be explored for electrolyte transport characterisation due to its time and resource efficiency. Transport properties could be characterised as a function of temperature, providing greater insight into the factors controlling them, and the impact that electrolyte additives have on transport should be investigated. Additionally, to better understand KIB rate performance it would be necessary to measure the transport and thermodynamic properties of the electrode materials, enabling accurate full-cell simulations to be performed.

In Chapter 4 the chemistry of the SEI that forms on both lithium and potassium metal is probed using X-ray photoelectron spectroscopy (XPS) depth profiling. Chemical SEI formation on lithium is investigated as the temperature, salt concentration, time and solvent are systematically varied. It is revealed that electrolyte solvation plays an important role in controlling the species that are available for reduction at the lithium surface. At low concentration and temperature the SEI is rich in organic components from solvent reduction as this dominates the solvation shell, but the SEI becomes more anion derived at high temperature and concentration and when using a more weakly solvating solvent. Comparison with impedance results suggest that the organic-rich SEI is porous, allowing electrolyte impregnation, and it may densify over time, while the anion-derived SEI has a higher ionic conductivity. On lithium metal Li_2O is a major SEI component but no equivalent species is observed on potassium. Instead the SEI formed on electrodeposited potassium displays an intense peak that could be assigned

to KHF_2, and the differences in SEI chemistry are related to steric effects due to the different ionic radii of the Li^+ and K^+ cations.

The results in Chapters 3 and 4 demonstrate that electrolyte solvation is responsible for controlling both ionic transport and SEI formation, providing opportunities for rational electrolyte design. However, the ideal properties of an SEI are still not known, so future work should focus on understanding the link between SEI chemistry and electrochemical performance. Additionally, other techniques to identify the chemical species in the SEI, such as transmission electron microscopy, should be used to complement the XPS analysis presented here and determine the distribution of SEI species, and atomic force microscopy can be used to probe the mechanical properties of the SEI. The development of operando characterisation techniques to probe the SEI under realistic conditions is also still an important avenue for future research.

Finally, in Chapter 5 a two-phase Bi-Bi_2K alloy is developed as a reference electrode for accurate electrochemical characterisation in KIBs. The alloy displays a stable potential of 1.07 V vs. K^+/K, which is demonstrated to significantly reduce the amount of electrolyte decomposition that occurs compared to potassium metal. Its use as a reference electrode in place of potassium metal would enable KIB studies without influence from decomposition products formed at the potassium electrode, so it will be vital for accurate studies of the SEI that forms of graphite electrodes. Additionally, its high melting point would enable KIB cycling experiments to be performed at elevated temperatures.

The Bi-Bi_2K alloy is unable to function as a counter electrode in its current form, so the development of a stable counter electrode for KIBs is still a critical research area. Due to the proven potential stability of the Bi-Bi_2K alloy here such a counter electrode does not necessarily need to display a flat potential profile, but its potential should remain within the electrochemical stability window of the electrolyte. Alloying electrodes are unlikely to meet this requirement, so low-voltage cathode materials should be explored, such as the potassium iron hexacyanoferrate Prussian blue analogue.

In summary, degradation processes in LMBs and KIBs can only be understood through accurate characterisation of electrodes, electrolytes and their resulting interphases, providing guidelines for rational solutions to the challenges facing their commercialisation.

Appendices

A

Solid Electrolyte Interphase Reporting Checklist

Contents

A.1 Excess-Lithium Cells 148
A.2 Zero-Excess-Lithium Cells 150

A.1 Excess-Lithium Cells

□ = essential to report, ○ = should be reported where possible

1. **Lithium metal**

    □ Supplier

    □ Processing

        □ Surface cleaning steps

        □ Electrode preparation process

    ○ Surface characterisation

        ○ Measure surface topography with AFM

        ○ Determine native passivation layer chemistry with XPS

2. **Electrolyte**

    □ Salt(s), solvent(s) and additives

- ☐ Suppliers
- ☐ Concentrations of every component
- ☐ Processing/drying conditions

○ Purity

- ○ Measure water content with Karl Fischer titrator
- ○ Verify purity of solvents with ^{1}H and ^{13}C NMR
- ○ Verify purity of fluorinated salts/solvents with ^{19}F NMR

3. **SEI formation**

☐ Cell setup

- ☐ Cell geometry including lithium thickness and details about the separator used
- ☐ Volume of electrolyte used
- ☐ Counter electrode used

☐ Formation conditions

- ☐ Temperature during formation
- ☐ Formation time
- ☐ Current/potential history during formation

4. **Sample preparation**

☐ Rinsing

- ☐ Details of the solvent and the volume used

☐ Drying

- ☐ Drying temperature and time
- ☐ Atmosphere/vacuum level of drying environment

A.2 Zero-Excess-Lithium Cells

□ = essential to report, ○ = should be reported where possible

1. **Current collector**
    - □ Current collector material and supplier
    - □ Processing
        - □ Surface cleaning steps
        - □ Electrode preparation process
    - ○ Surface characterisation
        - ○ Measure surface topography with AFM
        - ○ Determine surface chemistry with XPS
2. **Electrolyte**
    - □ Salt(s), solvent(s) and additives
        - □ Suppliers
        - □ Concentrations of every component
        - □ Processing/drying conditions
    - ○ Purity
        - ○ Measure water content with Karl Fischer titrator
        - ○ Verify purity of solvents with ^{1}H and ^{13}C NMR
        - ○ Verify purity of fluorinated salts/solvents with ^{19}F NMR
3. **SEI formation**
    - □ Cell setup
        - □ Cell geometry and details about the separator used
        - □ Volume of electrolyte used
        - □ Counter electrode used
    - □ Formation conditions

- ☐ Temperature during formation
- ☐ Formation time
- ☐ Current/potential history during formation

4. **Sample preparation**

- ☐ Rinsing
  - ☐ Details of the solvent and the volume used
- ☐ Drying
  - ☐ Drying temperature and time
  - ☐ Atmosphere/vacuum level of drying environment

B

Additional X-ray Photoelectron Spectroscopy Data

Contents

B.1 Potassium Metal 153
B.2 LiFSI in G4 155
B.3 LiFSI in DME 162
B.4 KFSI in DME 163
B.5 KFSI in TEP 165

B.1 Potassium Metal

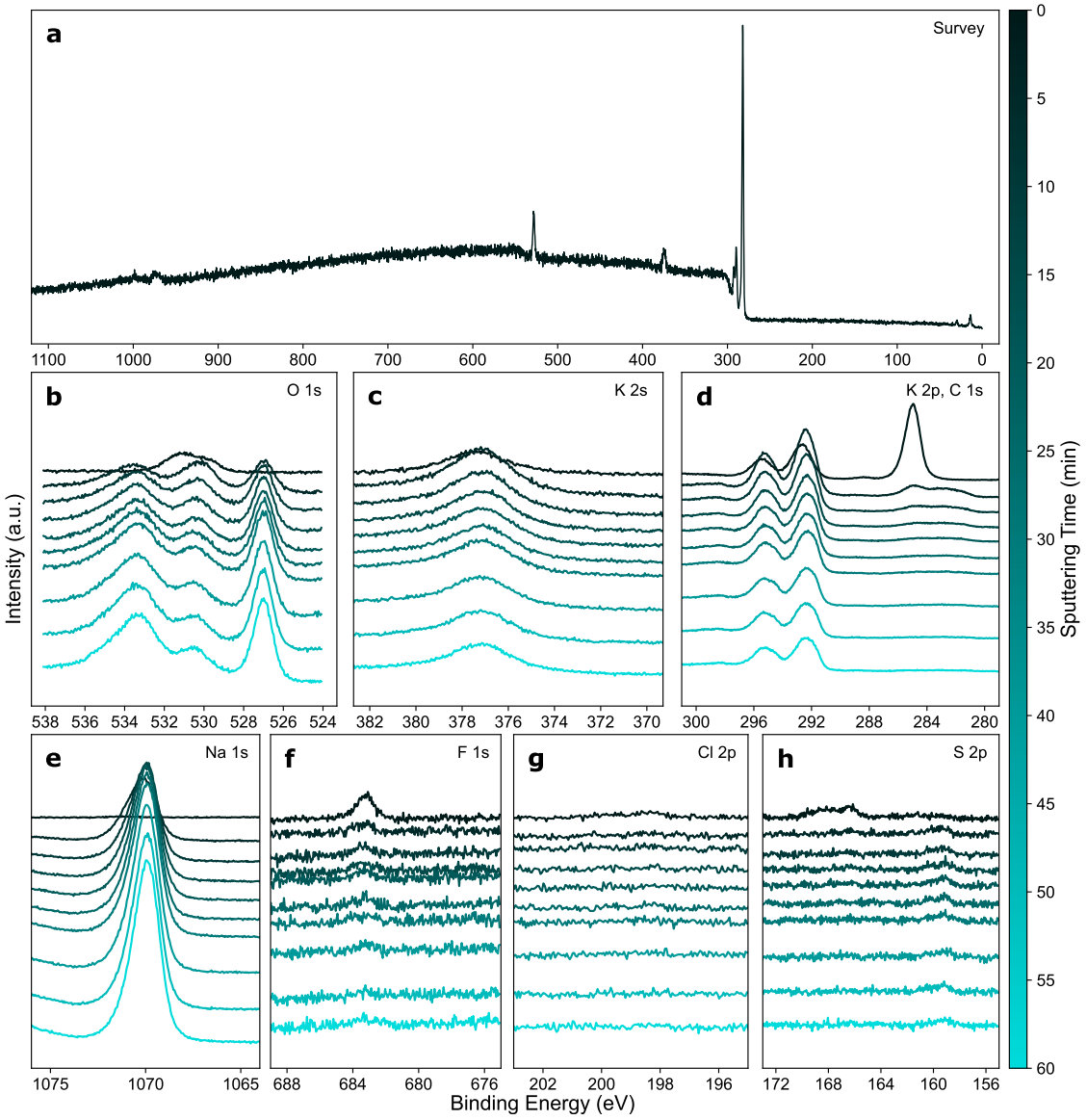


Figure B.1: XPS depth profiles from a potassium metal electrode produced using the standard preparation. (a) Survey spectrum. (b) O 1s region. (c) K 2s region. (d) K 2p and C 1s regions. (e) Na 1s region. (f) F 1s region. (g) Cl 2p region. (h) S 2p region.

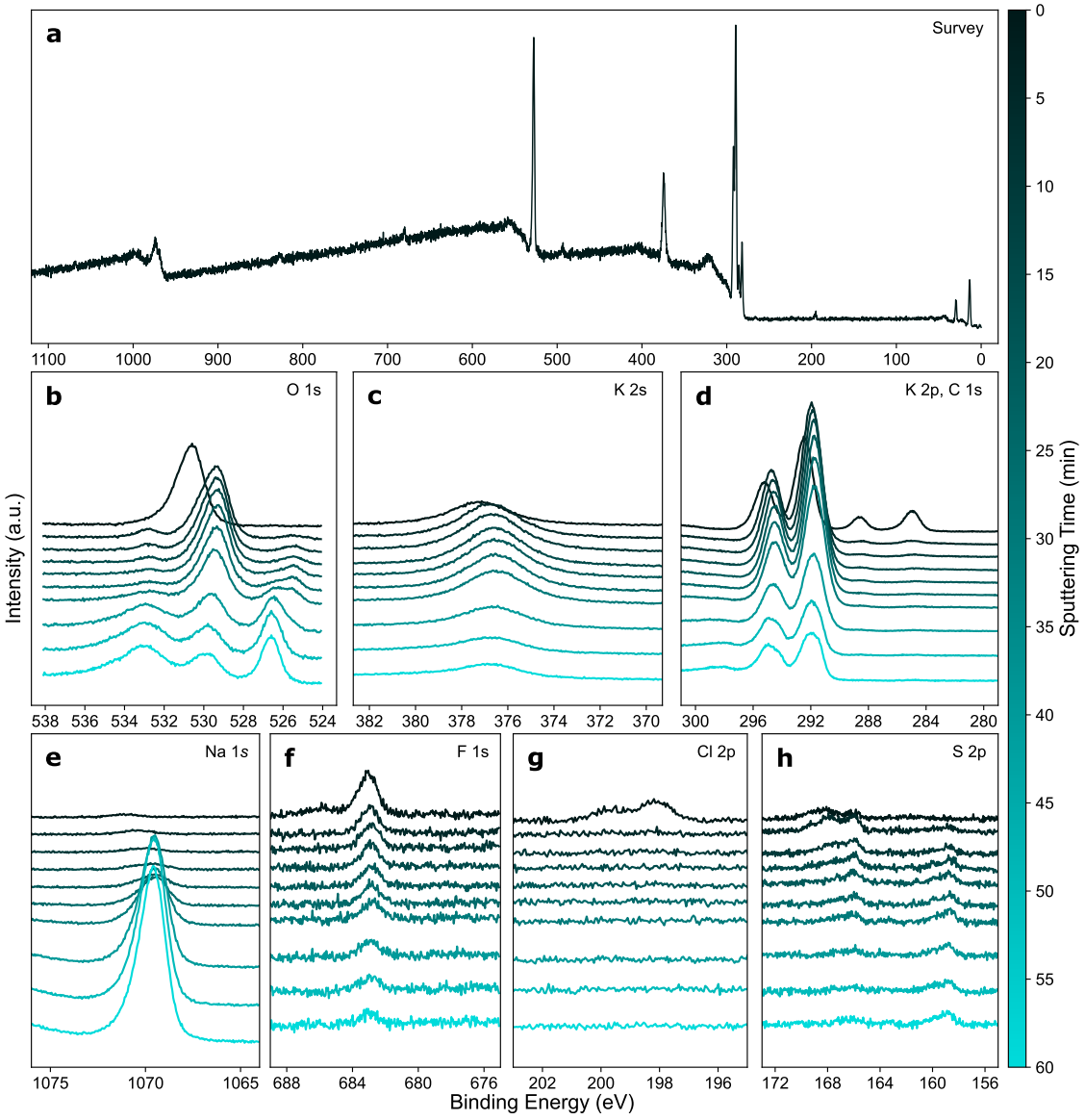


Figure B.2: XPS depth profiles from a processed potassium metal electrode. Survey spectrum. (b) O 1s region. (c) K 2s region. (d) K 2p and C 1s regions. (e) Na 1s region. (f) F 1s region. (g) Cl 2p region. (h) S 2p region.

B.2 LiFSI in G4

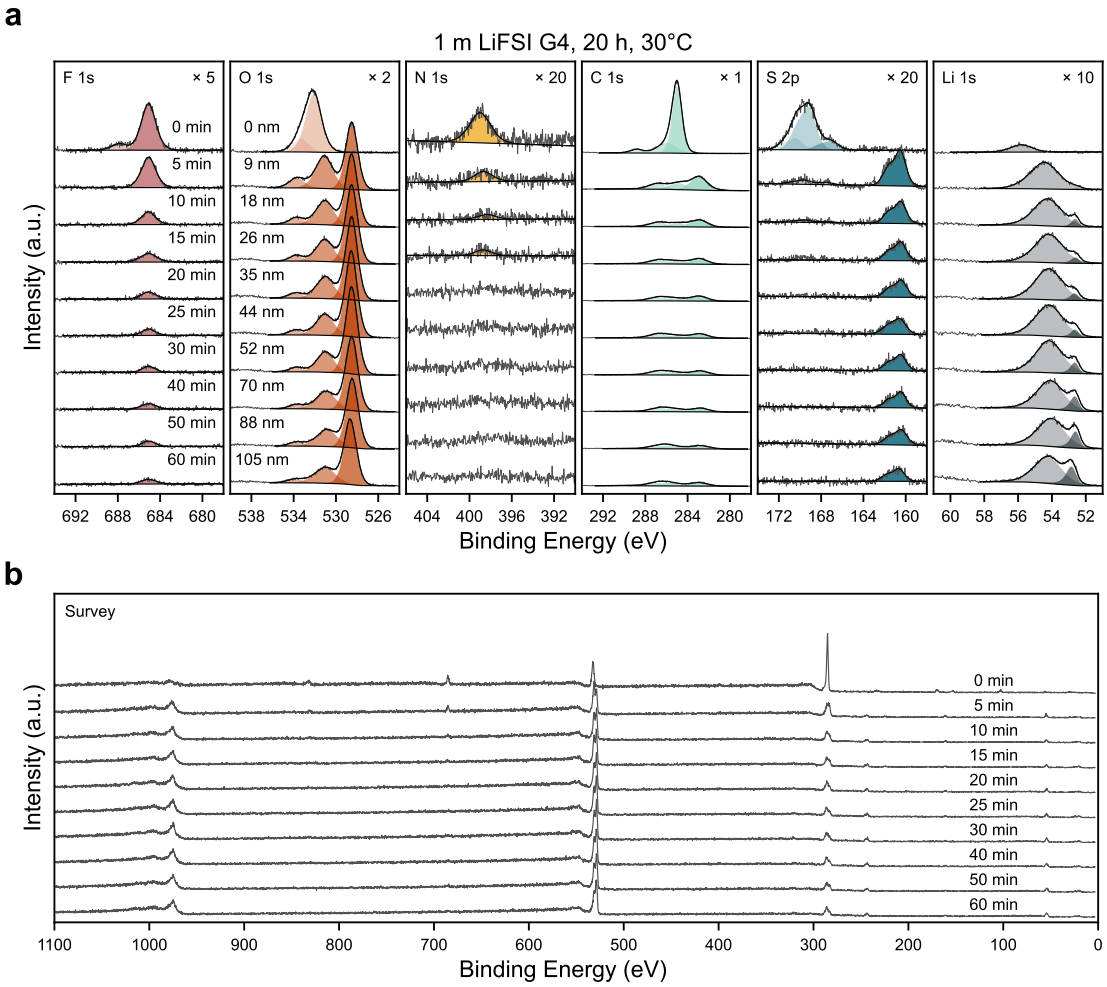


Figure B.3: XPS depth profiles from an SEI sample formed in 1 m LiFSI G4 for 20 h at 30°C without normalisation. (a) F 1s, O 1s, N 1s, C 1s, S 2p and Li 1s spectra. (b) Survey spectra.

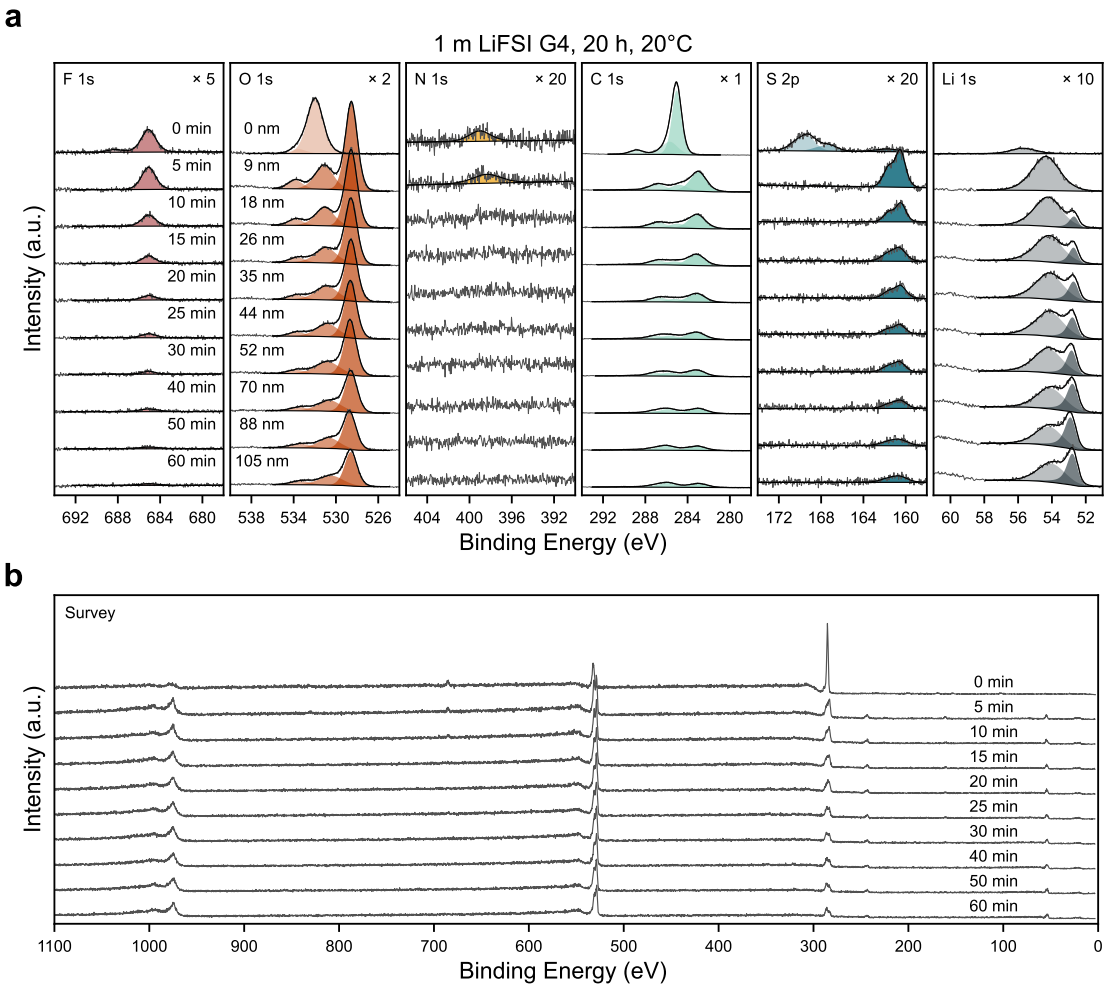


Figure B.4: XPS depth profiles from an SEI sample formed in 1 m LiFSI G4 for 20 h at 20°C without normalisation. (a) F 1s, O 1s, N 1s, C 1s, S 2p and Li 1s spectra. (b) Survey spectra.

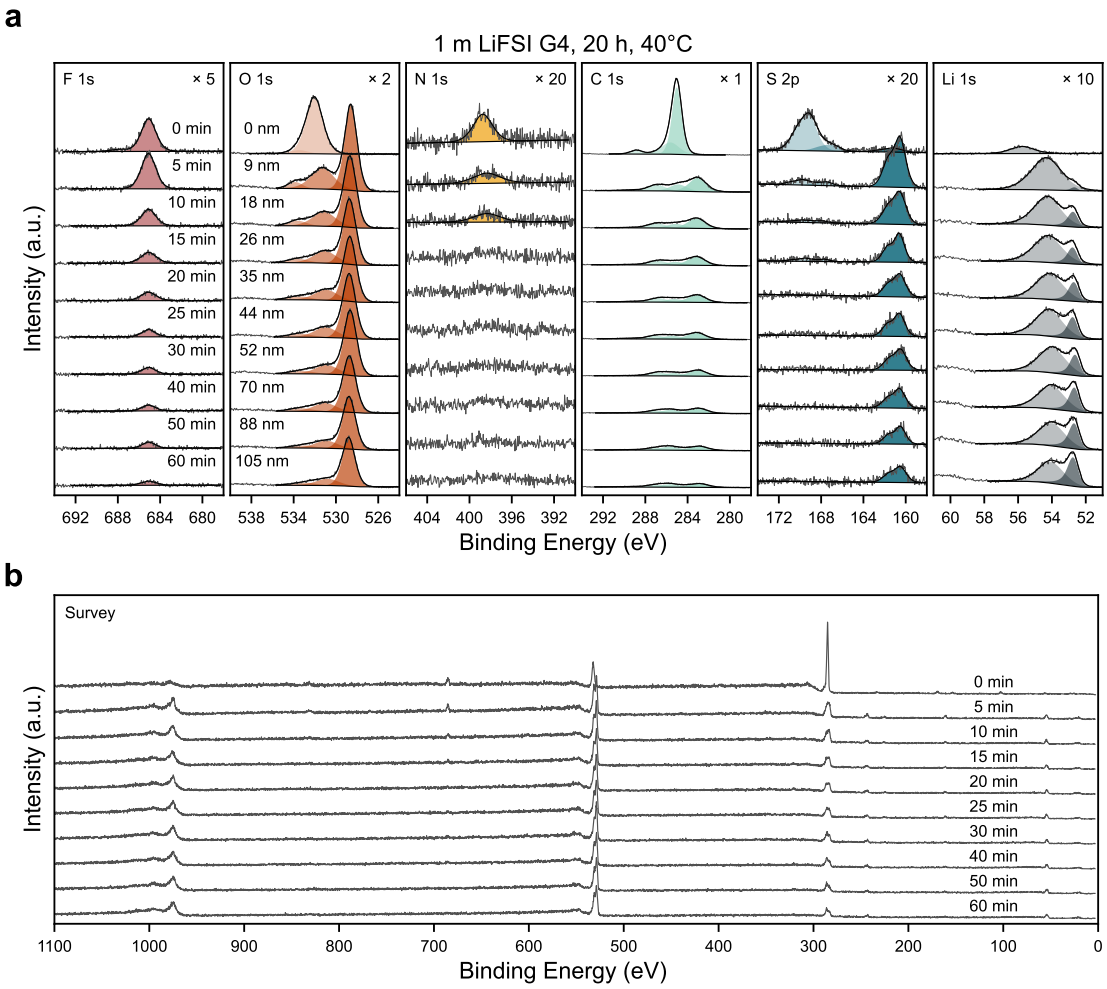


Figure B.5: XPS depth profiles from an SEI sample formed in 1 m LiFSI G4 for 20 h at 40°C without normalisation. (a) F 1s, O 1s, N 1s, C 1s, S 2p and Li 1s spectra. (b) Survey spectra.

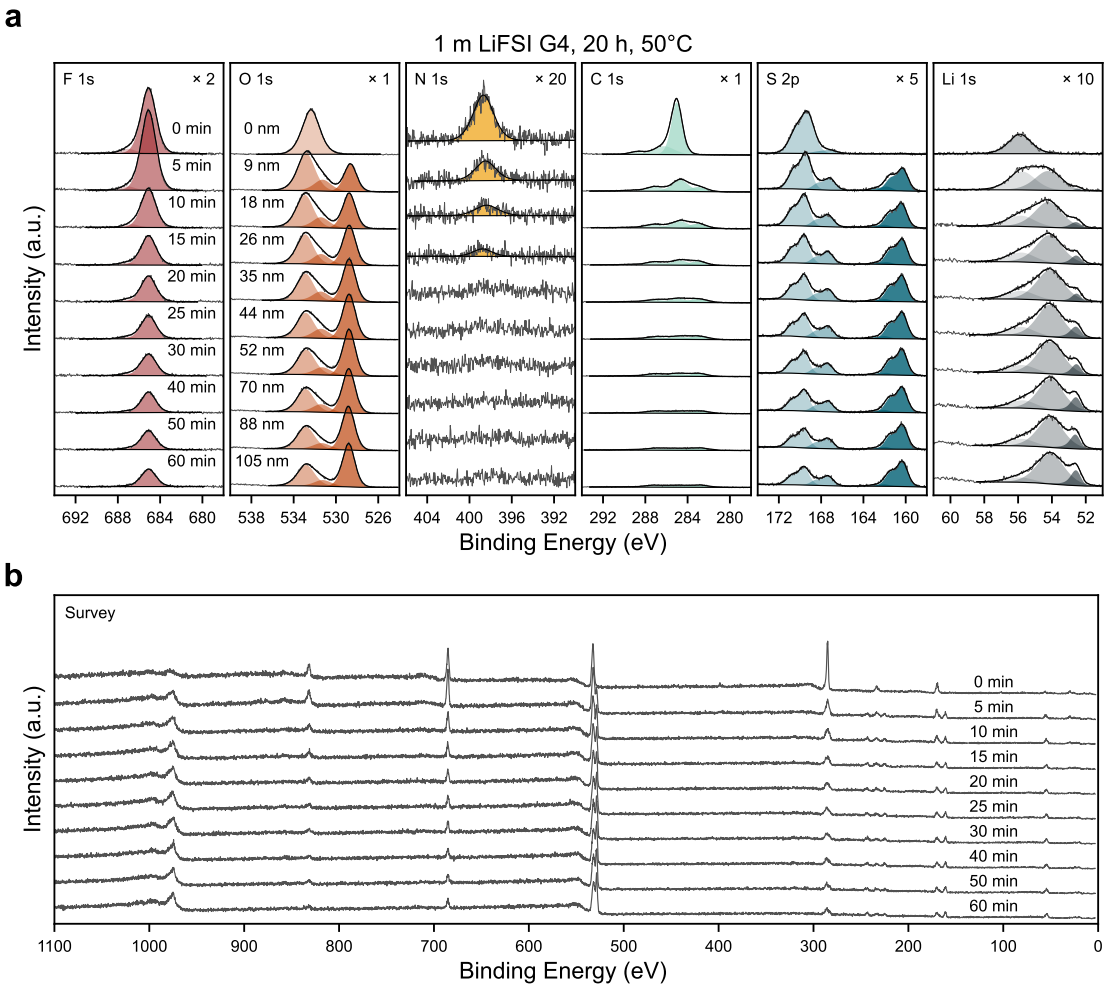


Figure B.6: XPS depth profiles from an SEI sample formed in 1 m LiFSI G4 for 20 h at 50°C without normalisation. (a) F 1s, O 1s, N 1s, C 1s, S 2p and Li 1s spectra. (b) Survey spectra.

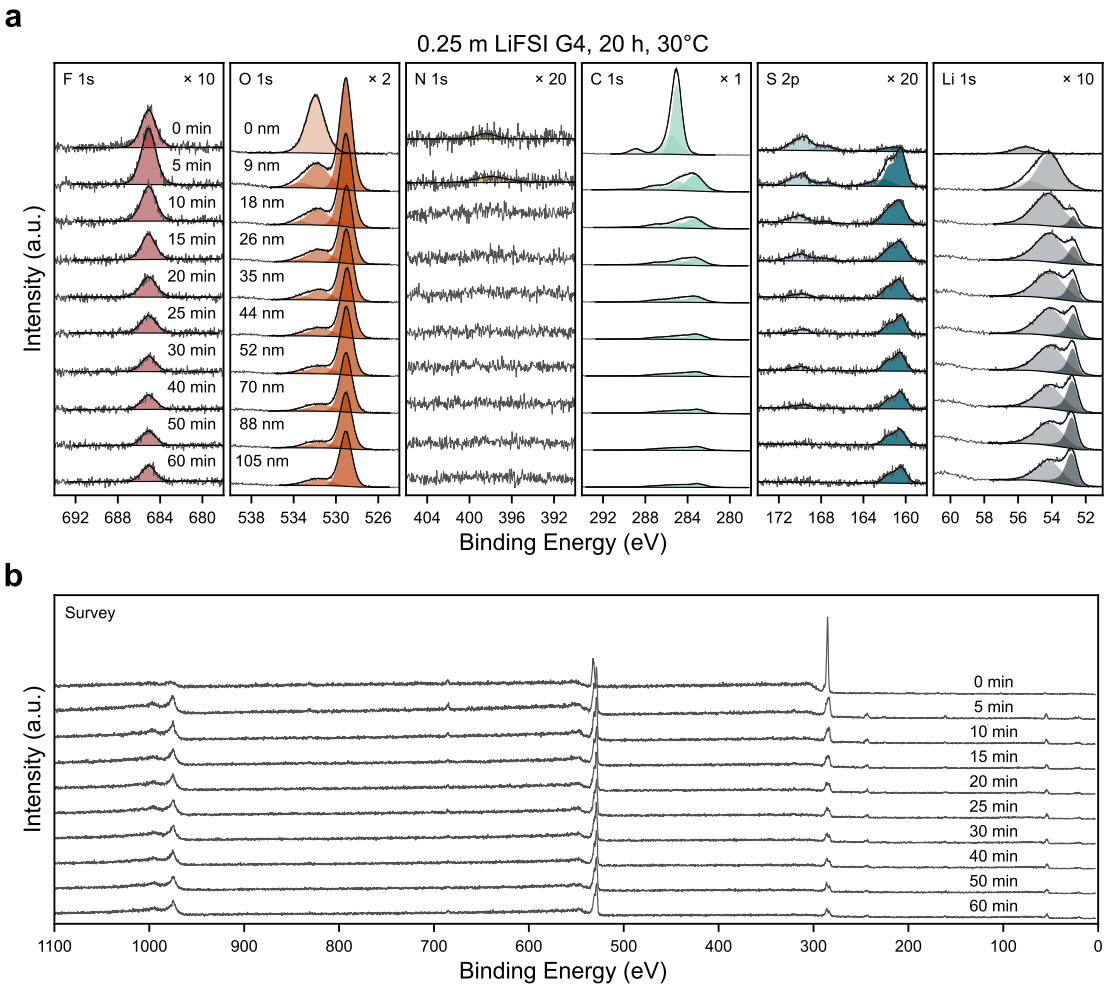


Figure B.7: XPS depth profiles from an SEI sample formed in 0.25 m LiFSI G4 for 20 h at 30°C without normalisation. (a) F 1s, O 1s, N 1s, C 1s, S 2p and Li 1s spectra. (b) Survey spectra.

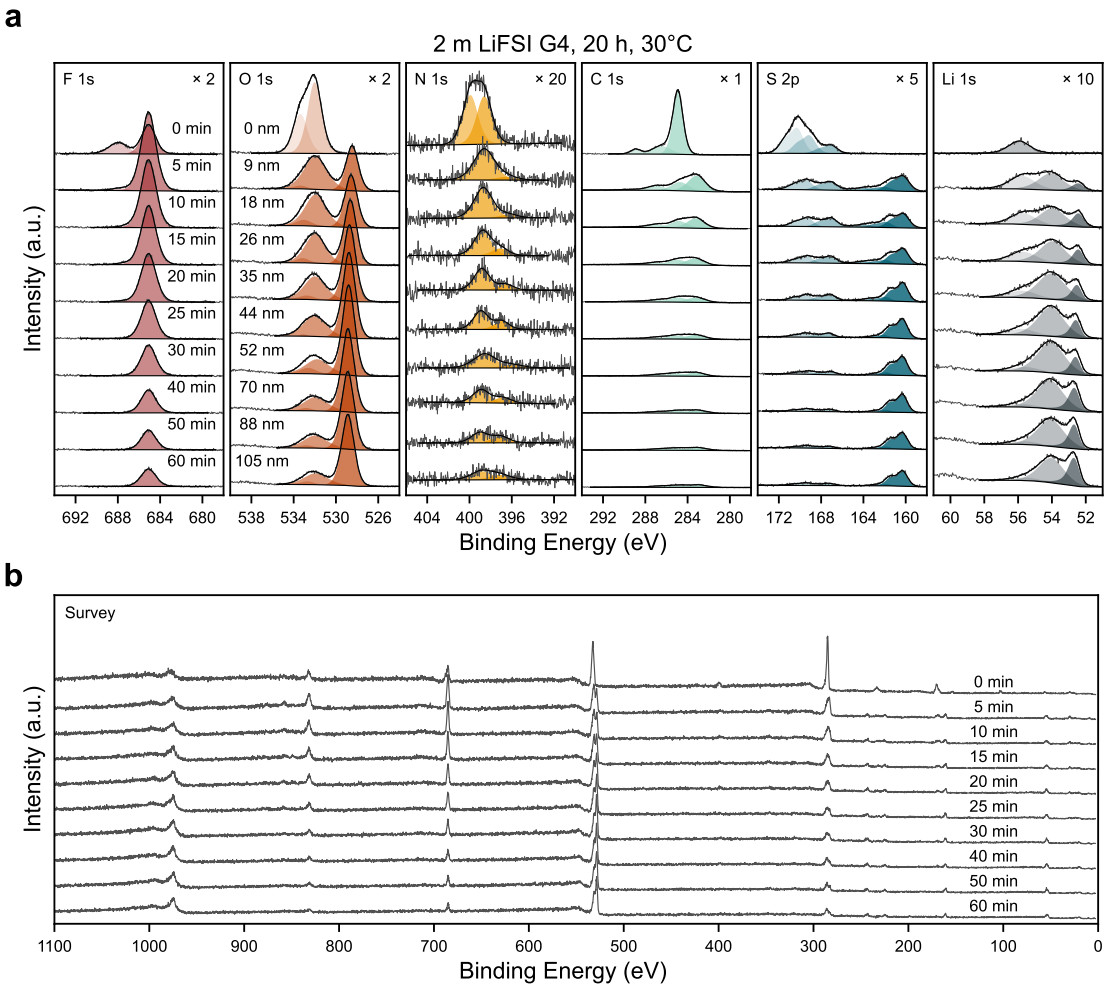


Figure B.8: XPS depth profiles from an SEI sample formed in 2 m LiFSI G4 for 20 h at 30°C without normalisation. (a) F 1s, O 1s, N 1s, C 1s, S 2p and Li 1s spectra. (b) Survey spectra.

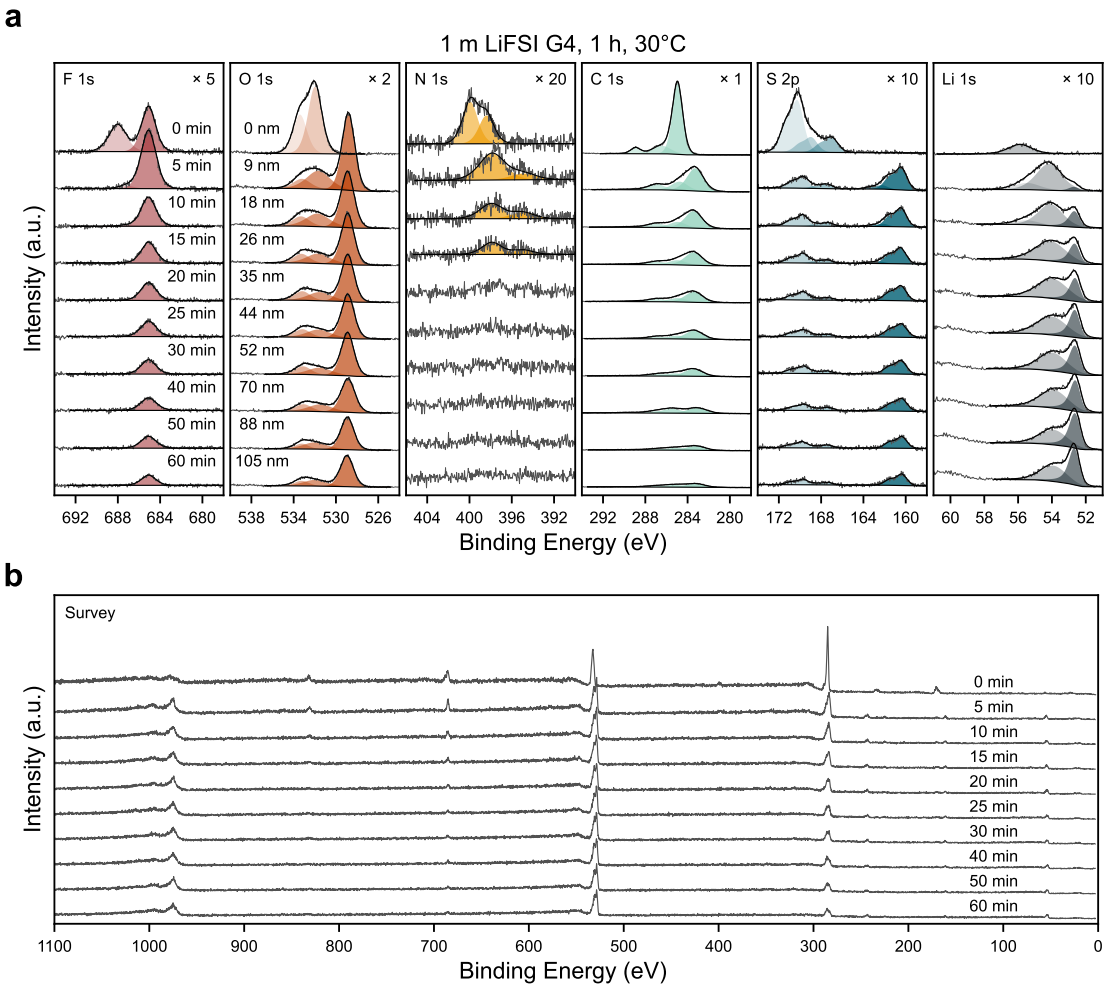


Figure B.9: XPS depth profiles from an SEI sample formed in 1 m LiFSI G4 for 1 h at 30°C without normalisation. (a) F 1s, O 1s, N 1s, C 1s, S 2p and Li 1s spectra. (b) Survey spectra.

B.3 LiFSI in DME

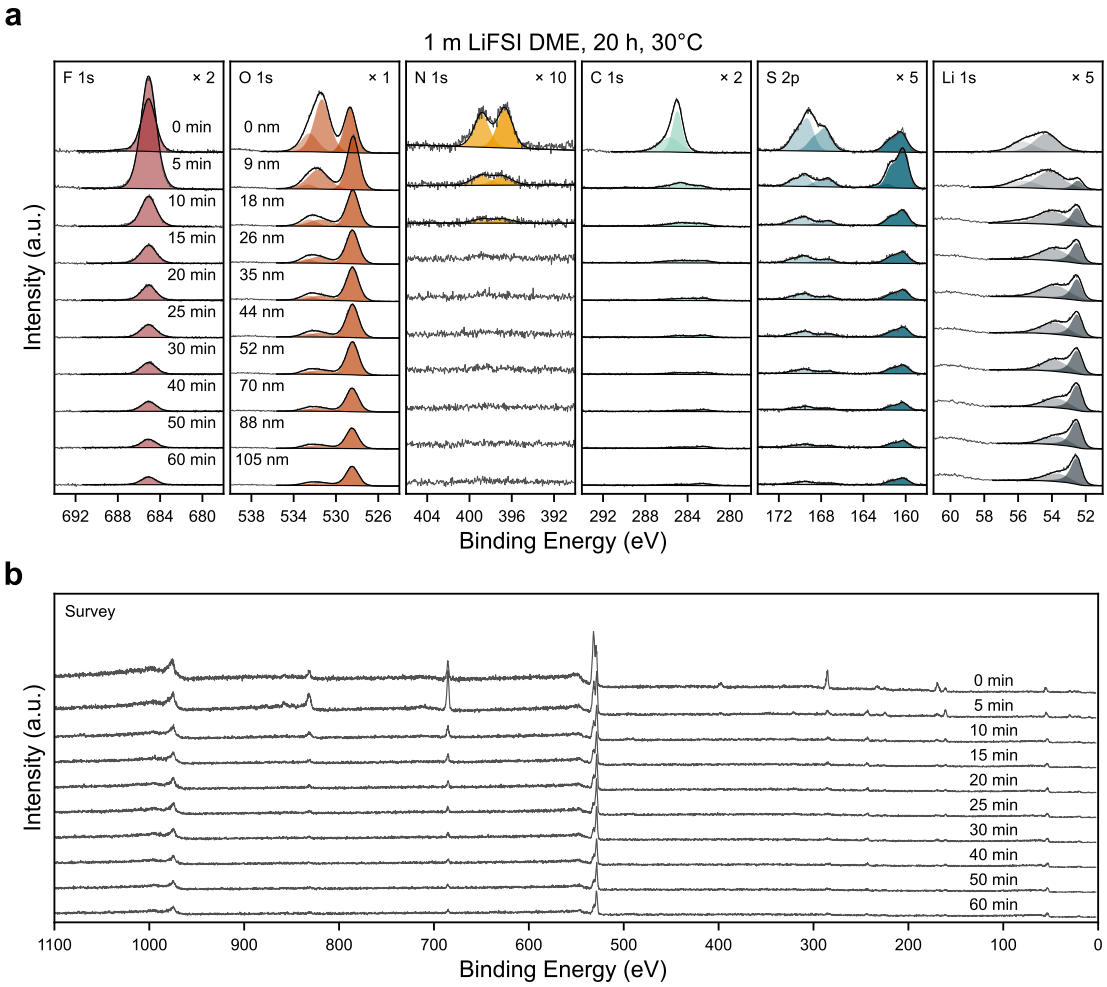


Figure B.10: XPS depth profiles from an SEI sample formed in 1 m LiFSI DME for 20 h at 30°C without normalisation. (a) F 1s, O 1s, N 1s, C 1s, S 2p and Li 1s spectra. (b) Survey spectra.

B.4 KFSI in DME

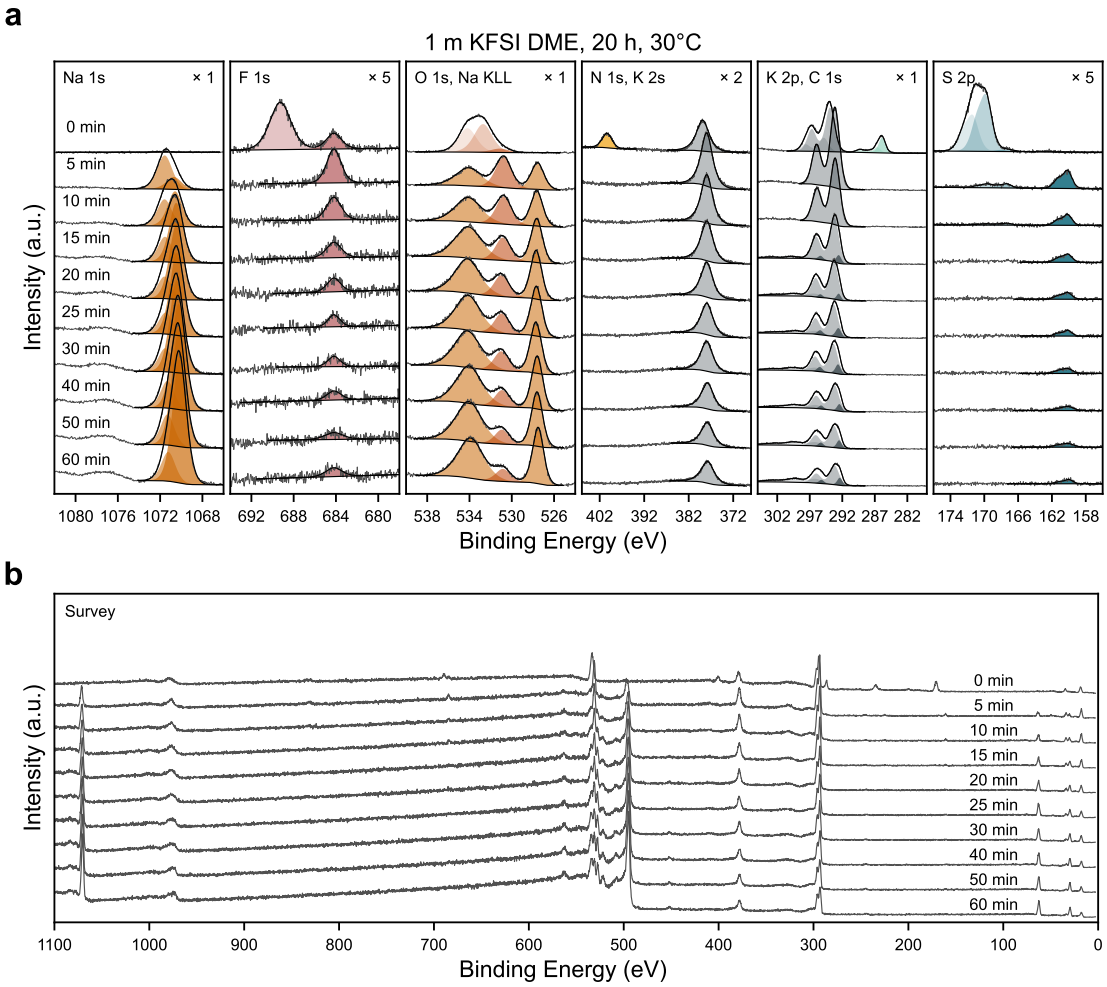


Figure B.11: XPS depth profiles from an SEI sample formed in 1 m KFSI DME for 20 h at 30°C without normalisation. (a) Na 1s, F 1s, O 1s, N 1s and K 2s, K 2p and C 1s, and S 2p spectra. (b) Survey spectra.

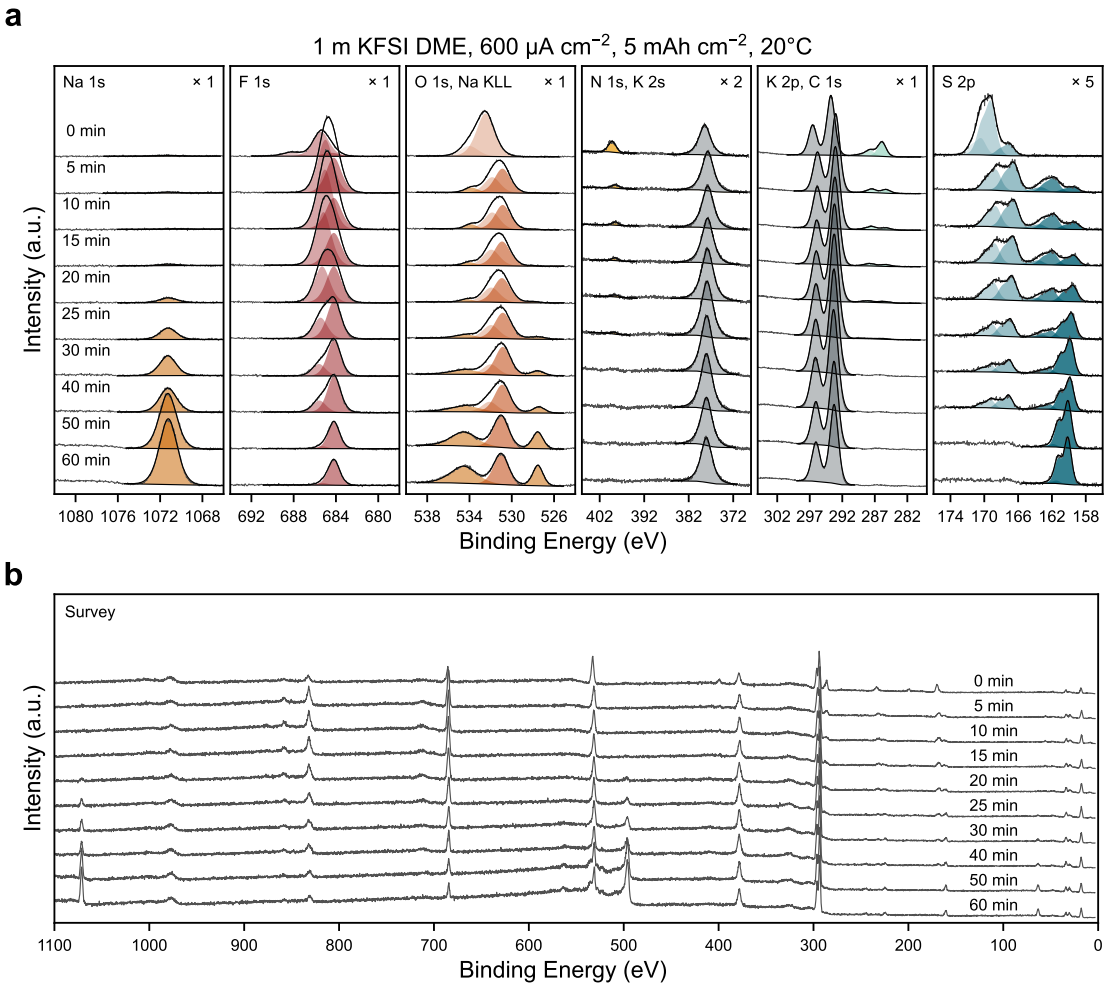


Figure B.12: XPS depth profiles from an SEI sample formed in 1 m KFSI DME by plating at 600 µA cm^{-2} to a capacity of 5 mAh cm^{-2} at 20°C without normalisation. (a) Na 1s, F 1s, O 1s, N 1s and K 2s, K 2p and C 1s, and S 2p spectra. (b) Survey spectra.

B.5 KFSI in TEP

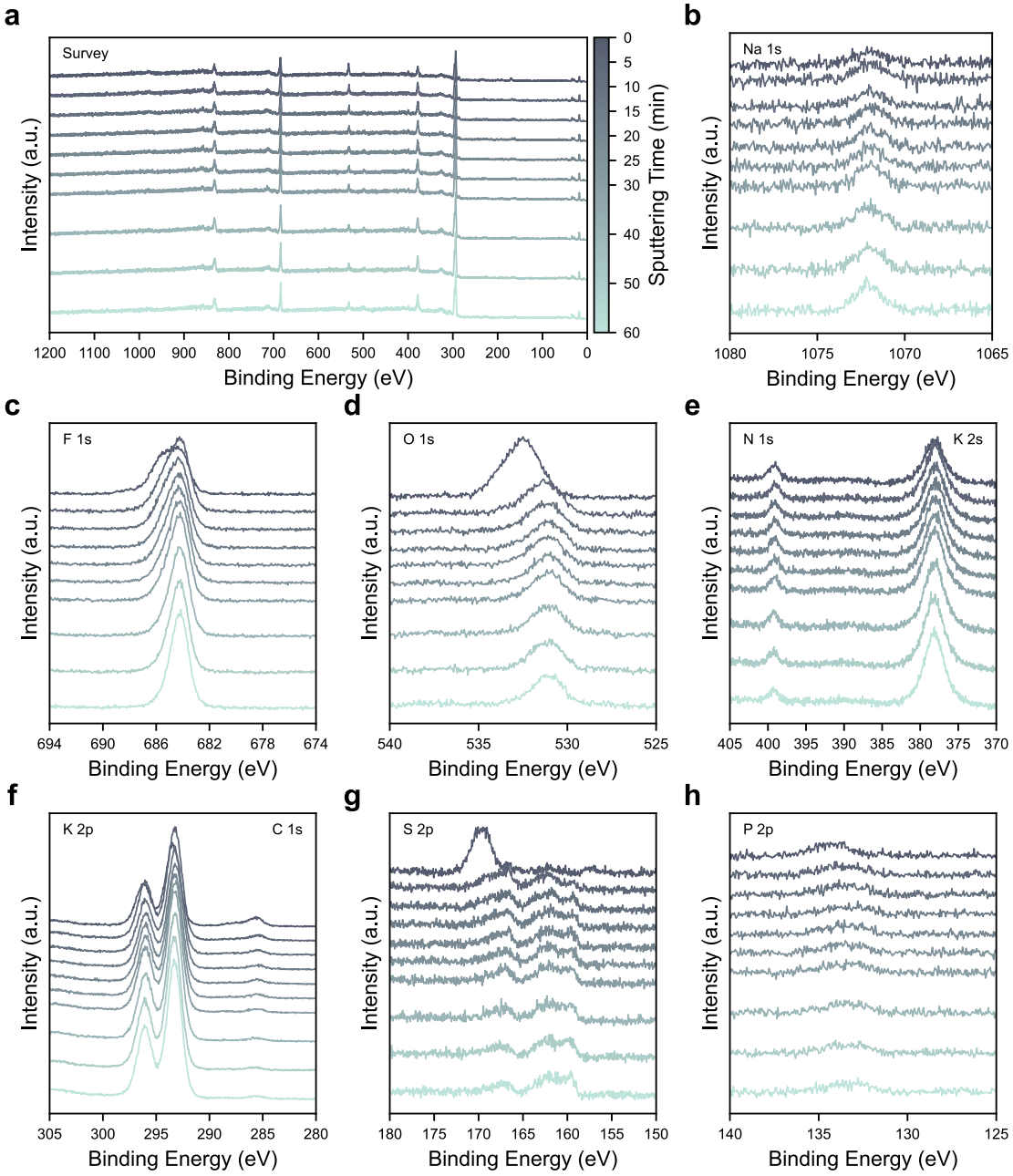


Figure B.13: Full potassium metal SEI XPS spectra. (a) Survey spectra. (b) Na 1s region. (c) F 1s region. (d) O 1s region. (e) N 1s and K 2s regions. (f) K 2p and C 1s regions. (g) S 2p region. (h) P 2p region. The SEI was formed by submersion in 2 m KFSI TEP for 20 h at 30°C.

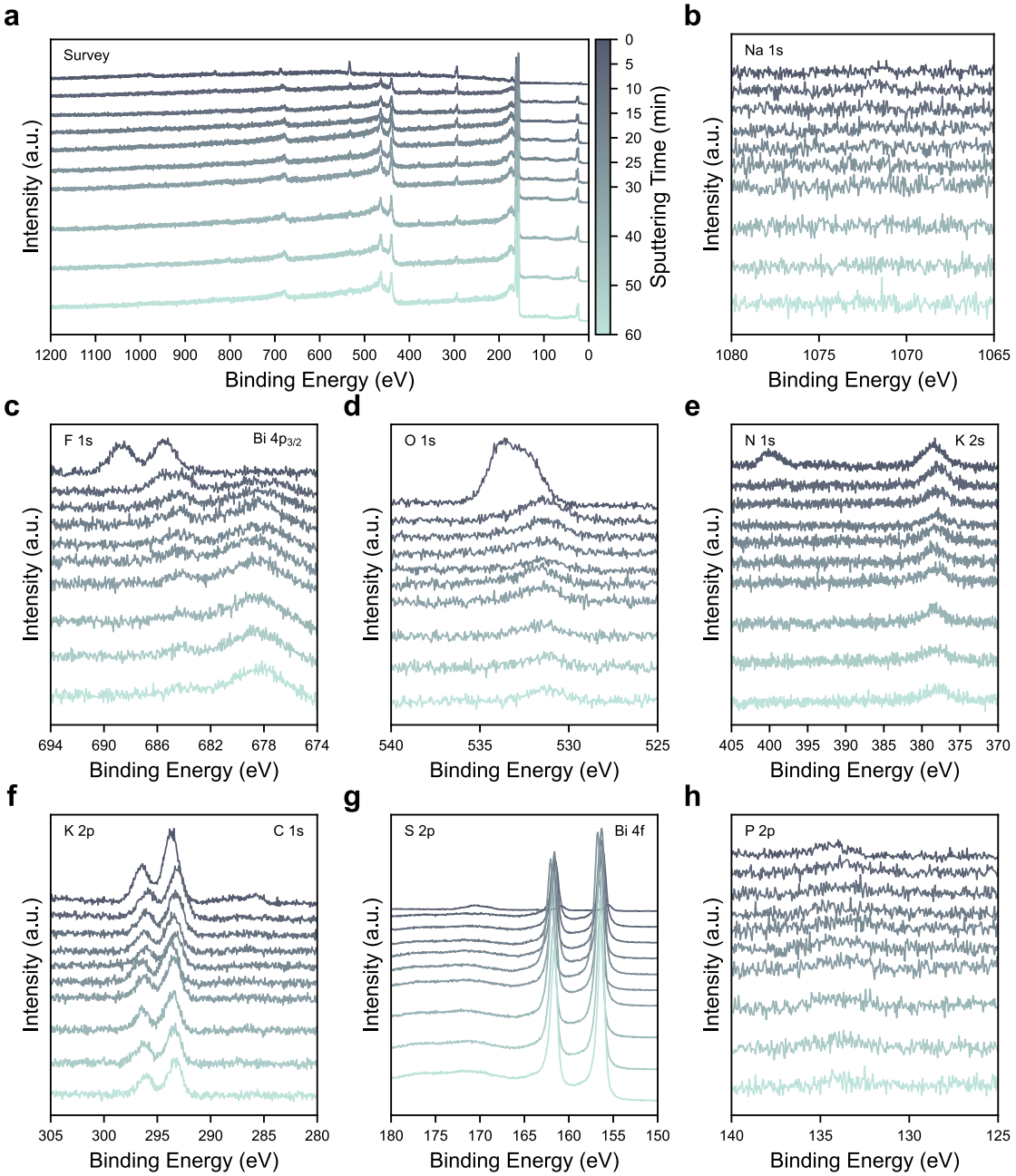


Figure B.14: Full Bi-Bi_2K SEI XPS spectra. (a) Survey spectra. (b) Na 1s region. (c) F 1s and Bi $4p_{3/2}$ regions. (d) O 1s region. (e) N 1s and K 2s regions. (f) K 2p and C 1s regions. (g) S 2p and Bi 4f regions. (h) P 2p region. The SEI was formed by submersion in 2 m KFSI TEP for 20 h at 30°C.

C

Electrolyte Transport Property Parameterisation

Contents

C.1 LiFSI in DME 167
C.2 KFSI in DME 168

All transport and thermodynamic properties measured in Chapter 3 were parameterised by fitting functions to the data points. If the functional form was known (Equation 3.4 for κ) then non-linear least squares fitting was used. Otherwise, least squares polynomial fits were used, with inverse variance weighting for the case of t_+^0.

The parameterised forms of t_+^0, κ, χ_M and D are given as a function of concentration (either molar, c, or molal, c_m) for LiFSI and KFSI in DME. All fits are from data gathered in the concentration range 0.25–2 m.

Approximate conversions between molal and molar concentrations are also provided.

C.1 LiFSI in DME

Cation transference number, t_+^0:

$$t_+^0 = 0.352 \tag{C.1}$$

Ionic conductivity, κ (mS cm^{-1}):

$$\kappa = 16.286 \left(\frac{c}{1.158}\right)^{1.085} \exp\left(-0.426(c-1.158)^2 - \frac{1.085}{1.158}(c-1.158)\right) \tag{C.2}$$

Thermodynamic factor, χ_M:

$$\chi_M = (1 + 0.052c_m)(1 - 2.663{c_m}^{\frac{1}{2}} + 2.287c_m) \tag{C.3}$$

Salt diffusivity, D ($\mathrm{m}^2\ \mathrm{s}^{-1}$):

$$D = 5.312 \times 10^{-10} - (2.358 \times 10^{-11})c_m \tag{C.4}$$

Concentration conversion:

$$c = 0.873c_m - 0.043{c_m}^2 \tag{C.5}$$

C.2 KFSI in DME

Cation transference number, t_+^0:

$$t_+^0 = 0.497 - 0.074c_m \tag{C.6}$$

Ionic conductivity, κ ($\mathrm{mS\ cm}^{-1}$):

$$\kappa = 15.970 \left(\frac{c}{1.493}\right)^{1.620} \exp\left(0.023(c - 1.493)^2 - \frac{1.620}{1.493}(c - 1.493)\right) \tag{C.7}$$

Thermodynamic factor, χ_M:

$$\chi_M = (1 + 0.071c_m)(1 - 1.833{c_m}^{\frac{1}{2}} + 1.608c_m) \tag{C.8}$$

Salt diffusivity, D ($\mathrm{m}^2\ \mathrm{s}^{-1}$):

$$D = 1.003 \times 10^{-9} - (3.104 \times 10^{-10})c_m + (3.633 \times 10^{-11}){c_m}^2 \tag{C.9}$$

Concentration conversion:

$$c = 0.859c_m - 0.051{c_m}^2 \tag{C.10}$$

D

Electrochemical Impedance Spectroscopy Fitting

Contents

D.1 Three-Electrode Cell 169
D.2 K||K Impedance Spectra 171
D.3 Bi-Bi_2K||Bi-Bi_2K Impedance Spectra 172

D.1 Three-Electrode Cell

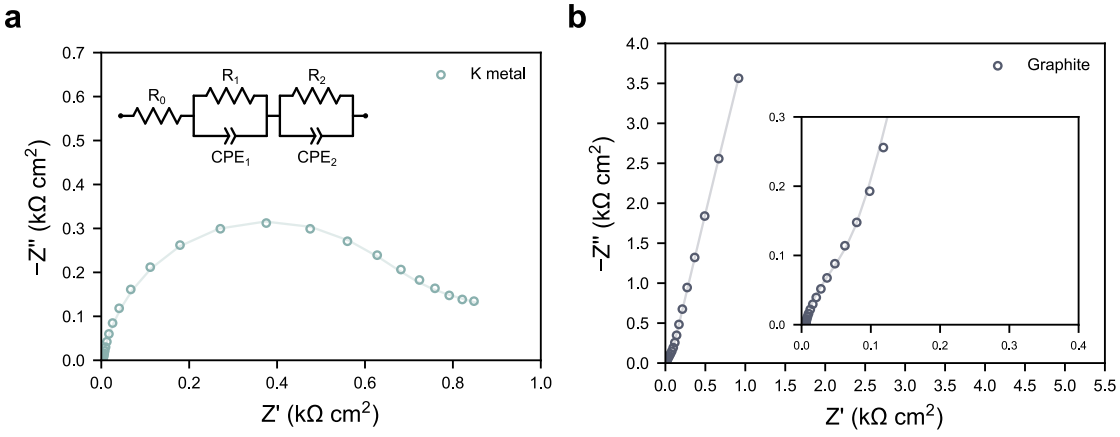


Figure D.1: Three-electrode impedance fitting. (a) Potassium metal impedance (normalised by geometric area) fitted with the equivalent circuit in the inset, where $R_1 + R_2$ represents the total interfacial resistance. Fitting results are presented in Table D.1. (b) Graphite impedance (normalised by geometric area) fitted with the same equivalent circuit as (a), where R_1 may result from cation migration through a surface layer and R_2 represents charge-transfer resistance. Fitting results are presented in Table D.2. Fitting was performed with impedance.py.[278]

Table D.1: Potassium metal three-electrode EIS fitting. Parameters determined from the equivalent circuit model fitting of the potassium metal impedance presented in Figures 5.17 and D.1a using impedance.py.[278]

Parameter	**Value**
R_0 (Ω cm^2)	1.3 ± 0.8
R_1 (Ω cm^2)	645 ± 25
Q_1 (µF s$^{n_1-1}$ cm^{-2})	20.8 ± 0.5
n_1	0.91 ± 0.01
R_2 (Ω cm^2)	405 ± 45
Q_2 (mF s$^{n_2-1}$ cm^{-2})	1.1 ± 0.1
n_2	0.62 ± 0.04

Table D.2: Graphite three-electrode EIS fitting. Parameters determined from the equivalent circuit model fitting of the graphite electrode presented in Figures 5.17 and D.1b using impedance.py.[278]

Parameter	**Value**
R_0 (Ω cm^2)	6 ± 0.6
R_1 (Ω cm^2)	53 ± 2
Q_1 (µF s$^{n_1-1}$ cm^{-2})	73 ± 14
n_1	0.93 ± 0.03
R_2 (kΩ cm^2)	450 ± 100
Q_2 (µF s$^{n_2-1}$ cm^{-2})	102.2 ± 0.2
n_2	0.855 ± 0.001

D.2 K||K Impedance Spectra

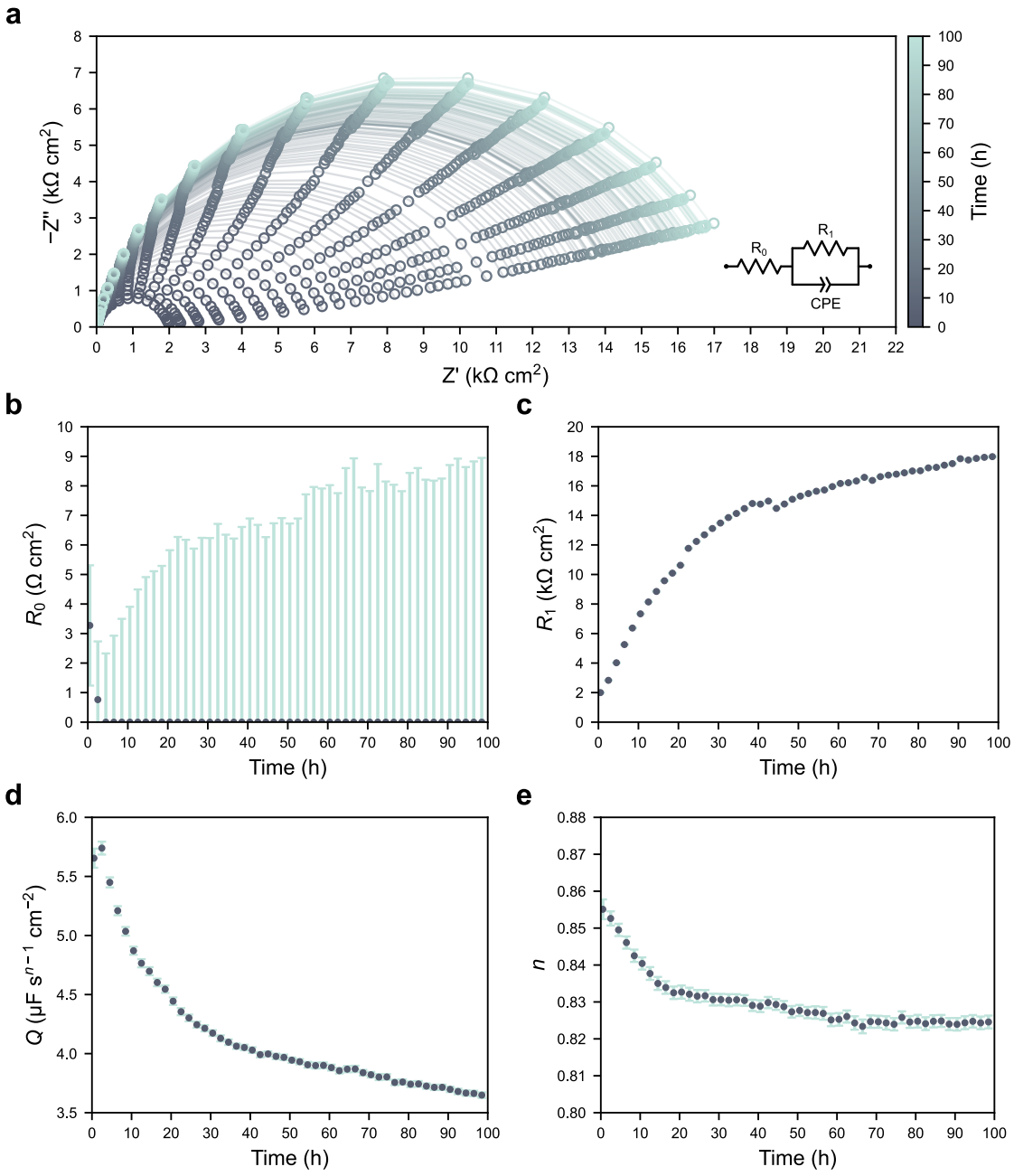


Figure D.2: Exemplar K||K impedance spectra. (a) Impedance spectra measured during rest (normalised by geometric area) fitted with the equivalent circuit in the inset using impedance.py.[278] (b) Fitted series resistance, R_0 values. (c) Fitted interfacial resistance, R_1 values. (d) Fitted constant-phase element Q values. (e) Fitted constant-phase element n values. Measurements were performed in 2 m KFSI TEP at 30°C.

D.3 Bi-Bi_2K||Bi-Bi_2K Impedance Spectra

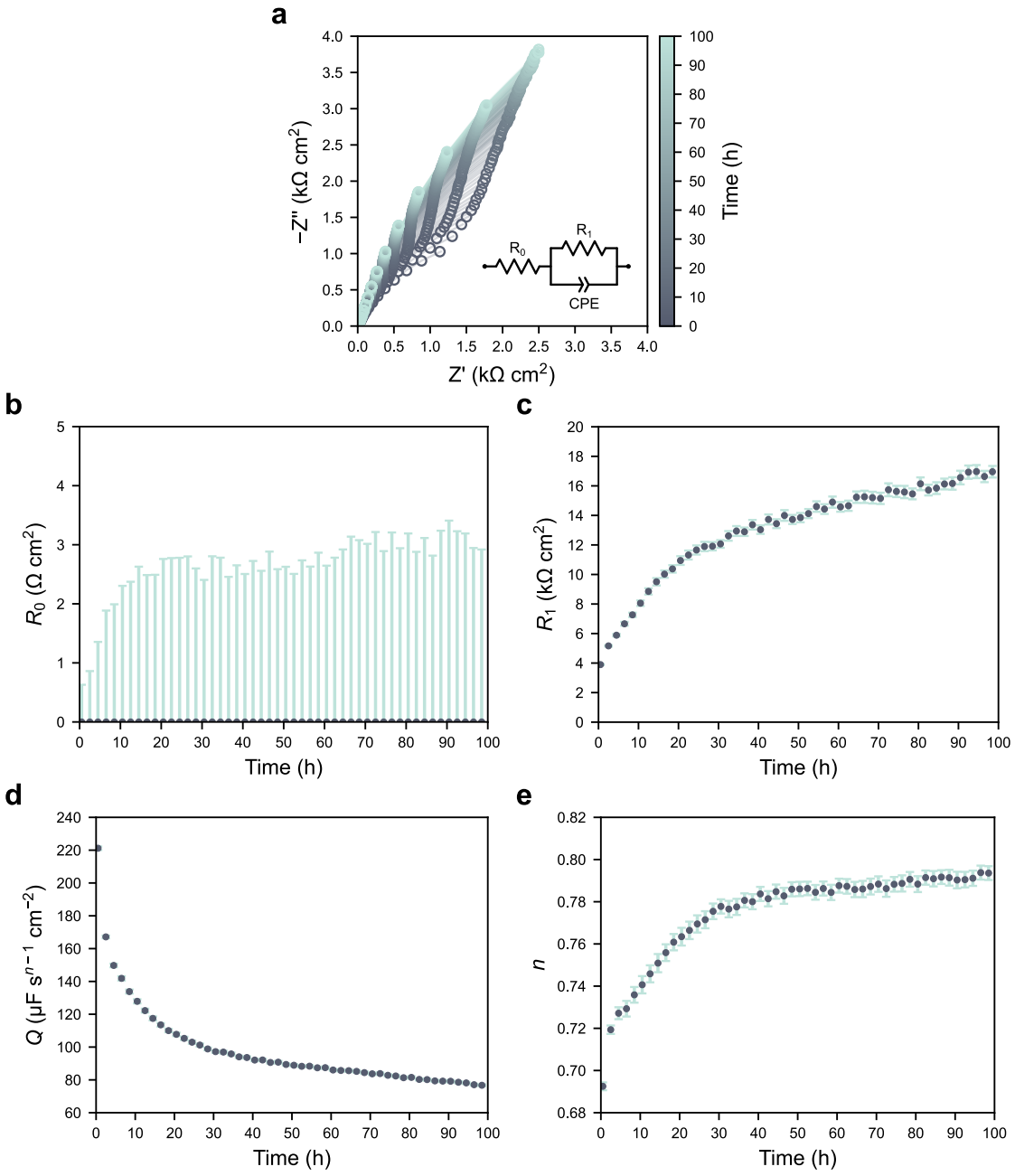


Figure D.3: Exemplar Bi-Bi_2K||Bi-Bi_2K impedance spectra. (a) Impedance spectra measured during rest (normalised by approximate geometric area) fitted with the equivalent circuit in the inset using impedance.py.[278] (b) Fitted series resistance, R_0 values. (c) Fitted interfacial resistance, R_1 values. (d) Fitted constant-phase element Q values. (e) Fitted constant-phase element n values. Measurements were performed in 2 m KFSI TEP at 30°C.

References

1. IEA. Global Critical Minerals Outlook 2024. `www.iea.org/reports/global-critical-minerals-outlook-2024` (2024).
2. Marie, J.-J. & Gifford, S. Developments in Lithium-Ion Battery Cathodes. `www.faraday.ac.uk/insights/insight-18-developments-in-lithium-Ion-battery-cathodes/` (2023).
3. Zhu, P., Slater, P. R. & Kendrick, E. Insights into Architecture, Design and Manufacture of Electrodes for Lithium-Ion Batteries. *Mater. Des.* **223,** 111208 (2022).
4. Xu, K. Electrolytes and Interphases in Li-Ion Batteries and Beyond. *Chem. Rev.* **114,** 11503–618 (2014).
5. Wang, H., Yu, Z., Kong, X., Kim, S. C., Boyle, D. T., Qin, J., Bao, Z. & Cui, Y. Liquid Electrolyte: The Nexus of Practical Lithium Metal Batteries. *Joule* **6,** 588–616 (2022).
6. Cuberg. Cuberg Cell Performance Validation. `https://www.datocms-assets.com/40252/1659129214-cuberg-cell-validation-july-2022.pdf` (2022).
7. Viswanathan, V., Epstein, A. H., Chiang, Y. M., Takeuchi, E., Bradley, M., Langford, J. & Winter, M. The Challenges and Opportunities of Battery-Powered Flight. *Nature* **601,** 519–525 (2022).
8. Xu, K. Navigating the Minefield of Battery Literature. *Commun. Mater.* **3,** 31 (2022).
9. Liu, J. *et al.* Pathways for Practical High-Energy Long-Cycling Lithium Metal Batteries. *Nat. Energy* **4,** 180–186 (2019).
10. Hobold, G. M., Lopez, J., Guo, R., Minafra, N., Banerjee, A., Meng, Y. S., Shao-Horn, Y. & Gallant, B. M. Moving Beyond 99.9% Coulombic Efficiency for Lithium Anodes in Liquid Electrolytes. *Nat. Energy* **6,** 951–960 (2021).
11. Xiao, J. *et al.* Understanding and Applying Coulombic Efficiency in Lithium Metal Batteries. *Nat. Energy* **5,** 561–568 (2020).
12. Albertus, P., Babinec, S., Litzelman, S. & Newman, A. Status and Challenges in Enabling the Lithium Metal Electrode for High-Energy and Low-Cost Rechargeable Batteries. *Nat. Energy* **3,** 16–21 (2018).
13. Peljo, P. & Girault, H. H. Electrochemical Potential Window of Battery Electrolytes: The HOMO–LUMO Misconception. *Energy Environ. Sci.* **11,** 2306–2309 (2018).
14. Goodenough, J. B. & Kim, Y. Challenges for Rechargeable Li Batteries. *Chem. Mater.* **22,** 587–603 (2010).
15. Peled, E. The Electrochemical Behavior of Alkali and Alkaline Earth Metals in Nonaqueous Battery Systems—The Solid Electrolyte Interphase Model. *J. Electrochem. Soc.* **126,** 2047–2051 (1979).
16. Fang, C. *et al.* Quantifying Inactive Lithium in Lithium Metal Batteries. *Nature* **572,** 511–515 (2019).
17. Zheng, J., Kim, M. S., Tu, Z., Choudhury, S., Tang, T. & Archer, L. A. Regulating Electrodeposition Morphology of Lithium: Towards Commercially Relevant Secondary Li Metal Batteries. *Chem. Soc. Rev.* **49,** 2701–2750 (2020).

18. IEA. *Global EV Outlook 2022* `https://www.iea.org/reports/global-ev-outlook-2022` (IEA, 2022).
19. Frith, J. T., Lacey, M. J. & Ulissi, U. A Non-academic Perspective on the Future of Lithium-Based Batteries. *Nat. Commun.* **14,** 1–17 (1 2023).
20. Sada, K., Darga, J. & Manthiram, A. Challenges and Prospects of Sodium-Ion and Potassium-Ion Batteries for Mass Production. *Adv. Energy Mater.* **13,** 2302321 (2023).
21. Yao, A., Benson, S. M. & Chueh, W. C. Critically Assessing Sodium-Ion Technology Roadmaps and Scenarios for Techno-Economic Competitiveness Against Lithium-Ion Batteries. *Nat. Energy* **10,** 404–416 (2025).
22. Dhir, S., Wheeler, S., Capone, I. & Pasta, M. Outlook on K-Ion Batteries. *Chem* **6,** 2442–2460 (2020).
23. Zhang, K.-Y. *et al.* Defect Engineering Unveiled: Enhancing Potassium Storage in Expanded Graphite Anode. *J. Colloid Interface Sci.* **664,** 607–616 (2024).
24. Hosaka, T., Kubota, K., Hameed, A. S. & Komaba, S. Research Development on K-Ion Batteries. *Chem. Rev.* **120,** 6358–6466 (2020).
25. Hurlbutt, K., Wheeler, S., Capone, I. & Pasta, M. Prussian Blue Analogs as Battery Materials. *Joule* **2,** 1950–1960 (2018).
26. Li, M., Wang, C., Wang, C., Lyu, Y., Wang, J., Xia, S., Mao, J. & Guo, Z. 10 Years Development of Potassium-Ion Batteries. *Adv. Mater.,* e2416717 (2025).
27. Gu, Z.-Y., Wang, X.-T., Zhao, X.-X., Cao, J.-M., Heng, Y.-L., Zheng, S.-H., Liu, Y., Guo, J.-Z., Wang, S.-Z. & Wu, X.-L. Advanced $K_3V_2(PO_4)_2O_2F$ Cathode for Rechargeable Potassium-Ion Batteries With High Energy Density. *Appl. Phys. Lett.* **124,** 183904 (2024).
28. Wu, Z., Zou, J., Chen, S., Niu, X., Liu, J. & Wang, L. Potassium-Ion Battery Cathodes: Past, Present, and Prospects. *J. Power Sources* **484,** 229307 (2021).
29. Onuma, H., Kubota, K., Muratsubaki, S., Ota, W., Shishkin, M., Sato, H., Yamashita, K., Yasuno, S. & Komaba, S. Phase Evolution of Electrochemically Potassium Intercalated Graphite. *J. Mater. Chem. A* **9,** 11187–11200 (2021).
30. Dhir, S., Cattermull, J., Jagger, B., Schart, M., Olbrich, L. F., Chen, Y., Zhao, J., Sada, K., Goodwin, A. & Pasta, M. Characterisation and Modelling of Potassium-Ion Batteries. *Nat. Commun.* **15,** 7580 (2024).
31. Wang, H., Zhai, D. & Kang, F. Solid Electrolyte Interphase (SEI) in Potassium Ion Batteries. *Energy Environ. Sci.* **13,** 4583–4608 (2020).
32. Xu, Y., Ding, T., Sun, D., Ji, X. & Zhou, X. Recent Advances in Electrolytes for Potassium-Ion Batteries. *Adv. Funct. Mater.* **33,** 2211290 (2022).
33. Wang, A. A. *et al.* Review of Parameterisation and a Novel Database (LiionDB) for Continuum Li-Ion Battery Models. *Prog. Energy* **4,** 032004 (2022).
34. Wang, A. A., Gunnarsdottir, A. B., Fawdon, J., Pasta, M., Grey, C. P. & Monroe, C. W. Potentiometric MRI of a Superconcentrated Lithium Electrolyte: Testing the Irreversible Thermodynamics Approach. *ACS Energy Lett.* **6,** 3086–3095 (2021).
35. Fawdon, J., Ihli, J., La Mantia, F. & Pasta, M. Characterising Lithium-Ion Electrolytes via *Operando* Raman Microspectroscopy. *Nat. Commun.* **12,** 4053 (2021).
36. Hou, T. & Monroe, C. W. Composition-dependent Thermodynamic and Mass-transport Characterization of Lithium Hexafluorophosphate in Propylene Carbonate. *Electrochim. Acta* **332,** 135085 (2020).
37. Wang, A. A., Hou, T., Karanjavala, M. & Monroe, C. W. Shifting-reference Concentration Cells to Refine Composition-dependent Transport Characterization of Binary Lithium-Ion Electrolytes. *Electrochim. Acta* **358,** 136688 (2020).

38. Zhao, J., Jagger, B., Olbrich, L. F., Ihli, J., Dhir, S., Zyskin, M., Ma, X. & Pasta, M. Transport and Thermodynamic Properties of KFSI in TEP by *Operando* Raman Gradient Analysis. *ACS Energy Lett.* **9,** 1537–1544 (2024).
39. Olbrich, L. F., Jagger, B., Ihli, J. & Pasta, M. *Operando* Raman Gradient Analysis for Temperature-Dependent Electrolyte Characterization. *ACS Energy Lett.* **9,** 3636–3642 (2024).
40. Bai, P., Li, J., Brushett, F. R. & Bazant, M. Z. Transition of Lithium Growth Mechanisms in Liquid Electrolytes. *Energy Environ. Sci.* **9,** 3221–3229 (2016).
41. Sand, H. J. S. On the Concentration at the Electrodes in a Solution, with Special Reference to the Liberation of Hydrogen by Electrolysis of a Mixture of Copper Sulphate and Sulphuric Acid. *Proc. Phys. Soc. Lond.* **17,** 496–534 (1899).
42. Maraschky, A. & Akolkar, R. Mechanism Explaining the Onset Time of Dendritic Lithium Electrodeposition via Considerations of the Li^+ Transport within the Solid Electrolyte Interphase. *J. Electrochem. Soc.* **165,** D696–D703 (2018).
43. Gireaud, L., Grugeon, S., Laruelle, S., Yrieix, B. & Tarascon, J. M. Lithium Metal Stripping/Plating Mechanisms Studies: A Metallurgical Approach. *Electrochem. Commun.* **8,** 1639–1649 (2006).
44. Cheng, X. B., Zhang, R., Zhao, C. Z. & Zhang, Q. Toward Safe Lithium Metal Anode in Rechargeable Batteries: A Review. *Chem. Rev.* **117,** 10403–10473 (2017).
45. Li, Y., Huang, W., Li, Y., Pei, A., Boyle, D. T. & Cui, Y. Correlating Structure and Function of Battery Interphases at Atomic Resolution Using Cryoelectron Microscopy. *Joule* **2,** 2167–2177 (2018).
46. Zhao, Q., Stalin, S. & Archer, L. A. Stabilizing Metal Battery Anodes Through the Design of Solid Electrolyte Interphases. *Joule* **5,** 1119–1142 (2021).
47. Gong, C. *et al.* Revealing the Role of Fluoride-Rich Battery Electrode Interphases by *Operando* Transmission Electron Microscopy. *Adv. Energy Mater.* **11,** 2003118 (2021).
48. Yu, Z. *et al.* Beyond Local Solvation Structure: Nanometric Aggregates in Battery Electrolytes and Their Effect on Electrolyte Properties. *ACS Energy Lett.* **7,** 461–470 (2022).
49. Cao, X., Jia, H., Xu, W. & Zhang, J.-G. Review—Localized High-Concentration Electrolytes for Lithium Batteries. *J. Electrochem. Soc.* **168,** 010522 (2021).
50. Jang, J., Sugimoto, T., Mizumo, T., Lee, J.-M., Chang, W.-S. & Mun, J. High-Voltage-Compatible Dual-Ether Electrolyte for Lithium Metal Batteries. *ACS Appl. Energy Mater.* **4,** 9032–9037 (2021).
51. Feng, X. *et al.* New Nonflammable Tributyl Phosphate Based Localized High Concentration Electrolytes for Lithium Metal Batteries. *Sustain. Energy Fuels* **6,** 2198–2206 (2022).
52. Zheng, X., Huang, L., Luo, W., Wang, H., Dai, Y., Liu, X., Wang, Z., Zheng, H. & Huang, Y. Tailoring Electrolyte Solvation Chemistry toward an Inorganic-Rich Solid-Electrolyte Interphase at a Li Metal Anode. *ACS Energy Lett.* **6,** 2054–2063 (2021).
53. Zhang, X.-Q., Cheng, X.-B., Chen, X., Yan, C. & Zhang, Q. Fluoroethylene Carbonate Additives to Render Uniform Li Deposits in Lithium Metal Batteries. *Adv. Funct. Mater.* **27,** 1605989 (2017).
54. Olana, B. N., Lin, S. D. & Hwang, B.-J. *In Situ* Diffuse Reflectance Infrared Fourier-Transformed Spectroscopy Study of Solid Electrolyte Interphase Formation from Lithium Bis(trifluoromethanesulfonyl)imide in 1,2-Dimethoxyethane and 1,3-Dioxolane with and without Lithium Nitrate Additive over Lithium and Copper Metal Anodes. *Electrochim. Acta* **416,** 140266 (2022).
55. Yoshii, K., Kiuchi, H., Taguchi, N., Shikano, M., Matsubara, E. & Sakaebe, H. Effects of Film Formation on the Electrodeposition of Lithium. *ChemElectroChem* **7,** 4336–4342 (2020).

56. Alvarado, J. *et al.* Bisalt Ether Electrolytes: A Pathway Towards Lithium Metal Batteries with Ni-Rich Cathodes. *Energy Environ. Sci.* **12,** 780–794 (2019).
57. Xu, R., Cheng, X.-B., Yan, C., Zhang, X.-Q., Xiao, Y., Zhao, C.-Z., Huang, J.-Q. & Zhang, Q. Artificial Interphases for Highly Stable Lithium Metal Anode. *Matter* **1,** 317–344 (2019).
58. Zhang, W., Zhang, S., Fan, L., Gao, L., Kong, X., Li, S., Li, J., Hong, X. & Lu, Y. Tuning the LUMO Energy of an Organic Interphase to Stabilize Lithium Metal Batteries. *ACS Energy Lett.* **4,** 644–650 (2019).
59. Hobold, G. M. & Gallant, B. M. Quantifying Capacity Loss Mechanisms of Li Metal Anodes beyond Inactive Li^0. *ACS Energy Lett.* **7,** 3458–3466 (2022).
60. Peled, E., Golodnitsky, D. & Ardel, G. Advanced Model for Solid Electrolyte Interphase Electrodes in Liquid and Polymer Electrolytes. *J. Electrochem. Soc.* **144,** L208–L210 (1997).
61. Lim, K., Fenk, B., Popovic, J. & Maier, J. Porosity of Solid Electrolyte Interphases on Alkali Metal Electrodes with Liquid Electrolytes. *ACS Appl. Mater. Interfaces* **13,** 51767–51774 (2021).
62. Ma, C., Xu, F. & Song, T. Dual-Layered Interfacial Evolution of Lithium Metal Anode: SEI Analysis via TOF-SIMS Technology. *ACS Appl. Mater. Interfaces* **14,** 20197–20207 (2022).
63. Zhou, Y. *et al.* Real-Time Mass Spectrometric Characterization of the Solid-Electrolyte Interphase of a Lithium-Ion Battery. *Nat. Nanotechnol.* **15,** 224–230 (2020).
64. Fang, C. *et al.* Pressure-Tailored Lithium Deposition and Dissolution in Lithium Metal Batteries. *Nat. Energy* **6,** 987–994 (2021).
65. Li, Y. *et al.* Atomic Structure of Sensitive Battery Materials and Interfaces Revealed by Cryo-Electron Microscopy. *Science* **358,** 506–510 (2017).
66. Cao, X. *et al.* Monolithic Solid–Electrolyte Interphases Formed in Fluorinated Orthoformate-Based Electrolytes Minimize Li Depletion and Pulverization. *Nat. Energy* **4,** 796–805 (2019).
67. Yu, Z. *et al.* Molecular Design for Electrolyte Solvents Enabling Energy-Dense and Long-Cycling Lithium Metal Batteries. *Nat. Energy* **5,** 526–533 (2020).
68. Han, B., Zhang, Z., Zou, Y., Xu, K., Xu, G., Wang, H., Meng, H., Deng, Y., Li, J. & Gu, M. Poor Stability of Li_2CO_3 in the Solid Electrolyte Interphase of a Lithium-Metal Anode Revealed by Cryo-Electron Microscopy. *Adv. Mater.* **33,** e2100404 (2021).
69. Zachman, M. J., Tu, Z., Choudhury, S., Archer, L. A. & Kourkoutis, L. F. Cryo-STEM Mapping of Solid-Liquid Interfaces and Dendrites in Lithium-Metal Batteries. *Nature* **560,** 345–349 (2018).
70. Wang, L. *et al.* Identifying the Components of the Solid-Electrolyte Interphase in Li-Ion Batteries. *Nat. Chem.* **11,** 789–796 (2019).
71. Wu, H., Jia, H., Wang, C., Zhang, J.-G. & Xu, W. Recent Progress in Understanding Solid Electrolyte Interphase on Lithium Metal Anodes. *Adv. Energy Mater.* **11** (2020).
72. Wu, J., Ihsan-Ul-Haq, M., Chen, Y. & Kim, J.-K. Understanding Solid Electrolyte Interphases: Advanced Characterization Techniques and Theoretical Simulations. *Nano Energy* **89** (2021).
73. Gu, Y. *et al.* Electrochemical Polishing of Lithium Metal Surface for Highly Demanding Solid-Electrolyte Interphase. *ChemElectroChem* **6,** 181–188 (2019).
74. Shkrob, I. A., Marin, T. W., Zhu, Y. & Abraham, D. P. Why Bis(fluorosulfonyl)imide Is a "Magic Anion" for Electrochemistry. *J. Phys. Chem. C* **118,** 19661–19671 (2014).
75. Han, B. *et al.* Cryo-Electron Tomography of Highly Deformable and Adherent Solid-Electrolyte Interphase Exoskeleton in Li-Metal Batteries with Ether-Based Electrolyte. *Adv. Mater.* **34,** e2108252 (2022).

76. Zhang, Z. *et al.* Capturing the Swelling of Solid-Electrolyte Interphase in Lithium Metal Batteries. *Science* **375,** 66–70 (2022).

77. Oyakhire, S. T., Gong, H., Cui, Y., Bao, Z. & Bent, S. F. An X-ray Photoelectron Spectroscopy Primer for Solid Electrolyte Interphase Characterization in Lithium Metal Anodes. *ACS Energy Lett.* **7,** 2540–2546 (2022).

78. Tan, J., Matz, J., Dong, P., Shen, J. & Ye, M. A Growing Appreciation for the Role of LiF in the Solid Electrolyte Interphase. *Adv. Energy Mater.* **11,** 2100046 (2021).

79. Yu, W., Yu, Z., Cui, Y. & Bao, Z. Degradation and Speciation of Li Salts during XPS Analysis for Battery Research. *ACS Energy Lett.* **7,** 3270–3275 (2022).

80. Brundle, C. R., Crist, B. V. & Bagus, P. S. Accuracy Limitations for Composition Analysis by XPS Using Relative Peak Intensities: LiF as an Example. *J. Vac. Sci. Technol. A* **39,** 013202 (2021).

81. Wi, S., Shutthanandan, V., Sivakumar, B. M., Thevuthasan, S., Prabhakaran, V., Roy, S., Karakoti, A. & Murugesan, V. *In Situ* X-ray Photoelectron Spectroscopy Analysis of Electrochemical Interfaces in Battery: Recent Advances and Remaining Challenges. *J. Vac. Sci. Technol. A* **40,** 010808 (2022).

82. Narayanan, S., Gibson, J. S., Aspinall, J., Weatherup, R. S. & Pasta, M. *In Situ* and *Operando* Characterisation of Li Metal – Solid Electrolyte Interfaces. *Curr. Opin. Solid State Mater. Sci.* **26,** 100978 (2022).

83. Huang, W., Wang, H., Boyle, D. T., Li, Y. & Cui, Y. Resolving Nanoscopic and Mesoscopic Heterogeneity of Fluorinated Species in Battery Solid-Electrolyte Interphases by Cryogenic Electron Microscopy. *ACS Energy Lett.* **5,** 1128–1135 (2020).

84. Brown, Z. L., Jurng, S., Nguyen, C. C. & Lucht, B. L. Effect of Fluoroethylene Carbonate Electrolytes on the Nanostructure of the Solid Electrolyte Interphase and Performance of Lithium Metal Anodes. *ACS Appl. Energy Mater.* **1,** 3057–3062 (2018).

85. Jurng, S., Brown, Z. L., Kim, J. & Lucht, B. L. Effect of Electrolyte on the Nanostructure of the Solid Electrolyte Interphase (SEI) and Performance of Lithium Metal Anodes. *Energy Environ. Sci.* **11,** 2600–2608 (2018).

86. He, M., Guo, R., Hobold, G. M., Gao, H. & Gallant, B. M. The Intrinsic Behavior of Lithium Fluoride in Solid Electrolyte Interphases on Lithium. *Proc. Natl. Acad. Sci. U.S.A.* **117,** 73–79 (2020).

87. Kim, S. C. *et al.* Potentiometric Measurement to Probe Solvation Energy and its Correlation to Lithium Battery Cyclability. *J. Am. Chem. Soc.* **143,** 10301–10308 (2021).

88. Ko, S., Obukata, T., Shimada, T., Takenaka, N., Nakayama, M., Yamada, A. & Yamada, Y. Electrode Potential Influences the Reversibility of Lithium-Metal Anodes. *Nat. Energy* **7,** 1217–1224 (2022).

89. Boyle, D. T., Kim, S. C., Oyakhire, S. T., Vila, R. A., Huang, Z., Sayavong, P., Qin, J., Bao, Z. & Cui, Y. Correlating Kinetics to Cyclability Reveals Thermodynamic Origin of Lithium Anode Morphology in Liquid Electrolytes. *J. Am. Chem. Soc.* **144,** 20717–20725 (2022).

90. Hobold, G. M., Wang, C., Steinberg, K., Li, Y. & Gallant, B. M. High Lithium Oxide Prevalence in the Lithium Solid–Electrolyte Interphase for High Coulombic Efficiency. *Nat. Energy* **9,** 580–591 (2024).

91. Shadike, Z. *et al.* Identification of LiH and Nanocrystalline LiF in the Solid-Electrolyte Interphase of Lithium Metal Anodes. *Nat. Nanotechnol.* **16,** 549–554 (2021).

92. Tao, M., Xiang, Y., Zhao, D., Shan, P., Sun, Y. & Yang, Y. Quantifying the Evolution of Inactive Li/Lithium Hydride and Their Correlations in Rechargeable Anode-free Li Batteries. *Nano Lett.* **22,** 6775–6781 (2022).

93. Tan, S. *et al.* Unravelling the Convoluted and Dynamic Interphasial Mechanisms on Li Metal Anodes. *Nat. Nanotechnol.* (2022).

94. Maraschky, A. & Akolkar, R. Temperature Dependence of Dendritic Lithium Electrodeposition: A Mechanistic Study of the Role of Transport Limitations within the SEI. *J. Electrochem. Soc.* **167,** 062503 (2020).

95. Boyle, D. T. *et al.* Resolving Current-Dependent Regimes of Electroplating Mechanisms for Fast Charging Lithium Metal Anodes. *Nano Lett.* **22,** 8224–8232 (2022).

96. Zhang, S. *et al.* Tackling Realistic Li^+ Flux for High-Energy Lithium Metal Batteries. *Nat. Commun.* **13,** 5431 (2022).

97. Vivier, V. & Orazem, M. E. Impedance Analysis of Electrochemical Systems. *Chem. Rev.* **122,** 11131–11168 (2022).

98. Zaban, A., Zinigrad, E. & Aurbach, D. Impedance Spectroscopy of Li Electrodes. 4. A General Simple Model of the Li-Solution Interphase in Polar Aprotic Systems. *J. Phys. Chem.* **100,** 3089–3101 (1996).

99. Single, F., Horstmann, B. & Latz, A. Theory of Impedance Spectroscopy for Lithium Batteries. *J. Phys. Chem. C* **123,** 27327–27343 (2019).

100. Guo, R. & Gallant, B. M. Li_2O Solid Electrolyte Interphase: Probing Transport Properties at the Chemical Potential of Lithium. *Chem. Mater.* **32,** 5525–5533 (2020).

101. Boyle, D. T., Kong, X., Pei, A., Rudnicki, P. E., Shi, F., Huang, W., Bao, Z., Qin, J. & Cui, Y. Transient Voltammetry with Ultramicroelectrodes Reveals the Electron Transfer Kinetics of Lithium Metal Anodes. *ACS Energy Lett.* **5,** 701–709 (2020).

102. Nojabaee, M., Kuster, K., Starke, U., Popovic, J. & Maier, J. Solid Electrolyte Interphase Evolution on Lithium Metal in Contact with Glyme-Based Electrolytes. *Small* **16,** e2000756 (2020).

103. Hobold, G. M., Kim, K.-H. & Gallant, B. M. Beneficial *vs.* Inhibiting Passivation by the Native Lithium Solid Electrolyte Interphase Revealed by Electrochemical Li^+ Exchange. *Energy Environ. Sci.* **16,** 2247–2261 (2023).

104. Shi, S., Lu, P., Liu, Z., Qi, Y., Hector L. G., J., Li, H. & Harris, S. J. Direct Calculation of Li-Ion Transport in the Solid Electrolyte Interphase. *J. Am. Chem. Soc.* **134,** 15476–87 (2012).

105. Benitez, L. & Seminario, J. M. Ion Diffusivity through the Solid Electrolyte Interphase in Lithium-Ion Batteries. *J. Electrochem. Soc.* **164,** E3159–E3170 (2017).

106. Lanjan, A., Moradi, Z. & Srinivasan, S. Multiscale Investigation of the Diffusion Mechanism within the Solid-Electrolyte Interface Layer: Coupling Quantum Mechanics, Molecular Dynamics, and Macroscale Mathematical Modeling. *ACS Appl. Mater. Interfaces* **13,** 42220–42229 (2021).

107. Ramasubramanian, A., Yurkiv, V., Foroozan, T., Ragone, M., Shahbazian-Yassar, R. & Mashayek, F. Lithium Diffusion Mechanism through Solid–Electrolyte Interphase in Rechargeable Lithium Batteries. *J. Phys. Chem. C* **123,** 10237–10245 (2019).

108. Ahmad, Z., Venturi, V., Hafiz, H. & Viswanathan, V. Interfaces in Solid Electrolyte Interphase: Implications for Lithium-Ion Batteries. *J. Phys. Chem. C* **125,** 11301–11309 (2021).

109. Zheng, J., Ju, Z., Zhang, B., Nai, J., Liu, T., Liu, Y., Xie, Q., Zhang, W., Wang, Y. & Tao, X. Lithium Ion Diffusion Mechanism on the Inorganic Components of the Solid–Electrolyte Interphase. *J. Mater. Chem. A* **9,** 10251–10259 (2021).

110. McBrayer, J. D., Apblett, C. A., Harrison, K. L., Fenton, K. R. & Minteer, S. D. Mechanical Studies of the Solid Electrolyte Interphase on Anodes in Lithium and Lithium Ion Batteries. *Nanotechnology* **32,** 502005 (2021).

111. Lee, S.-Y., Shangguan, J., Betzler, S., Harris, S. J., Doeff, M. M. & Zheng, H. Lithium Metal Stripping Mechanisms Revealed through Electrochemical Liquid Cell Electron Microscopy. *Nano Energy* **102,** 107641 (2022).

112. Wang, W.-W., Gu, Y., Wang, J.-H., Chen, Z.-B., Yin, X.-T., Wu, Q.-H., Yan, J.-W. & Mao, B.-W. Probing Mechanical Properties of Solid-Electrolyte Interphases on Li Nuclei by *In Situ* AFM. *J. Electrochem. Soc.* **169,** 020563 (2022).

113. Kitta, M. & Sano, H. Real-Time Observation of Li Deposition on a Li Electrode with *Operand* Atomic Force Microscopy and Surface Mechanical Imaging. *Langmuir* **33,** 1861–1866 (2017).

114. Shen, X., Zhang, R., Chen, X., Cheng, X.-B., Li, X. & Zhang, Q. The Failure of Solid Electrolyte Interphase on Li Metal Anode: Structural Uniformity or Mechanical Strength? *Adv. Energy Mater.* **10,** 1903645 (2020).

115. Yuan, S., Weng, S., Wang, F., Dong, X., Wang, Y., Wang, Z., Shen, C., Bao, J. L., Wang, X. & Xia, Y. Revisiting the Designing Criteria of Advanced Solid Electrolyte Interphase on Lithium Metal Anode under Practical Condition. *Nano Energy* **83,** 105847 (2021).

116. Saha, R. & Nix, W. D. Effects of the Substrate on the Determination of Thin Film Mechanical Properties by Nanoindentation. *Acta Mater.* **50,** 23–38 (2002).

117. Yoon, I., Jurng, S., Abraham, D. P., Lucht, B. L. & Guduru, P. R. *In Situ* Measurement of the Plane-Strain Modulus of the Solid Electrolyte Interphase on Lithium-Metal Anodes in Ionic Liquid Electrolytes. *Nano Lett.* **18,** 5752–5759 (2018).

118. Yoon, I., Jurng, S., Abraham, D. P., Lucht, B. L. & Guduru, P. R. Measurement of Mechanical and Fracture Properties of Solid Electrolyte Interphase on Lithium Metal Anodes in Lithium Ion Batteries. *Energy Storage Mater.* **25,** 296–304 (2020).

119. Gao, Y., Du, X., Hou, Z., Shen, X., Mai, Y.-W., Tarascon, J.-M. & Zhang, B. Unraveling the Mechanical Origin of Stable Solid Electrolyte Interphase. *Joule* **5,** 1860–1872 (2021).

120. Wang, W.-W., Gu, Y., Yan, H., Li, S., He, J.-W., Xu, H.-Y., Wu, Q.-H., Yan, J.-W. & Mao, B.-W. Evaluating Solid-Electrolyte Interphases for Lithium and Lithium-free Anodes from Nanoindentation Features. *Chem* **6,** 2728–2745 (2020).

121. Gu, Y. *et al.* Designable Ultra-Smooth Ultra-Thin Solid-Electrolyte Interphases of Three Alkali Metal Anodes. *Nat. Commun.* **9,** 1339 (2018).

122. Wang, J. *et al. In Situ* Self-Assembly of Ordered Organic/Inorganic Dual-Layered Interphase for Achieving Long-Life Dendrite-Free Li Metal Anodes in LiFSI-Based Electrolyte. *Adv. Funct. Mater.* **31,** 2007434 (2020).

123. Zhang, Q.-K. *et al.* Homogeneous and Mechanically Stable Solid–Electrolyte Interphase Enabled by Trioxane-Modulated Electrolytes for Lithium Metal Batteries. *Nat. Energy* (2023).

124. Boroujeni, S. M., Fill, A., Ridder, A. & Birke, K. P. Influence of Temperature and Electrolyte Composition on the Performance of Lithium Metal Anodes. *Batteries* **7,** 67 (2021).

125. Wang, J., Huang, W., Pei, A., Li, Y., Shi, F., Yu, X. & Cui, Y. Improving Cyclability of Li Metal Batteries at Elevated Temperatures and its Origin Revealed by Cryo-Electron Microscopy. *Nat. Energy* **4,** 664–670 (2019).

126. Thenuwara, A. C., Shetty, P. P. & McDowell, M. T. Distinct Nanoscale Interphases and Morphology of Lithium Metal Electrodes Operating at Low Temperatures. *Nano Lett.* **19,** 8664–8672 (2019).

127. Otto, S. K., Moryson, Y., Krauskopf, T., Peppler, K., Sann, J., Janek, J. & Henss, A. In-Depth Characterization of Lithium-Metal Surfaces with XPS and ToF-SIMS: Toward Better Understanding of the Passivation Layer. *Chem. Mater.* **33,** 859–867 (2021).

128. Haas, R. & Janek, J. The Influence of Oxygen Dissolved in the Liquid Electrolyte on Lithium Metal Anodes. *J. Electrochem. Soc.* **169,** 110527 (2022).

129. Kühn, S. P., Pfeiffer, F., Bela, M., Rodehorst, U., Weintz, D., Stan, M., Baghernejad, M., Winter, M. & Cekic-Laskovic, I. Back to the Basics: Advanced Understanding of the As-Defined Solid Electrolyte Interphase on Lithium Metal Electrodes. *J. Power Sources* **549,** 232118 (2022).

130. Xu, Y., Wu, H., Jia, H., Engelhard, M. H., Zhang, J.-G., Xu, W. & Wang, C. Sweeping Potential Regulated Structural and Chemical Evolution of Solid-Electrolyte Interphase on Cu and Li as Revealed by Cryo-TEM. *Nano Energy* **76,** 105040 (2020).

131. Liu, J., Pei, N., Hua, H., Deng, Y., Ma, H., Zhang, P. & Zhao, J. From Mosaic-Type to Heterojunction-Type SEI Films on the Li Anode: Decoupling Chemical and Electrochemical Degradation of the Electrolyte. *ACS Sustain. Chem. Eng.* **10,** 9232–9241 (2022).

132. Wang, W. W., Gu, Y., Yan, H., Li, K. X., Chen, Z. B., Wu, Q. H., Kranz, C., Yan, J. W. & Mao, B. W. Formation Sequence of Solid Electrolyte Interphases and Impacts on Lithium Deposition and Dissolution on Copper: An *In Situ* Atomic Force Microscopic Study. *Faraday Discuss.* **233,** 190–205 (2022).

133. Gu, Y. *et al.* Resolving Nanostructure and Chemistry of Solid-Electrolyte Interphase on Lithium Anodes by Depth-Sensitive Plasmon-Enhanced Raman Spectroscopy. *Nat. Commun.* **14,** 3536 (2023).

134. Cao, C. *et al.* Toward Unraveling the Origin of Lithium Fluoride in the Solid Electrolyte Interphase. *Chem. Mater.* **33,** 7315–7336 (2021).

135. Shin, W. & Manthiram, A. A Facile Potential Hold Method for Fostering an Inorganic Solid-Electrolyte Interphase for Anode-Free Lithium-Metal Batteries. *Angew. Chem., Int. Ed. Engl.* **61,** e202115909 (2022).

136. Oyakhire, S. T. *et al.* Correlating the Formation Protocols of Solid Electrolyte Interphases with Practical Performance Metrics in Lithium Metal Batteries. *ACS Energy Lett.* **8,** 869–877 (2023).

137. Shi, F., Pei, A., Boyle, D. T., Xie, J., Yu, X., Zhang, X. & Cui, Y. Lithium Metal Stripping Beneath the Solid Electrolyte Interphase. *Proc. Natl. Acad. Sci. U.S.A.* **115,** 8529–8534 (2018).

138. Aurbach, D., Zinigrad, E., Cohen, Y. & Teller, H. A Short Review of Failure Mechanisms of Lithium Metal and Lithiated Graphite Anodes in Liquid Electrolyte Solutions. *Solid State Ion.* **148,** 405–416 (2002).

139. Ding, J.-F., Xu, R., Xiao, Y., Zhang, S., Song, T.-L., Yan, C. & Huang, J.-Q. Dynamic Galvanic Corrosion of Working Lithium Metal Anode Under Practical Conditions. *Adv. Energy Mater.* **13,** 2204305 (2023).

140. Guo, R., Wang, D., Zuin, L. & Gallant, B. M. Reactivity and Evolution of Ionic Phases in the Lithium Solid–Electrolyte Interphase. *ACS Energy Lett.* **6,** 877–885 (2021).

141. Zhuo, Z., Lu, P., Delacourt, C., Qiao, R., Xu, K., Pan, F., Harris, S. J. & Yang, W. Breathing and Oscillating Growth of Solid-Electrolyte-Interphase upon Electrochemical Cycling. *Chem. Commun.* **54,** 814–817 (2018).

142. Tasaki, K., Goldberg, A., Lian, J.-J., Walker, M., Timmons, A. & Harris, S. J. Solubility of Lithium Salts Formed on the Lithium-Ion Battery Negative Electrode Surface in Organic Solvents. *J. Electrochem. Soc.* **156,** A1019 (2009).

143. Sayavong, P. *et al.* Dissolution of the Solid Electrolyte Interphase and Its Effects on Lithium Metal Anode Cyclability. *J. Am. Chem. Soc.* **145,** 12342–12350 (2023).

144. Harris, O. C., Lee, S. E., Lees, C. & Tang, M. Review: Mechanisms and Consequences of Chemical Cross-Talk in Advanced Li-Ion Batteries. *J. Phys. Energy* **2,** 032002 (2020).

145. Betz, J., Brinkmann, J.-P., Nölle, R., Lürenbaum, C., Kolek, M., Stan, M. C., Winter, M. & Placke, T. Cross Talk between Transition Metal Cathode and Li Metal Anode: Unraveling its Influence on the Deposition/Dissolution Behavior and Morphology of Lithium. *Adv, Energy Mater.* **9,** 1900574 (2019).

146. Zhang, X.-Q., Wang, X.-M., Li, B.-Q., Shi, P., Huang, J.-Q., Chen, A. & Zhang, Q. Crosstalk Shielding of Transition Metal Ions for Long Cycling Lithium–Metal Batteries. *J. Mater. Chem. A* **8,** 4283–4289 (2020).

147. Kim, H.-S., Jeong, G., Leem, H. J., Lee, M. A., Lee, J.-N., Woo, S.-G. & Yu, J. Positive Electrode–Li Metal Crosstalk Behavior-Induced Morphology Change of Li Deposits. *J. Mater. Chem. A* **10,** 17659–17667 (2022).

148. Langdon, J. & Manthiram, A. Crossover Effects in Lithium-Metal Batteries with a Localized High Concentration Electrolyte and High-Nickel Cathodes. *Adv. Mater.* **34,** e2205188 (2022).

149. Madec, L., Gabaudan, V., Gachot, G., Stievano, L., Monconduit, L. & Martinez, H. Paving the Way for K-Ion Batteries: Role of Electrolyte Reactivity through the Example of Sb-Based Electrodes. *ACS Appl. Mater. Interfaces* **10,** 34116–34122 (2018).

150. Allgayer, F., Maibach, J. & Jeschull, F. Comparing the Solid Electrolyte Interphases on Graphite Electrodes in K and Li Half Cells. *ACS Appl. Energy Mater.* **5,** 1136–1148 (2022).

151. Koster, D., Du, G., Battistel, A. & La Mantia, F. Dynamic Impedance Spectroscopy Using Dynamic Multi-frequency Analysis: A Theoretical and Experimental Investigation. *Electrochim. Acta* **246,** 553–563 (2017).

152. Wang, M., Zhang, C., Yan, S., Chen, T., Fang, H. & Yuan, X. Wide-Field Super-Resolved Raman Imaging of Carbon Materials. *ACS Photonics* **8,** 1801–1809 (2021).

153. Holler, M. *et al.* Three-Dimensional Imaging of Integrated Circuits with Macro- to Nanoscale Zoom. *Nat. Electron.* **2,** 464–470 (2019).

154. Moulder, J., Stickle, W., Sobol, P. & Bomben, K. *Handbook of X-ray Photoelectron Spectroscopy* (ed Chastain, J.) (Perkin-Elmer Corporation, 1992).

155. Stevie, F. A. & Donley, C. L. Introduction to X-ray Photoelectron Spectroscopy. *J. Vac. Sci. Technol. A* **38,** 063204 (2020).

156. Tanuma, S., Powell, C. J. & Penn, D. R. Calculations of Electron Inelastic Mean Free Paths. IX. Data for 41 Elemental Solids Over the 50 eV to 30 keV Range. *Surf. Interface Anal.* **43,** 689–713 (2011).

157. Major, G. H., Fairley, N., Sherwood, P. M. A., Linford, M. R., Terry, J., Fernandez, V. & Artyushkova, K. Practical Guide for Curve Fitting in X-ray Photoelectron Spectroscopy. *J. Vac. Sci. Technol. A* **38,** 061203 (2020).

158. Morgan, D. J. XPS Insights: Asymmetric Peak Shapes in XPS. *Surf. Interface Anal.* **55,** 567–571 (2023).

159. Shard, A. G. Practical Guides for X-ray Photoelectron Spectroscopy: Quantitative XPS. *J. Vac. Sci. Technol. A* **38,** 041201 (2020).

160. Brundle, C. R. & Crist, B. V. X-ray Photoelectron Spectroscopy: A Perspective on Quantitation Accuracy for Composition Analysis of Homogeneous Materials. *J. Vac. Sci. Technol. A* **38,** 041001 (2020).

161. Boettcher, S. W., Oener, S. Z., Lonergan, M. C., Surendranath, Y., Ardo, S., Brozek, C. & Kempler, P. A. Potentially Confusing: Potentials in Electrochemistry. *ACS Energy Lett.* **6,** 261–266 (2020).

162. Newman, J. & Thomas-Alyea, K. E. *Electrochemical Systems, 3rd Edition* (Wiley, 2004).

163. Huggins, R. A. The Relation Between the Gibbs Phase Rule and Reference Electrodes. *Ionics* **4,** 129–140 (1998).

164. Xiao, Y., Xu, R., Yan, C., Huang, J.-Q., Zhang, Q. & Ouyang, M. A Toolbox of Reference Electrodes for Lithium Batteries. *Adv. Funct. Mater.* **32,** 2108449 (2021).

165. Wood, K. N., Kazyak, E., Chadwick, A. F., Chen, K. H., Zhang, J. G., Thornton, K. & Dasgupta, N. P. Dendrites and Pits: Untangling the Complex Behavior of Lithium Metal Anodes through *Operando* Video Microscopy. *ACS Cent. Sci.* **2,** 790–801 (2016).

166. Wang, S., Zhang, J., Gharbi, O., Vivier, V., Gao, M. & Orazem, M. E. Electrochemical Impedance Spectroscopy. *Nat. Rev. Methods Primers* **1,** 41 (2021).

167. Lazanas, A. C. & Prodromidis, M. I. Electrochemical Impedance Spectroscopy—A Tutorial. *ACS Meas. Sci. Au* **3,** 162–193 (2023).

168. Li, M., Feng, M., Luo, D. & Chen, Z. Fast Charging Li-Ion Batteries for a New Era of Electric Vehicles. *Cell Rep. Phys. Sci.* **1,** 100212 (10 2020).

169. Tomaszewska, A. *et al.* Lithium-Ion Battery Fast Charging: A Review. *eTransportation* **1,** 100011 (2019).

170. Matsuda, Y. Behavior of Some Ions in Mixed Organic Electrolytes of High Energy Density Batteries. *J. Electrochem. Soc.* **128,** 2552 (1981).

171. Landesfeind, J., Hosaka, T., Graf, M., Kubota, K., Komaba, S. & Gasteiger, H. A. Comparison of Ionic Transport Properties of Non-Aqueous Lithium and Sodium Hexafluorophosphate Electrolytes. *J. Electrochem. Soc.* **168,** 040538 (2021).

172. Okoshi, M., Yamada, Y., Komaba, S., Yamada, A. & Nakai, H. Theoretical Analysis of Interactions Between Potassium Ions and Organic Electrolyte Solvents: A Comparison with Lithium, Sodium, and Magnesium Ions. *J. Electrochem. Soc.* **164,** A54–A60 (2017).

173. Abe, T., Fukuda, H., Iriyama, Y. & Ogumi, Z. Solvated Li-Ion Transfer at Interface Between Graphite and Electrolyte. *J. Electrochem. Soc.* **151,** A1120 (2004).

174. Bergstrom, H. K., Fong, K. D. & McCloskey, B. D. Interfacial Effects on Transport Coefficient Measurements in Li-Ion Battery Electrolytes. *J. Electrochem. Soc.* **168,** 060543 (2021).

175. Landesfeind, J. & Gasteiger, H. A. Temperature and Concentration Dependence of the Ionic Transport Properties of Lithium-Ion Battery Electrolytes. *J. Electrochem. Soc.* **166,** A3079–A3097 (2019).

176. Nyman, A., Behm, M. & Lindbergh, G. Electrochemical Characterisation and Modelling of the Mass Transport Phenomena in $LiPF_6$–EC–EMC Electrolyte. *Electrochim. Acta* **53,** 6356–6365 (2008).

177. Valoen, L. O. & Reimers, J. N. Transport Properties of $LiPF_6$-based Li-Ion Battery Electrolytes. *J. Electrochem. Soc.* **152,** A882 (2005).

178. Lundgren, H., Behm, M. & Lindbergh, G. Electrochemical Characterization and Temperature Dependency of Mass-transport Properties of $LiPF_6$ in EC:DEC. *J. Electrochem. Soc.* **162,** A413–A420 (2015).

179. Lundgren, H., Scheers, J., Behm, M. & Lindbergh, G. Characterization of the Mass-transport Phenomena in a Superconcentrated LiTFSI:Acetonitrile Electrolyte. *J. Electrochem. Soc.* **162,** A1334–A1340 (2015).

180. Steinrück, H.-G. *et al.* Concentration and Velocity Profiles in a Polymeric Lithium-Ion Battery Electrolyte. *Energy Environ. Sci* (2020).

181. Bazak, J. D., Allen, J. P., Krachkovskiy, S. A. & Goward, G. R. Mapping of Lithium-Ion Battery Electrolyte Transport Properties and Limiting Currents with *In Situ* MRI. *J. Electrochem. Soc.* **167,** 140518 (2020).

182. Hosaka, T., Muratsubaki, S., Kubota, K., Onuma, H. & Komaba, S. Potassium Metal as Reliable Reference Electrodes of Nonaqueous Potassium Cells. *J. Phys. Chem. Lett.* **10,** 3296–3300 (2019).

183. Xiao, N., McCulloch, W. D. & Wu, Y. Reversible Dendrite-Free Potassium Plating and Stripping Electrochemistry for Potassium Secondary Batteries. *J. Am. Chem. Soc.* **139,** 9475–9478 (2017).

184. Hosaka, T., Fukabori, T., Matsuyama, T., Tatara, R., Kubota, K. & Komaba, S. 1,3,2-Dioxathiolane 2,2-Dioxide as an Electrolyte Additive for K-metal Cells. *ACS Energy Lett.* **4,** 3643–3649 (2021).

185. Aspinall, J., Armstrong, D. E. J. & Pasta, M. EBSD-Coupled Indentation: Nanoscale Mechanics of Lithium Metal. *Mater. Today Energy* **30,** 101183 (2022).

186. Caracciolo, L., Madec, L. & Martinez, H. XPS Analysis of K-based Reference Compounds to Allow Reliable Studies of Solid Electrolyte Interphase in K-Ion Batteries. *ACS Appl. Energy Mater.* **4,** 11693–11699 (2021).

187. Encyclopædia Britannica, Inc. Potassium. `www.britannica.com/science/potassium` (accessed 2025-03-31) (2025).

188. Xue, L., Gao, H., Zhou, W., Xin, S., Park, K., Li, Y. & Goodenough, J. B. Liquid K-Na Alloy Anode Enables Dendrite-Free Potassium Batteries. *Adv. Mater.* **28,** 9608–9612 (2016).

189. Popovic, J. Review–Recent Advances in Understanding Potassium Metal Anodes. *J. Electrochem. Soc.* **169,** 030510 (2022).

190. Crist, B. V. Argon Implanted into Graphite, by XPS. *Surf. Sci. Spectra* **1,** 376–380 (1992).

191. Schmitz, R., Müller, R., Krüger, S., Schmitz, R. W., Nowak, S., Passerini, S., Winter, M. & Schreiner, C. Investigation of Lithium Carbide Contamination in Battery Grade Lithium Metal. *J. Power Sources* **217,** 98–101 (2012).

192. Kanamura, K., Shiraishi, S., Tamura, H. & Takehara, Z. X-Ray Photoelectron Spectroscopic Analysis and Scanning Electron Microscopic Observation of the Lithium Surface Immersed in Nonaqueous Solvents. *J. Electrochem. Soc.* **141,** 2379–2385 (1994).

193. Fonseca Rodrigues, M.-T., Maroni, V. A., Gosztola, D. J., Yao, K. P. C., Kalaga, K., Shkrob, I. A. & Abraham, D. P. Lithium Acetylide: A Spectroscopic Marker for Lithium Deposition During Fast Charging of Li-Ion Cells. *ACS Appl. Energy Mater.* **2,** 873–881 (2018).

194. Pan, J. S., Wee, A. T. S., Huan, C. H. A., Tan, H. S. & Tan, K. L. Argon Incorporation and Silicon Carbide Formation During Low Energy Argon-Ion Bombardment of Si(100). *J. Appl. Phys.* **79,** 2934–2941 (1996).

195. Luthin, J., Plank, H., Roth, J. & Linsmeier, C. Ion Beam-Induced Carbide Formation at the Titanium–Carbon Interface. *Nucl. Instrum. Methods Phys. Res. B* **182,** 218–226 (2001).

196. Diederichsen, K. M., McShane, E. J. & McCloskey, B. D. Promising Routes to a High Li^+ Transference Number Electrolyte for Lithium Ion Batteries. *ACS Energy Lett.* **2,** 2563–2575 (2017).

197. Bruce, P. G. & Vincent, C. A. Steady State Current Flow in Solid Binary Electrolyte Cells. *J. Electroanal. Chem.* **225,** 1–17 (1987).

198. Wang, A. A., Greenbank, S., Li, G., Howey, D. A., Monroe, C. W., Howey, A. & Monroe, C. W. Current-driven Solvent Segregation in Lithium-Ion Electrolytes. *Cell Rep. Phys. Sci.* **3,** 101047 (2022).

199. Mönich, C., Andersson, R., Hernández, G., Mindemark, J. & Schönhoff, M. Seeing the Unseen: Mg^{2+}, Na^+, and K^+ Transference Numbers in Post-Li Battery Electrolytes by Electrophoretic Nuclear Magnetic Resonance. *J. Am. Chem. Soc.* **146,** 11105–11114 (2024).

200. Casteel, J. F. & Amis, E. S. Specific Conductance of Concentrated Solutions of Magnesium Salts in Water-Ethanol System. *J. Chem. Eng. Data* **17,** 55–59 (1972).

201. Zhang, P., Jin, H., Wang, T. & Wang, M. Insight into the Effect of Lithium-dendrite Suppression by Lithium bis(fluorosulfony)imide/1,2-dimethoxyethane Electrolytes. *Electrochim. Acta* **277,** 116–126 (2018).

202. Hosaka, T., Kubota, K., Kojima, H. & Komaba, S. Highly Concentrated Electrolyte Solutions for 4 V Class Potassium-Ion Batteries. *Chem comm* **54,** 8387–8390 (2018).

203. Raccichini, R., Dibden, J. W., Brew, A., Owen, J. R. & García-Aráez, N. Ion Speciation and Transport Properties of LiTFSI in 1,3-Dioxolane Solutions: A Case Study for Li-S Battery Applications. *J. Phys. Chem. B* **122,** 267–274 (2018).

204. Le Pham, P. N., Gabaudan, V., Boulaoued, A., Åvall, G., Salles, F., Johansson, P., Monconduit, L. & Stievano, L. Potassium-Ion batteries using KFSI in Monoglyme Electrolytes: Implications of Cation Solvation on the K^+-graphite (Co-)intercalation Mechanism. *Energy Storage Mater.* **45,** 291–300 (2022).

205. Zhang, Q., Mao, J., Pang, W. K., Zheng, T., Sencadas, V., Chen, Y., Liu, Y. & Guo, Z. Boosting the Potassium Storage Performance of Alloy-Based Anode Materials via Electrolyte Salt Chemistry. *Adv. Energy Mater.* **8,** 1703288 (2018).

206. Wang, L. *et al.* TiS_2 as a High Performance Potassium Ion Battery Cathode in Ether-Based Electrolyte. *Energy Storage Mater.* **12,** 216–222 (2018).

207. Yim, C.-H. & Abu-Lebdeh, Y. A. Connection between Phase Diagram, Structure and Ion Transport in Liquid, Aqueous Electrolyte Solutions of Lithium Chloride. *J. Electrochem. Soc.* **165,** A547–A556 (2018).

208. Stewart, S. & Newman, J. Measuring the Salt Activity Coefficient in Lithium-battery Electrolytes. *J. Electrochem. Soc.* **155,** A458 (2008).

209. Pitzer, K. S. *Activity Coefficients in Electrolyte Solutions, 2nd Edition* (CRC Press, 2018).

210. Zhang, X., Meng, J., Wang, X., Xiao, Z., Wu, P. & Mai, L. Comprehensive Insights into Electrolytes and Solid Electrolyte Interfaces in Potassium-Ion Batteries. *Energy Storage Mater.* **38,** 30–49 (2021).

211. Harned, H. S. & French, D. M. A Conductance Method for the Determination of the Diffusion Coefficients of Electrolytes. *Ann. NY Acad. Sci.* **46,** 267–284 (1945).

212. Newman, J. & Chapman, T. W. Restricted Diffusion in Binary Solutions. *AIChE J* **19,** 343–348 (1973).

213. Ma, Y., Doyle, M., Fuller, T. F., Doeff, M. M., De Jonghe, L. C. & Newman, J. The Measurement of a Complete Set of Transport Properties for a Concentrated Solid Polymer Electrolyte Solution. *J. Electrochem. Soc.* **142,** 1859–1868 (1995).

214. Ehrl, A., Landesfeind, J., Wall, W. A. & Gasteiger, H. A. Determination of Transport Parameters in Liquid Binary Lithium Ion Battery Electrolytes. *J. Electrochem. Soc.* **164,** A826–A836 (2017).

215. Thompson, S. D. & Newman, J. Differential Diffusion Coefficients of Sodium Polysulfide Melts. *J. Electrochem. Soc.* **136,** 3362–3369 (1989).

216. Nečas, D. & Klapetek, P. Gwyddion: An Open-Source Software for SPM Data Analysis. *Open Phys.* **10,** 181–188 (2012).

217. Fairley, N. *et al.* Systematic and Collaborative Approach to Problem Solving Using X-ray Photoelectron Spectroscopy. *Appl. Surf. Sci. Adv.* **5,** 100112 (2021).

218. Wang, H., Yu, Z., Kong, X., Kim, S. C., Boyle, D. T., Qin, J., Bao, Z. & Cui, Y. Liquid Electrolyte: The Nexus of Practical Lithium Metal Batteries. *Joule* **6,** 588–616 (2022).

219. Di Lecce, D., Marangon, V., Jung, H.-G., Tominaga, Y., Greenbaum, S. & Hassoun, J. Glyme-Based Electrolytes: Suitable Solutions for Next-Generation Lithium Batteries. *Green Chem.* **24,** 1021–1048 (2022).

220. Olbrich, L., Pianta, N., Jagger, B. & Pasta, M. EIS Investigation of the SEI Formed on Lithium Metal Anodes. *In Preparation.*

221. She, F., Gao, A., Jiang, P., Zhou, Y., Zhang, X., Yang, M., Gong, L., Chen, J., Lu, X. & Xie, F. Exploring the Stability of Lithium Metal Surface by X-ray Photoelectron Spectroscopy. *Vacuum* **211,** 111893 (2023).

222. Liang, Y., Burton, M., Jagger, B., Guo, H., Ihli, J. & Pasta, M. *In Situ* XPS Investigation of the SEI Formed on LGPS and LAGP with Metallic Lithium. *Chem. Commun.* **60,** 12597–12600 (2024).

223. Wang, Y.-Y., Zhang, X.-Q., Zhou, M.-Y. & Huang, J.-Q. Mechanism, Quantitative Characterization, and Inhibition of Corrosion in Lithium Batteries. *Nano Res. Energy* **2** (2023).

224. Wood, D. L., Li, J. & An, S. J. Formation Challenges of Lithium-Ion Battery Manufacturing. *Joule* **3,** 2884–2888 (2019).

225. Yu, W. *et al.* Electrochemical Formation of Bis(fluorosulfonyl)imide-Derived Solid-Electrolyte Interphase at Li-Metal Potential. *Nat. Chem.* **17,** 246–255 (2025).

226. Biesinger, M. C. Accessing the Robustness of Adventitious Carbon for Charge Referencing (Correction) Purposes in XPS Analysis: Insights from a Multi-User Facility Data Review. *Appl. Surf. Sci.* **597,** 153681 (2022).

227. Narayanan, S., Ulissi, U., Gibson, J. S., Chart, Y. A., Weatherup, R. S. & Pasta, M. Effect of Current Density on the Solid Electrolyte Interphase Formation at the Lithium|Li_6PS_5Cl Interface. *Nat. Commun.* **13,** 7237 (2022).

228. Henderson, J. D., Payne, B. P., McIntyre, N. S. & Biesinger, M. C. Enhancing Oxygen Spectra Interpretation by Calculating Oxygen Linked to Adventitious Carbon. *Surf. Interface Anal.* **57,** 214–220 (2025).

229. Wood, K. N. & Teeter, G. XPS on Li-Battery-Related Compounds: Analysis of Inorganic SEI Phases and a Methodology for Charge Correction. *ACS Appl. Energy Mater.* **1,** 4493–4504 (2018).

230. Menkin, S., O'Keefe, C. A., Gunnarsdottir, A. B., Dey, S., Pesci, F. M., Shen, Z., Aguadero, A. & Grey, C. P. Toward an Understanding of SEI Formation and Lithium Plating on Copper in Anode-Free Batteries. *J. Phys. Chem. C* **125,** 16719–16732 (2021).

231. Tian, N., Hua, C., Wang, Z. & Chen, L. Reversible reduction of Li_2CO_3. *J. Mater. Chem. A* **3,** 14173–14177 (2015).

232. Lacey, M. J., Yalamanchili, A., Maibach, J., Tengstedt, C., Edström, K. & Brandell, D. The Li–S battery: An Investigation of Redox Shuttle and Self-Discharge Behaviour with $LiNO_3$-Containing Electrolytes. *RSC Adv.* **6,** 3632–3641 (2016).

233. Fujita, Y., Motohashi, K., Ding, J., Tsukasaki, H., Mori, S., Sakuda, A. & Hayashi, A. Lithium Sulfite Enhances Cycle Performance of All-Solid-State Batteries with Li_2S-Based Positive Electrode Materials. *ACS Appl. Energy Mater.* **7,** 5447–5456 (2024).

234. Srout, M., Carboni, M., Gonzalez, J. A. & Trabesinger, S. Insights into the Importance of Native Passivation Layer and Interface Reactivity of Metallic Lithium by Electrochemical Impedance Spectroscopy. *Small* **19,** e2206252 (2023).

235. Drvarič Talian, S., Moškon, J., Tchernychova, E., Dominko, R. & Gaberšček, M. Influence of the Cell Casing on the Impedance of the Lithium Metal Electrode. *J. Electrochem. Soc.* **170,** 110529 (2023).

236. Santos, E. & Schmickler, W. The Crucial Role of Local Excess Charges in Dendrite Growth on Lithium Electrodes. *Angew. Chem., Int. Ed. Engl.* **60,** 5876–5881 (2021).

237. Wan, C., Hu, M. Y., Borodin, O., Qian, J., Qin, Z., Zhang, J.-G. & Hu, J. Z. Natural Abundance ^{17}O, ^{6}Li NMR and Molecular Modeling Studies of the Solvation Structures of Lithium Bis(fluorosulfonyl)imide/1,2-Dimethoxyethane Liquid Electrolytes. *J. Power Sources* **307,** 231–243 (2016).

238. Zhao, J., Jagger, B., Sun, S., Xu, Y. & Pasta, M. *Operando* Raman Gradient Analysis for Data-Driven Electrolyte Discovery. *In Preparation.*

239. Wildersinn, L., Stottmeister, D., Jeschull, F., Gross, A. & Hofmann, A. Decomposition of Binary Mixtures of DMC/EC, EMC/EC, and DEC/EC on Potassium Surfaces; GC, XPS, and Calculation. *ACS Appl. Mater. Interfaces.* **17,** 10055–10072 (2025).

240. Stoch, J. & Ladecka, M. An XPS Study of the KCl Surface Oxidation in Oxygen Glow Discharge. *Appl. Surf. Sci.* **31,** 426–436 (1988).

241. Dupin, J.-C., Gonbeau, D., Vinatier, P. & Levasseur, A. Systematic XPS Studies of Metal Oxides, Hydroxides and Peroxides. *Phys. Chem. Chem. Phys.* **2,** 1319–1324 (2000).

242. Han, Y., Vijaya Kumar Saroja, A. P., Tinker, H. R. & Xu, Y. Interphases in the Electrodes of Potassium Ion Batteries. *J. Phys. Mater.* **5,** 022001 (2022).

243. Zhang, Y., Yi, X., Fu, H., Wang, X., Gao, C., Zhou, J., Rao, A. M. & Lu, B. Reticular Elastic Solid Electrolyte Interface Enabled by an Industrial Dye for Ultrastable Potassium-Ion Batteries. *Small Struct.* **5,** 2300232 (2024).

244. Liu, Q., Rao, A. M., Han, X. & Lu, B. Artificial SEI for Superhigh-Performance K-Graphite Anode. *Adv. Sci.* **8,** 2003639 (2021).

245. Ells, A. W., May, R. & Marbella, L. E. Potassium Fluoride and Carbonate Lead to Cell Failure in Potassium-Ion Batteries. *ACS Appl. Mater. Interfaces* **13,** 53841–53849 (2021).

246. Alshangiti, O., Galatolo, G., Di Mino, C., Headen, T. F., Christianson, J., Merotto, S., Rees, G. J., Delavoux, Y., Swadzba-Kwasny, M. & Pasta, M. Imidazolium-Based Ionic Liquid Electrolytes for Fluoride Ion Batteries. *ACS Energy Lett.* **9,** 6104–6108 (2024).

247. Qin, L., Schkeryantz, L., Zheng, J., Xiao, N. & Wu, Y. Superoxide-Based K-O_2 Batteries: Highly Reversible Oxygen Redox Solves Challenges in Air Electrodes. *J. Am. Chem. Soc.* **142,** 11629–11640 (2020).

248. Fujimoto, R., Tatara, R., Hosaka, T., Igarashi, D. & Komaba, S. Stability of RbO_2 as a Discharge Product of Metal-O_2 Batteries. *J. Am. Chem. Soc.* **147,** 6747–6752 (2025).

249. Kruh, R., Fuwa, K. & McEver, T. E. The Crystal Structures of Alkali Metal Bifluorides. *J. Am. Chem. Soc.* **78,** 4256–4258 (1956).

250. Xu, Y. *et al.* 2023 Roadmap for Potassium-Ion Batteries. *J. Phys. Energy* **5,** 021502 (2023).

251. Panasenko, I., Bäuerle, M. & Jeschull, F. How Reference Electrodes Improve Our Understanding of Degradation Processes in Half and Full Cell Potassium-Ion Battery Setups. *Electrochim. Acta* **513,** 145551 (2025).

252. Linsenmann, F., Pritzl, D. & Gasteiger, H. A. A Reference Electrode for *In Situ* Impedance Measurements in Sodium-Ion Batteries. *J. Electrochem. Soc.* **166,** A3668–A3674 (2019).

253. Santhosha, A. L., Medenbach, L., Buchheim, J. R. & Adelhelm, P. The Indium-Lithium Electrode in Solid-State Lithium-Ion Batteries: Phase Formation, Redox Potentials, and Interface Stability. *Batteries & Supercaps* **2,** 524–529 (2019).

254. Aspinall, J., Chart, Y., Guo, H., Shrestha, P., Burton, M. & Pasta, M. Effect of Microstructure on the Cycling Behavior of Li–In Alloy Anodes for Solid-State Batteries. *ACS Energy Lett.* **9,** 578–585 (2024).

255. Okamoto, H. In-K (Indium-Potassium). *J. Phase Equilib.* **13,** 217–218 (1992).

256. Bruzzone, G. The $D1_3$ Structure Type in Intermetallic Compounds. *Acta Crystallogr. B* **25,** 1206–1207 (1969).

257. Cordier, G. & Müller, V. Verbindungen an der Zintl-Grenze: Darstellung und Kristallstruktur von $Na_{17}Ga_{29}In_{12}$ und $K_{17}In_{41}$. *Z. Naturforsch. B* **49,** 721–728 (1994).

258. Sevov, S. C. & Corbett, J. D. A Remarkable Hypoelectronic Indium Cluster in K_8In_{11}. *Inorg. Chem.* **30,** 4875–4877 (1991).

259. Gu, Y., Ru Pei, Y., Zhao, M., Cheng Yang, C. & Jiang, Q. Sn-, Sb- and Bi-Based Anodes for Potassium Ion Battery. *Chem. Rec.,* e202200098 (2022).

260. Lei, K., Wang, C., Liu, L., Luo, Y., Mu, C., Li, F. & Chen, J. A Porous Network of Bismuth Used as the Anode Material for High-Energy-Density Potassium-Ion Batteries. *Angew. Chem. Int. Ed. Engl.* **57,** 4687–4691 (2018).

261. Ud Din, M. A., Li, C., Zhang, L., Han, C. & Li, B. Recent Progress and Challenges on the Bismuth-Based Anode for Sodium-Ion Batteries and Potassium-Ion Batteries. *Mater. Today Phys.* **21,** 100486 (2021).

262. Liu, S., Mao, J., Zhang, Q., Wang, Z., Pang, W. K., Zhang, L., Du, A., Sencadas, V., Zhang, W. & Guo, Z. An Intrinsically Non-flammable Electrolyte for High-Performance Potassium Batteries. *Angew. Chem. Int. Ed. Engl.* **59,** 3638–3644 (2020).

263. Deng, L. *et al.* Defect-Free Potassium Manganese Hexacyanoferrate Cathode Material for High-Performance Potassium-Ion Batteries. *Nat. Commun.* **12,** 2167 (2021).

264. Yao, X. *et al.* Voltage Plateau Variation in a Bismuth-Potassium Battery. *J. Mater. Chem. A* **10,** 2917–2923 (2022).

265. Petric, A. & Pelton, A. D. The Bi-K Bismuth-Potassium System. *J. Phase Equilib.* **12,** 29–33 (1991).

266. Kang, S. D. & Chueh, W. C. Galvanostatic Intermittent Titration Technique Reinvented: Part I. A Critical Review. *J. Electrochem. Soc.* **168,** 120504 (2021).

267. Zhang, Q., Mao, J., Pang, W. K., Zheng, T., Sencadas, V., Chen, Y., Liu, Y. & Guo, Z. Boosting the Potassium Storage Performance of Alloy-Based Anode Materials via Electrolyte Salt Chemistry. *Adv. Energy Mater.* **8,** 1703288 (2018).

268. Zhang, R., Bao, J., Wang, Y. & Sun, C. F. Concentrated Electrolytes Stabilize Bismuth-Potassium Batteries. *Chem. Sci.* **9,** 6193–6198 (2018).

269. Emmerling, F., Längin, N., Petri, D., Kroeker, M. & Röhr, C. Alkali Metal Bismuthides ABi and ABi_2 (A = K, Rb, Cs) – Synthesis, Crystal Structure, Properties. *Z. Anorg. Allg. Chem.* **630,** 171–178 (2004).

270. Schneider, C. A., Rasband, W. S. & Eliceiri, K. W. NIH Image to ImageJ: 25 Years of Image Analysis. *Nat. Methods* **9,** 671–675 (2012).

271. AZO Materials. An Insight to Bismuth. `www.azom.com/properties.aspx?ArticleID=590` (accessed 2025-03-31) (2001).

272. Wang, W.-W., Gu, Y., Wang, J.-H., Chen, Z.-B., Yin, X.-T., Wu, Q.-H., Yan, J.-W. & Mao, B.-W. Probing Mechanical Properties of Solid-Electrolyte Interphases on Li Nuclei by *In Situ* AFM. *J. Electrochem. Soc.* **169,** 020563 (2022).

273. Cometto, C., Yan, G., Mariyappan, S. & Tarascon, J.-M. Means of Using Cyclic Voltammetry to Rapidly Design a Stable DMC-Based Electrolyte for Na-Ion Batteries. *J. Electrochem. Soc.* **166,** A3723–A3730 (2019).

274. Lin, Y., Chen, J., Zhang, H. & Wang, J. *In-Situ* Construction of High-Mechanical-Strength and Fast-Ion-Conductivity Interphase for Anode-Free Li Battery. *J. Energy Chem.* **80,** 207–214 (2023).

275. Zhao, L.-K., Gao, X.-W., Gu, Q., Ge, X., Ding, Z., Liu, Z. & Luo, W.-B. Realizing a Dendrite-Free Metallic-Potassium Anode Using Reactive Prewetting Chemistry. *eScience* **4,** 100201 (2024).

276. Fantauzzi, M., Elsener, B., Atzei, D., Rigoldi, A. & Rossi, A. Exploiting XPS for the Identification of Sulfides and Polysulfides. *RSC Adv.* **5,** 75953–75963 (2015).

277. Coelho, A. A. TOPAS-Academic, V6. Coelho Software: Brisbane (2016).

278. Murbach, M. D., Gerwe, B., Dawson-Elli, N. & Tsui, L.-k. impedance.py: A Python Package for Electrochemical Impedance Analysis. *J. Open. Source Softw.* **5,** 2349 (2020).

279. Oliver, W. C. & Pharr, G. M. An Improved Technique for Determining Hardness and Elastic Modulus Using Load and Displacement Sensing Indentation Experiments. *J. Mater. Res.* **7,** 1564–1583 (1992).